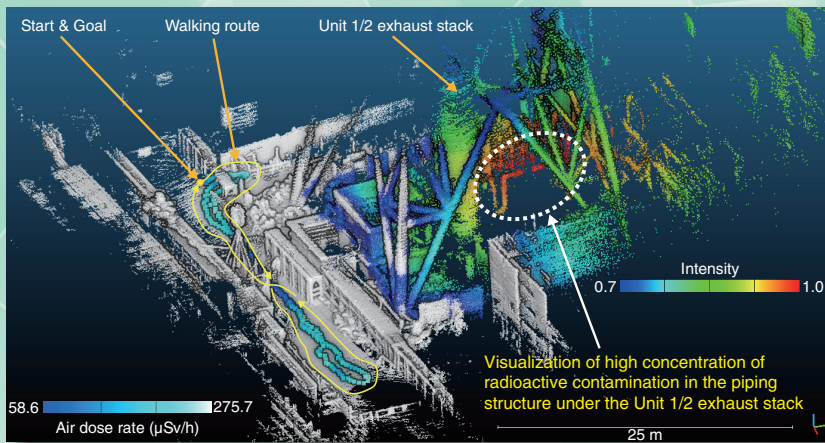


# JAEA R&D Review

## 2022-23



3D map visualizing the air dose rate and highly contaminated region near Unit 1/2 exhaust stack at TEPCO's Fukushima Daiichi NPS (Topic 1-10)



HTR-Hydrogen Production Test Facility (Chapter 6, Highlight)

## *Message from President KOGUCHI*



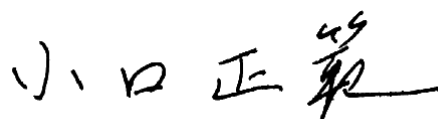
We sincerely thank you for your understanding and continued support for the research and development (R&D) activities of the Japan Atomic Energy Agency (JAEA).

The mission of JAEA is to contribute to the welfare and prosperity of human society through nuclear science and technology (S&T). JAEA has been working on this mission, prioritizing safety, and taking measures against COVID-19.

In response to the accident at the Fukushima Daiichi Nuclear Power Station, we have been working on the R&D of decommissioning and environmental recovery while developing an R&D base in Fukushima Prefecture. Additionally, we are striving to create pioneering research results in material science using neutrons and synchrotron radiation at JRR-3 and J-PARC, etc., in advanced research aimed at discovering new principles and phenomena and in research on improving safety. In the development of fast reactors and advanced reactors, we are undertaking R&D on high-temperature gas-cooled reactor technology, which is expected to achieve carbon neutrality by 2050. We also aim for an early resumption of the operation of the experimental fast reactor Joyo. Furthermore, we will safely and steadily proceed with R&D on radioactive waste treatment and disposal technology and the decommissioning of nuclear facilities, such as Monju, Fugen, Tokai Reprocessing Plants, etc.

In the Future Vision “JAEA 2050+”, JAEA states that it will achieve a “New Era Nuclear S&T” that contributes to solving social issues by promoting the synergy between nuclear energy and other fields. As one of our efforts to achieve this goal, we established JAEA Innovation Hub last year to promote innovation activities. We will continue to strengthen our efforts to disseminate R&D results, such as bridging R&D results for application to the industry.

In this publication, we introduce the latest R&D results obtained from the R&D activities of JAEA. We hope that this publication will help you understand our R&D activities. We would appreciate your continued encouragement and support.



January 2023  
KOGUCHI Masanori  
President, JAEA



About This Publication and the JAEA Organizational Outline	10
--	----

# 1 Research and Development Related to the Accident at TEPCO's Fukushima Daiichi NPS

<b>Highlight</b>	Assistance in Environmental Restoration and Decommissioning	12
<b>1-1</b>	<b>Degradation of Fuel Debris Under the Effect of Ionizing Radiation</b> – Formation of Solid Solution Improves Stability to Oxidative Degradation – Yuta Kumagai	14
<b>1-2</b>	<b>Criticality Evaluation of Fuel Debris with Unclear Material Composition</b> – Development of a New Subcritical Depletion Code for Monitoring Noble Gases – Eka Sapta Riyana	15
<b>1-3</b>	<b>Clarifying the Failure Mechanism of the Lower Part of the RPV</b> – Melting Test Assuming a Eutectic Reaction in the Complex Structure of a BWR – Takuya Yamashita	16
<b>1-4</b>	<b>How to Effectively Remove Iodate from Solutions?</b> – Coprecipitation of Iodate with Barite (BaSO <sub>4</sub> ) Was Evaluated at a Molecular Level – Kohei Tokunaga	17
<b>1-5</b>	<b>Characterization of Radioactive Waste for Safe Storage</b> – Effect on the Chemical Composition of Carbonate Slurry – Takuma Horita	18
<b>1-6</b>	<b>Realization of <math>\gamma</math>-Ray Nuclide Analysis Under Severe Radiation Fields</b> – Development of a $\gamma$ -Ray Spectrometry System Specific to High Dose Rates for Simple Nondestructive Assays – Masaaki Kaburagi	19
<b>1-7</b>	<b>In-situ Monitoring System for Radioactive Aerosols</b> – Real-Time Monitoring of Alpha Aerosols to Improve Worker Safety – Youichi Tsubota	20
<b>1-8</b>	<b>Simultaneous Measurement of the Energy Spectra of Alpha, Beta, and Gamma Rays</b> – Development of a Portable Continuous Air-Monitoring System for Detecting Alpha/Beta/Gamma Radioactive Material – Yuki Morishita	21
<b>1-9</b>	<b>Novel Single-End Readout-Type Optical Fiber Radiation Sensor</b> – Highly Sensitive Position Detection by Photon Wavelength Analysis Using a New Spectroscopy System – Yuta Terasaka	22
<b>1-10</b>	<b>Visualization of Radioactive Contamination at the Decommissioning Site on a Three-Dimensional Map</b> – Understanding Invisible Radioactive Contamination in a Virtual Space and Reducing Worker Exposure – Yuki Sato	23
<b>1-11</b>	<b>Impact of Extreme Typhoons on Radiocesium Discharge</b> – Comparison of Effects of Two Typhoons–Etau in 2015 and Hagibis in 2019 – Takahiro Nakanishi	24
<b>1-12</b>	<b>Approaching the Secrets of Long-Term Cesium Retention in Lichen</b> – Computational Chemistry Solves the Energetics of Complexation of Metabolites with Cesium – Masahiko Machida	25

<b>1-13</b>	<b>Rapid Analysis for Long Half-Life <sup>99</sup>Tc</b> – ICP-MS Analysis with Solid-Phase Extraction and Gas-Phase Reaction – Makoto Matsueda	26
<b>1-14</b>	<b>Selective Detection of Trace Sr Isotopes Using Lasers</b> – Simplified Pretreatment of Samples Containing Isobars and Stable Isotopes – Yoshihiro Iwata	27
<b>1-15</b>	<b>Toward Confident Hot-Spot Visualization Using an Unmanned Helicopter</b> – Improvement of Detection Accuracy by Selecting Data on the Flight Conditions – Yoshiaki Shikaze	28
<b>1-16</b>	<b>Research on the Decreasing Trend of Atmospheric Radiocesium Concentration After the Accident</b> – Assessing the Decrease Rate Based on Governmental Monitoring Results – Tomohisa Abe	29
<b>1-17</b>	<b>Why Does the Air Dose Rate in Urban Areas Decline Quickly?</b> – Reduction Effect Revealed by the Behavior of Radioactive Cesium – Kazuya Yoshimura	30

## **2** Research on Nuclear Safety and Emergency Preparedness

<b>Highlight</b>	<b>Implementing Continuous Improvements in Safety and Emergency Preparedness</b>	31
<b>2-1</b>	<b>Understanding Reactor Risk Profiles Against External Events</b> – Probabilistic Assessment of Internal Flooding-Induced Risks by a Dynamic Approach – Kotaro Kubo	32
<b>2-2</b>	<b>Understanding Containment Vessel Flow During Severe Accident</b> – Mass Transport Behavior Depending on the Relative Location of Outer Cooling and Initial Stratification – Satoshi Abe	33
<b>2-3</b>	<b>Fuel Debris Form Prediction in a Severe Accident</b> – Measurements of Mass Fractions of Agglomerated Debris Settled on the Floor of a PCV – Yuzuru Iwasawa	34
<b>2-4</b>	<b>Parameter Determination for Assessing the Sheltering Effectiveness in Japanese Houses</b> – Obtaining Data on Penetration Factor and Deposition Rate of Particulate and Elementary Iodine by Real House and Chamber Experiment – Jun Hirouchi	35
<b>2-5</b>	<b>How Much Can Nuclear Piping Withstand Huge Earthquakes</b> – Development of Seismic Fragility Evaluation Method for Aged Piping – Yoshihito Yamaguchi	36
<b>2-6</b>	<b>A Path Toward Recycling and Landfill of Asbestos Waste Arising from Decommissioning</b> – Development of Evaluation Method for Exposure Dose by Cleared Asbestos Waste – Taro Shimada	37

## 3

## Advanced Scientific Research

<b>Highlight</b>	Fundamental Sciences to Realize the New Era of Nuclear Science and Technology	38
<b>3-1</b>	<b>What is the Chemical Behavior of the Heaviest Element?</b> – A Small Breach of the Periodic Law Found in the Volatility of Element 105, Dubnium – Tetsuya K. Sato	39
<b>3-2</b>	<b>Probing the Strong Interaction with Superconducting Detectors</b> – Drastic Precision Improvement in the X-Ray Spectroscopy of Kaonic Atoms – Tadashi Hashimoto	40
<b>3-3</b>	<b>Slow Dynamics of Electrons in Uranium Compounds</b> – Approaching the Mystery of Superconductors Leading to Quantum Computers – Yo Tokunaga	41
<b>3-4</b>	<b>Topology-Based Manipulation of Magnets in Spintronics</b> – New Principle for Power Saving in Magnetic Memories – Yasufumi Araki	42
<b>3-5</b>	<b>Insight into Designing Highly Efficient <i>Ortho-Para</i> Hydrogen Conversion Catalysts</b> – Demonstration of Fast <i>Ortho-Para</i> Conversion of H <sub>2</sub> on a Stepped Surface – Hirokazu Ueta	43
<b>3-6</b>	<b>Unveiling the Retention Mechanisms of Uranium (VI) on Host Rocks</b> – Surface Sorption Process Related to Two Types of Sorption Species – Huiyang Mei	44
<b>3-7</b>	<b>Towards Understanding the Coherent Properties of Bosons</b> – Determination of the Josephson Current in a Bose–Einstein Condensate – Shun Uchino	45

## 4

## Nuclear Science and Engineering Research

<b>Highlight</b>	Fundamental Technologies for Nuclear Energy Innovation	46
<b>4-1</b>	<b>Development of a Low-Cost Transportable Device for Detecting Nuclear Materials</b> – Successful Experimental Demonstration of a New Nondestructive Method – Masao Komeda	47
<b>4-2</b>	<b>Connecting Nuclear Data with Transport Calculation</b> – Development of Nuclear Data Processing Code FRENDY Version 2 – Kenichi Tada	48
<b>4-3</b>	<b>Unveiling the Mystery of the Radiation Damage that Does Not Follow the Conventional Theory</b> – Radiation Damage Mechanism in Ceramics Irradiated with Swift Heavy Ions – Norito Ishikawa	49

<b>4-4</b>	<b>Detailed Radioactive Plume Dispersion and Dose Calculations Considering Buildings in Local Areas</b> – Development of a Local-Scale High-Resolution Atmospheric Dispersion and Dose Assessment System – Hiromasa Nakayama	50
<b>4-5</b>	<b>Nuclear Fuel Cycle Simulator NMB4.0 Released</b> – Development of Fast, Versatile, and Flexible NMB4.0 to Contribute to the Planning of Future Nuclear Energy Utilization Strategies – Kenji Nishihara	51
<b>4-6</b>	<b>Toward the Realization of a Reliability-Oriented Accelerator for the Accelerator-Driven System</b> – Robust Beam Optics Design of a 30-MW LINAC for Nuclear Transmutation – Bruce Yee-Rendon	52
<b>4-7</b>	<b>Improving Adsorption Capacity for Medical Radioisotopes</b> – Elucidation of Molybdate Ion Adsorption Mechanism in Alumina – Yoshitaka Fujita	53

## 5 Neutron and Synchrotron Radiation Research

<b>Highlight</b>	<b>Contributions to Innovative Achievement in Science and Technology</b>	54
<b>5-1</b>	<b>Beam Measurement Using Light Produced by Beam-Gas Interaction</b> – Development of a Gas Sheet Beam Profile Monitor – Ippei Yamada	55
<b>5-2</b>	<b>Acceleration of Neutron Measurement by Deep Learning</b> – Over 10-Fold Acceleration of Neutron Reflectometry Measurement by an Accurate Noise Reduction Method – Hiroyuki Aoki	56
<b>5-3</b>	<b>Wide Bandwidth Neutron-Spin Polarizer</b> – A Breakthrough in Neutron-Polarizing Supermirror with Very High Critical Momentum Transfer – Ryuji Maruyama	57
<b>5-4</b>	<b>Discovery of Coupled Fluctuations with Protein Domain Structures and Active Sites</b> – Analysis of Protein Dynamics by Neutron Scattering and Molecular Simulation – Hiroshi Nakagawa	58
<b>5-5</b>	<b>Development of Nuclear Vitrification by Neutron Scattering</b> – Nanoscopic Structure of Borosilicate Glass with Additives – Ryuhei Motokawa	59
<b>5-6</b>	<b>Fabrication of Environment-Friendly Piezoelectric Materials</b> – Local Structural Analysis of $\text{Bi}_{0.5}\text{Na}_{0.5}\text{TiO}_3$ in the High-Temperature Phase – Yasuhiro Yoneda	60
<b>5-7</b>	<b>How Heavy Electrons are Formed in Eu-Based Compounds</b> – Direct Observation of the Band Structure of Eu 4f Orbitals, Which Have Magnetic and Localized Characteristics, by Synchrotron Radiation Experiments – Ikuto Kawasaki	61

## 6

## HTGR Hydrogen and Heat Application Research

## Highlight

Research and Development on HTGR, Hydrogen Production, and Heat Application Technologies 62

- 
- 6-1** **New Seismic Classification of the HTTR**  
– Appropriate Seismic Classification Based on Technical Knowledge and Operation Experience – Masato Ono 63
- 
- 6-2** **Challenge to Measure the Power Distribution in Very-High-Temperature Core Environments**  
– Development of a Power Distribution Measurement Method Using Neutrons Leaked from an HTGR Core – Yuji Fukaya 64
- 
- 6-3** **For Reducing the Cost of Construction of High-Temperature Gas-Cooled Reactors**  
– Development of Cesium Trap Material for Coated Fuel Particles – Jun Aihara 65
- 
- 6-4** **Upgrading H<sub>2</sub> Production Efficiency in the IS Process**  
– Corrosion Stability Improvement of the H<sub>2</sub> Separation Membrane for HI Decomposition – Odtsetseg Myagmarjav 66
- 
- 6-5** **Achievement of Longer-Term H<sub>2</sub> Production in IS Process**  
– Introduction of a Novel Operating Procedure Using a Closed-Loop System – Nobuyuki Tanaka 67
- 
- 6-6** **Development of a Novel RPV Cooling System for HTGRs**  
– Comparison of the Structural Differences Between RPV Cooling Systems and Effects of External Parameters on RPV Cooling – Kuniyoshi Takamatsu 68
- 
- 6-7** **Toward More Accurate Core Analysis of High-Temperature Gas-Cooled Reactors**  
– Development of a Core Analysis Method with Specified Graphite Porosities – Shoichiro Okita 69
- 

## 7

## Research and Development of Fast Reactors

## Highlight

Development of the Technology Base and Infrastructure Toward Improving the Fast Reactor Cycle 70

- 
- 7-1** **Fast Simulation Method for Chemically Reacting Flows**  
– Efficient Numerical Simulation for Developing New-Generation Nuclear Plants – Wataru Kosaka 71
- 
- 7-2** **Understanding Aerosol Behavior in Fast Reactor Accidents**  
– Test on Aerosol Transport Behavior Using the MET Facility – Ryota Umeda 72
- 
- 7-3** **Failure Prediction of Fast Reactor Components**  
– Cyclic Loading Test and Failure Prediction of Multiperforated Plates – Masanori Ando 73
-

<b>7-4</b>	<b>Capturing the Oxygen Diffusion Phenomena in Nuclear Fuel</b> – Measurement and Evaluation of the Oxygen Self-Diffusion Coefficient of MOX Fuel – Masashi Watanabe	74
<b>7-5</b>	<b>Development of Fast Reactor Fuel for Reduction of Radioactive Waste</b> – Evaluation of Thermal Conductivity of High Am-Bearing Mixed Oxide Fuel on Stoichiometry – Keisuke Yokoyama	75
<b>7-6</b>	<b>Evaluation of Experiments in the Prototype Fast Reactor Monju</b> – Solving Discrepancy Between Measurement and Calculation – Kazuya Ohgama	76
<b>7-7</b>	<b>Toward Realization of Advanced MOX Fuels</b> – Measurement of Slight Variations in the Oxygen Content of Fuels – Shun Hirooka	77

## **8** Research and Development on Fuel Reprocessing, Decommissioning, and Radioactive Waste Management

<b>Highlight</b>	<b>Toward Decommissioning Nuclear Facilities and Managing Radioactive Waste</b>	78
<b>8-1</b>	<b>Toward the Design of the Disposal Facilities Considering the Environmental Standards</b> – Change in Uranium Concentration in Groundwater Depending on the Facility Layout and Structure – Rina Ogawa	80
<b>8-2</b>	<b>Establishment of a Treatment Method for Nuclear Fuel Material for Safe Storage</b> – Stabilization Treatment of Nuclear Fuel Material Containing Organic Compounds – Kohei Tada	81
<b>8-3</b>	<b>Toward Stabilization of Hazardous and Radio-Active Wastes</b> – Characterization of Lead Stabilized with Alkali-Activated Material – Junya Sato	82
<b>8-4</b>	<b>Coating Removal Technique for Painted Steel Surface</b> – Performance Evaluation of Laser Cleaning – Ikumi Yamane	83
<b>8-5</b>	<b>Decommissioning of a Facility with a History of Contamination Caused by a Fire Disaster in a Controlled Area</b> – Collective Dismantling of the Uranium Enrichment Laboratory Using a Large Isolation Tent – Junya Kokusen	84
<b>8-6</b>	<b>Dismantling a Tank Containing Liquid with <math>\alpha</math> Nuclides</b> – Exposure Reduction Measures and Acquisition of Work Data for Future – Yuta Yokozuka	85
<b>8-7</b>	<b>New Method to Observe Fault Displacement Using a Conventional Device</b> – Significant Progress Toward Greatly Enhanced Underground Utilization – Eiichi Ishii	86
<b>8-8</b>	<b>Prediction of the Low-Permeability Domain in Soft Rock</b> – Estimation of the Effective Hydraulic Conductivity by Hydromechanical Simulation – Yusuke Ozaki	87

<b>8-9</b>	<b>Discriminating Tephra with Similar Chemical Compositions</b> – Development of a Method for the in Situ Chemical Composition Analysis of Volcanic Glasses – Saya Kagami	88
<b>8-10</b>	<b>Prediction of Radionuclide Migration by a Thermodynamic Sorption Model</b> – Assessing the Impact of the Transition of Repository Condition on Radionuclide Migration – Yuki Sugiura	89
<b>8-11</b>	<b>Migration Behavior of Carbon-14 in Buffer Material</b> – Diffusion Experiments of Carboxylic Acid and Alcohol in Compacted Bentonite – Takamitsu Ishidera	90

## 9

**Computational Science and E-Systems Research**

<b>Highlight</b>	Computational Science for Nuclear Research and Development	91
<b>9-1</b>	<b>Deep-Learning Model for High-Resolution Steady Flow Prediction</b> – Convolutional Neural Networks for Multiresolution Steady Flow Prediction – Yuichi Asahi	92
<b>9-2</b>	<b>Acceleration of Multiscale Fluid Simulation on GPU Supercomputer</b> – Communication Reducing Method for Local Mesh Refinement – Yuta Hasegawa	93
<b>9-3</b>	<b>Detecting the Quantum Fluctuation of Water</b> – High-Precision Calculations of Water Using the General-Purpose Molecular Simulation Code PIMD – Motoyuki Shiga	94
<b>9-4</b>	<b>Clarification of the Fundamental Properties of Radium</b> – <i>Ab Initio</i> Molecular Dynamics Simulations and Extended X-Ray Absorption Fine Structure Measurements Revealed the Hydration Structure of Barium – Akiko Yamaguchi	95

## 10

**Development of Science & Technology for Nuclear Nonproliferation**

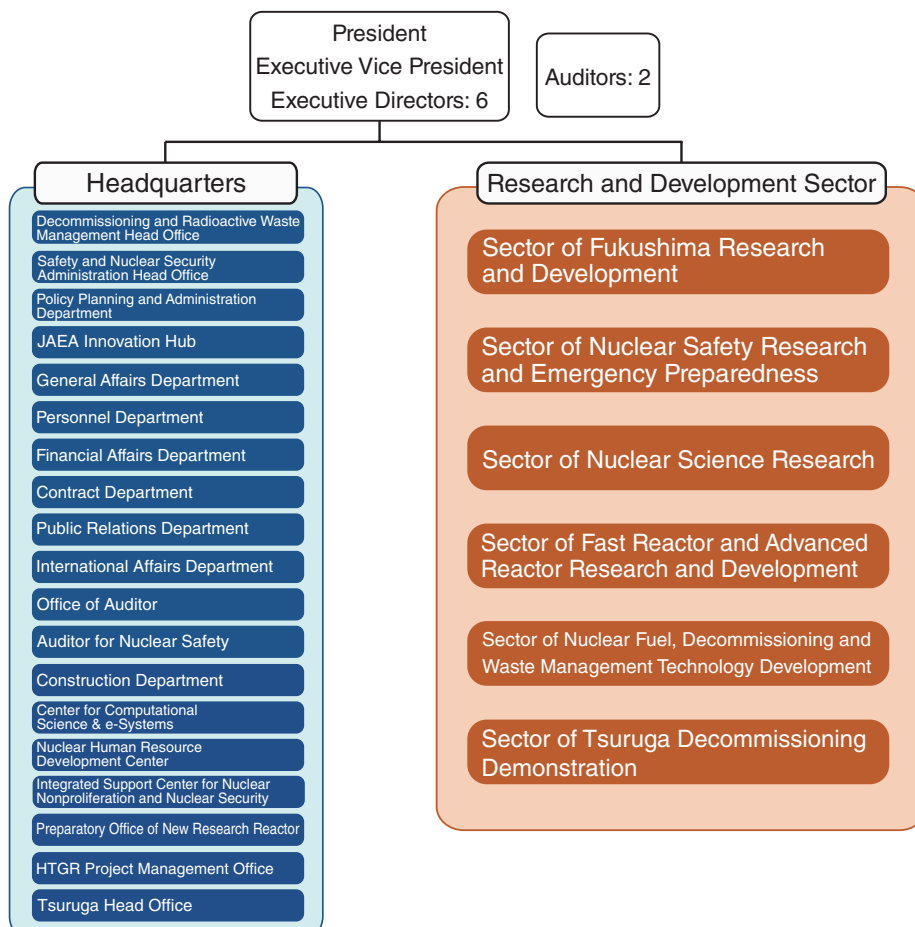
<b>Highlight</b>	Development of Technology and Human Capacity Building in the Fields of Nuclear Nonproliferation and Nuclear Security to Support the Peaceful Use of Nuclear Energy	96
<b>10-1</b>	<b>Development of a Compact Nondestructive Analysis System for Measuring Nuclear Material</b> – Demonstration of Neutron Resonance Transmission Analysis System Using a Laser-Driven Neutron Source – Kota Hironaka, Jaehong Lee	97

# About This Publication and the JAEA Organizational Outline

This publication introduces the latest research and development (R&D) conducted by the Japan Atomic Energy Agency (JAEA) in various fields of. Each chapter presents the activities of a single sector. The R&D sectors perform their activities through R&D centers or institutes, which are based in one to several locations. These centers and institutes are located throughout Japan, as highlighted in the map below. The following introduction outlines the research undertaken within each sector.

1. **The Sector of Fukushima Research and Development** promotes R&D on the decommissioning and environmental restoration following the accident at the Fukushima Daiichi Nuclear Power Station (1F) of the Tokyo Electric Power Company Holdings, Inc. (TEPCO). This sector promotes the development of the essential R&D infrastructure for 1F decommissioning efforts.
2. **The Nuclear Safety Research Center and Nuclear Emergency Assistance and Training Center in the Sector of Nuclear Safety Research and Emergency Preparedness** technically supports regulatory bodies by implementing various areas of nuclear safety research at the Nuclear Science Research Institute. Further, in Hitachinaka City, Ibaraki Prefecture, they perform R&D for nuclear emergency monitoring and protective measures.
3. **The Advanced Science Research Center in the Sector of Nuclear Science Research** strengthens the fundamental research in advanced atomic energy science by investigating novel phenomena, inventing new material, and creating innovative technology toward the future vision of JAEA called “JAEA2050+”. To this end, seven research themes have been organized under three divisions: advanced actinides nuclear science, advanced nuclear materials science, and advanced theoretical physics.
4. **The Nuclear Science and Engineering Center at the Nuclear Science Research Institute in the Sector of Nuclear Science Research** undertakes fundamental research into vital technologies that are required for using nuclear energy.
5. **The Materials Sciences Research Center and J-PARC Center in the Sector of Nuclear Science Research** are engaged in research on the use of neutrons. The research is conducted at the research reactor JRR-3 (the Nuclear Science Research Institute) and the Japan Proton Accelerator Research Complex (J-PARC). Research on the use of synchrotron radiation is performed at the Harima SR Radioisotope Laboratory.
6. **The Headquarters and the HTGR Research and Development Center in the Sector of Fast Reactor and Advanced Reactor Research and Development at the Oarai Research and Development Institute** aim to advance the development of high-temperature gas-cooled reactor (HTGR) technology, technology for hydrogen production through high-temperature water splitting, and technology for coupling hydrogen production plants with HTGR.

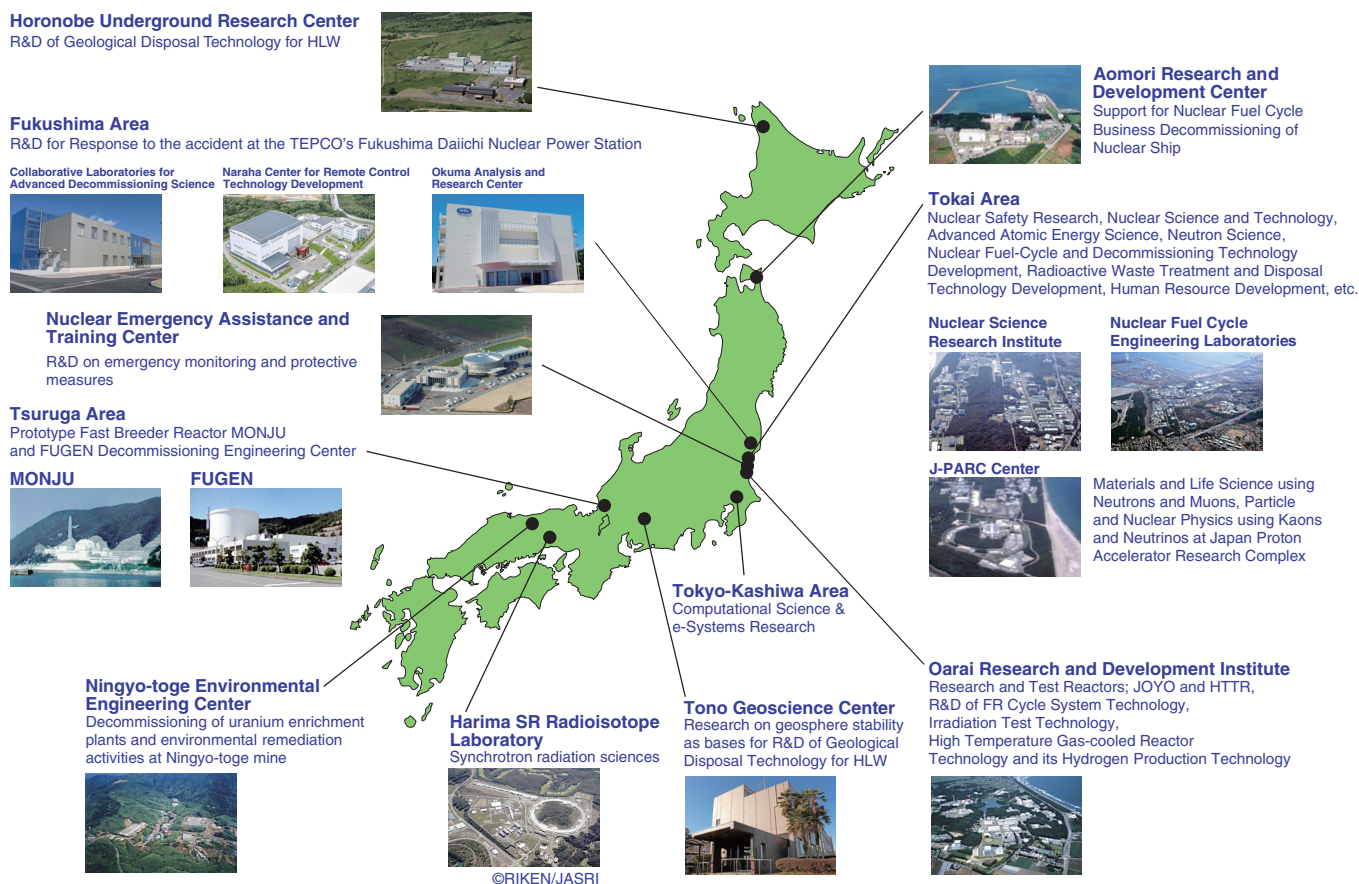
## JAEA -Organizational Outline-



As of January, 2023

7. **The Headquarters, the Fast Reactor Cycle System Research and Development Center, and the Tsuruga Comprehensive Research and Development Center in the Sector of Fast Reactor and Advanced Reactor Research and Development** aim to establish fast reactor (FR) cycles to address long-term energy security and global environmental issues. This work includes enhancing the safety of the FR system at the Oarai Research and Development Institute, compiling results on the prototype fast breeder reactor Monju (MONJU), developing inspection and repair technologies for the FR system at the Tsuruga Comprehensive Research and Development Center, and manufacturing plutonium fuel and reprocessing spent FR fuel at the Nuclear Fuel Cycle Engineering Laboratories in cooperation with the Sector of Nuclear Fuel, Decommissioning and Waste Management Technology Development.
8. **The Sector of Nuclear Fuel, Decommissioning and Waste Management Technology Development** advances technologies for the safety and rational decommissioning of nuclear power facilities and measures for the processing and disposing of radioactive waste. It operates at the Aomori Research and Development Center, the Nuclear Fuel Cycle Engineering Laboratories, and the Ningyo-toge Environmental Engineering Center. The sector also performs multidisciplinary R&D aimed at improving the reliability of the geological disposal of high-level radioactive waste in Japan. One vital field is the establishment of techniques for evaluating the long-term stability of the geological environment. This research is performed at the Tono Geoscience Center. The primary focus of the Horonobe Underground Research Center and the Nuclear Fuel Cycle Engineering Laboratories is safety assessment and improvement of technologies for the design of geological disposal facilities. The Nuclear Fuel Cycle Engineering Laboratories also focus on developing nuclear fuel cycle technology.
9. **The Center for Computational Science & e-Systems** aims to advance simulation technologies and fundamental technologies in computational science. Further, it aims to improve the operation and maintenance of computer systems and networks. These activities are primarily conducted at the Nuclear Science Research Institute and the Kashiwa Office.
10. **The Integrated Support Center for Nuclear Nonproliferation and Nuclear Security (ISCN)** is involved in strengthening nuclear nonproliferation and nuclear security both domestically and internationally. This is achieved through the development of technologies for IAEA safeguards and nuclear detection and forensics, policy research and analysis, capacity-building support activities targeting Asian countries, operation of CTBT international monitoring facilities (located in Japan), and provision of coordination and support by the JAEA for nuclear fuel transportation. These efforts are primarily undertaken at Head Office and the Nuclear Science Research Institute.

## R&D Institutes/Centers of JAEA



## Assistance in Environmental Restoration and Decommissioning

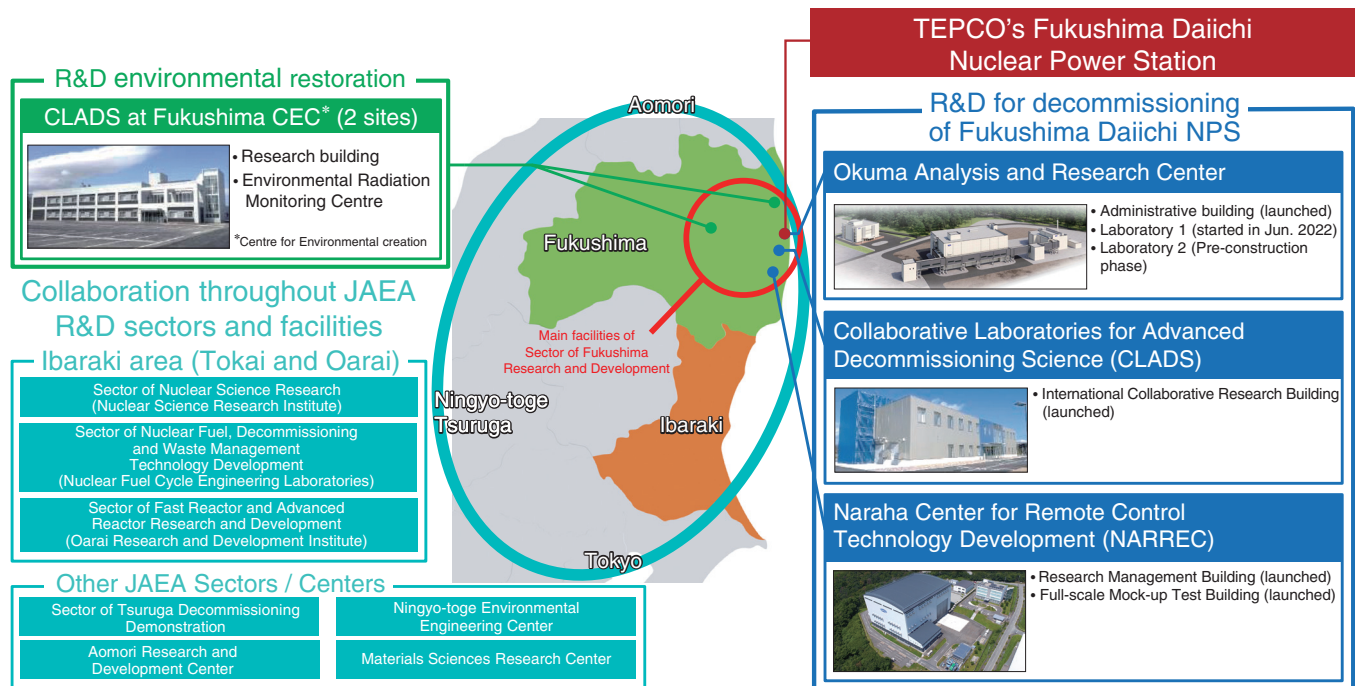


**Fig.1-1 Research and development (R&D) facilities of Sector of Fukushima Research and Development and the status of collaboration throughout the JAEA R&D sectors and facilities**

The Sector of Fukushima Research and Development has been proceeding with the development work of the facilities that will serve as research bases in Fukushima to conduct R&D related to TEPCO's Fukushima Daiichi NPS (1F) decommissioning and environmental restoration of Fukushima. In addition, the entire JAEA has been working cross sectionally on urgent issues related to 1F decommissioning.

Soon after the accident at the TEPCO's Fukushima Daiichi NPS (1F), the JAEA, as the only organization conducting comprehensive research and development (R&D) on nuclear energy in Japan, commenced activities in Fukushima. The Fukushima Research and Development (R&D) Sector has been establishing R&D facilities in Fukushima and is working on R&D for the decommissioning of the 1F and for environmental recovery in the surrounding area by collaborating with other JAEA R&D sectors (Fig.1-1).

The three facilities located in Hamadori area on the Pacific coast of Fukushima are the Collaborative Laboratories for Advanced Decommissioning Science (CLADS) at Tomioka, Naraha Center for Remote Control Technology Development (NARREC), and Okuma Analysis and Research Center. They are a part of the Fukushima Innovation Coast Initiative (field of decommissioning), a national project that aims to build a new industrial base in Hamadori area to restore the industries that were lost because of the Great East Japan Earthquake and the nuclear disaster. These facilities conduct R&D for decommissioning, etc. according to their respective roles. As R&D for decommissioning, we mainly work on R&D related to fuel debris retrieval, accident progression scenario analysis, treatment and disposal of radioactive waste, remote control technology, etc. and contribute to 1F decommissioning (Fig.1-2).

During fuel debris retrieval, it is necessary to conduct an accurate safety and risk assessment to safely and reliably implement a series of processes, including retrieval from the

reactor, transfer, storage, and management. We are conducting R&D related to understanding fuel debris properties and the situation inside a reactor. For example, an estimate of the state of degradation of fuel debris that has been most likely exposed to water for a long period is an index to understand the properties of the fuel debris to be retrieved (Topic 1-1). It is also important to evaluate the possibility of criticality due to changes in the ratio of nuclear fuel material and water, shape, etc. when retrieving fuel debris (Topic 1-2). In addition, to understand the current fuel debris properties and the situation inside the reactor, it is important to estimate the accident progress scenario and the situation inside the reactor immediately after the accident. Therefore, it is essential to study the failure mechanism that takes into account the unique structure of the 1F reactor to estimate the situation inside the reactor at the time of the accident (Topic 1-3).

To safely and stably store the radioactive waste generated in the 1F accident and during the decommissioning and to dispose it in the future, it is necessary to consider appropriate treatment and disposal methods for radioactive waste. As one approach toward this purpose, in the treatment of contaminated water containing a wide variety of radioactive substances and compounds, it is important to develop new element removal technologies that are different from the existing ones to prepare for unexpected treatment conditions (Topic 1-4). In addition, when storing radioactive waste, it is necessary to consider a management method different from that applied for general waste, considering the effects of radiation (Topic 1-5).

R&D for decommissioning of 1F	R&D for environmental restoration	Constructing the R&D facilities
<ul style="list-style-type: none"> <li>➢ Handling the fuel debris (Topics 1-1 and 1-2)</li> <li>➢ Clarifying 1F accident progression scenario (Topic 1-3)</li> <li>➢ Treatment and disposal of radioactive wastes (Topics 1-4 and 1-5)</li> <li>➢ Remote handling techniques (Topics 1-6, 1-7, 1-8, 1-9, and 1-10)</li> </ul>	<ul style="list-style-type: none"> <li>➢ Environmental dynamics (Topics 1-11, 1-12, 1-13, and 1-14)</li> <li>➢ Environmental monitoring and mapping (Topics 1-15, 1-16, and 1-17)</li> </ul>	<ul style="list-style-type: none"> <li>➢ Operating NARREC</li> <li>➢ Operating and building Okuma Analysis and Research Center</li> <li>➢ Constructing research infrastructure and promoting basic research at CLADS</li> </ul>

**Fig.1-2 R&D efforts related to the response to the accident at the 1F based on medium-/long-term plans**

R&D is carried out by extracting the items to be implemented for each field based on the three pillars: “R&D for decommissioning”, “R&D related to environmental restoration”, and “construction of R&D infrastructure”.

For conducting decommissioning work in an environment with a high radiation dose, it is necessary to develop a radiation-measuring device and a remote identification method for ensuring work efficiency and reducing worker exposure to radiation. Therefore, we are developing detectors that can perform measurements even in harsh environments and equipment that can visualize contaminated areas. As an example of detector development, we have developed detectors that can operate under high dose-rate radiation fields and high humidity environment (Topics 1-6 and 1-7) and a detector that can quickly measure alpha/beta/gamma rays (Topic 1-8). In addition, we developed a new method to measure the distribution of radioactive material using optical fibers (Topic 1-9) and a device that can visualize contamination locations three-dimensionally by combining a detector that measures distribution of radioactive contamination and three-dimensional environment modeling device that uses a laser (Topic 1-10).

For R&D related to environmental restoration, CLADS has established a research base in Research Building (Miharu town) and Environmental Radiation Monitoring Centre (Minamisoma City) of the Fukushima Prefectural Centre for Environmental Creation, and has been working on environmental dynamics research and the development of environmental monitoring and mapping technologies through collaboration among Fukushima Prefecture, National Institute for Environmental Studies, and JAEA (Fig.1-2).

With regard to environmental dynamics research, it is important to focus on the transfer and accumulation of <sup>137</sup>Cs, a major radionuclide among the radioactive materials discharged into the environment as a result of the 1F accident, to provide basic information to resolve the concerns based on scientific findings, and to determine the zones for which the evacuation order is to be repealed and specific restoration and rehabilitation sites. Therefore, we are conducting R&D to elucidate the dynamics of radioactive Cs in the natural environment, such as the trend of changes in the amount of radioactive Cs discharged into river systems during typhoons (Topic 1-11), and to elucidate the transfer behavior of radioactive Cs ecosystems via computational studies on the retention mechanism of radioactive Cs in living organisms (Topic 1-12).

Radionuclides present in the environment may include <sup>90</sup>Sr and <sup>99</sup>Tc in addition to <sup>137</sup>Cs. Hence, a method for analyzing these nuclides is required (Topics 1-13 and 1-14).

For environmental monitoring and mapping (Topic 1-15), it is important to measure radiation dose rates, predict and evaluate exposure doses to contribute to decision-making by local governments on policy scheduling and considering the zones for which the evacuation order is to be lifted (Topics 1-16 and 1-17).

We have been generating R&D results that are the key to achieving the milestones of the medium-/long-term roadmap for decommissioning. We are evaluating the data that contribute to the planning of the lifting of evacuation orders by local governments for environmental restoration and providing these data to the relevant organizations. We are also working to promote the understanding of local residents and others by disseminating and sharing information on the status of decommissioning and other initiatives through collaborative projects with local communities and educational institutions, events, and press releases. Furthermore, we contribute to the improvement of technology, regional revitalization, and job creation in Hamadori area of Fukushima through the participation of local companies and the promotion of technology transfers in the implementation of R&D results in the field.

In the fourth medium- to long-term plan starting in FY2022, priority is given to “contribution to the experimental removal of fuel debris”, “treatment and disposal of radioactive waste, and measures for disposal of Advanced Liquid Processing System (ALPS) treated water”, and “provision and dissemination of information contributing to the release of the Specific Reconstruction and Revitalization Sites” as the main tasks at present. In addition to promoting safe, reliable, and prompt decommissioning processes that are technically challenging, such as fuel debris removal, we will continue to conduct surveys and R&D for environmental restoration to create an environment in which residents can live safely and securely. In the area of research facility development, we have commenced the operation of the Okuma Analysis and Research Center Analysis and Research Facility laboratory 1, which will conduct analysis of the radioactive solid waste generated during decommissioning and third-party analysis of ALPS-treated water. In addition, we will utilize the technologies, knowledge, and experience we have accumulated through decommissioning for back-end measures of nuclear facilities and share them widely with the rest of the world to contribute to improving the safety of nuclear facilities in worldwide.

# 1-1 Degradation of Fuel Debris Under the Effect of Ionizing Radiation

## — Formation of Solid Solution Improves Stability to Oxidative Degradation —

**Table 1-1 Examples of simulated debris samples prepared in this study**

The starting materials, heat treatment conditions, and typical phases formed in the samples are listed. Formation of a solid solution of  $\text{UO}_2$  with other metal ions, i.e.,  $\text{UO}_2(\text{s.s.})$ , was observed.

Sample	Starting materials*	Heat treatment	Major U phase
USZr 1200-O	$\text{UO}_2$ , Zr, SUS 304	1200 °C, 2% $\text{O}_2$	$\text{U}_3\text{O}_8$
USZr 1600-O	$\text{UO}_2$ , Zr, SUS 304	1600 °C, 2% $\text{O}_2$	$\text{UO}_2(\text{s.s.})$ (low Zr)
USZr 1600-A	$\text{UO}_2$ , Zr, SUS 304	1600 °C, Ar	$\text{UO}_2$
USZrO <sub>2</sub> 1600-O	$\text{UO}_2$ , ZrO <sub>2</sub> , SUS 304	1600 °C, 2% $\text{O}_2$	$\text{UO}_2(\text{s.s.})$ (high Zr)

\*The atomic ratio in the starting materials is as follows  
 U: Zr: Fe+Cr+Ni (SUS 304) = 1: 1: 1

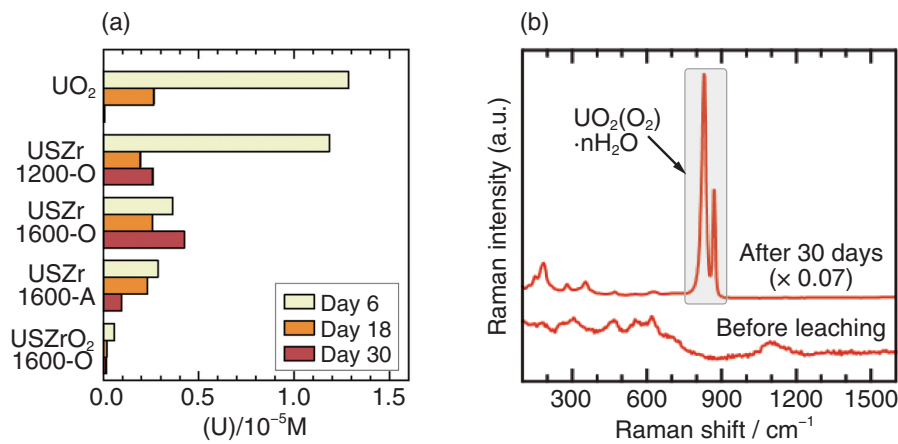


**Fig.1-3 (a) U concentrations in the leachate and (b) Raman spectra of uranyl peroxides formed on USZr1600-O by immersion in an aqueous  $\text{H}_2\text{O}_2$  solution**

Similarly, the formation of uranyl peroxides was observed on the other samples, except for USZrO<sub>2</sub>1600-O.

The fuel debris generated in the accident at TEPCO's Fukushima Daiichi Nuclear Power Station remains in the reactors, and substantial time and effort will be required for the retrieval of the debris. The debris has been most likely exposed to water since the accident. Contact with water results in the degradation of the debris matrix due to the radiolysis of water. Water radiolysis generates oxidants such as hydrogen peroxide ( $\text{H}_2\text{O}_2$ ), which can oxidize uranium to hexavalent U(VI). According to previous studies on uranium (IV) oxide ( $\text{UO}_2$ ) and spent fuels, U oxidation proceeds at the interface with water, and the matrix gradually dissolves because U(VI) has a higher water-solubility than U(IV). Hence, to examine the possible degradation processes of fuel debris, we performed leaching experiments using simulated fuel debris.

The simulated debris samples were prepared from powders of  $\text{UO}_2$ , stainless steel (SUS 304), and zirconium metal (Zr) or oxide ( $\text{ZrO}_2$ ) by heat treatment under various conditions (Table 1-1). After analyzing the phase composition of the samples, the simulated debris samples were immersed in an aqueous  $\text{H}_2\text{O}_2$  solution for up to 30 days.  $\text{H}_2\text{O}_2$  was added because it is the water radiolysis product that has major impact on U oxidation. After certain periods of immersion, the

samples were analyzed by Raman spectroscopy, and chemical analysis of the leached elements was performed.

The analysis of the leached elements showed significant dissolution of U from the samples. The reaction of  $\text{H}_2\text{O}_2$  concurrently induced the precipitation of uranyl peroxides,  $\text{UO}_2(\text{O}_2) \cdot n\text{H}_2\text{O}$  ( $n = 2$  or  $4$ ). Because of these two processes, the dissolved U concentration once increased and then decreased with leaching time (Fig.1-3 (a)). The formation of uranyl peroxides was clearly confirmed by the Raman spectroscopy results (Fig.1-3 (b)). These results demonstrate that uranyl peroxides are the possible alteration products of fuel debris from the  $\text{H}_2\text{O}_2$  reaction.

In contrast, the sample in which formation of a U-Zr oxide solid solution proceeded to a remarkable degree (USZrO<sub>2</sub>1600-O) showed much less U dissolution and no Raman signal of uranyl peroxides. This finding indicates that formation of the oxide solid solution of Zr with  $\text{UO}_2$  improves the durability of fuel debris against the  $\text{H}_2\text{O}_2$  reaction.

This work was supported by JAEA Nuclear Energy S&T and Human Resource Development Project through concentrating wisdom (Grant number JPJA18P18071886).

(Yuta Kumagai)

### Reference

Kumagai, Y. et al., Uranium Dissolution and Uranyl Peroxide Formation by Immersion of Simulated Fuel Debris in Aqueous  $\text{H}_2\text{O}_2$  Solution, Journal of Nuclear Science and Technology, vol.59, issue 8, 2022, p.961–971.

## 1-2 Criticality Evaluation of Fuel Debris with Unclear Material Composition — Development of a New Subcritical Depletion Code for Monitoring Noble Gases —

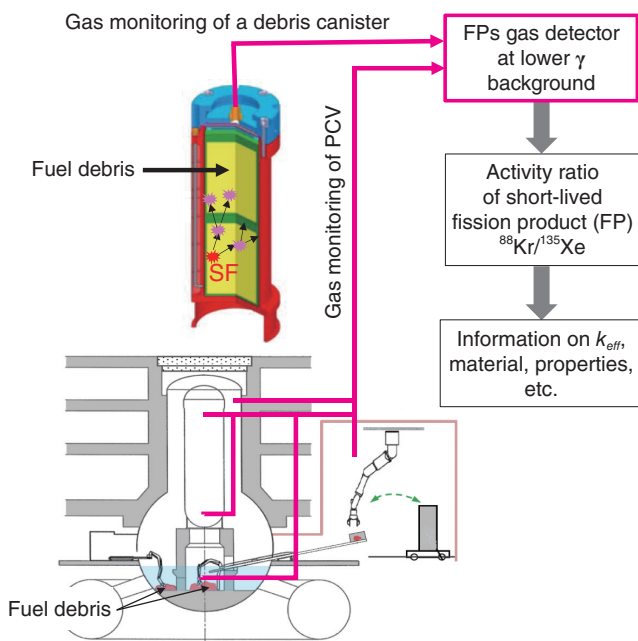


**Fig.1-4 Concept of criticality evaluation by noble-gas monitoring**

In this method, gas is collected from various locations in the fuel debris storage canister (top) or the primary containment vessel (PCV; bottom), and the radioactivity of  $^{88}\text{Kr}$  and  $^{135}\text{Xe}$  are remotely monitored. The criticality at each location is evaluated from the relationship between the activity ratio of  $^{88}\text{Kr}/^{135}\text{Xe}$  and the neutron multiplication (criticality) (Fig.1-5) obtained in advance.

For the safe retrieval and management of fuel debris in the TEPCO's Fukushima Daiichi NPS, it is important to evaluate the criticality and quantity of nuclear materials in fuel debris. The fuel debris continuously produces short half-life fission products (FPs) such as  $^{88}\text{Kr}$  and  $^{135}\text{Xe}$  by spontaneous fission (SF) and induced fission (IF) reactions. The amounts of  $^{88}\text{Kr}$  and  $^{135}\text{Xe}$  produced in the SF and IF reactions are different.

Using this characteristic, as shown in Fig.1-4, we developed a method to evaluate the criticality (neutron multiplication and quantity of fuel material) of fuel debris with unclear material composition in the primary containment vessel (PCV) or fuel debris storage canister. First, gas is collected from a PCV or fuel debris storage canister; subsequently, the activity ratio of  $^{88}\text{Kr}$  and  $^{135}\text{Xe}$  is measured remotely at a place with low background activity. Next, by predicting the correlation between the  $^{88}\text{Kr}/^{135}\text{Xe}$  activity ratio and the neutron multiplication factor in advance via calculations, the criticality of the system can be evaluated.

To implement this method, it is necessary to predict accurately the correlation between the quantities of these FPs produced in the subcritical system and the neutron multiplication factor in advance. We developed a subcritical depletion calculation

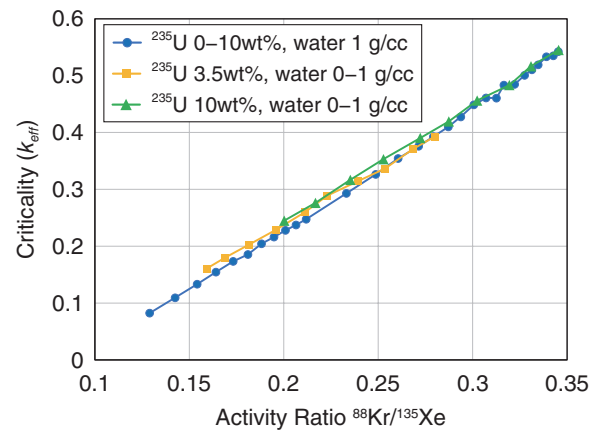


**Fig.1-5 Correlation between activity ratio and neutron multiplication**

The correlation between  $^{88}\text{Kr}/^{135}\text{Xe}$  activity ratio and neutron multiplication is obtained by applying the newly developed Monte Carlo simulation code to canisters containing fuel debris with different uranium and water contents. Since the neutron multiplication factor changes linearly, the criticality can be evaluated from the activity ratio of  $^{88}\text{Kr}/^{135}\text{Xe}$ .

code, for the first time in the world, based on the Monte Carlo method that can evaluate the correlation between the amount of the FPs and the neutron multiplication factor considering the SF and IF reactions. The code development was performed by incorporating the theory of the SF and IF reactions, algorithm, and necessary nuclear data into the original code OpenMC of the Massachusetts Institute of Technology.

Fig.1-5 shows a calculation result obtained using the new code for the fuel debris storage canister. In the calculation, the quantity of  $^{235}\text{U}$  and water content in the fuel debris, which are difficult to be measured, were varied as parameters, and the correlation between the  $^{88}\text{Kr}/^{135}\text{Xe}$  activity ratio and the neutron multiplication was calculated by three-dimensional Monte Carlo simulation. It was shown that the neutron multiplication factor changes linearly regardless of the parameters and that it is possible to evaluate the criticality from the measured  $^{88}\text{Kr}/^{135}\text{Xe}$  activity ratio.

We expect the newly developed code will be used in the future for designing systems for monitoring the criticality in the PCV and for developing nondestructive measurement technologies for fuel debris.

(Eka Saptar Riyana)

### Reference

Riyana, E. S. et al., Depletion Calculation of Subcritical System with Consideration of Spontaneous Fission Reaction, Journal of Nuclear Science and Technology, vol.59, issue 4, 2022, p.424-430.

# 1-3 Clarifying the Failure Mechanism of the Lower Part of the RPV

## — Melting Test Assuming a Eutectic Reaction in the Complex Structure of a BWR —

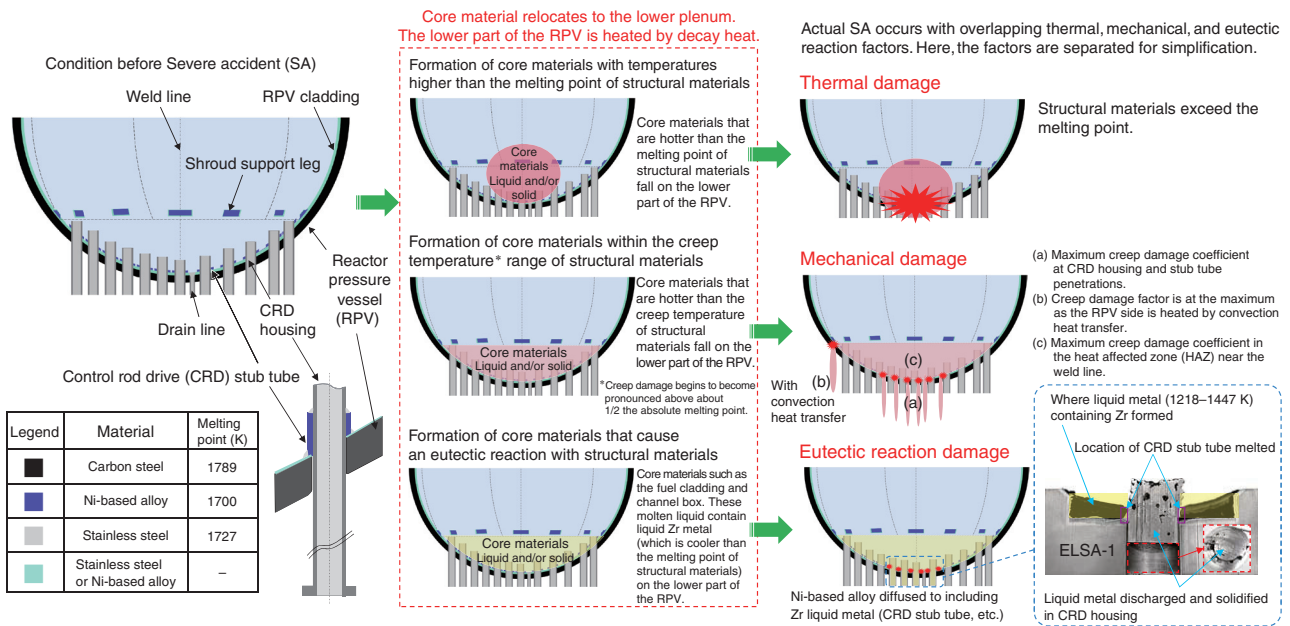


**Fig.1-6 Failure mechanism at the lower part of the RPV**

The main assumed RPV failure factors are thermal, mechanical, and eutectic reaction damage. To verify the damage caused by the eutectic reaction, ELSA-1 test was conducted. The test results indicated the possibility of molten metal remaining in the CRD housing of the 1F2.

The decommissioning of the TEPCO's Fukushima Daiichi NPS (1F) is in progress. Severe accident (SA) analyses, simulated tests, and internal investigation are being performed to understand the internal state of 1F. The failure mechanism of the lower part of the reactor pressure vessel (RPV) has not been clarified as yet. One reason for the lack of clarification is that most of SA analyses and simulated tests refer to a pressurized water reactor (PWR) system. The lower part of the RPV of a boiling water reactor (BWR), which is the same as the 1F, has control rod drive (CRD) rods. The failure mechanism of this system is more complicated than that in a PWR system. However, very little is known about their failure mechanism.

In collaboration with TEPCO, we examined the failure mechanism of the lower part of the RPV (Fig.1-6), taking into account the structure and material composition of the complex substructure specific to a BWR. We evaluated the transition of the core energy during an accident. In 1F Unit 2 (1F2), the core energy increased until the core slumping was small, and the core fuel did not reach the temperature at which it completely melts. It is estimated that most of the core fuel that relocated to the lower plenum was in an unmelted state. In this case, a molten pool was formed at the lower plenum because of the melting of metallic materials such as the fuel cladding, control rod, and channel box.

Under these conditions, the RPV could have been damaged by eutectic melting. In this study, we conducted the Experiment

on Late In-vessel Severe Accident Phenomena (ELSA)-1, which focused on the damage caused by eutectic melting, to elucidate the failure mechanism of the lower part of the RPV in 1F2.

In this test, assuming that the core fuel relocated to the lower part of the RPV in the early phase of the accident, a test bundle simulating the lower part of the RPV was filled with metal (SUS304-83wt% Zr alloy) and heated using a graphite heater. The test bundle simulated CRD penetration with many nickel-based alloy parts, which are assumed to react with the molten metal pool materials and structural materials of a CRD. The temperature condition during the test was set based on the results of the SA analysis of 1F2.

From the test results, it was verified that depending on the melt pool conditions, the lower part of the RPV can be damaged by eutectic reaction and melting even under conditions in which thermal or creep failure does not occur. The test results indicated the possibility of the molten metal remaining in the CRD housing of 1F2.

In the future, we would like to study scenarios of failure of the lower part of the RPV under conditions involving other overlapping factors, and we would like to advance the understanding of the state of 1F for fuel debris retrieval. We also aim to summarize the knowledge that will be useful for advancing SA analysis codes.

(Takuya Yamashita)

### Reference

Yamashita, T. et al., BWR Lower Head Penetration Failure Test Focusing on Eutectic Melting, Annals of Nuclear Energy, vol.173, 2022, 109129, 15p.

# 1-4 How to Effectively Remove Iodate from Solutions?

— Coprecipitation of Iodate with Barite ( $\text{BaSO}_4$ ) Was Evaluated at a Molecular Level —

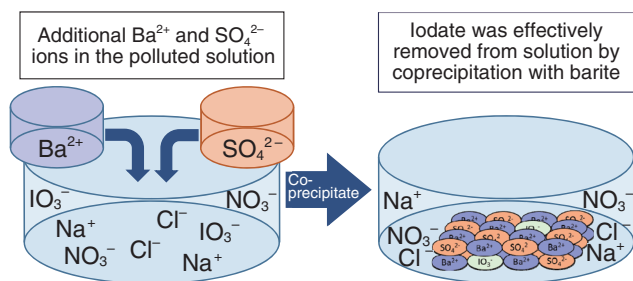


**Fig.1-7 Design of  $\text{IO}_3^-$  coprecipitation with barite**

We add  $\text{BaCl}_2$  and  $\text{Na}_2\text{SO}_4$  into a solution containing iodate by adjusting the  $[\text{Ba}^{2+}]/[\text{SO}_4^{2-}]$  molar ratio. Barite is rapidly precipitated, and iodate is effectively removed from solution even in the presence of competitive anions in solution.

Radioactive iodine ( $^{129}\text{I}$ ) is of great concern owing to its high environmental mobility and long-term radiotoxicity ( $^{129}\text{I}$ : half-life =  $1.6 \times 10^7$  years). In the environment, iodine exists in two oxidation states (-1, +5), and it is mostly dissolved in natural water and radioactive liquid wastes as iodide ( $\text{I}^-$ ) and iodate ( $\text{IO}_3^-$ ). To date, the formation of  $\text{AgI}$  is the only method available for  $\text{I}^-$  removal, and there is no effective method for removing  $\text{IO}_3^-$  from contaminated natural water and waste liquid. In the present study, we developed a new technique for removing radioactive  $\text{IO}_3^-$  from aqueous solutions by using barite ( $\text{BaSO}_4$ ). Although a variety of toxic and/or radioactive elements in the cationic form and selenium (Se) oxyanions can be removed from aqueous solutions by coprecipitation with barite, the removal of  $\text{IO}_3^-$  had not been investigated yet.

Barite is rapidly precipitated by mixing  $\text{BaCl}_2$  aqueous solution in  $\text{Na}_2\text{SO}_4$  aqueous solution (= coprecipitation). A diagram of  $\text{IO}_3^-$  coprecipitation with barite is shown in Fig.1-7. This study investigated the coprecipitation of  $\text{IO}_3^-$  with barite and found that  $\text{IO}_3^-$  can be effectively removed by this method. The main parameter affecting iodate removal is the  $[\text{Ba}^{2+}]/[\text{SO}_4^{2-}]$  molar ratio in the initial aqueous solution. Results showed that iodate was effectively removed from the aqueous solution by coprecipitation when the  $[\text{Ba}^{2+}]/[\text{SO}_4^{2-}]$  ratio was high. Extended X-ray absorption fine structure analysis also indicated that the incorporated  $\text{IO}_3^-$  was strongly bound to the crystal lattice of barite by the substitution of the  $\text{SO}_4^{2-}$  site in the structure when the  $\text{IO}_3^-$  concentration was low. It is believed that the charge compensation problem due to the substitution of  $\text{IO}_3^-$  for  $\text{SO}_4^{2-}$  was achieved by the substitution of  $\text{Na}^+$  for the nearest  $\text{Ba}^{2+}$

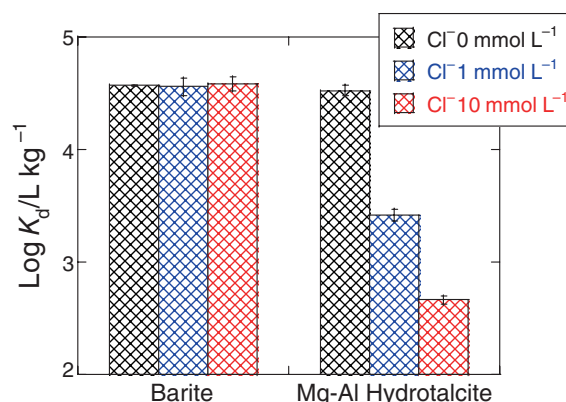


**Fig.1-8 Comparison of iodate removal between barite and Mg-Al layered double hydroxide (LDH)**

The  $K_d$  values of iodate for barite and Mg-Al LDH in the presence of  $\text{Cl}^-$  ions are estimated. The  $K_d$  of Mg-Al LDH decreased with increasing competitive  $\text{Cl}^-$  concentration, while that of barite was nearly independent of the  $\text{Cl}^-$  concentrations.

because  $\text{Na}^+$ , which was not detected in the barite prepared without  $\text{IO}_3^-$ , was detected in the  $\text{IO}_3^-$ -bearing barite ( $2\text{IO}_3^- + 2\text{Na}^+ \leftrightarrow \text{Ba}^{2+} + \text{SO}_4^{2-}$ ).

Subsequently, we investigated the influence of competitive anions on  $\text{IO}_3^-$  removal efficiencies by comparing with adsorption on hydrotalcite-like Mg-Al layered double hydroxide (LDH). Mg-Al LDH is a well-known inorganic layered mineral with a high anion exchange capacity, and the anion is intercalated into interlayer spaces. Many papers have reported on the removal of anionic contaminants by LDH. Fig.1-8 shows the distribution coefficient ( $K_d$ ) of  $\text{IO}_3^-$  for barite prepared under the optimum condition and that for the Mg-Al LDH with and without the addition of  $\text{NaCl}$  in the initial aqueous solution.  $K_d$  is the ratio of concentrations of a solute (in this case,  $\text{IO}_3^-$ ) between a liquid phase and a solid phase (barite or Mg-Al LDH). The higher the  $K_d$ , the higher is the selectivity of the solute to the solid phase. The  $K_d$  of Mg-Al LDH decreased with increasing competitive  $\text{Cl}^-$  concentration, while that of for barite was nearly independent of the  $\text{Cl}^-$  concentrations. At an initial  $\text{Cl}^-$  concentration of 10 mmol  $\text{L}^{-1}$ , the  $K_d$  of barite was two orders of magnitude greater than that of Mg-Al LDH. Hence, the coprecipitation method using barite performs better than the conventional adsorption method using LDH for  $\text{IO}_3^-$  removal when competitive anions are present.  $\text{IO}_3^-$  was also effectively removed from aqueous solutions in the presence of  $\text{NO}_3^-$  and  $\text{SO}_4^{2-}$ , which are also environmentally common anions. Coprecipitation with barite will be a promising tool for removing radioactive  $\text{IO}_3^-$  from various aqueous solutions contaminated with  $\text{IO}_3^-$ .

(Kohei Tokunaga)

## Reference

Tokunaga, K. et al., Effective Removal of Iodate by Coprecipitation with Barite: Behavior and Mechanism, Chemosphere, vol.266, 2021, 129104, 10p.

# 1-5 Characterization of Radioactive Waste for Safe Storage

## — Effect on the Chemical Composition of Carbonate Slurry —

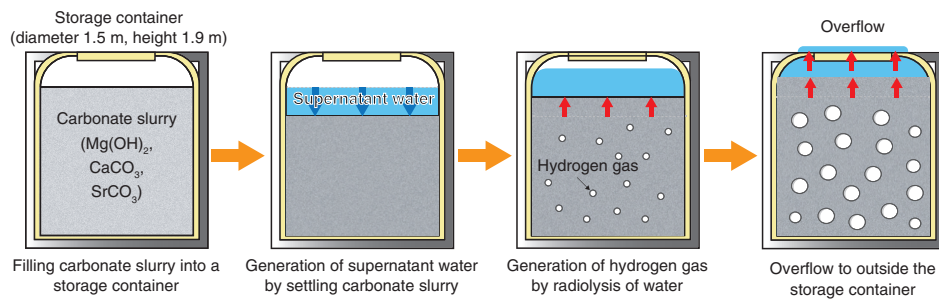


**Fig.1-9 Estimated behavior of expansion of slurry and rise of the supernatant water level in a storage container**

Estimated behavior of the overflow of supernatant water is as follows: carbonate slurry in a storage container generates supernatant water because of gravity sedimentation. Simultaneously, hydrogen gas is generated by radiolysis in the settled slurry layer, and it pushes up the supernatant water along with the slurry, causing an overflow.

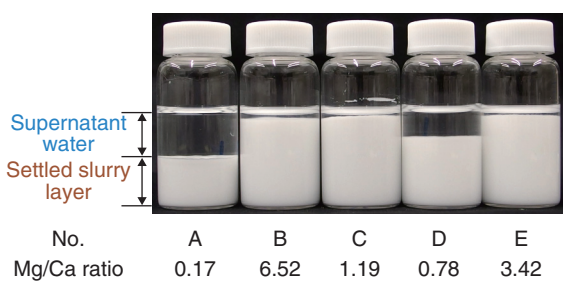


**Fig.1-10 Appearance of a simulated carbonate slurry**

Comparison of the settleability on simulated slurries prepared at suspended solids concentration of 150 g/L using raw water with different Mg/Ca ratios as shown in the figure. Slurry A, which has the highest Ca content, showed the highest settleability at 2 weeks.

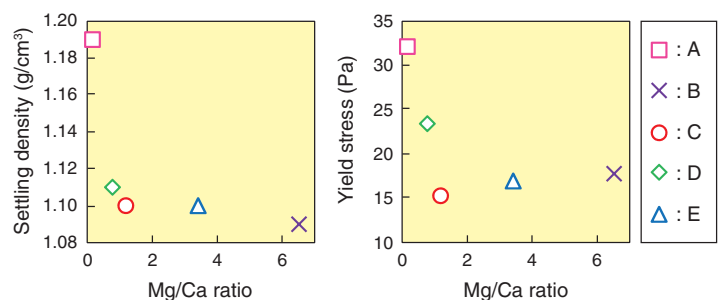


**Fig.1-11 Effect of Mg/Ca ratio in raw water on the density and yield stress of the settled slurry**

The highest settling density and yield stress were observed for slurry A, which has a low Mg/Ca ratio in raw water.

In TEPCO's Fukushima Daiichi NPS, supernatant water leaked from some storage containers filled with slurry waste (carbonate slurry), which mainly comprised carbonate precipitates generated from the Advanced Liquid Processing System (ALPS). Retention of hydrogen gas bubbles generated by the radiolysis of water by  $\beta$  ray-emitting radionuclides in the slurry was presumed to be responsible for the overflow (Fig.1-9), but similar events were not observed in most of the storage containers stored at the same time. For clarifying conditions leading to the overflow to occur, it is necessary to focus on the properties of the slurry itself. In this study, we examined artificial slurry that simulates the composition in the storage container where the overflow occurred. The density of the settled slurry layer, which is considered to affect bubble retention behavior, and the yield stress as an index related to the behavior of bubbles in a settled slurry layer were measured under nonradioactive conditions to clarify the effect of composition.

Investigation of the analytical records of magnesium (Mg) and calcium (Ca) concentrations [in ppm] in water before ALPS treatment (inlet water) during the period when overflow of slurry was observed showed that Mg and Ca concentrations were higher in this period than in the other periods.

Therefore, we prepared five simulated inlet waters (raw water)

with different Mg/Ca ratios. Carbonates and other substances were precipitated from these raw waters and concentrated until the concentration of the suspended solids reached 150 g/L using a cross-flow filtration technique, which is the same method used in ALPS. Settling tests were conducted over a period of two weeks. The two weeks of standing, settling density, and yield stress were measured.

These results showed that the lower the Mg/Ca ratio in raw water (i.e., the higher ratio of Ca), the higher is settleability, and the higher are the settling density and yield stress after static storage (Fig.1-10, Fig.1-11). Such differences in yield stress and other characteristics due to the differences in raw water composition may be responsible for the differences in the bubble retention characteristics in storage containers.

In conclusion, we clarified the effects of the Mg/Ca ratio of raw water on the settling density and yield stress of the simulated slurry and clarified that information on the composition of the inlet water is important for simulating overflowing slurry in a storage container. Based on the characteristics of the carbonate slurry clarified in this study, we plan to evaluate the bubble retention behavior under radioactive conditions via irradiation tests.

(Takuma Horita)

### Reference

Horita, T. et al., Preparation of Carbonate Slurry Simulating Chemical Composition of Slurry in Overflowed High Integrity Container and Evaluation of Its Characteristics, JAEA-Technology 2021-012, 2021, 34p. (in Japanese).

# 1-6 Realization of $\gamma$ -Ray Nuclide Analysis Under Severe Radiation Fields

— Development of a  $\gamma$ -Ray Spectrometry System Specific to High Dose Rates for Simple Nondestructive Assays —

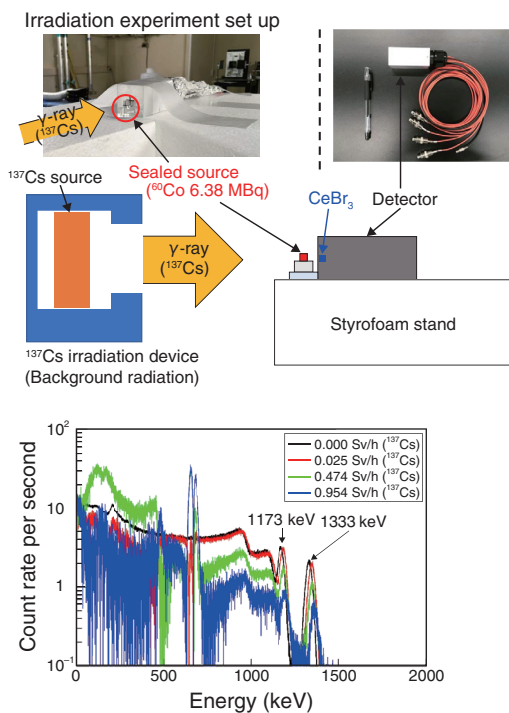


**Fig.1-14 Subtracted spectra (Spectra subtracted from BG radiation)**

From the sealed  $^{60}\text{Co}$  source +  $^{137}\text{Cs}$  BG spectra (Fig.1-13 Red line), BG radiation spectra (Fig.1-13 Black line) were subtracted. Then, the BG radiation was removed and spectra only due to  $^{60}\text{Co}$  could be obtained.

During the decommissioning of the TEPCO's Fukushima Daiichi NPS (1F), radiation measurements in severe environments (high dose rates and narrow places) are being explored. In addition to measurements of major contaminant radionuclides ( $^{137}\text{Cs}$  and  $^{90}\text{Sr}$ ), nondestructive assays for  $^{154}\text{Eu}$ ,  $^{60}\text{Co}$ , and  $^{244}\text{Cm}$ , and nuclear materials (U and Pu) will be targeted for the 1F radiation measurements. To realize simple nondestructive assays, which can identify various  $\gamma$ -ray nuclides in high dose-rate radiation fields without heavy shielding, we are developing compact radiation detectors.

To meet the demands, we developed a  $\gamma$ -ray spectrometry system specific to environments at high dose rates. The system is mainly composed of (I) a small  $\text{CeBr}_3$  scintillator package (5 mm  $\times$  5 mm  $\times$  5 mm), (II) a fast digital signal-processing system, and (III) a photomultiplier tube with additional power supplies to the later dynode stages. In  $\gamma$ -ray fields ( $^{137}\text{Cs}$  and  $^{60}\text{Co}$ ) at dose rates greater than 1 Sv/h, it was already demonstrated that the system had sufficient energy resolution for use in radionuclide analysis (5.2% at 662 keV and 4.2% at 1333 keV).

Furthermore, identifications of radionuclides except for  $^{137}\text{Cs}$  are required in 1F. The  $\gamma$ -ray spectroscopy of a sealed  $^{60}\text{Co}$  source (6.38 MBq) was performed (Fig.1-12) while varying the intensity of the  $^{137}\text{Cs}$  radiation (i.e., background radiation: BG radiation).

Fig.1-13 shows the  $\gamma$ -ray spectra of the  $^{60}\text{Co}$  source and the BG radiation (red line), and those attributed only to the BG

**Fig.1-12 Radioactive source ( $^{60}\text{Co}$ ) measurement in  $^{137}\text{Cs}$  radiation field**  
By varying the irradiation dose rate in the standard radiation field ( $^{137}\text{Cs}$ ),  $\gamma$ -ray spectral measurement of a 6.38 MBq sealed radioactive source ( $^{60}\text{Co}$ ) was performed.

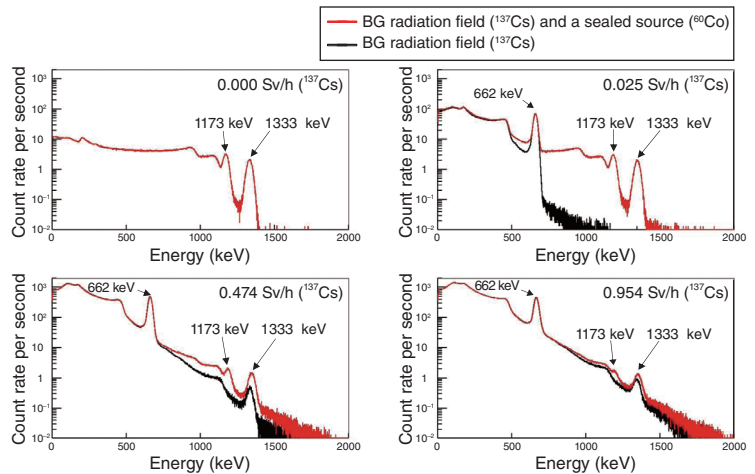


**Fig.1-13 Influence of background (BG) radiation on the radioactive source ( $^{60}\text{Co}$ ) measurement**

For varying irradiation dose rate from  $^{137}\text{Cs}$  (0.000, 0.025, 0.474, and 0.954 Sv/h), the varying  $\gamma$ -ray spectra of the radioactive source ( $^{60}\text{Co}$  6.38 MBq) were acquired. The  $\gamma$ -ray spectra ( $^{60}\text{Co}$ ) were buried because of the total effects of the  $^{137}\text{Cs}$   $\gamma$ -rays as the irradiation dose rate increased.

radiation (black line). As the BG dose rate increased, the full energy peaks of  $^{60}\text{Co}$  (1173 and 1333 keV) were buried with the continuum owing to the BG radiation. The phenomenon occurred when multiple 662 keV  $\gamma$ -rays emitted from  $^{137}\text{Cs}$  ( $^{137\text{m}}\text{Ba}$ ) were detected within time intervals shorter than the pulse rising time (sum effect); this problem cannot be solved by pulse signal-processing. Therefore,  $\gamma$ -ray spectra subtracted from the BG radiation (i.e., subtracted spectra) were introduced (Fig.1-14). In the subtracted spectra, the peak at 1173 keV, which was buried within the  $\gamma$ -ray spectra, was identified at 0.954 Sv/h, and the  $^{60}\text{Co}$  nuclide was identified. To quantify the source intensity, effective areas of the full energy peak for the subtracted spectra ( $S_p$ ) were estimated. A comparison of  $S_p$  without BG irradiation (0.000 Sv/h) to those at 0.954 Sv/h showed that  $S_p$  was one-fifth (0.23) at 1173 keV and one-fourth (0.27) at 1333 keV.

In this research, to integrate the specific  $\gamma$ -ray spectrometry system and spectral analysis, a  $\gamma$ -ray nuclide that was not the principal nuclide ( $^{137}\text{Cs}$ ) was successfully identified under the BG radiation field at a dose rate of almost 1 Sv/h. The system will be developed further for use under higher dose rates, and the influence of BG radiations on quantifications of radionuclides will be reduced.

This research was performed in collaboration with the University of Tokyo and the National Institute of Advanced Industrial Science and Technology.

(Masaaki Kaburagi)

## Reference

Kaburagi, M. et al., Identification and Quantification of a  $^{60}\text{Co}$  Radiation Source Under an Intense  $^{137}\text{Cs}$  Radiation Field Using an Application-Specific  $\text{CeBr}_3$  Spectrometer Suited for Use in Intense Radiation Fields, Journal of Nuclear Science and Technology, vol.59, issue 8, 2022, p.983–992.

# 1-7 In-situ Monitoring System for Radioactive Aerosols

## — Real-Time Monitoring of Alpha Aerosols to Improve Worker Safety —

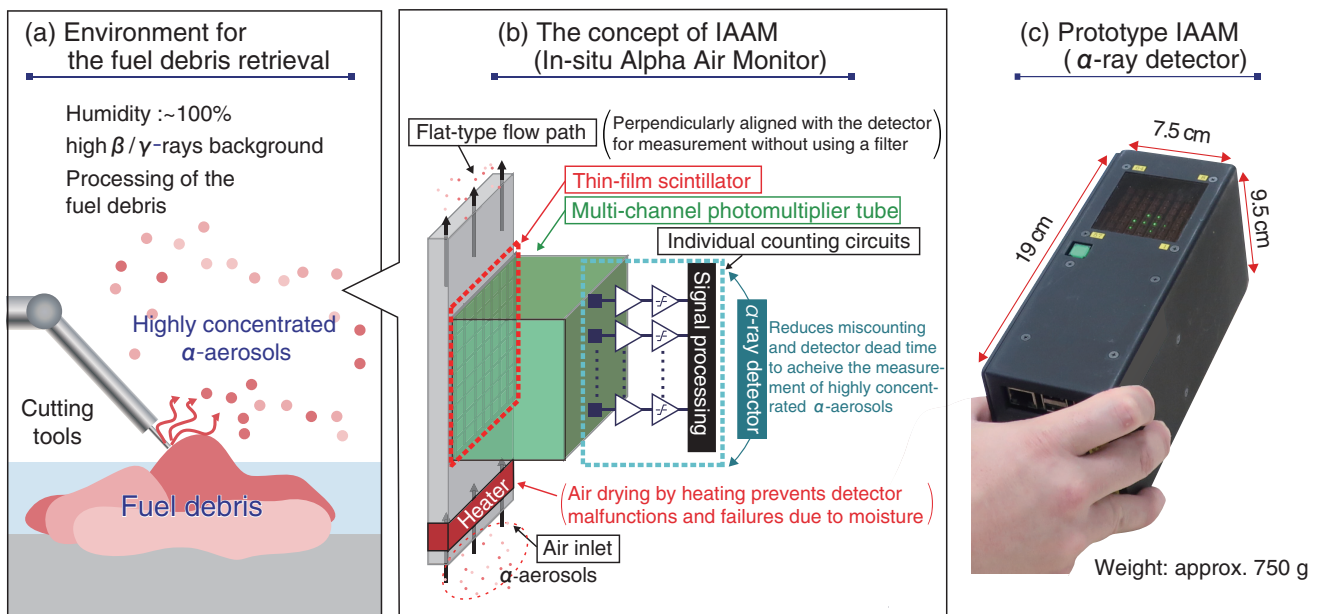


**Fig.1-15  $\alpha$ -Aerosol monitoring inside 1F primary containment vessels (PCVs) by the in-situ Alpha Air Monitor (IAAM)**

(a) Aiming for the in-situ monitoring of highly concentrated  $\alpha$ -aerosols in a high-humidity, high-dose environment, (b) we designed the IAAM that combines an air dryer, flat-type flow path, and specially designed  $\alpha$ -ray detector. The prototype of the IAAM is shown in (c).

The decommissioning of the Fukushima Daiichi Nuclear Power Station (1F) will involve large-scale retrieval of nuclear fuel debris (NFD) from the damaged reactor in the future. During the processing of the NFD, the fine particles originating from NFD will be scattered into the primary containment vessel (PCV). In particular, particles containing alpha nuclides ( $\alpha$ -aerosols) can result in a drastically high effective dose upon inhalation. Therefore, it is important to monitor their concentration on a real-time basis inside the 1F-PCVs. However, in the humid and high-dose environment in the 1F-PCVs, a conventional  $\alpha$ -dust monitor, which collects aerosols on a filter and continuously measures  $\alpha$ -rays using a semiconductor detector, is almost impossible to apply because of problems such as the malfunctioning of the detector due to moisture, clogging of the filter, upper limit of the measurement range, and  $\beta/\gamma$ -ray sensitivity.

To achieve  $\alpha$ -aerosol monitoring inside 1F-PCVs, we defined four requirements: (1) reliable operation under high humidity, (2)  $\alpha$ -aerosol monitoring without using a filter, (3) high concentration  $\alpha$ -aerosol measurement, and (4) selective measurement of  $\alpha$ -aerosols in a high  $\beta/\gamma$ -ray environment. The In situ Alpha Air Monitor (IAAM) was designed to satisfy these requirements (Fig.1-15). The key designs of the system are as follows.

- (1) Air drying in the flow path prevents detector malfunctions due to moisture in the air.
- (2) The  $\alpha$ -aerosol measurement can be performed without

using a filter by placing the  $\alpha$ -ray detector perpendicular to a “flat-type flow path” whose width is sufficiently smaller than the range of the  $\alpha$ -rays.

- (3) By combining a thin-film scintillator with a multichannel photomultiplier tube, the scintillation due to radiation incidence is separated into 64 groups for counting, thereby reducing the occurrence of signal miscounting and detector dead states. By adopting this method,  $\alpha$ -aerosol concentrations of up to  $3.2 \times 10^2 \text{ Bq/cm}^3$  ( $>30$  times that in a 1F-PCVs) can be measured.
- (4) The thickness of the thin-film scintillator and the threshold for signal processing are optimized for the selective measurement of  $\alpha$ -rays. Therefore, even in high  $\gamma$ -ray environments of 100 mSv/h, only  $\alpha$ -aerosols can be selectively measured.

The developed IAAM can monitor  $\alpha$ -aerosol concentrations in-situ under the conditions expected in the 1F-PCVs, and thus, it has the capability to promptly detect abnormal fluctuations in concentrations, etc. and is expected to remarkably improve safety. In the future, we aim to operate the system in the 1F environment. The ability to measure highly concentrated  $\alpha$ -aerosols is expected to contribute to improving worker safety during the decommissioning of nuclear fuel facilities other than 1F.

This research was conducted in collaboration with the Research Institute for Radiation Medicine, Hiroasaki University. (Youichi Tsubota)

### Reference

Tsubota, Y. et al., Development of an In-situ Continuous Air Monitor for the Measurement of Highly Radioactive Alpha-Emitting Particulates ( $\alpha$ -Aerosols) Under High Humidity Environment, Nuclear Instruments and Methods in Physics Research Section A, vol.1030, 2022, 166475, 7p.

# 1-8 Simultaneous Measurement of the Energy Spectra of Alpha, Beta, and Gamma Rays

— Development of a Portable Continuous Air-Monitoring System for Detecting Alpha/Beta/Gamma Radioactive Material —

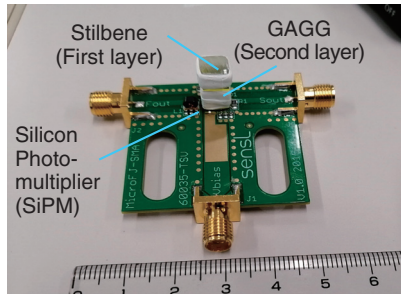


**Fig.1-16 Developed phoswich alpha/beta/gamma detector**

The first layer is a stilbene scintillator for detecting alpha and beta particles. The second layer is a GAGG scintillator for detecting gamma rays.

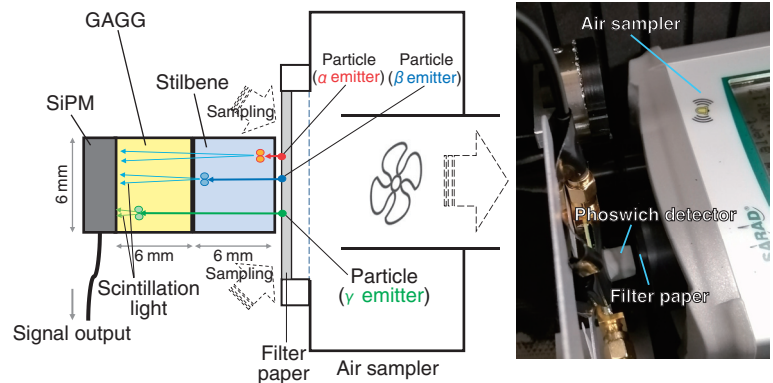


**Fig.1-17 Portable continuous air-monitoring system**

Schematic drawing (left) and a photo (right). This system can continuously measure the alpha/beta/gamma rays from the radioactive materials collected on a filter paper.

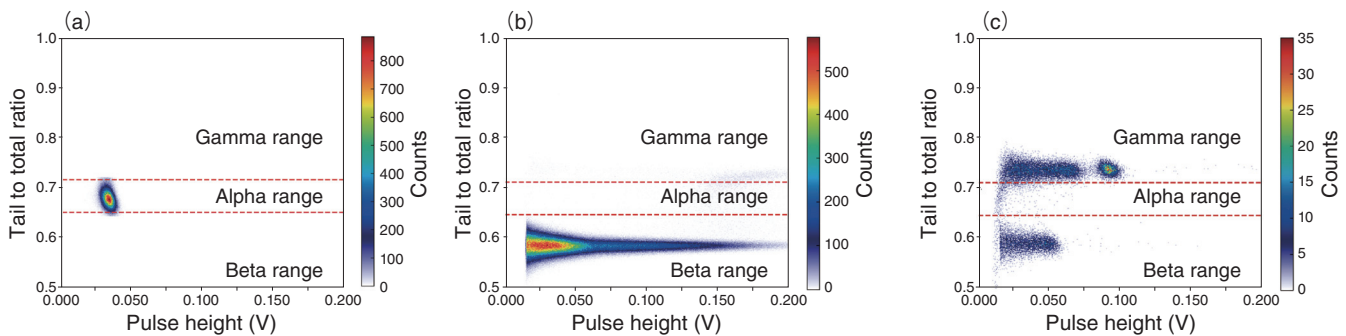


**Fig.1-18 Discrimination results using PSD technology**

A single detector can measure alpha/beta/gamma ray energy spectra simultaneously (previously, three different detectors had to be used to measure them individually). (a) The alpha particles emitted from  $^{241}\text{Am}$  source, (b) beta particles emitted from  $^{90}\text{Sr}$ – $^{90}\text{Y}$  source, and (c) gamma rays emitted from  $^{137}\text{Cs}$  source. The gamma rays also deposit energy in the first layer. Therefore, counts can be confirmed in the beta region as well.

During the decommissioning of nuclear facility sites, such as the TEPCO's Fukushima Daiichi NPS, radioactive contamination occurs because of alpha, beta, and gamma nuclides. Conventionally, alpha nuclides can be measured using ZnS(Ag) scintillation counters. Beta nuclides can be measured using Geiger–Müller (GM) counters or plastic scintillators. Gamma nuclides can be measured using ionization chambers or NaI(Tl) scintillation detectors. Thus, three different detectors must be used for alpha, beta, and gamma rays, which is time-consuming.

In this work, a new phoswich alpha/beta/gamma detector was proposed and developed (Fig.1-16). A portable continuous air-monitoring system using the proposed phoswich detector was also developed for detecting unknown radioactive air contamination (Fig.1-17).

In the developed detector, the first layer is a stilbene scintillator (Size:  $6 \times 6 \times 6$  mm), and the second layer is the  $\text{Gd}_3(\text{Ga}, \text{Al})_5\text{O}_{12}(\text{Ce})$  (GAGG) scintillator of the same size as the first layer. The bottom of the GAGG scintillator is optically coupled to a silicon photomultiplier (SiPM). The output signal from the SiPM is transferred to a waveform digitizer, and a pulse

shape discrimination technique is applied. The alpha, beta, and gamma rays were correctly discriminated (Fig.1-18).

The alpha energy resolution of 5.5 MeV alpha particles was  $22.1\% \pm 0.21\%$  at the full width at half maximum (FWHM), whereas the gamma energy resolution of the 0.662 MeV gamma rays was  $10.3\% \pm 0.18\%$  FWHM. The energy spectra obtained from the simulations agree well with those obtained from measurements.

In addition, continuous alpha-nuclide air measurements were conducted in the basement of a concrete building where the  $^{222}\text{Rn}$  concentration was approximately  $200 \text{ Bq/m}^3$ . The developed portable continuous air-monitoring system was used for this purpose. The measured peaks, which correspond to  $^{212}\text{Bi}$  (6.1 MeV),  $^{214}\text{Po}$  (7.7 MeV), and  $^{212}\text{Po}$  (8.8 MeV), were observed in the alpha spectrum by separating the beta and gamma rays.

The developed monitoring system is potentially efficient for the early detection of unknown released radioactive materials from nuclear facilities under decommissioning.

This work was supported in part by JSPS KAKENHI Grant-in-Aid for Early-Career Scientists (JP19K15482).

(Yuki Morishita)

## Reference

Morishita, Y., Development of a Portable Alpha-Beta-Gamma Radioactive Material Continuous Air-Monitoring System, Nuclear Instruments and Methods in Physics Research Section A, vol.1027, 2022, 166258, 7p.

# 1-9 Novel Single-End Readout-Type Optical Fiber Radiation Sensor

## — Highly Sensitive Position Detection by Photon Wavelength Analysis Using a New Spectroscopy System —

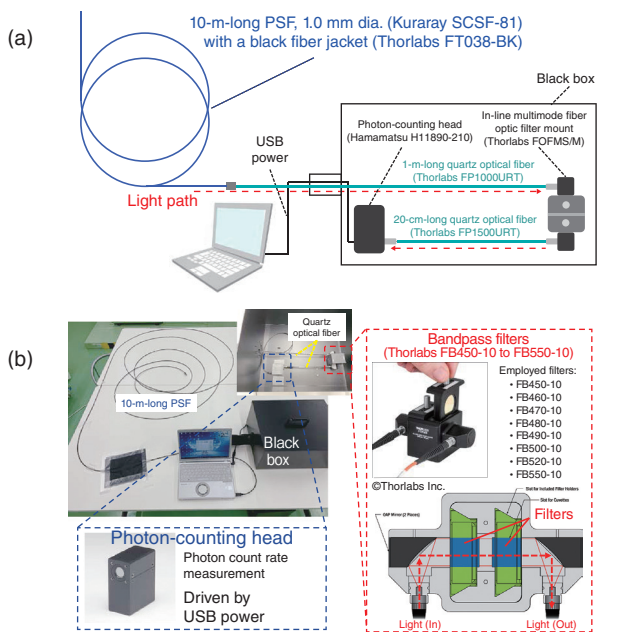


**Fig.1-19 Single-end readout-type position-sensitive optical fiber radiation sensor**

(a) System configuration and (b) photograph of the detector. The light emitted at the plastic scintillation fiber was transmitted to the photon-counting head via bandpass filters and quartz optical fibers, providing a remarkable improvement in detection efficiency.

We are developing a method to measure the distribution of radioactive material using optical fibers to reduce worker exposure in the decommissioning environment of the TEPCO's Fukushima Daiichi NPS (1F). Optical fibers are used not only as light transmission paths, which is their general usage, but also in many applications where the optical fiber itself is used as a radiation sensor. A typical example is the time-of-flight (TOF) method; this method is used to determine the incident position of radiation to the fiber from the time difference of the light reaching both ends of the fiber. However, for the TOF method, light should be detected at both ends of the fiber; this requirement is unsuitable for applications such as inserting a sensor into a narrow space with a high dose rate. To solve this problem, we developed a single-end readout-type position-sensitive optical fiber radiation sensor in collaboration with Nagoya University and attempted to verify its principle. In this study, we aimed to improve the detection efficiency of the single-end readout-type position-sensitive optical fiber radiation sensor based on a new spectroscopy system to broaden the range of applications.

Fig.1-19 shows the system configuration of the detector. In this detector, the light emitted at the plastic scintillation fiber was transmitted to the photon-counting head (a photomultiplier tube) via bandpass filters and quartz optical fibers, and the photon

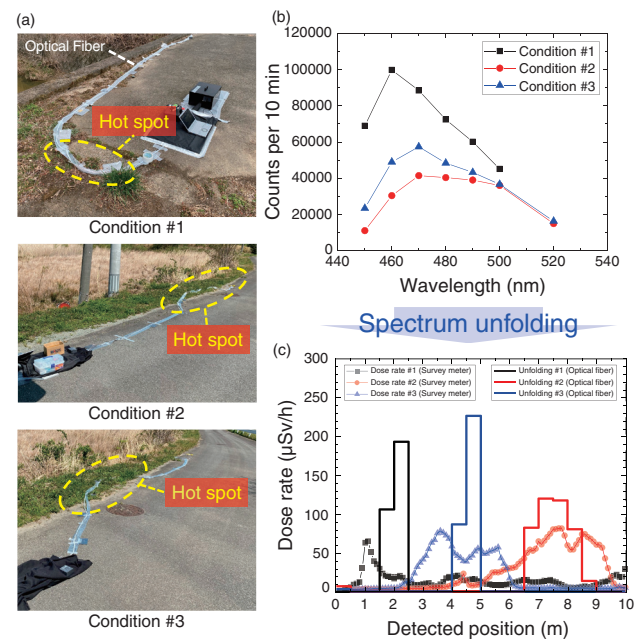


**Fig.1-20 Field experiment at the difficult-to-return zone in Fukushima Prefecture**

(a) Images of three measurement conditions, (b) count rate spectra for the three measurement conditions, (c) comparison between the dose rate distribution measured using the survey meter and that estimated using the optical fiber. With the newly developed single-end readout-type optical fiber radiation sensor, we successfully detected hot spots of less than  $100 \mu\text{Sv/h}$ .

count rate was measured. Here, the bandpass filters transmitted light only with a specific wavelength. By sequentially replacing the bandpass filters (transmission wavelengths: 450 nm, ..., 550 nm), a count rate spectrum reflecting the wavelength dependency of light attenuation in the optical fiber was obtained. This helped realize a highly sensitive single-end readout type optical fiber radiation sensor using the unfolding method (a type of inverse estimation method). Fig.1-20 shows the result of the demonstration test in the outdoor environment of the difficult-to-return zone in Fukushima Prefecture. The hot-spot locations with a maximum surface dose rate of less than  $100 \mu\text{Sv/h}$  were roughly detected under three measurement conditions. These results suggest that the detection limit improved remarkably; it was previously several tens of  $\text{mSv/h}$ . These improvements in the detection limit and demonstration in the outdoor environment are promising results that will lead to the practical application of this sensor in the reactor buildings of the 1F.

This work was partially supported by the JAEA Nuclear Energy S&T and Human Resource Development Project through concentrating wisdom (JPJA19B19206529), "Measurement Methods for the Radioactive Source Distribution Inside Reactor Buildings using a One-dimensional Optical Fiber Radiation Sensor".

(Yuta Terasaka)

### Reference

Terasaka, Y. et al., First Demonstration of a Novel Single-End Readout Type Position-Sensitive Optical Fiber Radiation Sensor Based on Wavelength-Resolved Photon Counting, Nuclear Instruments and Methods in Physics Research Section A, vol.1034, 2022, 166793, 6p.

# 1-10 Visualization of Radioactive Contamination at the Decommissioning Site on a Three-Dimensional Map

— Understanding Invisible Radioactive Contamination in a Virtual Space and Reducing Worker Exposure —

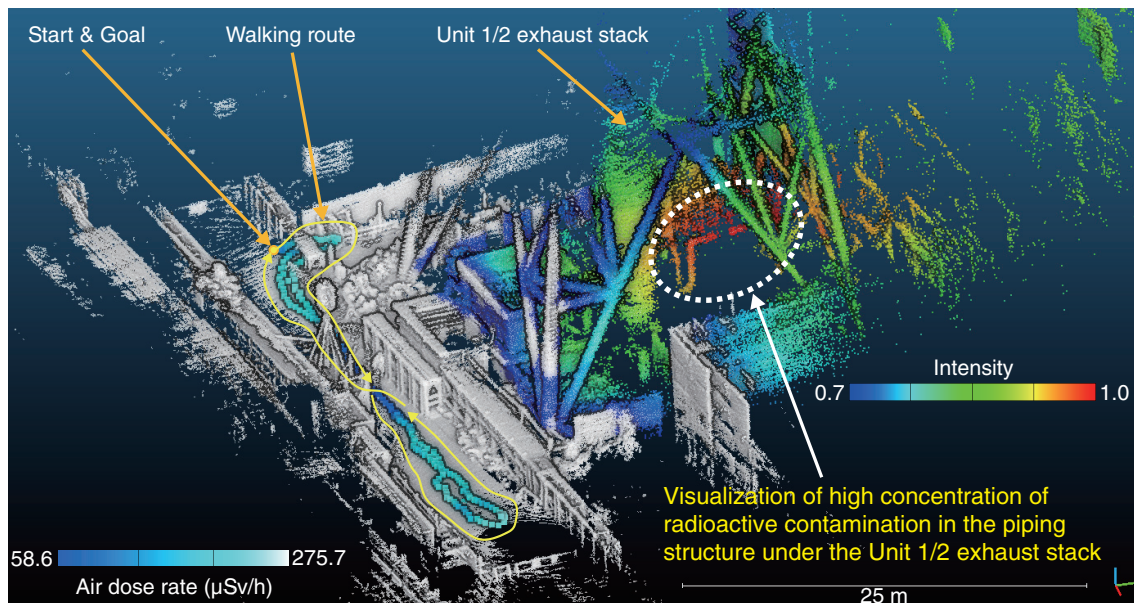


**Fig.1-21 Three-dimensional (3D) map visualizing the air dose rate and highly contaminated region near Unit 1/2 exhaust stack at 1F**

Image of a radioactive hotspot visualized by a Compton camera and dose rate information acquired by a survey meter are displayed in color on the 3D environment model acquired by the SLAM device incorporated in iRIS. The color display shows the dose rate along the walking route on the passageway (left in the figure) and the radioactive hotspot visualized by the Compton camera (right in the figure). The intensity of the color bar on the right side of the figure indicates that the closer the color is to red, the greater is the amount of radioactive substances accumulated. Using iRIS, it is possible to visualize radioactive contamination in three dimensions.

Eleven years have passed since the accident at TEPCO's Fukushima Daiichi NPS (1F), but areas with high dose rates still remain inside the 1F building where it is difficult for workers to enter and work for long hours. It is extremely important to understand the distribution of radioactive contamination in these work environments to reduce the exposure of the workers to radiation and to develop work plans.

Against this background, we devised an integrated Radiation Imaging System (iRIS) that visualizes the distribution of radioactive contamination in the work environment in three dimensions.

We have developed a system that can scan the contamination distribution in the work environment at once while moving. This system combines combining a Compton camera, a type of gamma-ray imager, and a 3D-LiDAR-based SLAM (Simultaneous Localization and Mapping) device. This demonstration test was conducted in the vicinity of the exhaust stack of Unit 1/2 of the 1F with the cooperation of TEPCO. The lower part of the exhaust stack has a high dose rate, making it difficult for workers to enter and stay for a long period of time. Conventional fixed-point measurement (two-dimensional imaging) using the Compton camera requires the measurement of the target region from multiple viewpoints to identify the location of the radioactive hotspot, and thus it is necessary to repeatedly move the Compton camera and take measurements.

In contrast, with iRIS, data acquisition can be completed in less than 5 min by continuously measuring the radioactive contamination distribution as the operator walks along a passageway with a relatively low dose rate and without entering the lower part of the exhaust stack. Furthermore, by displaying the images of the radioactive hotspot as acquired by the Compton camera in color on a 3D environment model of the work environment acquired using the SLAM device, we successfully plotted a 3D map visualizing the hotspot on the pipe below the exhaust stack (Fig.1-21). Simultaneously, the dose rates along the trajectory of the operator can be displayed on the 3D map by combining the measurement data acquired with the survey meter. In the future, we will conduct demonstration tests inside the reactor building of the 1F.

The results of this study have been introduced in several debriefing sessions and journal articles<sup>\*1,2</sup> after the press release. (Yuki Sato)

\*1 Sato, Y., Development of an integrated Radiation Imaging System, *Inspection Engineering*, vol.27, no.5, 2022, p.9-15 (in Japanese).

\*2 Sato, Y., 3D Visualization of Radioactive Contamination Using an integrated Radiation Imaging System (iRIS), *Isotope News*, no.781, 2022, p.19-23 (in Japanese).

## Reference

Sato, Y. et al., Radiation Imaging Using an integrated Radiation Imaging System Based on a Compact Compton Camera Under Unit 1/2 Exhaust Stack of Fukushima Daiichi Nuclear Power Station, *Journal of Nuclear Science and Technology*, vol.59, issue 6, 2022, p.677-687.

# 1-11 Impact of Extreme Typhoons on Radiocesium Discharge

## — Comparison of Effects of Two Typhoons—Etau in 2015 and Hagibis in 2019—

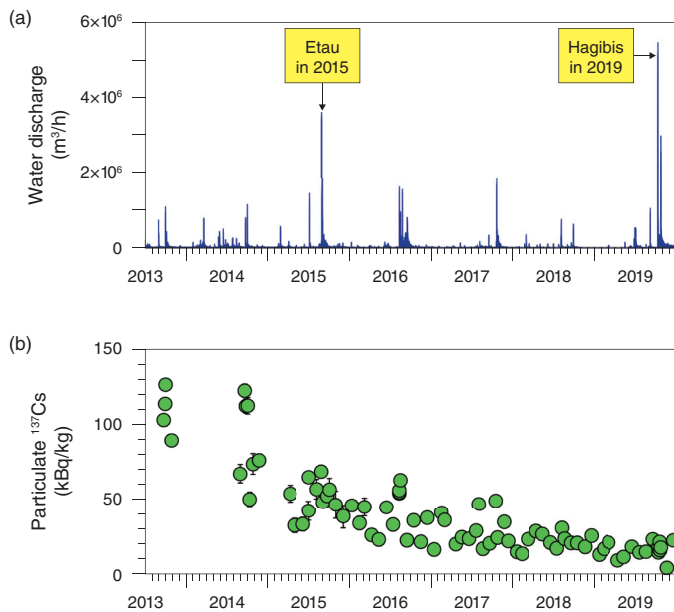


**Fig.1-22 Water discharge and particulate <sup>137</sup>Cs concentration**  
 (a) In the Ukedo river, the river discharges during typhoons Etau and Hagibis were extraordinarily high during the observation period.  
 (b) The concentration of particulate <sup>137</sup>Cs decreased with time regardless of the amount of sediment discharge.

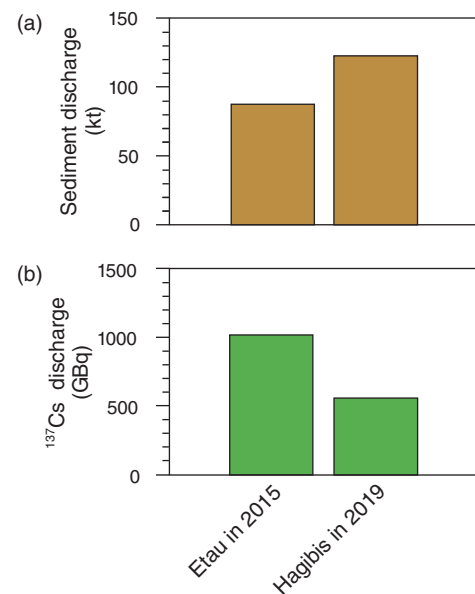


**Fig.1-23 Comparison of sediment and radiocesium (RCs) discharges of typhoons Etau and Hagibis**  
 Typhoon Hagibis had a higher sediment discharge and smaller <sup>137</sup>Cs discharge than typhoon Etau because of the decrease in the concentration of particulate <sup>137</sup>Cs with time.

Radiocesium (RCs) released by the accident at the TEPCO's Fukushima Daiichi NPS (1F) is transported by the river system. In the past, JAEA developed a simulation model named MERCURY, which was designed based on the observation results until the end of 2017, and used this model to calculate the RCs discharge through rivers into the ocean after the accident at 1F. However, continuous RCs observation in representative rivers is indispensable to obtain the empirical data to verify whether unexpected Cs discharge caused by the intensified and frequent heavy rain disasters in recent years can be predicted by a simulation model. In this study, we observed the amount of RCs discharge caused by the extreme typhoon Hagibis that struck Japan in October 2019 and compared this event with typhoon Etau that struck in September 2015 and was the largest flood event since the accident at 1F.

Since autumn 2013, JAEA has continuously observed the water and sediment discharges from the Ukedo River near 1F and periodically measured the RCs concentration in sediments (particulate RCs). The flood caused by the typhoon Hagibis recorded the largest water discharge during the observation

period (September 2013–December 2019) (Fig.1-22(a)), and 73% of the annual sediment discharge in 2019 occurred during this typhoon. That is, the sediment discharge during floods dominates the annual RCs discharge. In addition, it was also clarified that particulate RCs concentrations decreased with time regardless of the amount of sediment discharge (Fig.1-22(b)). Therefore, the amount of RCs discharged during typhoon Hagibis was half that of typhoon Etau, though the amount of sediments discharged during Hagibis was about 1.4 times that discharged by Etau (Fig.1-23). Considering the decreasing trend of the particulate RCs concentration, the RCs discharge caused by unexpected flood events in the future will be less than the RCs discharges of typhoons Etau and Hagibis.

The RCs discharge during typhoon Hagibis as calculated by MERCURY (353 GBq) was consistent with the observation results. Therefore, the usefulness of MERCURY was reconfirmed. We will continue to observe rivers and further advance MERCURY.

(Takahiro Nakanishi)

### Reference

Nakanishi, T. et al., Impact of Extreme Typhoon Events on the Fluvial Discharge of Particulate Radiocesium in Fukushima Prefecture, Journal of Coastal Research, special issue no.114, 2021, p.310–314.

# 1-12 Approaching the Secrets of Long-Term Cesium Retention in Lichen

— Computational Chemistry Solves the Energetics of Complexation of Metabolites with Cesium —

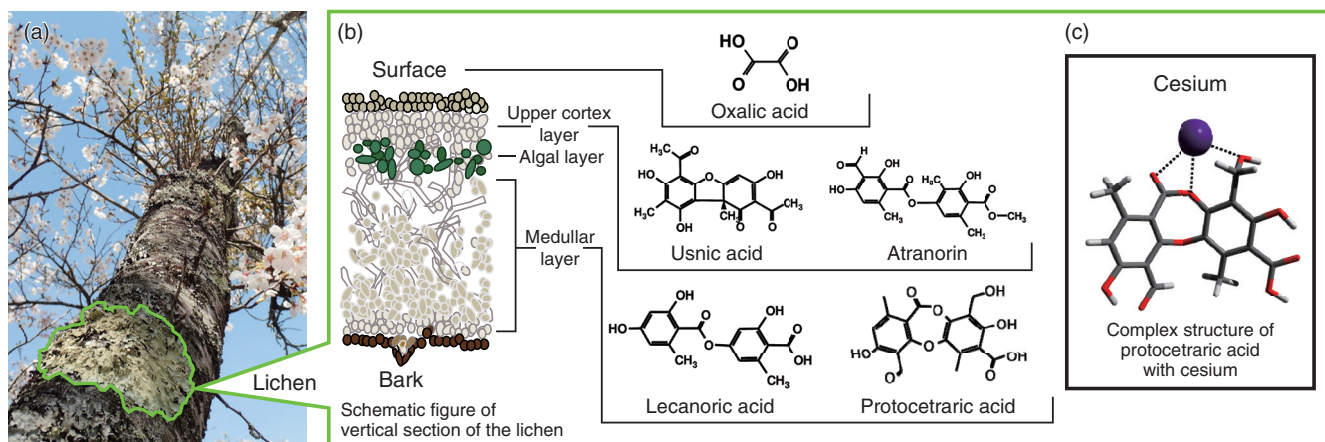


**Fig.1-24 Lichen: their living form (a), organizational structures with secreted metabolites (b), and complex structures with cesium (c)**

The living form of a lichen (*Parmotrema tinctorum*) on the stem of a cherry tree (a), its schematic internal structure with the secreted metabolites (b), and the complex form of protocetraric acid with cesium (c). The calculation shows that metabolites secreted in the upper cortex layer and the ones in medullar layer form complexes with cesium as they are in the dehydrated states and nondehydrated states, respectively.

Lichens are symbiotic associations between fungi and algae (or cyanobacteria) that grow on the surfaces of rocks, trees, and walls of houses and buildings (Fig.1-24). They can be easily found if one carefully looks for them around one's house.

Such unique lichens have been well-known to retain radioactive cesium for a long time, but the retention mechanism remains unknown. Knowledge of this mechanism may be important to understand the ecological dynamics of radioactive cesium.

In this study, we propose a hypothesis that some parts of metabolites, which are the chemical products of the fungi, form complexes with cesium, and we try to confirm this hypothesis via computational chemical calculations.

First, we choose the representative metabolites of *Parmotrema tinctorum* that has been identified as a retainer of radioactive cesium in Fukushima, and we calculate their complexation energies with cesium and other alkaline metals using the computational chemistry scheme.

However, we need a new computation scheme to effectively find many candidates of complexation forms because the complexes show not only one but multiple forms. To solve this problem, we split the computation into two stages—the first one obtains many complexes with low precision but high speed, and the second one adopts high-precision calculations with parallel computing for the structures obtained in the first step

by using supercomputers. This stepwise scheme is effective and successfully yields many complexations with reasonable speed.

According to the calculations, usnic acid and atranorin produced in the upper cortex, as shown in Fig.1-24, show strong complex formation with alkali metal ions in their dehydrated states, while lecanoric and protocetraric acids in medulla show strong complex formations in the nondehydrated states. In particular, protocetraric acid coordinates with cesium ion via three oxygens (colored red in Fig.1-24) and has the strongest formation energy. These results suggest that the upper cortex metabolites trap alkali ions in their dehydrated states if neutral to weakly alkaline pH water penetrates into the lichen body, while those in the medullar layer do the same if acidic-to-neutral pH water penetrates into the lichen body. This indicates that lichens can respond to any pH cases to retain a sufficient number of alkali ions and cesium.

Thus, we obtained the knowledge that several metabolites contribute to the strong alkali-ion retention mechanism through complex formation. We believe that this is a key idea to understand the cesium retention mechanism. In the future, we will continue to investigate not only cesium retention but also the metabolite functions of living organisms by using the same computation scheme and thereby solve the mysteries of living creatures.

(Masahiko Machida)

## Reference

Suno, H., Machida, M. et al., Quantum Chemical Calculation Studies Toward Microscopic Understanding of Retention Mechanism of Cs Radioisotopes and Other Alkali Metals in Lichens, Scientific Reports, vol.11, 2021, 8228, 13p.

# 1-13 Rapid Analysis for Long Half-Life $^{99}\text{Tc}$

## — ICP-MS Analysis with Solid-Phase Extraction and Gas-Phase Reaction —

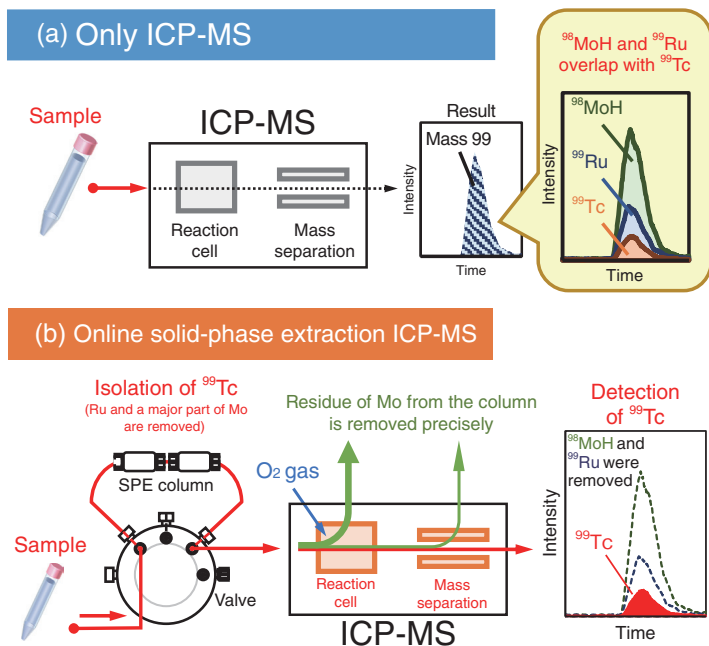


**Fig.1-25 (a) Typical inductively coupled plasma–mass spectrometry (ICP-MS) analysis and (b) proposed online solid-phase extraction ICP-MS**

The precise quantification of  $^{99}\text{Tc}$  is prevented because of overlapping with the same mass of  $^{99}\text{Ru}$  and  $^{98}\text{MoH}$ . The proposed method involves the separation of  $^{99}\text{Ru}$  and  $^{98}\text{MoH}$  to determine  $^{99}\text{Tc}$  correctly.

Technetium-99 ( $^{99}\text{Tc}$ ) is an artificial radionuclide with a long half-life of 210,000 years and a pure beta emitter.  $^{99}\text{Tc}$  is produced as one of the fission products and in yields equal to the yields of cesium-137 and strontium-90 (approximately 6%) from nuclear material such as uranium-235. Specific seaweeds accumulate  $^{99}\text{Tc}$ , although they transport it widely in the marine environment. The concentration of  $^{99}\text{Tc}$  in seaweeds and the annual discharge amounts in nuclear-reprocessing plants in foreign countries were reported to have a reasonable correlation. Similarly, it is expected that  $^{99}\text{Tc}$  will become one of the important tracers for monitoring the transport of radionuclides around the sea in Japan. However, there is no official analytical method for  $^{99}\text{Tc}$  in Japan. In this study, we developed an analytical method to understand  $^{99}\text{Tc}$  transport in the environment.

The radioanalytical method used for  $^{99}\text{Tc}$  (beta counting) needs the separation of all other beta nuclides—this pretreatment process is complicated and time-consuming. The analysis is concentrated on a large sample volume to detect an ultratrace level of  $^{99}\text{Tc}$  because of the low sensitivity compared with mass spectrometry. In this study, an analytical method using inductively coupled plasma–mass spectrometry (ICP-MS) to measure  $^{99}\text{Tc}$  with a small sample volume was developed. ICP-MS enables rapid and highly sensitive determination of specific mass numbers (in this case, mass number 99 is selected). However, the quantification of  $^{99}\text{Tc}$  with typical ICP-MS analysis is prevented by coexisting signal-overlapping materials, namely, ruthenium-99 ( $^{99}\text{Ru}$ ) and  $^{98}\text{MoH}$  (created from molybdenum-98

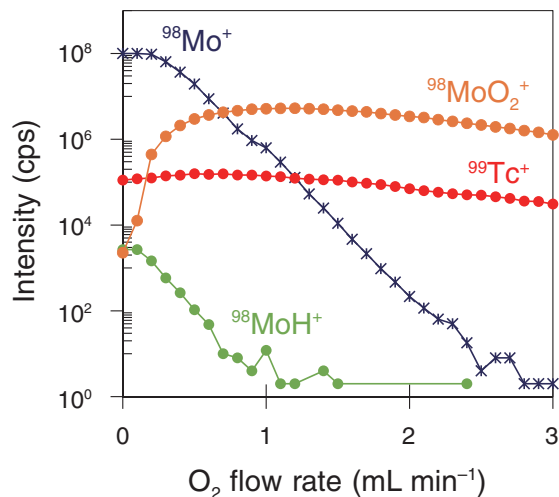


**Fig.1-26 Gas-phase reaction of oxygen and elements ( $^{98}\text{Mo}$  and  $^{99}\text{Tc}$ ) in the reaction cell of ICP-MS**

$^{98}\text{Mo}$  and  $^{98}\text{MoH}$  decreases logarithmically and are converted  $^{98}\text{MoO}_2$  with increasing  $\text{O}_2$  content, whereas the  $^{99}\text{Tc}$  remains constant.  $\text{O}_2$  reaction enables mass discrimination, and this method supports the precise quantification of  $^{99}\text{Tc}$  in samples containing enriched  $^{98}\text{Mo}$ .

( $^{98}\text{Mo}$ ) and hydrogen in the equipment), which have the same mass number as  $^{99}\text{Tc}$  (Fig.1-25(a)). Therefore, we developed an analytical system equipped with multistage separation with a solid-phase extraction (SPE) column packed with a selective adsorption resin for  $^{99}\text{Tc}$ , and we adopted a gas-phase reaction with oxygen in the reaction cell of ICP-MS for the effective separation of the interfering materials (Fig.1-25(b)). The SPE column eliminated  $^{99}\text{Ru}$  and  $^{98}\text{Mo}$ , and their concentrations decreased to values lower than 1/4000 and 1/3000, respectively. However, the concentrations of  $^{99}\text{Ru}$  and  $^{98}\text{Mo}$  are 400 times and 1.6 billion times higher than that of  $^{99}\text{Tc}$  in the Japan Sea. Thus, the required removal rate of  $^{98}\text{Mo}$  was not achieved. Then, the gas-phase reaction with oxygen in the reaction cell of ICP-MS discriminated precisely between  $^{99}\text{Tc}$  and  $^{98}\text{Mo}$  by converting  $^{98}\text{Mo}$  and  $^{98}\text{MoH}$  to  $^{98}\text{MoO}_2$  (mass number: 130) via an oxidative reaction, while  $^{99}\text{Tc}$  remained nonreactive (Fig.1-26). The synergistic effect of SPE and gas-phase reaction enables analysis of samples containing high concentration of  $^{98}\text{Mo}$ , which has a concentration a trillion higher than that of  $^{99}\text{Tc}$ .

We performed measurements for a seawater reference material (certified value: 159-250 mBq/L) using this proposed method, and the obtained values ( $200.1 \pm 9.6$  mBq/L) were in agreement with those of the reference material. The online SPE ICP-MS contributes to wide-area research of  $^{99}\text{Tc}$  in the environment owing to the high-throughput analysis (analytical time: within 30 min per sample).

(Makoto Matsueda)

### Reference

Matsueda, M. et al., Online Solid-Phase Extraction-Inductively Coupled Plasma-Quadrupole Mass Spectrometry with Oxygen Dynamic Reaction for Quantification of Technetium-99, ACS Omega, vol.6, issue 29, 2021, p.19281–19290.

# 1-14 Selective Detection of Trace Sr Isotopes Using Lasers

## — Simplified Pretreatment of Samples Containing Isobars and Stable Isotopes —

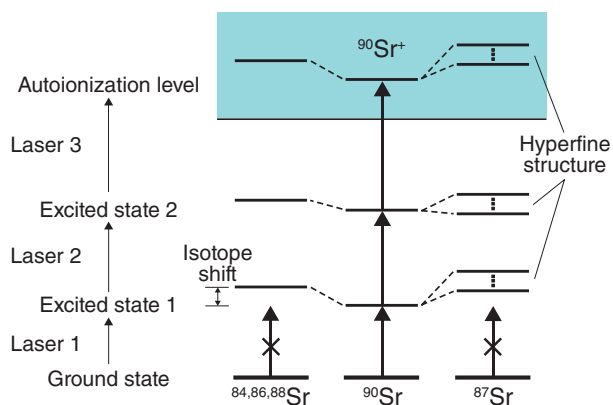


**Fig.1-27 Element and isotope-selective laser resonance ionization of  $^{90}\text{Sr}$  atoms**

Owing to the presence of isotope shifts and hyperfine structures ( $^{87}\text{Sr}$  only),  $^{90}\text{Sr}$  atoms can be isotope-selectively ionized using wavelength-tuned lasers.

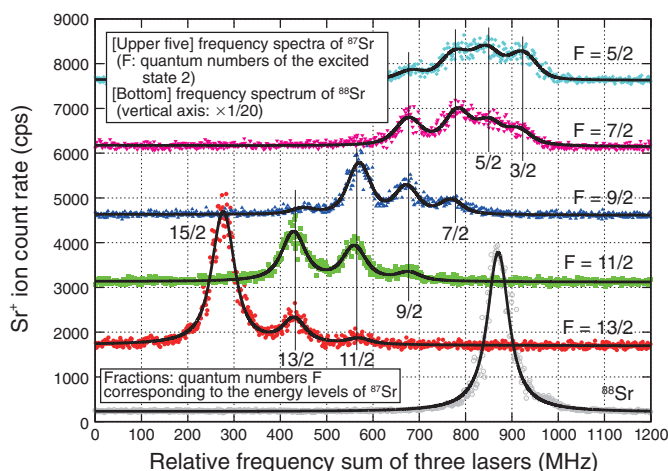


**Fig.1-28 Example of the observed  $^{88}\text{Sr}$  and  $^{87}\text{Sr}$  frequency spectra**

Laser-3 frequency is scanned to observe the spectra of  $^{88}\text{Sr}$  and  $^{87}\text{Sr}$  using scheme (B) 689.4 nm–472.4 nm–404.2 nm. Splitting of the energy level of  $^{87}\text{Sr}$  due to the hyperfine structure of the autoionization level can be observed.

**Table 1-2 Measured optical isotopic selectivities of  $^{90}\text{Sr}$  with respect to stable Sr isotopes ( $^{84}\text{Sr}$ ,  $^{86}\text{Sr}$ ,  $^{87}\text{Sr}$ , and  $^{88}\text{Sr}$ )**

The measured  $^{90}\text{Sr}$  optical isotopic selectivities with respect to stable Sr isotopes ranged from  $10^3$  to  $10^5$  for both resonance ionization schemes: (A) 689.4 nm–487.4 nm–393.8 nm and (B) 689.4 nm–472.4 nm–404.2 nm.

Scheme	$^{84}\text{Sr}$	$^{86}\text{Sr}$	$^{87}\text{Sr}$	$^{88}\text{Sr}$
(A)	$4 \times 10^5$	$1 \times 10^4$	$2 \times 10^5$	$5 \times 10^3$
(B)	$6 \times 10^5$	$3 \times 10^3$	$2 \times 10^5$	$1 \times 10^4$

Strontium 90 ( $^{90}\text{Sr}$ , half-life of 28.8 years) is one of the major radionuclides that was released into the environment during the TEPCO's Fukushima Daiichi NPS accident in 2011. Because its biochemical behavior is similar to that of calcium,  $^{90}\text{Sr}$  tends to accumulate in the human bones, causing long-term internal exposure.

Several methods have been reported so far for determining  $^{90}\text{Sr}$ . These methods are classified into radiation measurement and mass spectrometry. The former is the conventional method of detecting  $\beta$  radiation from  $^{90}\text{Y}$ , and it requires a time-consuming process of  $^{90}\text{Y}$  separation; therefore, it is considered unsuitable for rapid analysis. The latter is a method of detecting  $^{90}\text{Sr}^+$  ions after ionization, and an example is inductively coupled plasma mass spectrometry (ICP-MS). However, ICP-MS suffers from isobaric interference caused by zirconium 90 ( $^{90}\text{Zr}$ ), and mass spectral interference of  $^{88}\text{Sr}$  in samples with high concentrations of stable Sr isotopes.

In this work, we developed a device for measuring  $\text{Sr}^+$  ions using a quadrupole mass spectrometer, where three wavelength-tuned lasers are used for element- and isotope-selective laser resonance ionization of  $^{90}\text{Sr}$  atoms, as shown in Fig.1-27. Isotope shifts of

stable Sr isotopes ( $^{84}\text{Sr}$ ,  $^{86}\text{Sr}$ ,  $^{87}\text{Sr}$ , and  $^{88}\text{Sr}$ ) and energy-level splitting of  $^{87}\text{Sr}$  due to the hyperfine structure were observed for each of the two ionization schemes: (A) 689.4 nm–487.4 nm–393.8 nm and (B) 689.4 nm–472.4 nm–404.2 nm, both of which are expected to have high isotopic selectivity. Fig.1-28 shows an example of the observed  $^{88}\text{Sr}$  and  $^{87}\text{Sr}$  frequency spectra using scheme (B) where Laser-3 (404.2 nm) frequency was scanned. The measured  $^{90}\text{Sr}$  optical isotopic selectivities with respect to the stable Sr isotopes ranged from  $10^3$  to  $10^5$  for both schemes, as shown in Table 1-2. Compared to the existing mass spectrometry, our method is expected to greatly simplify the sample pretreatment process, especially in the analysis of soil and marine samples containing large amounts of  $^{90}\text{Zr}$  and stable Sr isotopes, respectively.

A part of this work was supported by the JAEA Nuclear Energy S&T and Human Resource Development Project through concentrating wisdom (JPJA18B18071760), "Development of technology for rapid analysis of strontium-90 with low isotopic abundance using laser resonance ionization".

(Yoshihiro Iwata)

### Reference

Iwata, Y. et al., Isotope Shift and Hyperfine Structure Measurements on Triple Resonance Excitation to the Autoionizing Rydberg State of Atomic Strontium, Journal of Quantitative Spectroscopy and Radiative Transfer, vol.275, 2021, 107882, 9p.

# 1-15 Toward Confident Hot-Spot Visualization Using an Unmanned Helicopter

## — Improvement of Detection Accuracy by Selecting Data on the Flight Conditions —

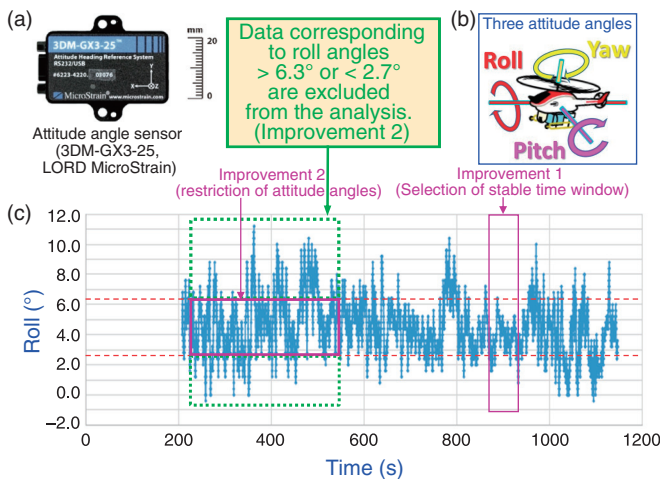


**Fig.1-29 Additional functions to the measurement system: attitude angle sensor**  
 Attitude angle sensor (a), three attitude angles (b), and the obtained roll angle data (c).

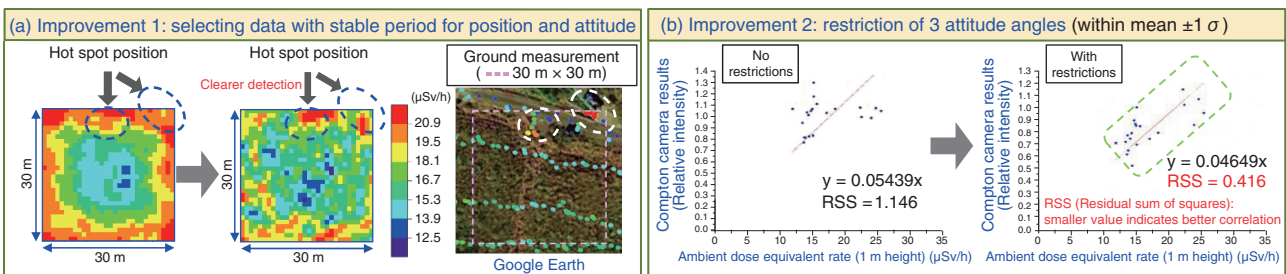


**Fig.1-30 Examples of improvement of the analysis method**

(a) Improvement 1 in the ambient dose equivalent rate map by selecting a time zone with stable position and attitude, and (b) improvement 2 in correlation with ground measurements by restricting the attitude angle.

Unmanned helicopters that can quickly move and take measurements over a wide area from the sky are expected to be used to accurately grasp the contamination status of radioactive materials released widely by the accident at TEPCO's Fukushima Daiichi NPS and to improve the efficiency of decontamination work. A Compton camera that can visualize the contamination distribution has often been used for measurements on the ground. We developed a Compton camera measurement system mounted on an unmanned helicopter and performed a measurement test in an area with a high dose rate in Fukushima Prefecture. The incident angle of radiation is important in the measurement by the Compton camera; however, there was a problem that the measurement accuracy deteriorated because of the instability of its posture in the sky under strong wind conditions. Therefore, we focused on the characteristics of autonomous-type unmanned helicopters that can rapidly return to the programmed position against sudden wind. We tried to improve the accuracy of hot-spot detection by adding new equipment (the attitude angles sensor (Fig.1-29), etc.) to the Compton camera system for recording the flight conditions better.

The Compton camera system mounted on an unmanned helicopter R-MAX G-I was tested at a field in Okuma, Fukushima Prefecture. Measurements (duration: about 15 min) were performed during hovering flight, in which gamma-ray source images were recorded from fixed positions about 20 m above the hot spots identified from previous ground measurements.

Based on the results, we obtained the distribution of the ambient dose equivalent rate at a height of 1 m and compared it with

the values of ground-level measurement using survey meters. During the 15-min flight, the attitude angles were sometimes greatly disturbed (Fig.1-29(c)). Therefore, to identify the radiation source position more accurately, we implemented the following two improvements.

**Improvement 1:** Use of data for about 1 min (Fig.1-29(c), 870–934s) in which the posture was relatively stable, instead of using all the measurement data throughout 15 min. This enabled a clearer recognition of the hot spots in the upper right of the area (Fig.1-30(a)).

**Improvement 2:** Even during the period when the posture was unstable (Fig.1-29(c), 224–546 s), use of only the data within the stable range of the three attitude angles enabled clearer recognition of the hot spots. The residual sum of squares (RSS), an indicator of the correlation between the aerial and ground-level measurement results, decreases as the distribution of the plots approaches the regression line (i.e., the correlation is better) over the entire dose rate range. The decrease in the RSS from 1.15 to 0.42 with improvement 2 (Fig.1-30(b)) indicates the improvement in the correlation. Good linearity in dose conversion leads to good reproducibility of ground-level values. Since reproducibility up to a high-dose-rate range is important for hot-spot detection, the improvement 2 resulted in improved hot-spot detection accuracy.

The accuracy of hot-spot detection and that of ambient dose equivalent rate distribution measurement were improved by incorporating data selection considering the flight conditions into the analysis. These results are expected to be utilized in future aerial hot-spot detection and contamination distribution measurement.

(Yoshiaki Shikaze)

### Reference

Shikaze, Y. et al., Improvement of Analysis Results from the GAGG Scintillator Compton Camera Operated on an Unmanned Helicopter by Selecting Stable Flight Conditions, *Journal of Nuclear Science and Technology*, vol.59, issue 1, 2022, p.44–54.

# 1-16 Research on the Decreasing Trend of Atmospheric Radiocesium Concentration After the Accident

## — Assessing the Decrease Rate Based on Governmental Monitoring Results —

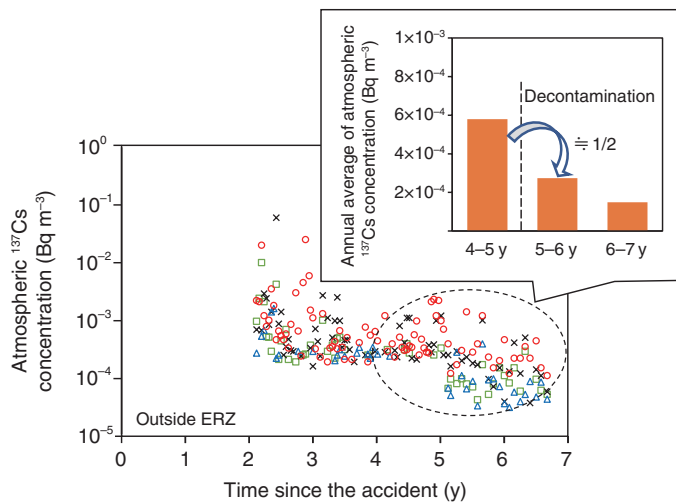


**Fig.1-31 Temporal changes in atmospheric  $^{137}\text{Cs}$  concentrations**  
The temporal changes in atmospheric  $^{137}\text{Cs}$  concentrations measured at four sites outside the entry-restricted zone (ERZ) indicated a decreasing trend at all sites. Additionally, the atmospheric  $^{137}\text{Cs}$  concentration decreased rapidly five years after the 1F accident because of decontamination and was reduced to about half of the previous year's value.

The atmospheric  $^{137}\text{Cs}$  concentrations have been monitored continuously to assess the internal exposure of residents after the TEPCO's Fukushima Daiichi NPS (1F) accident in March 2011. Evaluation of the resuspension factor (RF) is effective for assessing the internal exposure over a broad area because the atmospheric  $^{137}\text{Cs}$  concentration can be easily estimated from the  $^{137}\text{Cs}$  deposited on the ground surface, for which information is easily obtained over a broad area.

In this study, to evaluate the characteristics of the long-term variation trend of RF, we analyzed the results of atmospheric  $^{137}\text{Cs}$  concentration, which were continuously monitored and published by the Nuclear Regulation Authority (NRA) since the 1F accident. The influence of anthropogenic activities was assessed by comparing data obtained inside and outside the entry-restricted zone (ERZ), where human access is restricted.

The data used in this study were the data on atmospheric  $^{137}\text{Cs}$  concentrations at two sites within the ERZ and four sites outside the ERZ, obtained between May 2013 and November 2017. The  $^{137}\text{Cs}$  deposition on the ground surface was based on the data from the distribution map of  $^{137}\text{Cs}$  deposition, which was re-evaluated based on the 3rd Airborne Radiological Survey.

Atmospheric  $^{137}\text{Cs}$  concentrations showed a decreasing trend over time at all sites during the observation period. In particular,  $^{137}\text{Cs}$  concentrations outside ERZ probably decreased rapidly after five years after the 1F accident because of the

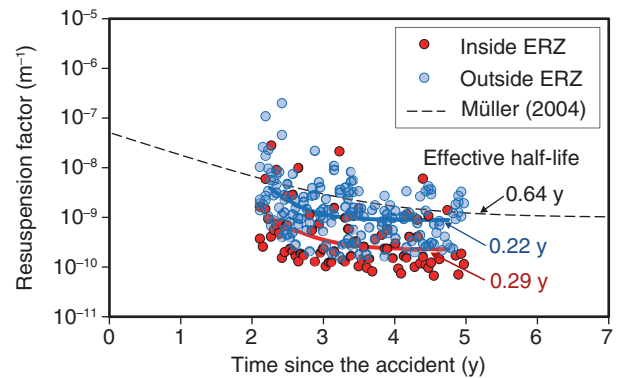


**Fig.1-32 Temporal changes in the resuspension factor (RF) and effective half-life**

The resuspension factor (RF; i.e., the ratio of dispersion from the ground surface to the air) before decontamination decreased faster outside the ERZ (0.22 years) than inside ERZ (0.29 years) and faster in Fukushima than during the Chernobyl accident (0.64 years), when compared in terms of the effective half-life (i.e., the time for the concentration to be halved).

effect of decontamination (Fig.1-31). To evaluate the influence of anthropogenic activities other than decontamination, we compared the trend of RF variation over the period from two years after the accident to five years after the accident before decontamination was performed, by fitting an exponential model (Fig.1-32). A comparison of the situations inside and outside the ERZ showed that the RF was higher and the effective half-life was smaller outside the ERZ. Within the ERZ, the main driver of resuspension is only natural phenomena such as wind; in contrast, outside the ERZ, the impact of anthropogenic activity is more remarkable, and therefore, the resuspended component is likely to reduce more rapidly by anthropogenic activity.

We also compared the variation trends of the RF values obtained in this study with the previously reported results related to the Chernobyl accident (Fig.1-32). The half-life of the Fukushima RF modeled in this study was found to be shorter than that of Müller's\* results, which were fitted by the same exponential model as in this study, especially outside ERZ.

These findings are considered important for determining the parameters for internal exposure assessment.

(Tomohisa Abe)

\*Müller, H. et al., Model Description of the Terrestrial Food Chain and Dose Module FDMT in RODOS PV6.0, RODOS(RA3)-TN(03)06, 2003, 55p.

### Reference

Abe, T. et al., Temporal Change in Atmospheric Radiocesium During the First Seven Years After the Fukushima Dai-ichi Nuclear Power Plant Accident, *Aerosol and Air Quality Research*, vol.21, issue 7, 2021, 200636, 11p.

# 1-17 Why Does the Air Dose Rate in Urban Areas Decline Quickly?

— Reduction Effect Revealed by the Behavior of Radioactive Cesium —

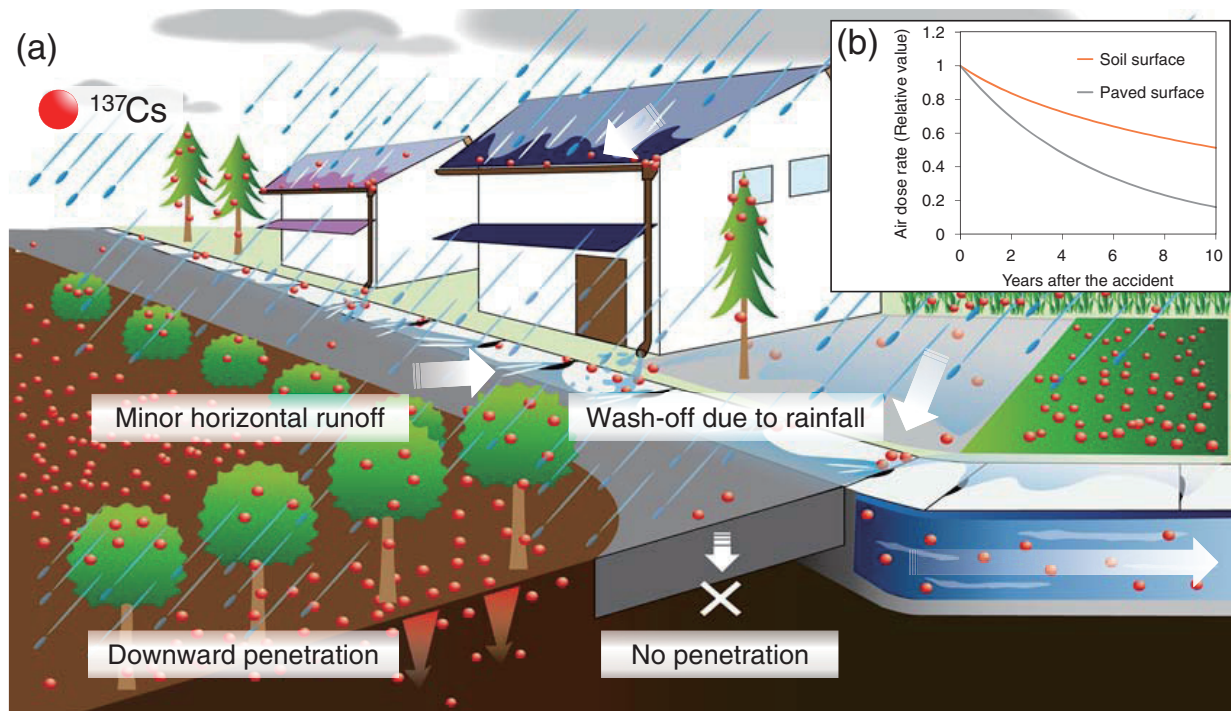


**Fig.1-33 (a) Overview of the behavior of  $^{137}\text{Cs}$  in urban areas and (b) decreasing trend of air dose rate estimated considering the behavior of  $^{137}\text{Cs}$**

Urban areas mainly have soil surfaces and other artificial surfaces such as paved surfaces and houses. The behavior of  $^{137}\text{Cs}$ , such as downward penetration and horizontal wash-off due to rainfall, differs between soil and paved surfaces, thereby affecting the decreasing trend of air dose rates.

The decreasing trend of air dose rates in urban areas is important for predicting future exposure doses and for decision making regarding the lifting of the evacuation-order zone around the TEPCO's Fukushima Daiichi NPS. Previous studies reported that air dose rates decrease faster in urban areas than in areas under other land use, such as forests and agricultural land, but the mechanism of this decrease has not been understood. This study reviewed previous studies on the behavior of radiocesium, which is a major source of radiation, in urban areas and evaluated the relationship between its behavior and the decreasing trend in air dose rates.

Unlike other land uses such as forests and agricultural land, urban areas are covered by artificial surfaces such as paved surfaces and houses in addition to the soil surface. Air dose rates decrease due to radioactive decay of radionuclides (especially radiocesium). Air dose rates also decrease due to the behavior of radionuclides on the ground surface, such as increased shielding by the soil due to downward infiltration of radionuclides, and horizontal wash-off associated with rainfall. While radioactive decay occurs universally, the behavior of these radionuclides differs between soil and artificial surfaces. Fig.1-33(a) shows an overview of the behavior of  $^{137}\text{Cs}$  in urban

areas. Most of the soil surfaces in urban areas are flat areas in parks and gardens, and since flat areas are not subject to soil erosion, little horizontal wash-off occurs during rainfall events, but there is a little downward penetration. On paved surfaces, in contrast,  $^{137}\text{Cs}$  has little downward penetration, but is washed away with rainfall, resulting in reduction of inventory with time. Thus, downward penetration of radiocesium on soil surfaces and horizontal wash-off of radiocesium on artificial surfaces contribute to the reduction of air dose rates.

Fig.1-33(b) shows decrease in air dose rate over time based on the previously reported downward migration rate of  $^{137}\text{Cs}$  on flat soil surfaces and the decrease rate of  $^{137}\text{Cs}$  inventory on paved surfaces. The faster decrease in air dose rates on paved surfaces than on soil surfaces indicates that the wash-off of  $^{137}\text{Cs}$  on artificial surfaces is more effective in reducing air dose rates. Therefore, artificial surfaces are thought to contribute to faster reductions in air dose rates than other land uses.

This study was partially supported by Research project on the Health Effects of Radiation organized by Ministry of the Environment, Japan.

(Kazuya Yoshimura)

## Reference

Yoshimura, K., Air Dose Rates and Cesium-137 in Urban Areas—Deposition, Migration, and Time Dependencies After Nuclear Power Plant Accidents, Journal of Nuclear Science and Technology, vol.59, issue 1, 2022, p.25–33.

## Implementing Continuous Improvements in Safety and Emergency Preparedness

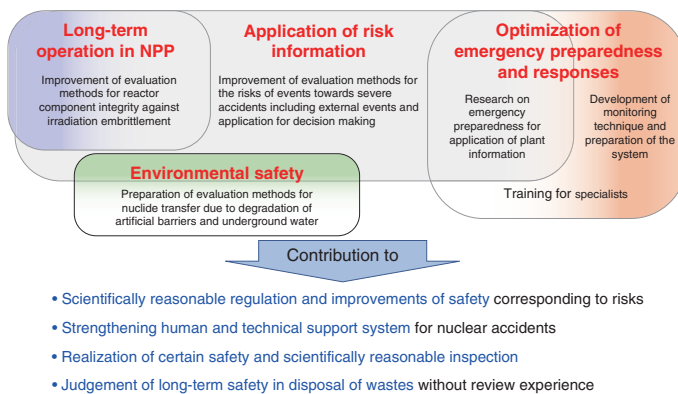


**Fig.2-1 Activities at the Sector of Nuclear Safety Research and Emergency Preparedness**

In accordance with the lessons learned from the accident at 1F and the trend in utilization of nuclear energy, we have prioritized pillars of research activities on application of risk information, optimization of emergency preparedness and responses, long-term operation in nuclear power plant (NPP), and environmental safety.

The Sector of Nuclear Safety Research and Emergency Preparedness has performed safety research in accordance with the lessons learned from the accident at the TEPCO's Fukushima Daiichi NPS (1F), as well as response to emergency situations as a designated public institution assigned in the Disaster Countermeasures Basic Act and training for personnel engaging nuclear emergency preparedness and responses in normal times. As shown in Fig.2-1, pillars of research activities have been prioritized, specifically, evaluation of the risks toward severe accidents beyond the design basis, nuclear emergency preparedness for appropriate and rapid response to nuclear accidents, research for long-term operation in nuclear power plants on neutron irradiation embrittlement of reactor pressure vessels using materials harvested from commercial reactors, and environmental safety research on disposal of nuclear wastes from 1F and intermediate depth disposal. Through these activities, we have provided technical support for nuclear regulatory administration and have contributed to strengthening of nuclear emergency preparedness and responses in related administrative agencies and local public bodies.

The safety research in Japan Atomic Energy Agency (JAEA) is featured by large-scale facilities where various accident conditions can be simulated. For example, the high-pressure thermal-hydraulic loop shown in Fig.2-2 has been constructed and used to develop sophisticated techniques to evaluate core heat transfer. The Nuclear Safety Research Reactor, shown in Fig.2-3, has been used to investigate the fuel failure limit and the effect of fuel failure on the nuclear reactor during a reactivity-initiated accident, which is a design-basis event. In addition, studies on ultra-trace analysis of nuclear materials for nuclear

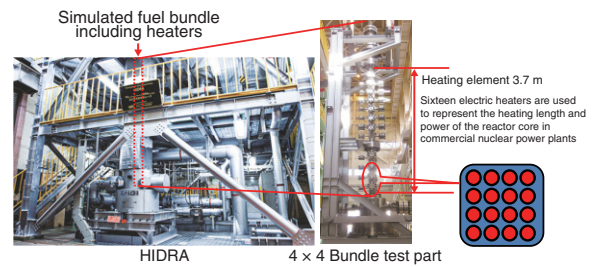


**Fig.2-2 High-pressure thermal-hydraulic loop (HIDRA)**  
Experiments performed using HIDRA help clarify reactor core cooling performance under severe thermal and hydraulic conditions beyond the design basis.

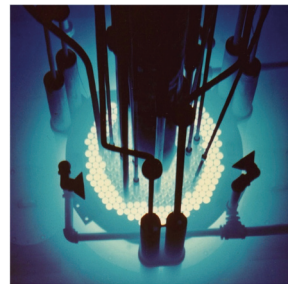


**Fig.2-3 Nuclear Safety Research Reactor (NSRR)**

The NSRR allows experiments simulating a rapid power increase during a reactivity-initiated accident and under high-temperature conditions beyond the design basis to be safely performed.

safeguards have also been performed. Furthermore, JAEA has acted as the operating agent in the OECD/NEA project on the analysis of information from the accident at 1F.

In the field of emergency preparedness and responses, the effectiveness of sheltering as a protective action has been evaluated to improve protection strategy. Moreover, techniques to integrate data obtained by different monitoring methods and investigate radioactivity distributions in coastal regions around 1F are under development. Background radioactivity monitoring of domestic nuclear power plants is continuously carried out in preparation for nuclear emergencies.

This chapter presents the results of the following recent research activities: evaluation of the risks toward core damage due to loss of safety function after internal flooding from ruptured pipes in a nuclear facility (Topic 2-1); experimental and numerical research on the flow in a containment vessel during a severe accident using a large-scale experimental facility (Topic 2-2); prediction of fuel debris form for the assessment of debris coolability in a severe accident (Topic 2-3); assessment of the sheltering effectiveness in Japanese houses in nuclear accidents (Topic 2-4); evaluation of failure probability of aged piping system in nuclear facilities against seismic ground motion (Topic 2-5); and, evaluation of exposure dose during treatment of asbestos waste arising from decommissioning of nuclear power plants (Topic 2-6).

The other topic related to 1F-accident, improvement of detection accuracy when unmanned helicopters measure the contamination status of radioactive materials released by the 1F-accident (Topic 1-15) was also detailed in Chapter 1.

# 2-1 Understanding Reactor Risk Profiles Against External Events

## — Probabilistic Assessment of Internal Flooding-Induced Risks by a Dynamic Approach —

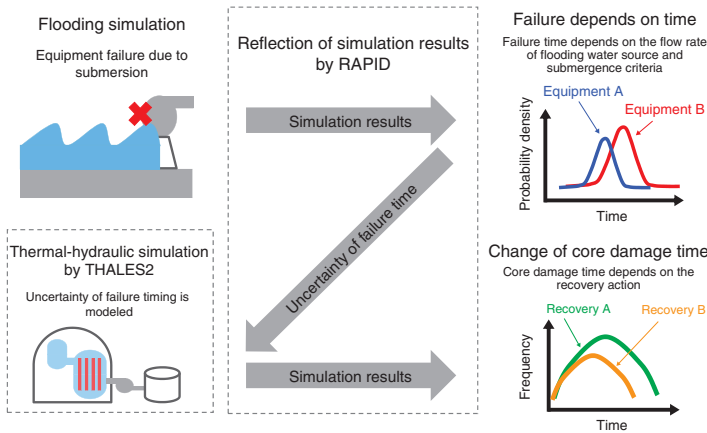


**Fig.2-4 Reflecting uncertainty evaluated by flooding simulation to thermal-hydraulic simulation**

Dynamic probabilistic risk assessment (DPRA) was performed considering plant response due to flooding. The probability distribution of failure timing of submerged equipment is analyzed by flooding simulation and reflected on thermal-hydraulics simulation.

Risk is an important safety related measure. The probabilistic risk assessment (PRA) has been used to evaluate the risk of nuclear reactors including external events such as earthquakes and tsunamis. This method utilizes tree-shaped diagrams to organize the effects of equipment failure. The obtained information (e.g., core damage frequency) can be used for various decision making situations to enhance safety. Japan Atomic Energy Agency (JAEA) is developing a dynamic PRA (DPRA), one of the advanced PRAs, and a computational tool named RAPID. DPRA links various simulations to the tree-shaped diagrams used in the conventional PRA. It can consider temporal effects like the failure timing which is difficult to manipulate in the conventional PRA. The DPRA of internal flooding has the advantage of allowing in-depth consideration of failure timing due to water propagation from ruptured pipes to adjacent rooms and their impact on the plant response.

DPRA of internal flooding at a turbine building in a pressurized water reactor was performed using RAPID. As shown in Fig.2-4, the results of flooding simulation were reflected on a thermal-hydraulics code of THALES2. For recovery actions, two were modeled; (1) isolation of flooding water sources and (2) drainage with pump. Core damage timing after the flooding occurrence and conditional core damage probabilities (CCDPs) were analyzed.

**Reference**

Kubo, K. et al., Simulation-Based Dynamic Probabilistic Risk Assessment of an Internal Flooding Initiated Accident in Nuclear Power Plant Using THALES2 and RAPID, Proceedings of the Institution of Mechanical Engineers, Part O: Journal of Risk and Reliability, 2022, 11p., doi.org/10.1177/1748006X221091604

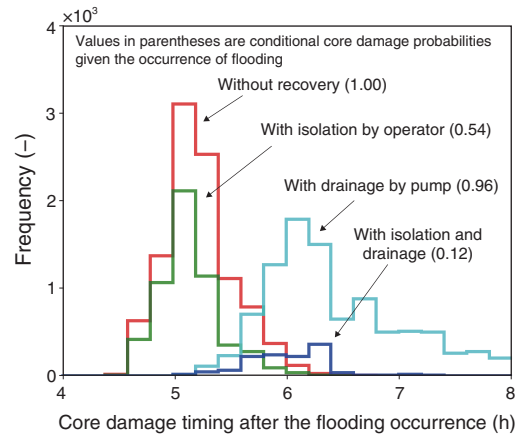


**Fig.2-5 Changes in core damage timing by recovery actions**

This figure shows the changes in frequency distributions of core damage timing after introducing recovery actions. It is difficult to obtain such explicit time-dependent information in the conventional static PRA.

Fig.2-5 shows the changes of core damage timing when recovery actions are taken. Here, 10,000 trials of Monte Carlo simulation have been conducted. The isolation can effectively reduce frequency of core damage after five hours. This reduction is attributed to the late-phase submergence being avoided. The drainage can postpone core damage timing by delaying the submergence timing. If these recovery actions are applied simultaneously, their synergistic effects can drastically diminish the occurrence of core damage. The combination reduces the CCDP given the occurrence of flooding by around one order of magnitude. The analysis illustrates that DPRA enables a more detailed assessment by considering failure timing due to flooding.

As shown in the results, DPRA enables risk analysts to understand the risk profiles of facilities in a more detailed manner. This understanding is helpful for risk-informed decision making such as establishing more effective safety improvement measures. In the future, risk assessments against other external events will be performed to verify the effectiveness of various countermeasures.

This research was conducted using the Oakbridge-CX at the University of Tokyo, the ICE X and HPE SGI 8600 at JAEA.

(Kotaro Kubo)

## 2-2 Understanding Containment Vessel Flow During Severe Accident

### — Mass Transport Behavior Depending on the Relative Location of Outer Cooling and Initial Stratification —

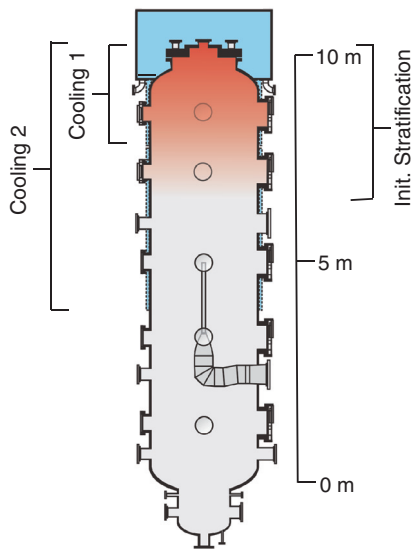


**Fig.2-6 Overview of the CIGMA experimental condition**

The test vessel is 11 m in height and 2.5 m in diameter. Cooling 1: the cooled region narrower than the initial stratification layer thickness, and Cooling 2: the cooled region wider than the initial stratification.

During a severe accident (SA) in a light water reactor, the atmosphere in the nuclear containment vessel changes to a high-temperature and high-pressure state due to the discharge of high-temperature gases from the primary system. Furthermore, a large amount of hydrogen is generated in the core by zirconium-steam reaction and the threat of hydrogen explosion increases when hydrogen concentration accumulates in a local compartment. In the Fukushima-Daiichi nuclear power plant accident, hydrogen leaked into the reactor building due to over temperature failure of the containment vessel which caused an explosion that severely wrecked the building.

To understand the heat and mass transport phenomena during SA, experimental and numerical research have been performed in Japan Atomic Energy Agency. The CIGMA facility has a large test vessel of 2.5 m in diameter and 11 m in height (see Fig.2-6) with a unique system of outer surface cooling. Thereby, the natural convection is driven in the test vessel. Gas transport phenomena such as localization and mixing by wall cooling is investigated. Figure 2-6 shows an example of the experiment related to the heat and mass transfer driven by the natural convection.

A representative fluid dynamic of a light gas, such as hydrogen in enclosure, is density stratification which is the formation of unmixed gas layers at the upper part of a vessel. In the two experiments shown in Fig.2-7, the initial stratification was formed by a mixture of air and helium (as a simulant of hydrogen), and then natural convection was driven by outer

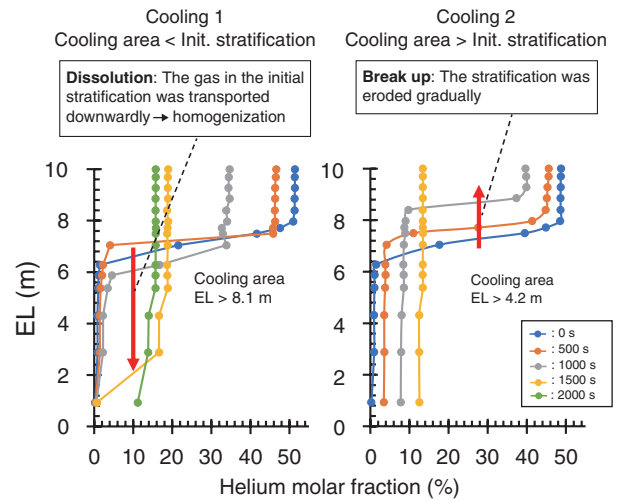


**Fig.2-7 Time transients of the vertical distributions of helium molar fraction**

Cooling 1: Stratification dissolution, and Cooling 2: Stratification break up.

cooling. The relative location between the outer cooling and initial stratification is of interest in this experiment series. The following explains the characteristic behaviors focusing on the time transient of gas composition:

Cooling 1: the cooled region was narrower than the initial stratification thickness; gas in the initial stratification was transported when the gas density in the stratification exceeded that in the lower part below stratification, and homogenization occurred. That is, the density stratification was dissolved by temperature reduction due to the outer cooling.

Cooling 2: the cooled region was wider than the initial stratification thickness; the stratification was gradually eroded by the shear stress due to flow at the bottom of the stratification. Therefore, the helium molar fraction in the initial stratification decreased from the lower elevation. Consequently, the stratification was broken up.

The findings will help understand the different mode of stratified gas mixing by natural circulation in the containment vessel during SA, and will be a foundation for proposing the optimization of the accident management measure. In addition, the experimental data is useful for validating the numerical simulation including Computational Fluid Dynamics.

The construction of the CIGMA facility used in this research activity were conducted under the auspices of the Nuclear Regulation Authority in Japan.

(Satoshi Abe)

#### Reference

Abe, S. et al., Experimental Investigation of Natural Convection and Gas Mixing Behaviors Driven by Outer Surface Cooling With and Without Density Stratification Consisting of an Air-Helium Gas Mixture in a Large-Scale Enclosed Vessel, *Annals of Nuclear Energy*, vol.166, 2022, 108791, 18p.

## 2-3 Fuel Debris Form Prediction in a Severe Accident

### — Measurements of Mass Fractions of Agglomerated Debris Settled on the Floor of a PCV —

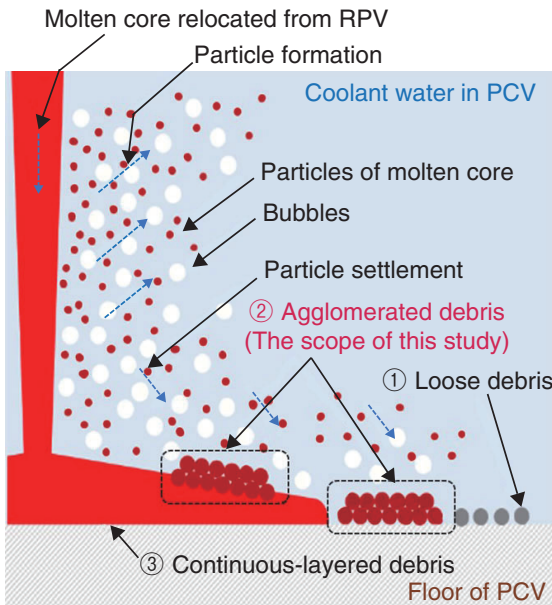


**Fig.2-8 Assumed forms of settled debris in water coolant on a floor of a primary containment vessel (PCV) in a severe accident (SA)**

In a SA, the settled debris on the floor of a CV shows the different forms (①–③) depending on melt relocation conditions from a reactor pressure vessel (RPV). This study focused the agglomerated debris.

In a severe accident (SA), high-temperature molten core (melt) can relocate in a primary containment vessel (PCV) due to rupture of a reactor pressure vessel (RPV). The molten core-concrete interaction (MCCI) threatens the PCV integrity due to concrete ablation by the melt. To prevent and mitigate the MCCI, Japanese utilities have employed the strategy that injects coolant water in a PCV before rupture of the RPV. The assessment of debris coolability on the floor of a PCV is important in evaluating the effectiveness of the employed strategy.

The settled debris on a floor is supposed to show three different forms depending on melt relocation conditions (e.g., physical properties of melt, coolant water depth, melt and coolant temperatures) as shown in Fig.2-8. The loose debris settles by individual solidification of particles detached from the melt. The agglomerated debris settles by merging of particles in a liquid state with others when the particle settles. The continuous-layered debris settles by direct impingement and spreading of the melt. The debris coolability decreases due to the agglomerated or continuous-layered debris settlement because contact areas with coolant water of these debris become smaller than those of the loose debris.

To evaluate debris coolability, the mass fractions and deposition area of the settled debris need to be predicted. This study focused on the agglomerated debris and carried out the experiments of simulant melt (a low-melting-point metal)

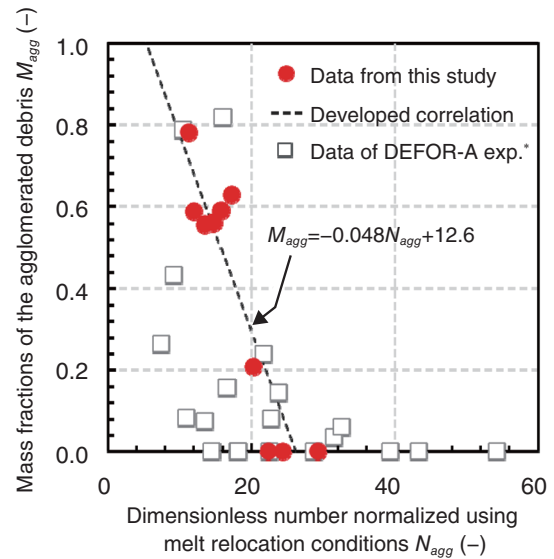


**Fig.2-9 Development of a correlation to predict mass fractions of agglomerated debris using a dimensionless number**

Based on the experiments of simulant melt (a low-melting-point metal) injection into coolant water, we developed the correlation to predict mass fractions of the agglomerated debris using the dimensionless number.

injection into coolant water. Mass fractions of the agglomerated debris in the recovered debris from the experimental apparatus were measured. The systematic changes of melt relocation conditions (i.e., coolant water depth and, melt and coolant water temperatures) clarified dominant factors on mass fractions of the agglomerated debris.

This study has developed the correlation to predict mass fraction of the agglomerated debris using the dimensionless number expressed by simple products of the melt relocation conditions (Fig.2-9). The developed correlation predicted the overall trend of mass fractions of the agglomerated debris obtained from the DEFOR-A experiments\* conducted at the Royal Institute of Technology under the different melt relocation conditions using the oxide mixture as a simulant melt. The results indicate that the developed correlation is applicable to diverse melt relocation conditions.

Debris coolability to develop credible methods applicable to diverse melt relocation conditions supposed in a SA in actual reactors will be further investigated.

This study was conducted as part of collaborative research with the University of Tsukuba.

(Yuzuru Iwasawa)

\* Kudinov, P. et al., Agglomeration and Size Distribution of Debris in DEFOR-A Experiments with Bi<sub>2</sub>O<sub>3</sub>-WO<sub>3</sub> Corium Simulant Melt, Nuclear Engineering and Design, vol.263, 2013, p.284–295.

#### Reference

Iwasawa, Y. et al., Experiments of Melt Jet-Breakup for Agglomerated Debris Formation Using a Metallic Melt, Nuclear Engineering and Design, vol.386, 2022, 111575, 17p.

## 2-4 Parameter Determination for Assessing the Sheltering Effectiveness in Japanese Houses

— Obtaining Data on Penetration Factor and Deposition Rate of Particulate and Elementary Iodine by Real House and Chamber Experiment —

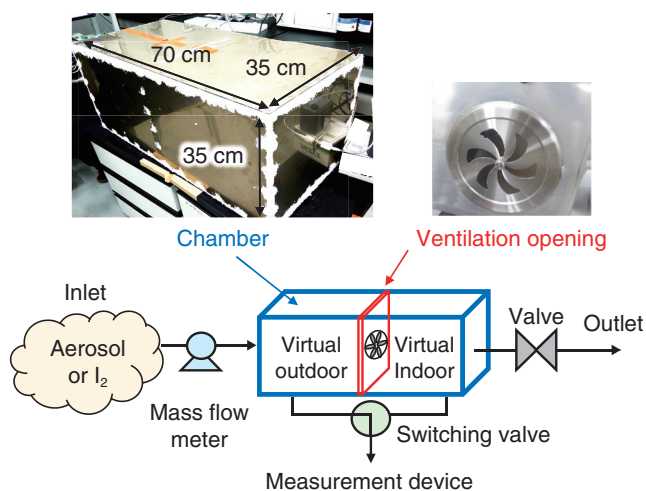


**Fig.2-10 Diagram of chamber experiment**

The chamber was divided in the middle with a ventilation opening. The penetration factor and deposition rate were determined based on the temporal variation in the concentrations of aerosol or  $I_2$  inside and outside the virtual room.

Sheltering is one of the countermeasures for protection against residents' exposure in nuclear accidents. The indoor radioactivity concentration is calculated mainly with (1) the “air exchange rate,” which represents the ratio of indoor volume exchanging per unit time, (2) the “penetration factor,” which represents the ratio of radioactive materials entering the house without adhering to openings, and (3) the “deposition rate,” which represents the rate of radioactive materials adhering to walls and floor surfaces.

Iodine is one of the most important nuclides for internal exposure in the early stage of nuclear accidents. The form of iodine discharged into the atmosphere can be categorized into three types depending on its chemical properties and behavior: (1) iodine attached to aerosols (particulate iodine); (2) gaseous elementary iodine ( $I_2$ ); and (3) gaseous organic iodine (e.g.,  $CH_3I$ ). The penetration factor and deposition rate differ among these forms, and the sheltering effectiveness depends on the proportion of each form. However, little is known about  $I_2$ , and these parameter values depend on the material of the floor surface and openings. Since house characteristics differ among countries, it is inappropriate to apply the parameter values of foreign countries to assess sheltering effectiveness in Japanese houses; therefore, it is necessary to provide the parameter values for Japanese houses.

In this study, experiments were conducted in real Japanese houses (real house experiment) to obtain the penetration factor and deposition rate in Japan. Due to the toxicity of  $I_2$ , its penetration factor and deposition rate was obtained only by experiments in a chamber simulating air exchange (chamber experiment). For particulate iodine, both experiments were

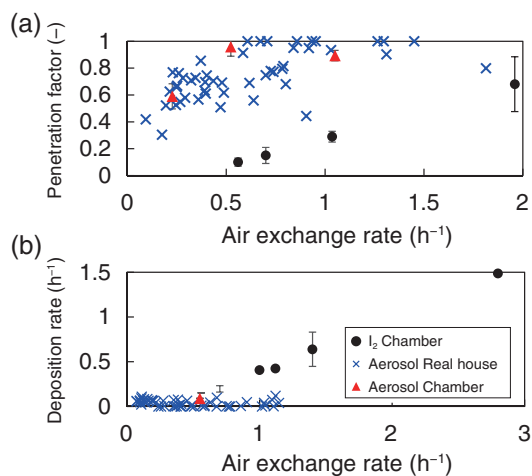


**Fig.2-11 Penetration factor (a) and deposition rate (b) in relation to air exchange rate**

For  $I_2$ , the penetration factor is smaller than that for aerosols and the deposition is larger, indicating that  $I_2$  is less penetrate and more easily deposits than particulate iodine. No difference between the real house and chamber experiments for aerosols indicates that the values obtained in the chamber experiments are applicable to real houses.

conducted to examine the applicability of the chamber experiment results to real houses. The behavior of particulate iodine was assumed to be the same as that of other aerosols with the same particle size, and the values obtained using aerosols ( $NaCl$ ) of  $0.3\text{--}1\ \mu\text{m}$  were used as the values for particulate iodine. This size is the same as that of particulate iodine observed during nuclear accidents. In the real house experiment, the penetration factor and deposition rate were determined by continuously measuring the aerosol concentrations indoors and outdoors. In the chamber experiment, these parameters were determined by alternately measuring the concentrations inside and outside the virtual room using a chamber separated in the middle by a ventilation opening (Fig.2-10).

The experimental results are shown in Fig.2-11. The penetration factor of aerosols and  $I_2$  are  $0.3\text{--}1$  and  $0.15\text{--}0.7$ , respectively, with  $I_2$  being smaller, indicating that  $I_2$  is less penetrate than particulate iodine. The deposition rate of aerosols and  $I_2$  are  $0.007\text{--}0.2\ \text{h}^{-1}$  and  $0.2\text{--}1.5\ \text{h}^{-1}$ , respectively, with  $I_2$  being larger, indicating that  $I_2$  is more easily deposited on surfaces than particulate iodine. Except for the deposition rate of aerosols, the values tended to increase with the air exchange rate.

The results of this study indicate that penetration factor and deposition rate differ between aerosols and  $I_2$ , prompting the need to assess the sheltering effectiveness according to the proportion of each form. In the future, the sheltering effectiveness in Japanese houses using these values is planned to be assessed.

A part of this study was conducted in FY2020, supported by the Nuclear Regulation Authority in Japan.

(Jun Hirouchi)

### Reference

Hirouchi, J. et al., Penetration Factor and Indoor Deposition Rate of Elementary and Particulate Iodine in a Japanese House for Assessing the Effectiveness of Sheltering for Radiation Exposures, *Journal of Radiological Protection*, vol.41, 2021, p.S139–S149.

## 2-5 How Much Can Nuclear Piping Withstand Huge Earthquakes — Development of Seismic Fragility Evaluation Method for Aged Piping —

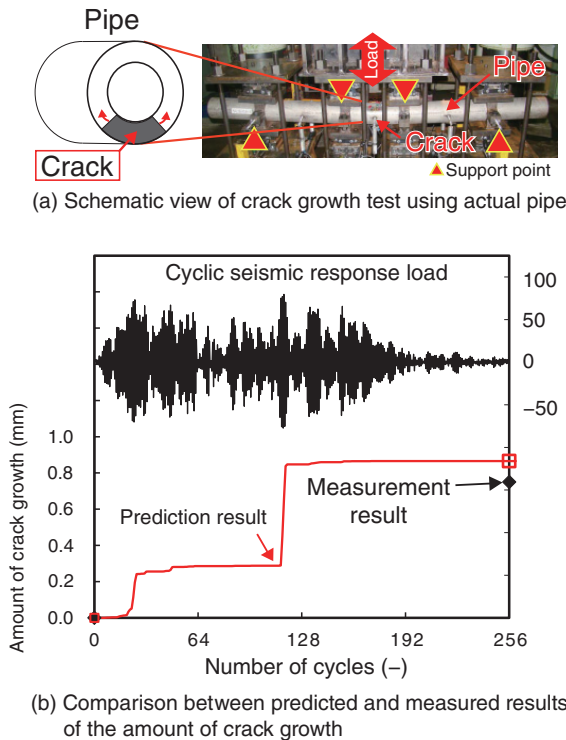


**Fig.2-12 Validation test of crack growth evaluation method**  
The crack growth evaluation method was validated by comparing the measured value of the amount of crack growth with the predicted value.

Based on the lessons learned from the Fukushima Daiichi nuclear power plant (NPP) accident, safety improvement assessments of NPPs have been requested throughout Japan. The seismic probabilistic risk assessment (SPRA) is an important methodology for safety improvement assessments. In SPRA, the core damage frequency is evaluated by considering the seismic fragilities which are determined based on the failure probabilities of components against seismic ground motions. Focusing on piping systems as the evaluation targets, cracks due to age-related degradation mechanisms have been reported. Therefore, to realistically evaluate seismic fragility of aged piping system with cracks, their decrease in strength due to initiation and propagation of cracks should be considered. However, there is presently no evaluation method and code for the seismic fragility evaluation of aged piping.

To develop a seismic fragility evaluation method for aged piping, first, a crack growth evaluation method through experiments and numerical analyses taking large seismic stress were taken into consideration. As shown in Fig.2-12, the developed method was validated through crack growth tests with actual pipes subjected to cyclic seismic response loading.

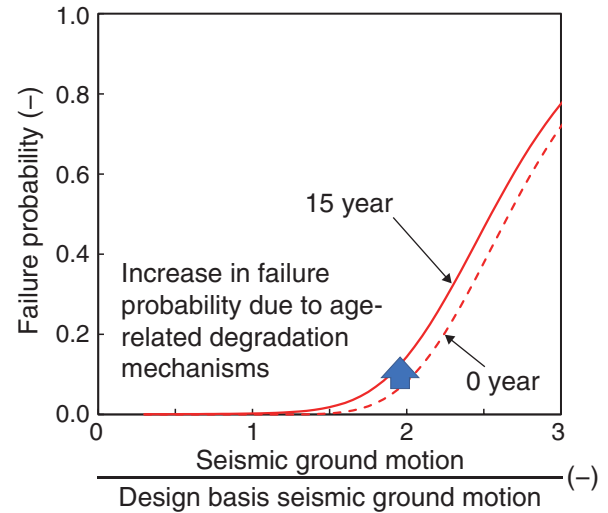


**Fig.2-13 Example of the relationship between the seismic ground motion ratio and failure probability at each service life**  
PASCAL-SP2 can calculate the failure probability by considering crack growth due to age-related degradation mechanisms and seismic stress and quantitatively evaluate the increase in fragility curve due to aging.

Then, the crack growth evaluation method was introduced into the probabilistic fracture mechanics analysis code PASCAL-SP which calculates the failure probability of piping by considering age-related degradation mechanisms and uncertainties of fracture mechanics influencing factors. Based on the improvements, PASCAL-SP2 was developed to calculate seismic fragility of aged piping. Finally, a guideline to enable engineers and analysts evaluate seismic fragility for aged piping systems without difficulty is developed. The guideline contains the procedure, recommended methods and models, and technical bases for the seismic fragility evaluation of piping using PASCAL-SP2. As shown in Fig.2-13, the increase in fragility due to age-related degradation mechanisms can be quantitatively evaluated using PASCAL-SP2 in accordance with the guideline. Activities related to the risk-informed applications in safety improvement assessments using developed PASCAL-SP2 and the guideline will continue to be promoted.

This study was performed under contract research entrusted by the Nuclear Regulation Authority of Japan.

(Yoshihito Yamaguchi)

### References

- Yamaguchi, Y. et al., User's Manual and Analysis Methodology of Probabilistic Fracture Mechanics Analysis Code PASCAL-SP Ver. 2 for Piping (Contract Research), JAEA-Data/Code 2020-021, 2021, 176p. (in Japanese).
- Yamaguchi, Y. et al., Guideline on Seismic Fragility Evaluation for Aged Piping (Contract Research), JAEA-Research 2020-017, 2021, 80p. (in Japanese).

## 2-6 A Path Toward Recycling and Landfill of Asbestos Waste Arising from Decommissioning — Development of Evaluation Method for Exposure Dose by Cleared Asbestos Waste —

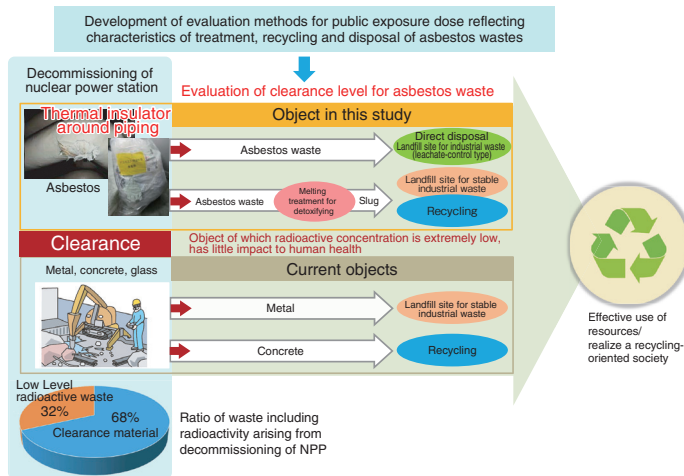


**Fig.2-14 Outline of clearance level evaluation for asbestos waste**

Methods for the treatment, landfill, and recycling of asbestos waste are different from those of metal and concrete. Therefore, we developed the evaluation method of public dose exposure for cleared asbestos waste based on the investigation of the actual treatment of asbestos waste and evaluated its clearance level for the first time.

Some of the radioactive wastes arising from decommissioning of nuclear power plants contain very low radioactive concentration that almost have no adverse effect on human health. Through the “clearance system,” these wastes can be recycled or placed in landfills as industrial wastes after approval and confirmation from the Nuclear Regulatory Authority (NRA) in Japan is obtained.

Previously, asbestos was not under the clearance system of Japan, and therefore has been stored at the radiation controlled area in the facility even if the radioactive concentration of asbestos waste is extremely low. In order to move forward with the treatment of asbestos waste, techniques for exposure evaluation reflecting the characteristics of special treatment and landfill for preventing the inhalation of asbestos fiber dispersed from the waste such as packaging reduplicated by water resisting material and detoxification melting are needed.

Therefore, the evaluation method for public exposure doses from asbestos waste with determination of exposure pathways and evaluation parameters has been developed (Fig.2-14).

Firstly, exposure pathways were determined based on the results of the investigation on actual treatments and landfill of asbestos waste as special industrial waste. The pathways regarding leachate-control landfill sites, which were not considered for metal and concrete waste, were added. Secondly, the range and distribution type (probability density) of the parameter values for all pathways were determined. Thirdly, representative and conservative values were determined from the ranges of parameters for deterministic analysis calculating

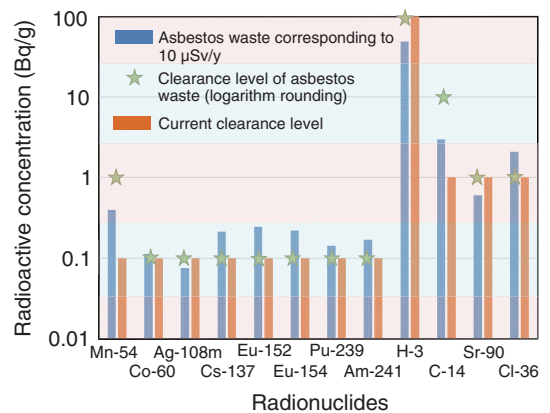


**Fig.2-15 Evaluation results of clearance levels of asbestos waste for typical radionuclides**

Minimum concentrations corresponding to 10  $\mu$ Sv/y were evaluated based on the results of exposure dose calculation. Clearance levels of asbestos waste were expressed in digit according to international standard. The values are the same as or greater than the current clearance levels.

public exposure doses for deriving clearance level. Finally, we conducted the probabilistic analysis using the range and distribution type of parameters to evaluate the effects of uncertainties of the parameters.

Clearance levels of asbestos waste for 33 radionuclides previously regulated in NRA ordinance for nuclear reactors were evaluated by the developed method using exposure dose calculation code PASCLR2 developed by Japan Atomic Energy Agency. The results show that the obtained clearance levels are the same as or greater than the current clearance levels derived for metal and concrete (Fig.2-15). In addition, exposure doses by probabilistic analysis were less than ten times of those in deterministic analysis. This result satisfies the regulatory requirement that the public doses are not sufficiently large even if combinations of extremely conservative values occur with low probabilities. Therefore, it was confirmed that the clearance levels by deterministic analysis were appropriate.

This made it possible to apply the current clearance level to the asbestos waste. As a result, it opens the way to appropriate treatment, recycle, and landfill of the waste. This advances future treatment and recycling of asbestos waste, which will be arising as decommissioning progresses, and help to realize a recycling-oriented society.

This research was a part of the result of contract work supported by the Nuclear Regulation Authority in Japan, “A study on decommissioning and clearance (FY2017–FY2020)”.

(Taro Shimada)

### Reference

Shimada, T. et al., Evaluation of Clearance Level for Radionuclides in Asbestos-Containing Wastes, Japanese Journal of Health Physics, vol.57, no.1, 2022, p.5–29. (in Japanese).

## Fundamental Sciences to Realize the New Era of Nuclear Science and Technology

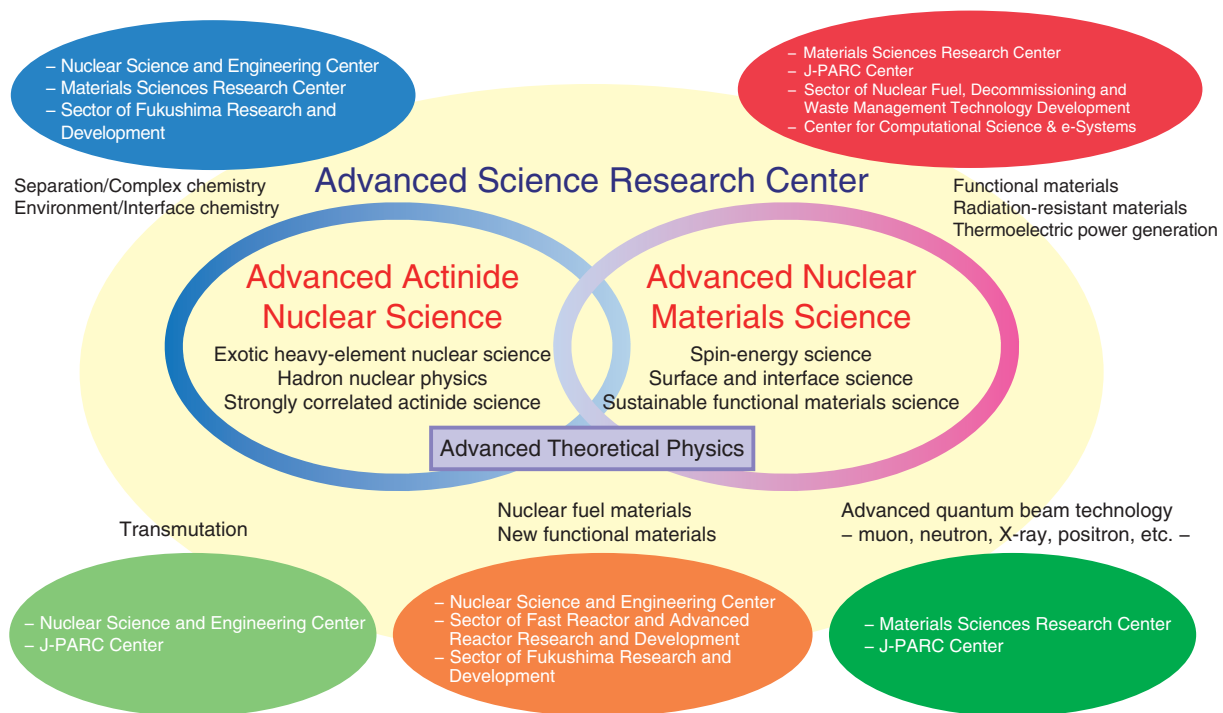


**Fig.3-1 Organization of the Advanced Science Research Center (ASRC) and its role in nuclear science**

The ASRC promotes basic research to discover novel principles and phenomena, to create new materials, and to generate innovative technologies. To this end, we strengthen collaboration with external organizations as well as other centers/sectors within the JAEA.

The Advanced Science Research Center (ASRC) strengthens basic research to discover novel principles and phenomena, create new materials, and generate innovative technologies. The objective is to realize the New Era of Nuclear Science, i.e., the future vision of the JAEA called “JAEA 2050 +”. In this context, we establish our role as a COE in the field of nuclear science by promoting cooperation between different fields and attracting excellent research personnel.

We have started a new midterm program by organizing seven research groups categorized in the fields of ①Advanced Actinide Nuclear Science, ②Advanced Nuclear Materials Science, and ③Advanced Theoretical Physics, as shown in Fig.3-1. Research results achieved in FY2021, which led to the new ASRC organization, will be highlighted below.

In the research on Heavy-element nuclear science, the volatility of a compound of dubnium (Db, atomic number 105) was investigated. It is found that the orbit of the outermost electron changes greatly because of relativistic effects as evidenced by a large deviation of Db from the trend of the elements in the same group in the periodic table (Topic 3-1). The hadron nuclear physics group measured the energy of the K mesons attached in the  $^3\text{He}$  and  $^4\text{He}$  nuclei at the J-PARC facility to determine the nuclear force between the K meson and nucleus (Topic 3-2). In future investigation, we expect to predict the internal structure of a neutron star, which is considered to be the largest nucleus in nature, more precisely. In strongly correlated

actinide science, the electronic structure of  $\text{UTe}_2$  material was investigated by the NMR method (Topic 3-3). A slow fluctuation was found in the case of the electric system. The results give an insight into “topological superconductivity”, which can be applied for next-generation quantum computing.

In spintronics research, we discovered a new principle to change the magnetization direction of an electron via topology-based manipulation (Topic 3-4). Compared to the traditional method, this approach can remarkably reduce the electric power consumption by a factor of 1/10,000 when used for magnetic memories. In the field of surface and interface science, a new technology was developed to visualize the time-dependent changes between ortho- and para-hydrogen molecules on the surface of palladium crystal (Topic 3-5). The results are important for a key technology to preserve and transport liquid hydrogen to promote the use of clean fuel. The surface science group investigated the effects of acid concentration on the adsorption of uranium, which is the major material component of spent fuel from nuclear reactors, on soil (Topic 3-6). This study contributes to the exploration of the geological disposal of radioactive waste material.

The theoretical physics group investigated the behavior of trapped cold atoms, which is a quantum many-body system with large controllability (Topic 3-7). The results will act as a seed to realize quantum circuits with cold atoms, called atomtronics.

## 3-1 What is the Chemical Behavior of the Heaviest Element?

— A Small Breach of the Periodic Law Found in the Volatility of Element 105, Dubnium —

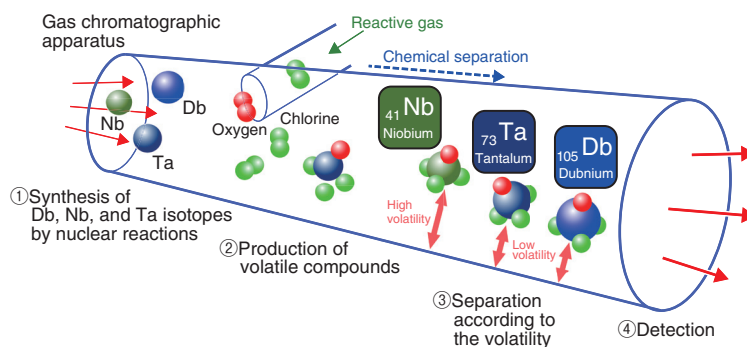


**Fig.3-2 Schematic diagram of the experiment**

Short-lived niobium (Nb), tantalum (Ta), and dubnium (Db) isotopes synthesized in nuclear reactions are quickly introduced into the experimental apparatus to synthesize their volatile oxychlorides. They are passed through a quartz separation column that is maintained at a fixed temperature by a gas stream. The transparent efficiency changes depending on the volatility. The volatility of the molecule can be determined from the correlation between the column temperature and yield.

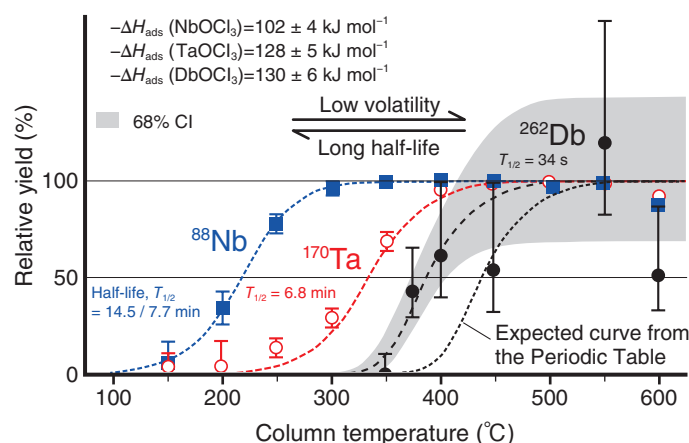


**Fig.3-3 Changes of relative yields with the column temperature for the oxychlorides of Nb, Ta, and Db**

The values of the adsorption enthalpy,  $-\Delta H_{\text{ads}}$ , as a measure of the adsorption strength, for the compounds on the separation column surface (quartz) can be obtained from the column temperature–yield curves. The curve shifts to higher temperatures for lower volatility and to lower temperatures for longer half-lives. Since the strength of adsorption on a solid surface should be correlated with volatility in the case of physisorption, the ease of each compound to transform into a gas can be estimated.

Heavy elements (atomic number  $Z > 103$ ) are called superheavy elements (SHEs). SHEs do not exist naturally on the Earth and are artificially synthesized in nuclear reactions. In such heavy elements, the velocity of the inner electrons moving around the nucleus approaches the speed of light, thereby eventually affecting the outermost electron orbits that characterize their chemical properties (relativistic effects). It has been pointed out that the chemical properties of the SHEs may be different from those expected according to the Periodic Table.

Dubnium (Db,  $Z = 105$ ) is an SHE that belongs to Group 5 elements and is a homolog of niobium (Nb) and tantalum (Ta) in the Periodic Table. The production rate of Db is extremely low (about 1 atom per 5 min), and its half-life is quite short (34 s for  $^{262}\text{Db}$ ). Hence, only one atom can be used at a time. The chemical properties of Db have not been investigated sufficiently due to the experimental difficulties.

In this work, we synthesized a Db isotope by using the

JAEA tandem accelerator and performed a chemical analysis of its volatile compound using an on-line gas chromatographic apparatus. The volatility of the Db compound was compared with the values for the Nb and Ta compounds (Fig.3-2).

We successfully produced and separated dubnium oxychloride ( $\text{DbOCl}_3$ ) and clarified that its volatility was comparable to that of the Ta compound, though it was expected to be lower than that of the Ta compound from the simple extrapolation of the Periodic Table (Fig.3-3). This unexpected volatility of Db is explained by considering the strong relativistic effect.

The results of this research were featured on the back cover of the “Angewandte Chemie”. This achievement is expected not only to lead to an understanding of the Periodic Table, but also to contribute to the improvement of the accuracy of theoretical chemical calculations, which are increasingly being used in molecular design and material science in recent years.

(Tetsuya K. Sato)

### Reference

Chiera, N. M., Sato, T. K. et al., Chemical Characterization of a Volatile Dubnium Compound,  $\text{DbOCl}_3$ , *Angewandte Chemie International Edition*, vol.60, issue 33, 2021, p.17871–17874.

## 3-2 Probing the Strong Interaction with Superconducting Detectors

### — Drastic Precision Improvement in the X-Ray Spectroscopy of Kaonic Atoms —

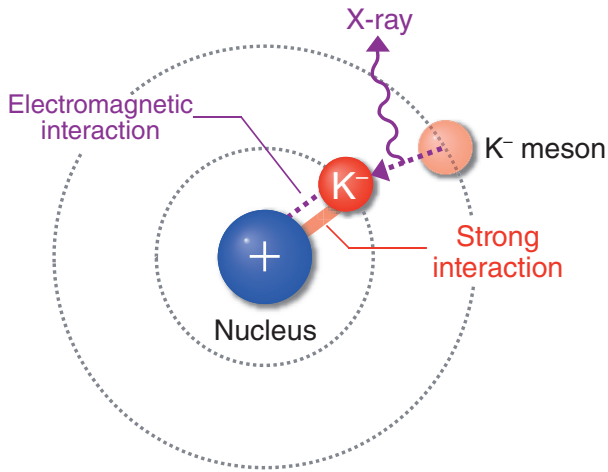


**Fig.3-4 Diagram of a kaonic atom**

$K^-$  mesons, which have a negative charge like electrons, can replace an electron in ordinary atoms to form kaonic atoms via electromagnetic interaction. Additionally, the strong interaction slightly changes the orbital energies, and consequently, the X-ray energies.

A kaonic atom is a system of a  $K^-$  meson and nucleus bound by electromagnetic interaction (Fig.3-4). We can study the strong interaction between a  $K^-$  meson and nucleus by measuring the X-rays emitted by kaonic atoms. Along with investigations of other particles with strange quarks, such as  $\Lambda$  particles, studies on  $K^-$  mesons will play an important role in elucidating the internal structure of neutron stars.

So far, the X-ray spectroscopy of kaonic atoms has suffered from the limited intensity of the  $K^-$  beam and the lack of X-ray detectors that can achieve both excellent energy resolution and good detection efficiency. We used the high-intensity  $K^-$  beam supplied by the J-PARC Hadron Experimental Facility to produce many kaonic atoms. The X-rays were then measured using superconducting transition-edge-sensor (TES) microcalorimeters.

The TES detector is a cryogenic detector with high energy resolution. It utilizes a rapid change in electrical resistance in a small temperature range at superconducting transition. Although a single pixel should be kept small for good resolution, a multipixel array realizes a reasonably large effective area. In this work, we used this detector at a charged-particle beamline for the

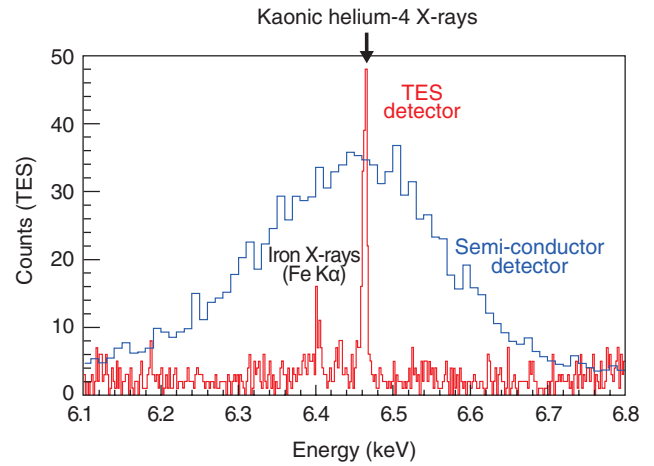


**Fig.3-5 X-ray spectra of 3d→2p transitions in kaonic helium-4 atoms**

We measured the X-ray spectra of kaonic helium atoms using a transition edge sensor (TES). The TES achieved excellent energy resolution compared to the conventional semiconductor detectors, and the peak energy was determined with high precision.

first time. The  $K^-$  beamlines are particularly harsh environments for a high-sensitivity sensor as they contain many background particles such as  $\pi^-$  mesons. We successfully performed the X-ray measurement of kaonic atoms with excellent energy resolution by minimizing the background particles incident on the detector and removing their effects during signal analysis (Fig.3-5).

We determined the energy shift due to the strong interaction in the 2p orbitals of kaonic helium-3 and helium-4 atoms, with about 10 times better accuracy than the previous measurements. This result provides a strong constraint on how attractive the strong interaction between the  $K^-$  meson and the nucleus is. With further X-ray measurements of other kaonic atoms and studies of recently discovered nuclear systems containing a  $K^-$  meson, we wish to reveal more details about the strong interaction of  $K^-$  mesons and how  $K^-$  mesons affect the properties of neutron stars.

This work was supported by JSPS KAKENHI Grant-in-Aid for Scientific Research (A) (JP16H02190) and MEXT Leading Initiative for Excellent Young Researchers Grant.

(Tadashi Hashimoto)

#### Reference

Hashimoto, T. et al., Measurements of Strong-Interaction Effects in Kaonic-Helium Isotopes at Sub-eV Precision with X-Ray Microcalorimeters, Physical Review Letters, vol.128, issue 11, 2022, 112503, 6p.

## 3-3 Slow Dynamics of Electrons in Uranium Compounds

— Approaching the Mystery of Superconductors Leading to Quantum Computers —

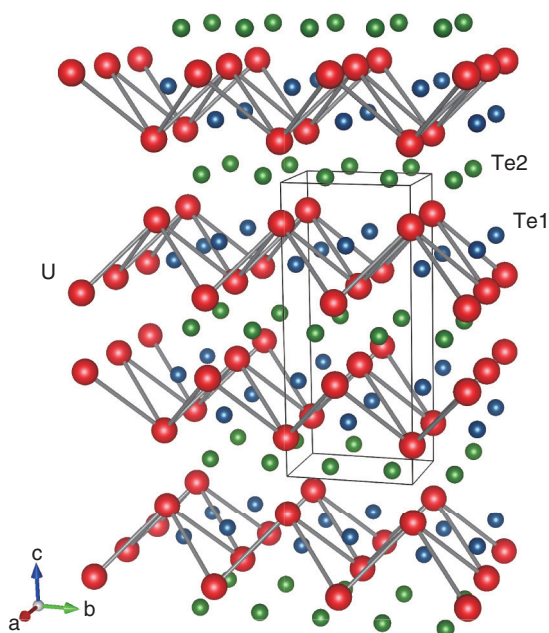


**Fig.3-6 Crystal structure of UTe<sub>2</sub>**  
Uranium atoms (red circles) form a characteristic zigzag structure in the crystal.

The discovery of new materials with new electronic properties is the foundation of technological innovations such as computers, mobile phones and the Internet that have the potential to dramatically change our social lives. Materials contain a huge number of electrons, about the same as Avogadro's number, and new electronic properties, such as new magnetism and superconductivity, often emerge when these electrons are strongly correlated with each other. Recently, strongly correlated uranium compounds have received much attention as a platform for discovering new electronic properties.

The uranium compound UTe<sub>2</sub> (Fig.3-6) is a novel superconductor. It discovered at the end of 2018. In ordinary spin-singlet superconductors, the spins of the pairing electrons responsible for superconductivity are aligned in opposite directions. However, in UTe<sub>2</sub>, the spins are aligned in the same direction, resulting in a new superconducting state called the spin-triplet state.

In this study, we used nuclear magnetic resonance (NMR) techniques to investigate the electronic states of UTe<sub>2</sub>. The NMR is an experimental technique that allows us to investigate the electronic state from a microscopic viewpoint. For this study, we grew a special UTe<sub>2</sub> single crystal enriched with NMR-observable <sup>125</sup>Te nuclei from 7% of their natural abundance

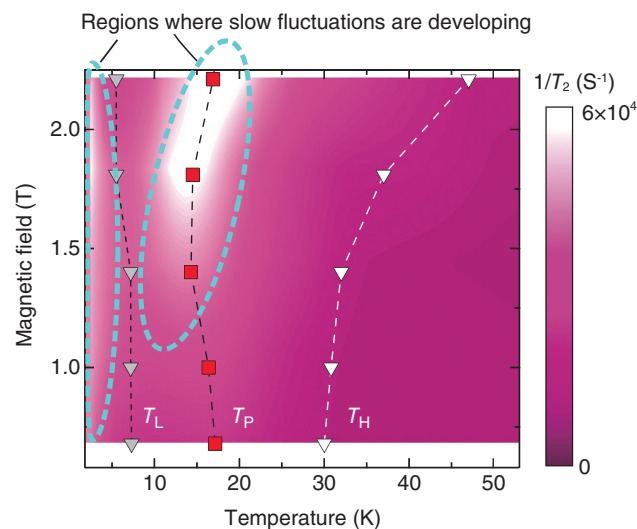


**Fig.3-7 Field-temperature phase diagram of the nuclear spin-spin relaxation rate ( $1/T_2$ )**

When the temperature decreases, the slow fluctuation of electrons starts to gradually develop below  $T_H$  ( $\nabla$ ), and the value of  $1/T_2$  increases. With further decrease in temperature, the fluctuations exhibit a peak at  $T_P$  ( $\blacksquare$ ) and decrease once; subsequently, they increase again below  $T_L$  ( $\nabla$ ).

to 99%. Using the crystal, we measured the nuclear spin-spin relaxation rate ( $1/T_2$ ) and investigated the strength of spin and charge fluctuations inside the material. We found that slow fluctuations with frequencies below the megahertz scale, which are extremely low for electronic systems, appear at low temperatures below about 30 K (Fig.3-7). The appearance of such slow fluctuations indicates the development of strong interactions (long-range correlations) between uranium atoms, which have the characteristic structure shown in Fig.3-6. The role played by such slow fluctuations in the mechanism of spin-triplet superconductivity remains to be clarified.

Uranium-based spin-triplet superconductors, such as UTe<sub>2</sub>, are now attracting much attention as systems that realize “topological superconductivity” in the bulk. The topological superconductivity is expected to be applied to next-generation quantum computing. If the mechanism of the spin-triplet superconductivity can be elucidated using UTe<sub>2</sub>, it may become possible to design and develop new topological superconductors by applying the mechanism.

This study was supported by JSPS KAKENHI Grant-in-Aid for Scientific Research (A) (JP20H00130) “Spin-triplet superconductivity on Uranium-based compounds”.

(Yo Tokunaga)

### Reference

Tokunaga, Y. et al., Slow Electronic Dynamics in the Paramagnetic State of UTe<sub>2</sub>, Journal of the Physical Society of Japan, vol.91, no.2, 2022, 023707, 5p.

## 3-4 Topology-Based Manipulation of Magnets in Spintronics

### — New Principle for Power Saving in Magnetic Memories —

(a) Magnetization direction ( $\uparrow/\downarrow$ )  $\leftrightarrow$  Digital information (0/1)

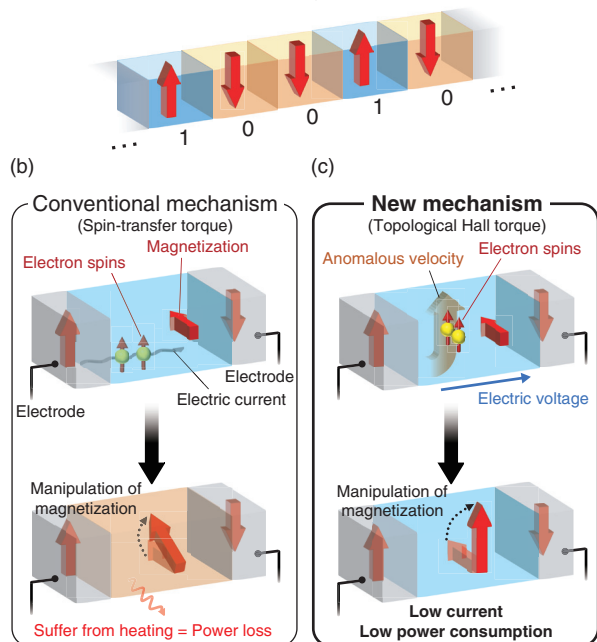


**Fig.3-8 Schematic depictions of the manipulation of magnets**  
 (a) Magnetic memories store digital information by manipulating the direction of magnetization. (b) The conventional technique called “spin-transfer torque” uses an electric current, but it suffers from high electric power consumption. (c) We discovered a new mechanism, i.e., the “topological Hall torque” based on the anomalous velocity of electrons. This mechanism has low power consumption.

Magnetic memories store information by associating a binary number (0 or 1) with the magnetization direction (for the north or south pole, respectively) (Fig.3-8(a)). Developing magnetic memories with higher operation speed and denser integrability requires us to reduce the electric power consumption in manipulating magnetization within nanometer-size domains. For this purpose, the technique called “spin-transfer torque (STT)”, which uses an electric current, has been commonly used for about a decade (Fig.3-8(b)). However, current injection in metals causes Joule heating because of the electric resistivity. To solve this crucial problem, we performed theoretical and experimental studies and discovered a new mechanism to manipulate magnetization with remarkably lower power consumption.

The key to this power-saving mechanism is “topology”. Topology is the character of the quantum-mechanical structure of electrons in materials. When an electric voltage is applied, an electron with a topological structure moves perpendicular to the voltage. This behavior, known as the “anomalous velocity”, is unaffected by the electric resistivity. In our theoretical work, we discovered a new mechanism for manipulating magnetization with lower power consumption by making use of the anomalous velocity. We coined the term the topological Hall torque (THT) for this mechanism (Fig.3-8(c)). Compared to the conventional STT, the THT requires only about 1/100 times smaller electric

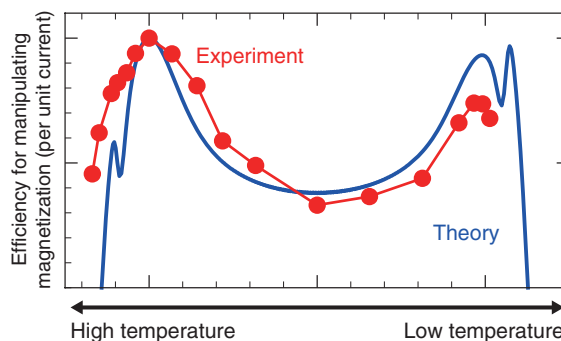


**Fig.3-9 Experimental verification of our new principle**

We measure the efficiency for manipulating magnetization in the metallic ferromagnet SrRuO<sub>3</sub>. The temperature-dependent two-peak structure (red line) is seen. This behavior is consistent with our theoretical estimation based on our new principle (blue line).

current for manipulating the magnetization. This means that the THT can drastically reduce the electric power consumption by a factor of 1/10,000.

We verified our theoretical proposal of the THT by the experimental measurement of a metallic ferromagnet, SrRuO<sub>3</sub>. We injected an electric current and observed the manipulation of magnetization at various temperatures. The efficiency of manipulating magnetization per unit current was so large that the theoretical estimation from the conventional STT cannot be applied. Moreover, a temperature-dependent two-peak structure was observed. Through model calculation, we clarified that both the magnitude and temperature dependence of the measured efficiency can be explained in terms of the THT (Fig.3-9). The THT in this system is described by the topological structure known as “Weyl points” in the electronic bands of SrRuO<sub>3</sub>.

Our new findings of the THT indicate a decisive role of topology in the manipulation of magnets. By selecting and designing materials with a strong topological structure, our idea can help develop future magnetic memories with remarkably less power consumption.

These works were partially supported by JSPS KAKENHI Grant-in-Aid for Scientific Research (S) (JP19H05622) and the Leading Initiative for Excellent Young Researchers.

(Yasufumi Araki)

#### References

Araki, Y. et al., Intrinsic Torques Emerging from Anomalous Velocity in Magnetic Textures, *Physical Review Letters*, vol.127, issue 27, 2021, 277205, 7p.  
 Yamanouchi, M., Araki, Y. et al., Observation of Topological Hall Torque Exerted on a Domain Wall in the Ferromagnetic Oxide SrRuO<sub>3</sub>, *Science Advances*, vol.8, issue 15, 2022, eabl6192, 6p.

### 3-5 Insight into Designing Highly Efficient *Ortho-Para* Hydrogen Conversion Catalysts — Demonstration of Fast *Ortho-Para* Conversion of H<sub>2</sub> on a Stepped Surface —

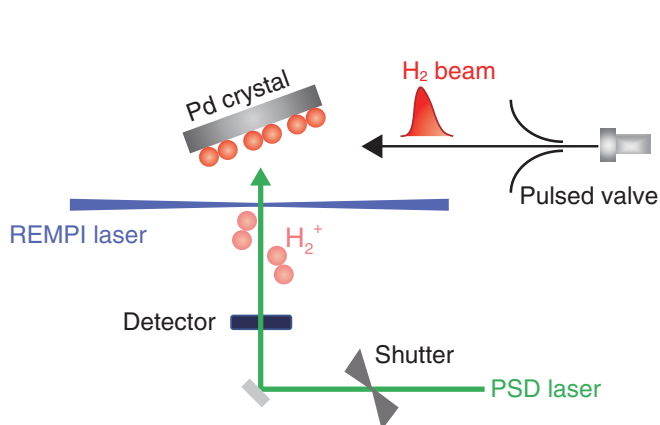


**Fig.3-10 Development of a measurement method for surface adsorbed H<sub>2</sub> *ortho-to-para* (*o-p*) conversion time based on a combination of a pulsed molecular beam, photo-stimulated desorption (PSD), and resonance-enhanced multiphoton ionization (REMPI) techniques**

First, a pulsed H<sub>2</sub> beam is sent to the surface, and then after a certain period of delay time the PSD laser irradiates the surface, and the photodesorbed H<sub>2</sub> is ionized state-selectively by the REMPI laser. Changing the delay time between the H<sub>2</sub> beam and PSD laser allows us to track the change in the nuclear-spin state of H<sub>2</sub> with surface adsorption time.

Hydrogen is promising as a clean energy source that does not produce greenhouse and harmful gases. Two nuclear-spin modifications exist for H<sub>2</sub>: *ortho*-H<sub>2</sub> (*o*-H<sub>2</sub>) and *para*-H<sub>2</sub> (*p*-H<sub>2</sub>). When liquefying and storing hydrogen, it is necessary to parahydrogenate the *o*-H<sub>2</sub> before liquefaction because liquefying hydrogen gas containing *o*-H<sub>2</sub> mixed in it causes heat generation due to the rotational energy of *o*-H<sub>2</sub>. This phenomenon is called the boil-off problem. Although it is known that *ortho-to-para* (*o-p*) conversion occurs on solid surface, the conversion is not efficient. In addition, the detailed conversion mechanism still remains unclear at present. Therefore, unraveling the conversion mechanism and developing a highly efficient conversion catalyst based on this knowledge are crucial to utilize hydrogen as an energy source.

In most of the past studies on *o-p* conversion on solid surfaces, H<sub>2</sub> in the physisorption state was focused. However, it is known that a unique molecular chemisorption of H<sub>2</sub> occurs on some stepped surfaces in addition to the typical adsorption scheme of physisorption. The previous studies indicate that the *o-p* conversion of molecularly chemisorbed H<sub>2</sub> is faster than that of physisorbed one. However, because of the limited time resolution of the measurement techniques used, it was difficult to probe the *o-p* conversion. Thus, a direct measurement of the conversion time was not possible. Against this background,

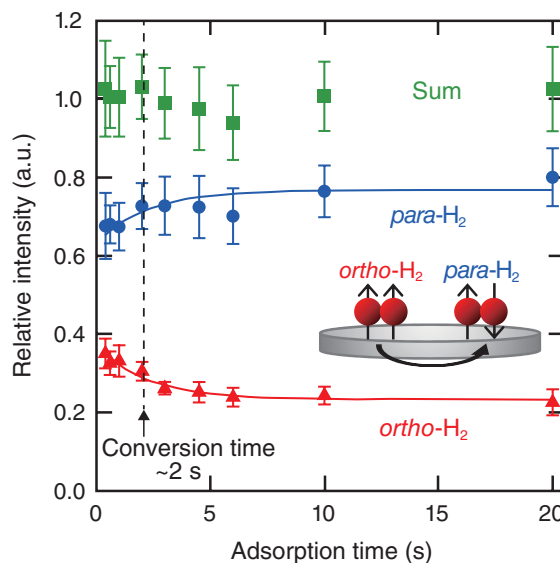


**Fig.3-11 Time evolution of the photodesorbed H<sub>2</sub> intensities for *o*-H<sub>2</sub>, *p*-H<sub>2</sub>, and their sum**

As the residence time on the surface increases, the intensity of *o*-H<sub>2</sub> decreases whereas that of *p*-H<sub>2</sub> increases. The conversion time is determined to be  $2.2 \pm 1.2$  s by fitting the data for *o*-H<sub>2</sub> with a single exponential function.

we recently developed a new method to determine the *o-p* conversion time by using a combination of a pulsed molecular beam, photostimulated desorption, and resonance-enhanced multiphoton ionization techniques. In this method, the time resolution was improved by about two orders of magnitude (Fig.3-10). We successfully tracked the change in the H<sub>2</sub> nuclear-spin state and experimentally determined the *o-p* conversion time of the molecularly chemisorbed H<sub>2</sub> on palladium (Pd) (210) face at a surface temperature of 50 K to be about 2 s (Fig.3-11). This value is 2–3 orders of magnitude smaller than those reported for physisorption systems, implying that the *o-p* conversion occurs rapidly. H<sub>2</sub> molecularly chemisorbs on top of the step-edge Pd atom. This fast conversion of H<sub>2</sub> in the molecular chemisorption state is a result of the strong interaction between H<sub>2</sub> and the Pd substrate which is ascribed to the unique step surface structure. The present study indicates the importance of the surface structure in *o-p* conversion and is expected to lead to the design of highly efficient conversion catalysts.

This research was funded by JSPS KAKENHI Grants No. JP17H01057, JP18H05518, and JP20K05337, and the Reimei Research Program (JAEA). H. U. is partially supported by MEXT, Leading Initiative for Excellent Young Researchers.

(Hirokazu Ueta)

#### Reference

Ueta, H. et al., Direct Measurement of Fast *Ortho-Para* Conversion of Molecularly Chemisorbed H<sub>2</sub> on Pd(210), *Physical Review B*, vol.102, issue 12, 2020, 121407(R), 5p.

## 3–6 Unveiling the Retention Mechanisms of Uranium (VI) on Host Rocks — Surface Sorption Process Related to Two Types of Sorption Species —

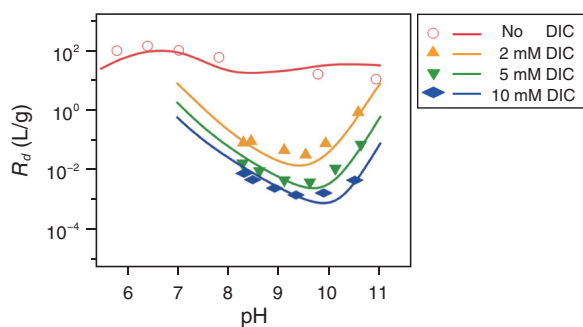


**Fig.3-12 Sorption experimental and modeling results**  
The experimental (points) and modeling (curves) distribution coefficient ( $R_d$ ) data are presented.

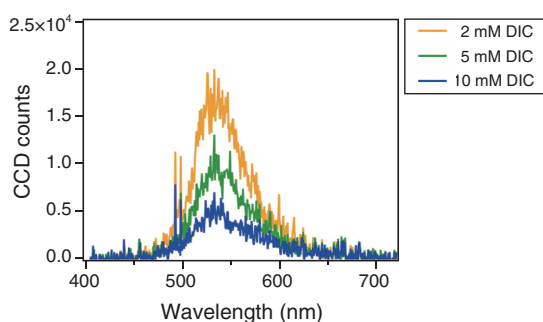


**Fig.3-14 Results of cryogenic fluorescence spectroscopy**  
The broad peaks centered around 535 nm indicate the coexistence of multiple sorption species.

In the geological disposal of high-level radioactive waste, radioactive wastes produced during nuclear power generation would be vitrified and disposed deep underground. As it will take tens of thousands of years to reduce the radiation level of the disposed waste, it is necessary to assess the safety and reliability of a geological disposal system. In geological disposal, the surrounding rocks, including clay minerals, act as a natural barrier for the sorption and retention of uranium-containing radionuclides. Therefore, it is important to evaluate the sorption process of radionuclides at the interface between clay minerals and groundwater. Groundwater contains a high concentration of dissolved carbonate (DIC) ions, which may affect the sorption of radionuclides to clay minerals via complexation with radionuclides. However, no quantitative evaluation method of this process is available at present, and this problem needs to be solved. In this study, the sorption trend of uranium (VI) (U(VI)) with DIC concentration and the sorption mechanism were investigated.

First, the batch sorption experiments were conducted to study U(VI) sorption on illite by varying the DIC concentration. The results showed that the distribution coefficient ( $R_d$ ) and sorption capacity of U(VI) decreased as the DIC concentration increased (Fig.3-12). Furthermore, the experimental data were analyzed by using a sorption complexation model, and it was found that two different surface sorption complexes should be considered to explain the sorption data (Fig.3-13).

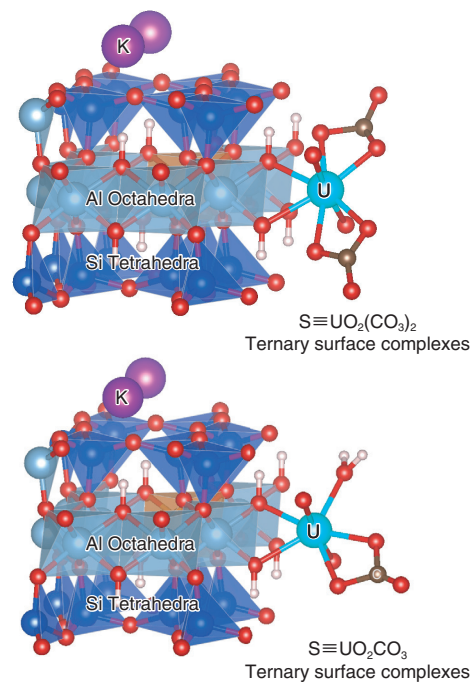


**Fig.3-13 Two schemes of sorption of U(VI) on illite surface originating from different complexes**

Difference of the surface complexes could be characterized by the number of carbonate ions.

To differentiate the sorption structures of the two complexes, spectroscopic measurement was conducted by cryogenic time-resolved laser fluorescence spectroscopy. This method is suitable for distinguishing the coordination geometry and binding state of ions and ligands around the U(VI) ions adsorbed on the illite surface. Our previous studies have shown that spectral measurements can distinguish the structures of adsorbed species. In this study, the sample was cooled to 3.3 K to improve the sensitivity of the spectroscopy. The results showed that the shapes of the fluorescence spectra detected with high sensitivity did not change. In addition, U(VI) was found to be sorbed on the illite surface though the sorption was suppressed at high DIC concentrations (Fig.3-14). Furthermore, the broad peaks centered around 535 nm indicates the presence of several sorption complexes. From the analysis of the decay curve of fluorescence, the existence of two species (complexes) was identified.

The quantitative relationship of the sorption of U(VI) on illite and the relevant sorption mechanisms were clarified in this study. This knowledge is expected to be useful for evaluating the sorption of radionuclides on common clay minerals.

This work was supported by METI, under “The project for validating assessment methodology in geological disposal (FY2020)”.

(Huiyang Mei)

### Reference

Mei, H. et al., Uranium (VI) Sorption on Illite Under Varying Carbonate Concentrations: Batch Experiments, Modeling, and Cryogenic Time-Resolved Laser Fluorescence Spectroscopy Study, *Applied Geochemistry*, vol.136, 2022, 105178, 8p.

## 3-7 Towards Understanding the Coherent Properties of Bosons — Determination of the Josephson Current in a Bose-Einstein Condensate —

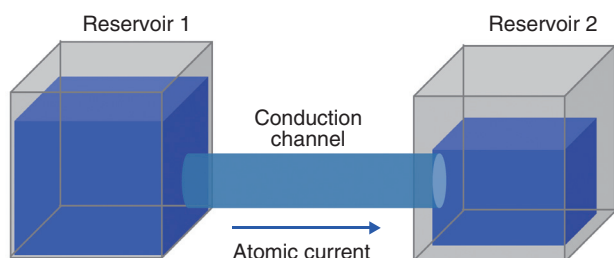


**Fig.3-15 Mesoscopic system realized with cold atoms**

In cold atoms, the two-terminal transport systems that consist of two macroscopic reservoirs and a conduction channel between them have been realized. Each reservoir traps atomic gases, and an atomic current between the reservoirs passes through the conduction channel.

Currently, quantum technologies that harness the principles of quantum mechanics, such as quantum computers, quantum communication, and cryptography, have garnered attention and become more competitive globally. To implement such technologies, however, it is necessary to understand quantum many-body systems in greater detail. Toward this end, cold atoms that are controllable artificial quantum systems have been in the spotlight as a platform for understanding the essence of quantum many-body systems.

Cold atoms trapped inside a vacuum chamber have been intensively studied since a Bose-Einstein condensate (BEC) was realized in 1995. One of the recent hot topics in the field of cold atoms is the study of mesoscopic systems (Fig.3-15).

Mesoscopic systems were originally investigated with electron systems such as semiconductors for which the microfabrication technology has been established. In particular, studies have focused on the quantum transport phenomena occurring through a mesoscopic sample. Recently, similar technology has been established for cold atoms, and thus, a connection with mesoscopic systems was created.

Mesoscopic systems with cold atoms allow the measurement of quantum phenomena that have remained elusive in electron systems. The mesoscopic transport with a BEC examined in

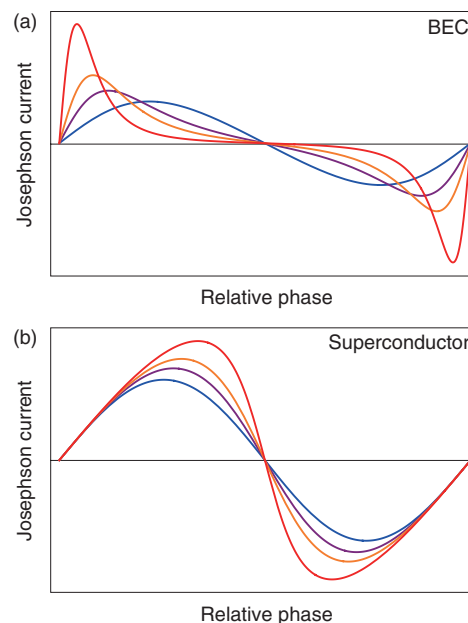


**Fig.3-16 Josephson currents in a Bose-Einstein condensate (BEC) and superconductor**

(a) Josephson current in a BEC. As the coupling between the reservoirs increases (blue  $\rightarrow$  purple  $\rightarrow$  yellow  $\rightarrow$  red), the deviation from the sinusoidal curve becomes remarkable. (b) Current-phase relation in a superconductor.

this work is one such phenomenon and is of importance to understand the coherent properties of Bose particles. A BEC is a macroscopic quantum state in which the quantum mechanical phase is fixed. If two BECs with a nonzero relative phase are attached, a dissipationless current, also known as the Josephson current, is generated. The Josephson current originally was discovered in superconductors in which electrons with opposite spins form pairs, thereby forming a condensate with a fixed phase.

In this work, the behavior of the Josephson current in a BEC is shown to differ from that in a superconductor despite the similarity between the BEC and superconductor. In particular, the transport mechanisms in the BEC and superconductor are different, leading to drastic differences in the current-phase relations of the strong coupling regime between the reservoirs (Fig.3-16). We expect that the outcome is relevant to realize and apply quantum circuits with cold atoms.

This work is supported by MEXT Leading Initiative for Excellent Young Researchers (JPMXS0320200002), JSPS KAKENHI Grant-in-Aid for Scientific Research (C) (JP21K03436), and Matsuo Foundation.

(Shun Uchino)

### Reference

Uchino, S., Tunneling Hamiltonian Analysis of DC Josephson Currents in a Weakly-Interacting Bose-Einstein Condensate, *Physical Review Research*, vol.3, issue 4, 2021, 043058, 13p.

## Fundamental Technologies for Nuclear Energy Innovation

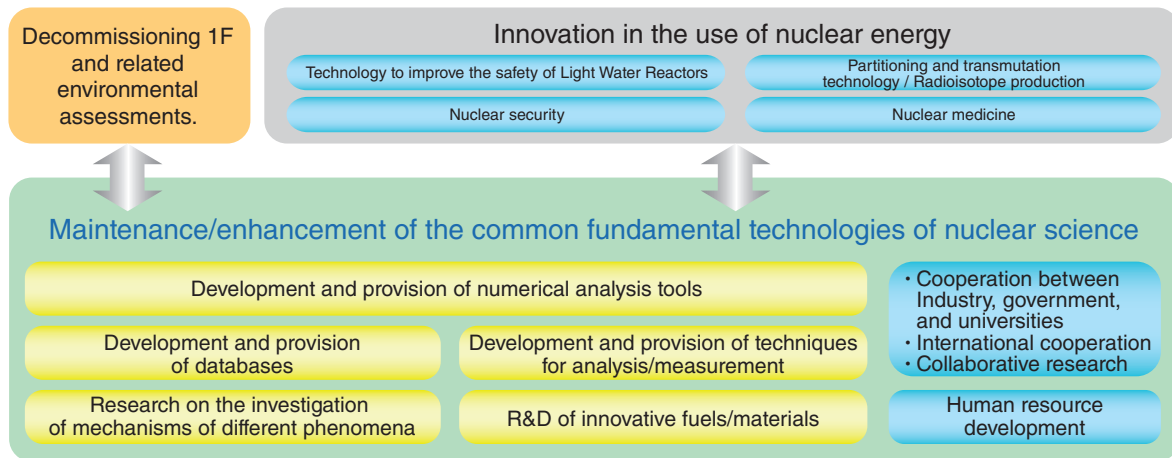


**Fig.4-1 Overview of nuclear science and engineering research**

NSEC maintains and enhances fundamental technologies for the use of nuclear energy and radiation. The center also aims to provide a knowledge base for decommissioning TEPCO's Fukushima Daiichi NPS (1F), contribute to improving the safety of light water reactors (LWRs), and develop partitioning and transmutation technologies to reduce the impact of radioactive wastes.

Common fundamental technologies and knowledge platforms, such as databases, numerical analysis tools, analytical technologies, and knowledge of phenomena mechanisms, are necessary to support the use of nuclear energy and radiation. In the JAEA's plan for its 4th mid-to-long term from JFY2022, the Nuclear Science and Engineering Center (NSEC) is going to advance the research and development (R&D) for the innovative use of nuclear energy and radiation through the improvement of simulation-related technologies. As summarized in Fig.4-1, the NSEC provides developed state-of-the-art fundamental technologies and nuclear science knowledge to industry, universities, and governmental agencies. The NSEC has also contributed to various applications, such as safety improvements of LWRs, the development of partitioning and transmutation technology to reduce the impact of radioactive wastes, the production of radioisotopes, and nuclear medicine. Recent results of the ongoing R&D activities at NSEC are introduced in this chapter.

The importance of inspections of radioactive materials at airports and ports are increasing for nuclear security. In order to facilitate the inspections, we have developed a low-cost transportable device for detecting radioactive materials. The device detects radioactive materials by the active method using a rotating neutron source of Cf-252. A demonstration experiment was conducted at Kyoto University and the device successfully detected 57 g of U-235. The introduction of the device into practical applications is expected (Topic 4-1).

A processing system for generating cross section files from nuclear data is necessary for the use of nuclear energy and radiation, such as reactor design and shielding analysis. We have developed FRENDY as one of the nuclear data processing systems. In January 2022, we released FRENDY version 2 including various new functions such as multi-group cross section generation function. The new functions increase the value of FRENDY and are expected to attract not only current users but also new users (Topic 4-2).

When ceramics including oxide, nuclear fuels are irradiated with high-energy ions such as fast fission products, radiation damage will be caused. With some ceramics, the observed sizes of radiation damage are different from those predicted using thermal spike theory. Our systematic study of observing surface nanostructure (nano-hill) showed that the difference

between predicted and observed sizes in CeO<sub>2</sub> is due to the high recrystallization capability of CeO<sub>2</sub> (Topic 4-3).

In order to estimate the air dose rates caused by release of radioactive materials in urban areas taking into consideration the influence of individual buildings, we developed a local-scale high-resolution atmospheric dispersion and dose assessment system LHADDAS, which consists of three modules; a local-scale high-resolution atmospheric dispersion model using large-eddy simulation LOHDIM-LES, a simulation code powered by lattice dose-response functions SIBYL, and a real-time urban dispersion simulation model based on a lattice Boltzmann method City LBM in cooperation with the CCSE of JAEA. LHADDAS is expected to use for the safety in emergency response to nuclear accidents and decommission of nuclear facilities (Topic 4-4).

Technologies to reduce the waste load generated from the use of various types of reactors are being developed for future nuclear energy utilization. In cooperation with the Tokyo Institute of Technology, we have developed and released a fast, versatile, and flexible nuclear fuel cycle simulator NMB4.0. NMB4.0 is expected to contribute to the R&D on reactor systems and nuclear fuel cycle technologies for the sustainable use of nuclear energy (Topic 4-5).

The development of an accelerator-driven nuclear transmutation system (ADS) is ongoing for reducing the impact of highly radioactive wastes. In order to reduce thermal fatigue due to the beam trips in the subcritical structure, stringent reliability is required for the ADS accelerators. We implemented the most recent advancements in the design of superconducting radiofrequency cavities to achieve high acceleration efficiency. Simulation results suggested the implementation will lead to the realization of more reliable ADS accelerators (Topic 4-6).

Technetium-99m, one of medical isotopes, is produced from molybdenum-99 (<sup>99</sup>Mo). From the view point of nuclear security, production of <sup>99</sup>Mo by neutron irradiation to <sup>98</sup>Mo is recently getting more attention than the partitioning and refinement of <sup>99</sup>Mo from irradiated highly-enriched uranium fuels. In order to gain sufficient amount of <sup>99</sup>Mo by neutron irradiation to <sup>98</sup>Mo, higher adsorption efficiency of <sup>99</sup>Mo to alumina (adsorber) is required. We investigated the mechanism of Mo adsorption to alumina and developed an improving method of alumina's Mo adsorption capacity (Topic 4-7).

## 4-1 Development of a Low-Cost Transportable Device for Detecting Nuclear Materials — Successful Experimental Demonstration of a New Nondestructive Method —

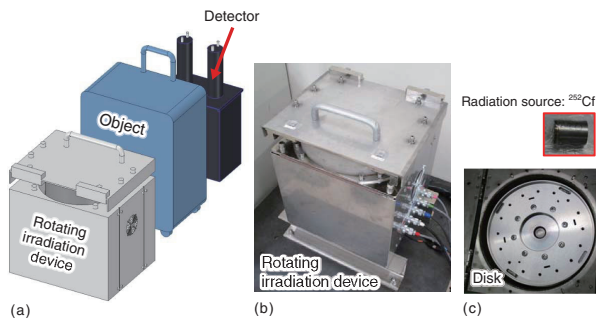


**Fig.4-2 (a) Device arrangement, (b) a rotating irradiation device, and (c) a disk and radiation source**

The object to be measured is placed close to the rotating device, and the detector is positioned on the other side of the object.

With the threat of terrorism increasing worldwide, security inspections for radioactive materials are being conducted at airports and ports. Notably, terrorism using nuclear materials is of much concern because of the serious damage it can cause to society, and nuclear material detection equipment for nuclear security is becoming increasingly important. The active method is one of the promising detection methods. In this method, the object containing the nuclear materials is irradiated by radiation, such as neutrons, and nuclear reactions are induced. The system detects nuclear materials by measuring the radiation originating from the nuclear reaction in the object. This method has a superior detection sensitivity and accuracy compared to the passive method. However, the active device has a significant drawback of being massive and expensive because it requires a radiation generator with periodically oscillating intensity.

In this study, we developed a new radiation generator to realize a low-cost and transportable device. In an active device, the intensity of the irradiated radiation must vary periodically. Therefore, we developed an irradiation device in which a radiation source is rotated to periodically change the intensity. Californium-252 ( $^{252}\text{Cf}$ ), which emits neutrons, was used as the radiation source.

The developed irradiation device (Fig.4-2) incorporates a disk (diameter: 31 cm) with a radiation source ( $^{252}\text{Cf}$ ) attached to its periphery. This disk can rotate up to 3,000 times per minute. The irradiation device is much less expensive (about 4 million yen)

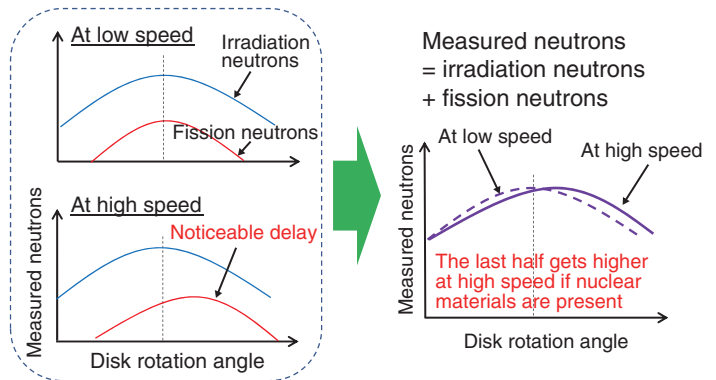


**Fig.4-3 Schematic of measurements**

The “delay” of the fission neutrons that is observed only at high speeds can be used to detect nuclear material.

than the conventional radiation generators (which cost about 30 million yen or more because they use accelerators). In addition, its compactness (width: 43 cm, depth: 35 cm, and height: 57 cm) allows it to be easily transported as required.

To explain the basic principle of the detection using this rotating irradiation device, the schematics of measurements are shown in Fig.4-3. Irradiation neutrons from the radiation source (blue line on the left side of Fig.4-3) pass through the object and are measured directly by the detector. The neutrons emitted by the fission reaction (red line on the left side of Fig.4-3) are measured by the detector with a slight delay at low rotation speed because neutrons must be slowed down before a fission reaction occurs. As the speed increases (e.g., 3000 rpm), the “delay” becomes more noticeable, and the distortion of the measured neutron spectrum can be observed (right side of Fig.4-3). Thus, the presence of nuclear materials can be determined by detecting the distortion. A demonstration experiment was conducted using the developed irradiation device at Kyoto University, and 57 g of uranium-235 ( $^{235}\text{U}$ ), which is well below the significant quantity (25 kg) of  $^{235}\text{U}$  as specified by the IAEA, was successfully detected. Because of its low cost and transportability, the developed device will be suitable for use for nuclear material inspections at not only airports and seaports but also large-scale events. The widespread use of the developed device is expected to deter nuclear terrorism.

(Masao Komeda)

### Reference

Komeda, M. et al., First Demonstration Experiment of the Neutron Rotation Method for Detecting Nuclear Material, *Annals of Nuclear Energy*, vol.159, 2021, 108300, 8p.

## 4-2 Connecting Nuclear Data with Transport Calculation

### — Development of Nuclear Data Processing Code FRENDY Version 2 —

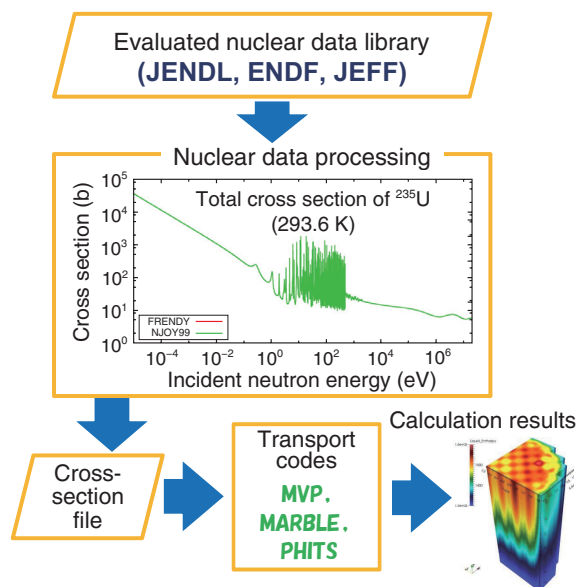


**Fig.4-4 Overview of nuclear data processing**

Nuclear data processing processes, such as generation of cross-section files, must be performed at each temperature point to use nuclear data libraries in transport calculation codes.

Particle transport calculation codes are used for various purposes such as reactor analysis and shielding calculation. The transport calculation codes require basic physical data such as reaction probabilities between neutrons and nuclei. The database of these basic physical data is called the evaluated nuclear data library. The JAEA has developed transport calculation codes such as MVP, MARBLE, and PHITS and an evaluated nuclear data library JENDL.

Transport calculation codes cannot handle evaluated nuclear data libraries directly. A process called nuclear data processing is required to convert these data into a cross section file format that can be handled by each transport calculation code. This process is illustrated in Fig.4-4. The nuclear data processing code is not just a converter. It has various data processing functions, as shown in Fig.4-5. Because the development of nuclear data processing codes requires not only knowledge of evaluated nuclear data libraries but also knowledge of each transport calculation code, only a few nuclear data processing codes have been developed.

The JAEA developed a nuclear data processing code FRENDY and released its first version, FRENDY version 1, as open-source software in March 2019. This code is widely used not only in Japan but also worldwide.

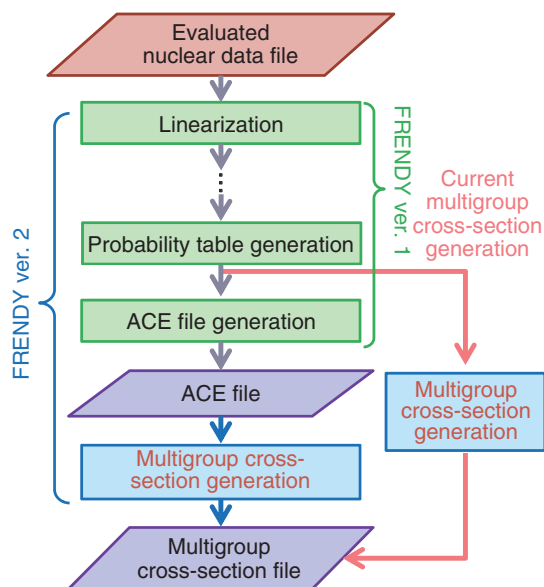


**Fig.4-5 Computational flow of multigroup cross-section file generation in FRENDY**

The multigroup cross-section file generation function is implemented in FRENDY version 2. This function generates a multigroup cross-section file from an ACE file, which is the cross-section file format used in the continuous energy Monte Carlo calculation code.

We have developed various functions after the release of FRENDY version 1. An example of the functions is the multigroup cross-section generation function, which is depicted in Fig.4-5. The development of the multigroup cross-section generation function for the multigroup transport calculation code, which is used for designing nuclear reactors and accelerators, was strongly desired by the industrial community. The development of the multigroup cross-section generation function received high praise; including a technical award from the Atomic Energy Society of Japan. These functions were compiled and released as the second version of FRENDY, called FRENDY version 2, in January 2022.

FRENDY can generate a multigroup cross-section file from an ACE file, which is the cross-section file format used in the continuous energy Monte Carlo calculation code, as shown in Fig.4-5. ACE files are widely used globally, and they can be downloaded from the websites of many institutions. FRENDY can easily generate multigroup cross-section files from the existing ACE files.

We implemented new features in FRENDY, such as the resonance interference effect between different nuclides. The use of these features will add to the importance of FRENDY.

(Kenichi Tada)

#### Reference

Yamamoto, A., Tada, K. et al., Multi-Group Neutron Cross Section Generation Capability for FRENDY Nuclear Data Processing Code, Journal of Nuclear Science and Technology, vol.58, issue 11, 2021, p.1165–1183.

## 4-3 Unveiling the Mystery of the Radiation Damage that Does Not Follow the Conventional Theory — Radiation Damage Mechanism in Ceramics Irradiated with Swift Heavy Ions —

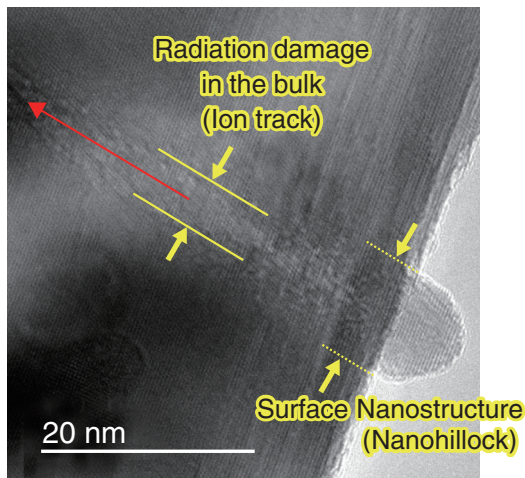


**Fig.4-6 Nanostructure created in CeO<sub>2</sub> irradiated with a swift heavy ion**

Transmission electron microscopy observation shows that an ion track is created along the ion trajectory and that this track is smaller than the nanohillock.

When ceramics are irradiated with swift heavy ion beams (with energy more than tens of mega electron volts), nanostructures called ion tracks are created along the ion paths. In many ceramics, the size of the ion tracks can be predicted by the conventional theory called the thermal spike theory. However, in some ceramics, the ion tracks observed in experiments were smaller than those predicted by the theory. Surprisingly, such size discrepancy was remarkable in ceramics with high radiation resistance. Why does the theory fail in these cases? Our systematic study of the surface nanostructure (nanohillock) has revealed the reason.

According to our transmission electron microscopy observations (Fig.4-6), the ion track size is smaller than the nanohillock size in CeO<sub>2</sub>, which is one of the highly radiation-resistant ceramics. In contrast, in ceramics with low radiation resistance, the sizes of the ion tracks and nanohillocks are similar.

The nanostructure formation process in ceramics with low radiation resistance is shown in Fig.4-7(a). First, a part of the surface protrudes during local melting along the ion path, and second, the molten region results in the formation of a damaged region by rapid cooling. This process is likely because the sizes of the nanohillock and ion track are similar in ceramics with

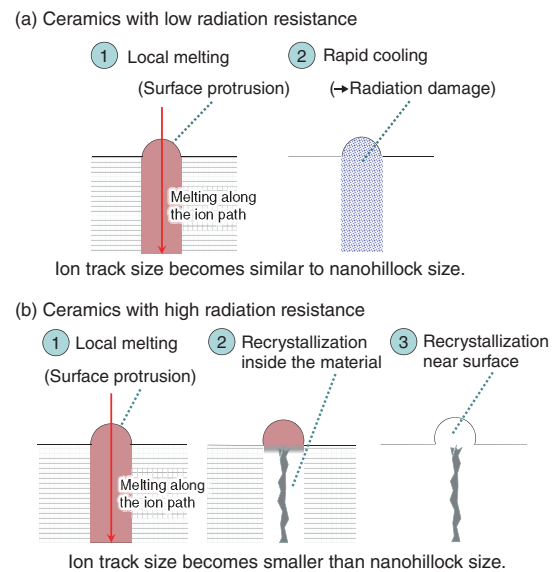


**Fig.4-7 Nanostructure formation processes by high-energy heavy ions**

Different processes can be assumed for (a) ceramics with low radiation resistance and (b) those with high radiation resistance.

low radiation resistance.

In contrast, in ceramics having high radiation resistance (Fig.4-7(b)), a part of the surface protrudes during local melting, and subsequently, the molten region partially recrystallizes. This causes the shrinkage of the damaged region, and finally, the protruded part near surface recrystallizes. This hypothesis can be validated as shown in Fig.4-6. The figure shows that the ion track is smaller than the nanohillock. This means that ion tracks shrink in radiation-resistant ceramics owing to the extremely fast recrystallization. The result strongly indicates that the recrystallization process was not assumed in the conventional theory. The well-aligned atomic layers inside nanohillocks further support the recrystallization process depicted in the third process in Fig.4-7(b).

In conclusion, the origin of high radiation resistance is the high recrystallization capability. By maximizing the recrystallization capability, a much higher radiation resistance can be achieved.

This work was supported by JSPS KAKENHI Grant-in-Aid for Scientific Research (C) (JP20K05389), “Clarification of Radiation Damage Mechanism by Surface Nanostructure Observation of Radiation-Resistant Ceramics”.

(Norito Ishikawa)

### Reference

Ishikawa, N. et al., Radiation Damage Mechanism in Ceramics Irradiated with Swift Heavy Ions, *Journal of Atomic Collision Research*, 2021, vol.18, issue 3, 2021, p.43–55. (in Japanese).

## 4-4 Detailed Radioactive Plume Dispersion and Dose Calculations Considering Buildings in Local Areas

### — Development of a Local-Scale High-Resolution Atmospheric Dispersion and Dose Assessment System —

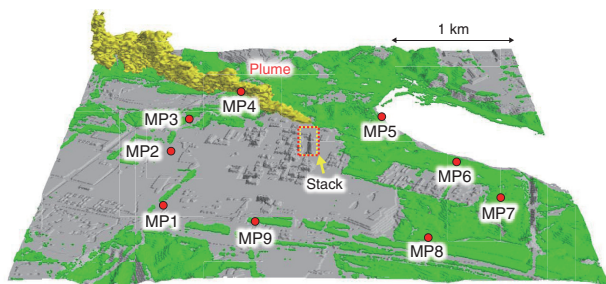


**Fig.4-8** Instantaneous plume dispersion field at Rokkasho Reprocessing Plant at 10:40 JST June 17th, 2008

We developed a local-scale high-resolution atmospheric dispersion and dose assessment system (LHADDAS) for the safety and consequence assessment of nuclear facilities and emergency response to nuclear accidents or deliberate releases of radioactive materials in built-up urban areas. The system was built in cooperation with the Center for Computational Science and e-Systems (CCSE). This system comprises three parts: (1) A component for the preprocessing of input files and a local-scale high-resolution atmospheric dispersion model using large-eddy simulation (LOHDIM-LES) for the main calculation<sup>\*1</sup>, (2) a real-time urban dispersion simulation model based on a lattice Boltzmann method (CityLBM)<sup>\*3</sup>, and (3) a simulation code powered by lattice dose-response functions (SIBYL) for the postprocessing of dose calculation<sup>\*2</sup>.

We examined the performance of LHADDAS using two application cases from our previous studies. The first case involved a controlled tracer plume dispersion in the vicinity of an actual nuclear facility and building arrays. The second focused on tracer gas dispersion in an actual central urban district. In this article, we describe the first application case of the LOHDIM-LES simulation of the actual tracer plume dispersion of radionuclides released from the nuclear fuel reprocessing plant in Rokkasho, Japan, as an example. The simulation period was from 09:00–19:30 Japan Standard Time (JST) on June 17th, 2008. Fig.4-8 shows an instantaneous shot of the tracer plume released into the atmosphere from a stack at 10:40 JST on June 17th. Fig.4-9 shows a comparison of the LOHDIM-LES results with the monitoring post (MP) data. An intermittent increase

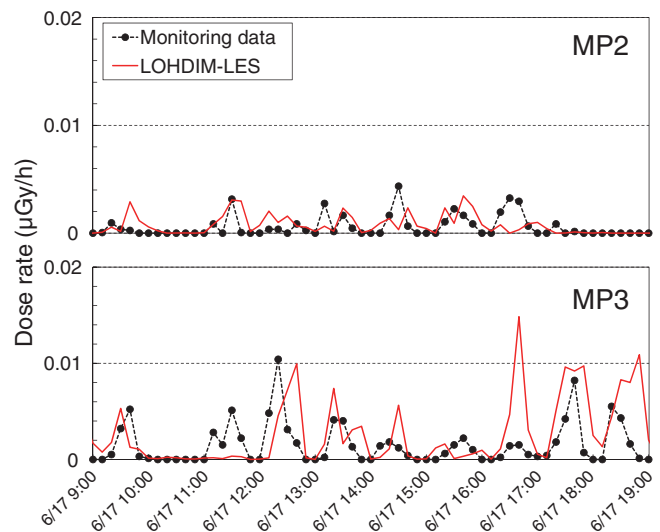


**Fig.4-9** Time series of the air dose rate at the monitoring posts (MPs) during the period from 09:00 JST to 19:00 JST June 17th, 2008

in the air dose rates at MP2 was noted. These rates frequently showed higher peaks at MP3 than at MP2. This result indicated that the main part of the plume was transported over MP3. These time variation patterns at the different MPs were simulated well by LOHDIM-LES integrated with the SIBYL module. The model performance of LOHDIM-LES and CityLBM was also demonstrated using the data collected during urban field experiments for the second application case.

LHADDAS has broad functionalities and performs extremely well in simulating turbulent flows, plume dispersion, and dry deposition under realistic meteorological conditions. It can simulate real-time tracer dispersion using a locally mesh-refined lattice Boltzmann method. Moreover, it can estimate the air dose rates of radionuclides from air concentration and surface deposition considering the influence of individual buildings.

(Hiromasa Nakayama)

<sup>\*1</sup> Nakayama, H. et al., Development of Local-Scale High-Resolution Atmospheric Dispersion Model Using Large-Eddy Simulation Part 6: Introduction of Detailed Dose Calculation Method, *Journal of Nuclear Science and Technology*, vol.58, issue 9, 2021, p.949–969.

<sup>\*2</sup> Satoh, D., Nakayama, H. et al., Simulation Code for Estimating External Gamma-Ray Doses from a Radioactive Plume and Contaminated Ground Using a Local-Scale Atmospheric Dispersion Model, *PLOS ONE*, vol.16, no.1, 2021, e0245932, 26p.

<sup>\*3</sup> Onodera, N., Nakayama, H. et al., Real-Time Tracer Dispersion Simulations in Oklahoma City Using the Locally Mesh-Refined Lattice Boltzmann Method, *Boundary-Layer Meteorology*, vol.179, issue 2, 2021, p.187–208.

#### Reference

Nakayama, H. et al., Development of Local-Scale High-Resolution Atmospheric Dispersion and Dose Assessment System, *Journal of Nuclear Science and Technology*, vol.59, issue 10, 2022, p.1314–1329.

## 4-5 Nuclear Fuel Cycle Simulator NMB4.0 Released

— Development of Fast, Versatile, and Flexible NMB4.0 to Contribute to the Planning of Future Nuclear Energy Utilization Strategies —

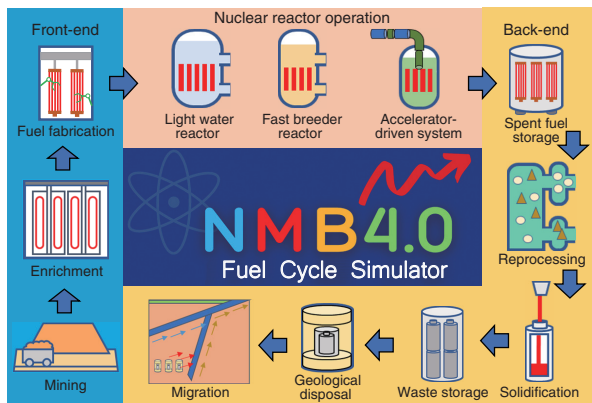


**Fig.4-10 Nuclear fuel cycle simulated by NMB4.0**

The amount of nuclear fuel material and fission product flowing through the entire process, from fuel mining to geologic disposal, can be evaluated.

Japan is currently developing various reactor types (fast reactors, light water reactors, small reactors, etc.) and reprocessing technologies to reduce the burden of waste disposal for future nuclear energy use. To commence full-scale development for realizing the new technology, it is necessary to clarify the effects of the introduction of such technology on the nuclear power industry. For this purpose, it is necessary to evaluate the advantages and disadvantages of the technology by clarifying the amount of nuclear fuel and waste to be handled in the nuclear fuel cycle and the scale of facilities required to handle them, as shown in Fig.4-10, assuming the timing and scale of the introduction of the new technology. A program called “nuclear fuel cycle simulator” is used for such evaluations. So far, no general-purpose simulator has been made publicly available in Japan, and many excellent simulators in other countries are not available to the public. However, to fairly evaluate new technologies such as those for reactor development, which is being undertaken by various organizations, it is essential to analyze these technologies using common scenarios and simulators. The inaccessibility of such simulators to the public has been a major obstacle. Therefore, the JAEA and Tokyo Institute of Technology (Tokyo Tech) jointly developed NMB4.0, a fast, versatile, and flexible simulator, and released it on the Tokyo Tech website (<https://nmb-code.jp>) in March 2022. NMB stands for Nuclear Material Balance. This simulator has the following features.

**Speed:** Conventional simulators have mostly calculated burnup changes in nuclear reactors for about 20–30 nuclear materials such as uranium and plutonium. However, to accurately evaluate the generation and disposal of radioactive waste, the NMB has the ability to calculate about 150 fission products produced by the fission of uranium. We successfully developed a solution method for solving the burnup equation with high speed and sufficient accuracy so that calculations requiring several hours with the conventional solution methods can be completed within a few minutes.

**Versatility:** NMB can analyze almost all the processes involved in nuclear power generation (Fig.4-10). For nuclear reactors, the database has been developed to allow analysis of not only light water reactors, which are the main type of modern reactors, but also futuristic reactors such as sodium-cooled fast reactors, gas-

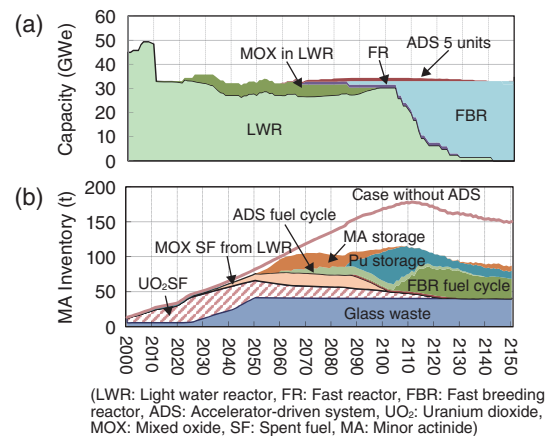


**Fig.4-11 Example of NMB4.0 analysis**

The figure (b) shows how minor actinides (Np, Am, and Cm) accumulate in the scenario of a full-scale transition to FBR in the second half of this century (Figure (a)). The partitioning of minor actinides starting in 2050 and transmutation by installing five Accelerator-Driven Systems (ADSs) starting in 2060 can reduce the amount of minor actinides accumulating before the full-scale operation of FBRs (brown line), thereby mitigating the burden on geological disposal.

cooled reactors, and accelerator-driven systems.

For the nuclear fuel cycle, we created a sufficiently accurate temperature calculation model and a substantial database for the geological disposal of radioactive waste, which is often not included in other simulators. For geological disposal, the rise in temperature of the repository must be considered when calculating the repository size, but this factor is not evaluated in many codes. NMB has a database that can evaluate the temperature of the geological repository design being considered in Japan, thus allowing the size of the repository to be evaluated within the code.

**Flexibility:** The future of nuclear power utilization in Japan is very vague because of uncertainties in the replacement of light water reactors, delays in the development of fast reactors, and difficulties in selecting a geological disposal site. Therefore, we designed the simulator to analyze a variety of scenarios, such as withdrawal or continuation of nuclear power use and changes in the timing of FBR introduction. (Analysis example: Fig.4-11) Furthermore, to adapt to various situations, the parameters are described by models without being fixed. For example, we created models to evaluate the amount of plutonium in fresh fuel for fast reactors or the amount of radioactive materials involved in the vitrification of radioactive waste, depending on the composition of the materials without predetermining them.

We openly invite users and developers to utilize NMB. We expect the users to include universities, research institutes, manufacturers, and electric power utilities, and hope that NMB will be useful in the research and development of future nuclear reactors and nuclear fuel cycle technologies and in planning implementation strategies for sustainable nuclear energy use. Furthermore, we would like to foster a community centered on NMB, continue to develop it to enhance evaluation functions such as economic efficiency and environmental impact, and fulfill the role of a research platform to realize evaluation researches across energy fields, including other power sources.

This research includes the results of a joint research project with Tokyo Tech (FY2021) entitled “Study on partitioning of radionuclides in spent fuel reprocessing and evaluation of various quantities in advanced nuclear fuel cycle”.

(Kenji Nishihara)

### Reference

Okamura, T., Nishihara, K. et al., NMB4.0: Development of Integrated Nuclear Fuel Cycle Simulator from the Front to Back-End, EPJ Nuclear Sciences & Technologies, vol.7, 2021, 19, 13p.

# 4-6 Toward the Realization of a Reliability-Oriented Accelerator for the Accelerator-Driven System — Robust Beam Optics Design of a 30-MW LINAC for Nuclear Transmutation —

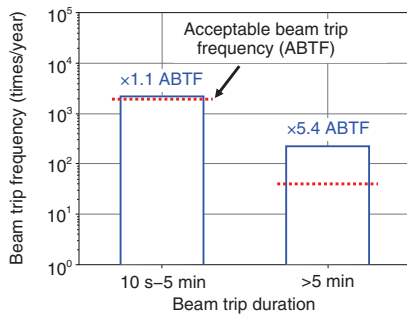


**Fig.4-12 Beam trip frequency for the accelerator-driven system (ADS)**

The beam trip frequency of J-PARC LINAC for FY2020 (blue bars) and that required for the ADS LINAC (red dotted line)\*. No beam trip less than 10 s occurred at the J-PARC LINAC.

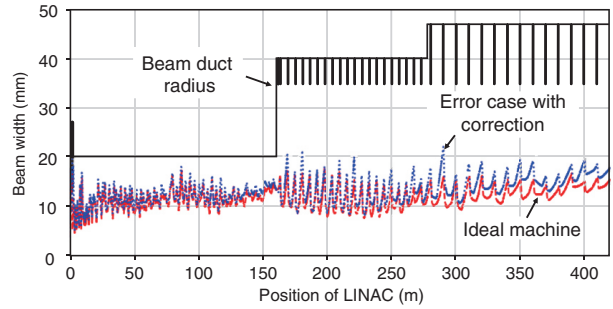


**Fig.4-14 Maximum horizontal beam width**

The ideal machine case (red dashed line), static error case with errors such as misalignments (blue dotted line), and beam duct radius (black solid line). The beam envelope is well contained in the beam duct radius, even when realistic errors are present.

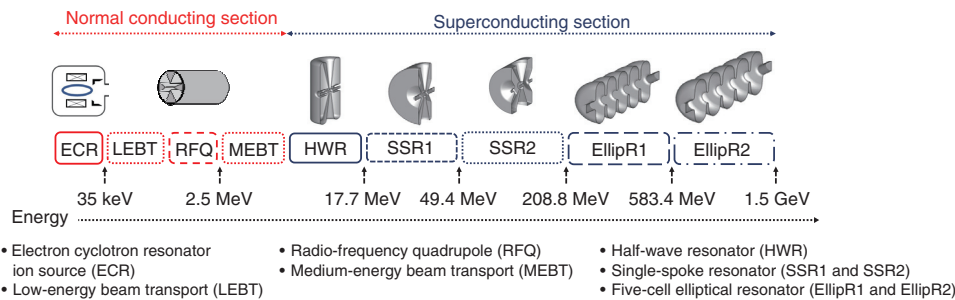


**Fig.4-13 Layout of the JAEA-ADS LINAC**

Most of the acceleration, from 2.5 MeV to 1.5 GeV, is achieved by the superconducting section (comprising the HWR, SSR1 and SSR2, and EllipR1 and EllipR2).

The Japan Atomic Energy Agency (JAEA) is developing an accelerator-driven system (ADS) for nuclear transmutation to deal with the problem of high-level radioactive waste disposal. The JAEA-ADS uses a 30-MW superconducting proton linear accelerator (LINAC) to produce spallation neutrons for a subcritical reactor. Stringent reliability is required for ADS accelerators to maintain the frequency of beam trips below a specific level, thus reducing the thermal fatigue in the subcritical reactor structures. Fig.4-12 compares the beam trip frequency of the J-PARC LINAC against the acceptable beam trip frequency (ABTF) for the JAEA-ADS LINAC. The major challenge is to reduce the frequency of beam trips longer than 5 min. The beam trip frequency for 10 s to 5 min is close to the ABTF. Therefore, JAEA-ADS LINAC adopted a reliability-oriented design to operate below the ABTF. As the first step, a robust design was explored for the JAEA-ADS LINAC to reduce the beam trip frequency caused by beam loss in the superconducting accelerator, which causes long beam stops. The robust design allows stable beam operation with an acceptable beam loss.

The JAEA-ADS LINAC accelerates a 20 mA proton beam to a final energy of 1.5 GeV by using normal conducting and superconducting radiofrequency cavities, as shown in Fig.4-13. We implemented the most recent advances in superconducting radiofrequency cavities to achieve high acceleration efficiency.

Because the JAEA-ADS LINAC runs at a higher current than the other ADS projects, the beam particles are subject to significant Coulomb repulsion forces that can induce unacceptable transverse beam size growth, causing considerable beam degradation and losses. Therefore, we set the parameters of all the elements in the LINAC to achieve a proper balance between the external fields applied by the elements and the internal ones due to the particles. Thus, we achieved efficient beam control.

We optimized the LINAC using simulations with a large number of protons ( $1 \times 10^8$ ) to run with beam losses two orders lower than the limit of hands-on maintenance for an ideal machine (without errors) and for feasible error scenarios. Fig.4-14 shows a comparison of the maximum horizontal beam widths obtained from simulation with 1000 different combinations of random misalignments and power supply jitters with a correction scheme against the ideal machine case. We found that the JAEA-ADS LINAC achieves proper control of the beam width and beam losses for realistic beam operations. Thus, we achieved a robust LINAC design that represents a step towards developing a reliability-oriented accelerator for the JAEA-ADS.

(Bruce Yee-Rendon)

\* Kondo, Y., Yee-Rendon, B. et al., Research and Developments of a Superconducting Linac for ADS, Journal of Plasma and Fusion Research, vol.98, no.5, 2022, p.222-226 (in Japanese).

**Reference**

Yee-Rendon, B. et al., Design and Beam Dynamic Studies of a 30-MW Superconducting Linac for an Accelerator-Driven Subcritical System, Physical Review Accelerators and Beams, vol.24, issue 12, 2021, 120101, 17p.

## 4-7 Improving Adsorption Capacity for Medical Radioisotopes — Elucidation of Molybdate Ion Adsorption Mechanism in Alumina —

**Table 4-1 Mo adsorption capacity of alumina and its element content in milked solution**

When the pH of the solution was lower, alumina adsorbed more molybdate ions, and Mo desorption and Al contamination also tended to increase.

pH of solution	Mo adsorption capacity (mg-Mo/g)	Contents in milked solution		
		Number of times	Mo desorption amount (mg-Mo/g- $\text{Al}_2\text{O}_3$ )	Amount of Al (mg)
pH2	74.1	1st	2.77	0.08
		2nd	2.33	0.06
pH4	61.5	1st	0.88	0.02
		2nd	0.92	0.02
pH6	53.8	1st	0.68	—
		2nd	0.62	—

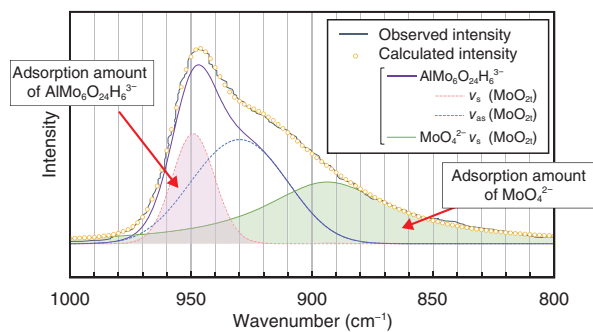


**Fig.4-15 Adsorption of molybdate ions in the Raman spectrum (for pH 4)**

The adsorption amounts of two molybdate ion species were compared considering their peak areas by fitting the Raman spectrum with the two ion peaks.

Technetium-99m ( $^{99\text{m}}\text{Tc}$ ), a representative nuclide for radiopharmaceutical, is a decay product of molybdenum-99 ( $^{99}\text{Mo}$ ). At present,  $^{99}\text{Mo}$  is produced by the fission of uranium (i.e., the fission method), but the activation method is attracting attention from the viewpoint of nuclear security. This method produces  $^{99}\text{Mo}$  via the neutron irradiation of  $^{98}\text{Mo}$ . However, compared to the fission method, the activation method can produce only a small amount of  $^{99}\text{Mo}$ . Extraction of  $^{99\text{m}}\text{Tc}$  from  $^{99}\text{Mo}$  is based on the phenomenon that only  $^{99\text{m}}\text{Tc}$  is eluted upon passing saline through alumina ( $\text{Al}_2\text{O}_3$ ) adsorbed  $^{99}\text{Mo}$  (milking). To extract an amount of  $^{99\text{m}}\text{Tc}$  equivalent to that extracted by the fission method, it is necessary to improve the Mo adsorption capacity of alumina. In this work, we focused on the molybdate ion, which is the Mo form adsorbed on alumina, and elucidated the adsorption mechanism.

First, alumina was immersed in solutions of different pH containing molybdate ions and was milked by a saline solution. More Mo was adsorbed at lower pH values, but the milked solution contained more Mo and Al (Table 4-1). Next, the amount of OH groups on the alumina surface increased at pH 4 and pH 6 compared to that before adsorption, but almost no change was observed at pH 2. Therefore, the OH groups on

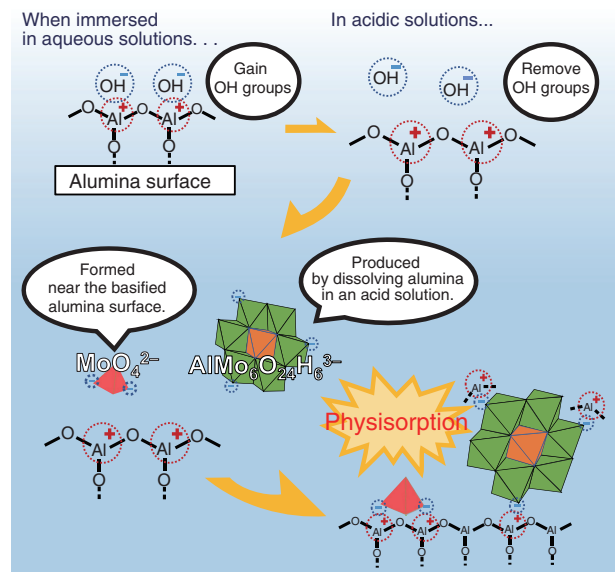


**Fig.4-16 Mechanism of molybdate ion adsorption in alumina**

i) Alumina gains OH groups on the surface when immersed in an aqueous solution. ii) When alumina is immersed in an acidic solution, the OH groups are removed, and the alumina surface becomes positively charged. iii) The release of  $\text{OH}^-$  makes the vicinity of the alumina surface basic and drives the formation of  $\text{MoO}_4^{2-}$ . iv) A small amount of alumina is dissolved in the acidic solution, and  $\text{AlMo}_6\text{O}_{24}\text{H}_6^{3-}$  is produced. v) These two anions are physisorbed at the positively charged sites on the alumina surface.

the surface increased upon immersion in the solution, but the formation of OH groups was suppressed when a large amount of Mo was adsorbed. Furthermore, the adsorbed molybdate ion species were investigated and were found to be ions containing Mo(VI). Finally, the adsorbed molybdate ion species were identified as  $\text{MoO}_4^{2-}$  and  $\text{AlMo}_6\text{O}_{24}\text{H}_6^{3-}$ , and these adsorption amounts were compared (Fig.4-15). From the increasing content of Mo and Al in milked solution with lower pH and the adsorption amount of two molybdate ion species, it was estimated that  $\text{AlMo}_6\text{O}_{24}\text{H}_6^{3-}$  has weak adsorbability.

Based on this result, we elucidated the Mo adsorption mechanism in alumina (Fig.4-16). The approaches found to improve the Mo adsorption capacity are as follows: 1) increasing the amount of surface OH groups by enlarging the surface area or controlling the crystal phase, and 2) optimizing the Mo solution for adsorption as  $\text{MoO}_4^{2-}$  ions. The results of this work will contribute to improve the adsorption property of alumina and the practical application of the activation method with excellent nuclear security.

This work was supported by JSPS KAKENHI Grant-in-Aid for Scientific Research (B) (JP17H04256).

(Yoshitaka Fujita)

### Reference

Fujita, Y. et al., Mechanisms Responsible for Adsorption of Molybdate Ions on Alumina for the Production of Medical Radioisotopes, Bulletin of the Chemical Society of Japan, vol.95, no.1, 2022, p.129-137.

## Contributions to Innovative Achievement in Science and Technology

In accordance with the Science and Technology Basic Plan formulated by the Government of Japan, we have aimed to contribute to the advancement of science and technology and the promotion of industry through innovative research into neutron and synchrotron radiation. This includes using the high-intensity proton accelerator at the Japan Proton Accelerator

Research Complex (J-PARC) and the high-performance and multipurpose research reactor JRR-3 and JAEA's synchrotron radiation beamlines at the Super Photon ring-8 GeV (SPring-8) (Fig.5-1), upgrading neutron facilities and devices, and pursuing world-leading research in fields that use neutron and synchrotron radiation, such as nuclear energy and materials sciences.



Materials and Life Science Experimental Facility (MLF) of J-PARC



JRR-3



SPring-8

Fig.5-1 Facilities used for neutron and synchrotron radiation research

### (1) Research and development of performance improvement of J-PARC

J-PARC comprises three proton accelerators, including a linear particle accelerator (linac), a 3-GeV rapid-cycling synchrotron (RCS), and a main ring synchrotron, and three experimental facilities. The facilities include the Materials and Life Science Experimental Facility (MLF) for a wide range of research fields using neutron and/or muon beams, the Hadron Experimental Facility for nuclear and particle physics experiments using K-mesons and other particles, and the Neutrino Experimental Facility for T2K particle physics experiments using neutrinos. These experimental facilities are open to researchers worldwide.

In FY2021, accelerator studies were conducted with a rated beam power of 1 MW; the beam loss at RCS was successfully reduced from 0.2% to 0.15%. At linac, a gas sheet beam monitor was developed as a nondestructive monitor with the aim of reducing beam loss and improving the beam quality of the existing wire-scanning-type profile monitor (Topic 5-1).

During FY2021, the proton beam power delivered to the MLF was increased from 600 kW to 700 kW, and the user program was carried out for 151 days. A wide range of experiments related to materials and life sciences were conducted at MLF with 21 neutron spectrometers and 3 muon instruments. With regard to neutron experiments, a deep-learning method was developed to remove statistical noise effectively from measured data in the structural analysis of the surface and/or interface of materials by learning about 1 million datasets acquired at a neutron reflectometer. This method yielded reliable structural analysis results without sacrificing resolution even when the data acquisition time was substantially shortened by one-tenth (Topic 5-2).

Furthermore, in the development of a neutron-polarizing super mirror for obtaining polarized neutrons that are useful for studying the microscopic magnetic structure of a sample, we found a specific condition of the Fe/Ge multilayer of the polarizing super mirror under which the saturation magnetization does not decrease even if layer thickness of the multilayer is reduced to a value less than the current minimum of 6 nm. Thus, the ratio  $m$  of the critical momentum transfer of the supermirror to that of natural Ni was improved from the existing value of  $m = 5$  to  $m > 6$  (Topic 5-3). This technique is expected to promote the research on the magnetic structure of a magnetic body.

### (2) Research and development at the Materials Sciences Research Center (MSRC)

Researchers at the MSRC aim to provide innovative results and seed research in a wide range of scientific, technological, and academic fields by developing and improving neutron and synchrotron radiation instruments for advanced structural and functional analysis in Tokai (JRR-3 and J-PARC) and in Harima (SPring-8).

In FY2021, in our research using neutron beams, we discovered that the domain motion of proteins controlled the local molecular structures that were the core of the catalytic reactions in proteins (Topic 5-4). This study revealed that the structure and fluctuation of amino acid residues contributing to the activity of the enzyme protein MurD were well controlled by the cooperative fluctuations of the domain structure. We also clarified the effect of additives on the hierarchical structure of borosilicate glasses, which are a type of host materials for high-level radioactive liquid waste (HLLW) (Topic 5-5). This study revealed that the size of the periodic structure composed of the SiO<sub>2</sub>-rich and B<sub>2</sub>O<sub>3</sub>-rich nanodomains in the glasses were strongly affected by the amount of Na<sub>2</sub>O additive, and the formation and suppression of the nanoscale structures in the glasses were also affected by the CaO/ZnO and Li<sub>2</sub>O additives. These findings are expected to contribute to the development of vitrification techniques for HLLW.

In our research on synchrotron radiation, we clarified the polarization mechanism of bismuth sodium titanate (BNT), which is expected to be a candidate for lead-free piezoelectric material (Topic 5-6). The result indicated that the displacement of Bi ions produced a large polarization in the high-temperature phase of BNT, and it provides an important clue to develop environment-friendly high-performance piezoelectric materials by controlling the size and shape of the ferroelectric domains. In addition, we revealed the energy band structure of EuNi<sub>2</sub>P<sub>2</sub>, which is the first heavy electron system among the Eu-based compounds (Topic 5-7). The result confirmed the presence of Eu 4*f* electron states at the Fermi level, indicating that the electronic and thermodynamic properties of this compound are markedly affected by the Eu 4*f*-derived heavy electrons. Further study is expected to contribute to a material design for developing new rare-earth-based superconducting materials.

## 5-1 Beam Measurement Using Light Produced by Beam-Gas Interaction — Development of a Gas Sheet Beam Profile Monitor —

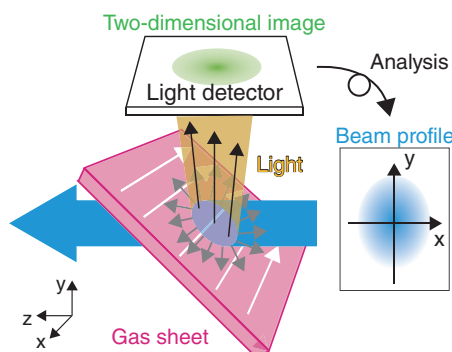


**Fig.5-2 Concept of a new profile monitor using a gas sheet**  
When the beam (blue) traveling along the z axis passes through the gas sheet (pink) flowing along the x axis, light (yellow and gray) is emitted from the gas particles that are excited by the beam–gas interaction. The cross-sectional beam profile can be obtained from an image captured using a camera with a proper analysis.

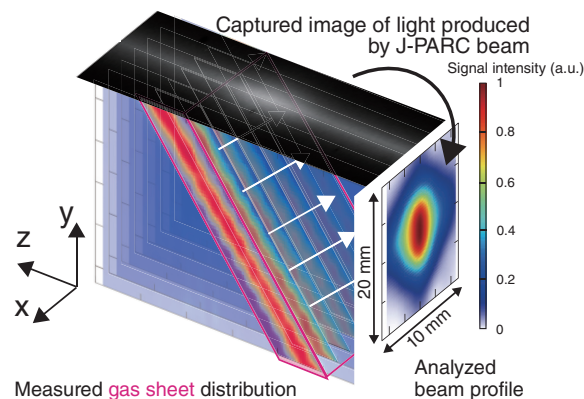


**Fig.5-3 Schematic diagram of beam profile measurement with the developed monitor**

In the image taken by J-PARC beam profile measurement, the light signal is detected as white plots, and the image shows that the beam passes through the gas sheet. The light signal is integrated along the vertical (y) axis because the image is taken from the top of the beam and monitor. Therefore, the image requires to be analyzed with the measured gas sheet information for obtaining the actual beam profile. The distribution shown on the right side of this figure and Fig.5-4 describe the analyzed profiles.

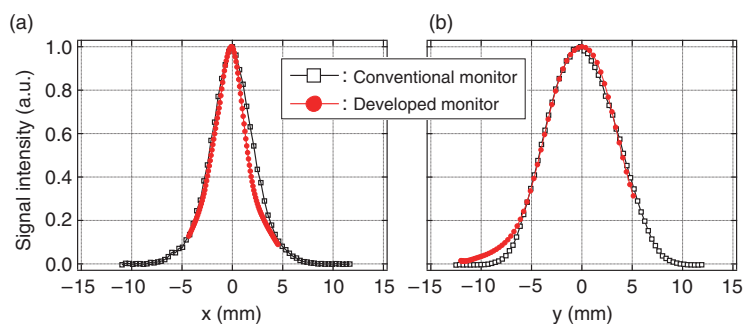


**Fig.5-4 Comparison of profiles measured with a conventional monitor and the new monitor along the (a) x axis and (b) y axis**

The profiles measured with the conventional wire-type monitor correspond to the integrated profiles along the x and y axes of the two-dimensional profile shown in Fig.5-3. The integrated profiles measured with the new monitor agree with the ones measured with the conventional monitor.

In a high-intensity ion accelerator such as that at J-PARC, the amount of radiation dose must be minimized because exposure of the accelerator components to a high radiation dose makes their maintenance difficult. A beam particle outside the design orbit may strike the beam pipe and radioactivate the pipe. To minimize the amount of radiation dose, suitable control of the beam based on constant monitoring of the beam orbit and beam profile is indispensable. In J-PARC, the beam profile is ordinarily measured by using a metal wire inserted into the beam orbit. The interaction of the beam and wire may induce the beam to be out of the design orbit and may radioactivate and/or break the wire itself. Therefore, the conventional beam profile monitor imposes a limit on increasing the beam intensity.

To measure a higher intensity beam profile, we developed an indestructible and noninvasive monitor with gas instead of a wire, as shown in Fig.5-2. When a beam particle passes through the vicinity of a gas particle, light is emitted from the gas particle because of beam–gas interaction. Since the spatial distribution of the light intensity is proportional to the beam profile, the beam profile can be obtained from an image of the light. We devised a method of injecting a gas formed into a sheet shape

to measure the cross-sectional beam profile with high signal intensities. A beam profile measurement result obtained with the developed monitor is shown in Fig.5-3. The produced light signal was detected as white plots, and the image shows that the beam passed through the sheet-shaped gas. Since the signal distribution of the image does not directly correspond to the beam profile, we also developed a profile analysis method. As shown in Fig.5-4, the profile analyzed by this method agreed with the profile measured with the wire-type monitor ordinary used at J-PARC.

The developed monitor with gas as well as the conventional monitor with the wire were expected to adversely influence the beam because the beam–gas interaction can scatter the beam. However, the beam quality improved upon injecting a small amount of gas because the plasma produced by beam–gas interaction in addition to the lights canceled the electric repulsive forces among the beam particles which induce a decrease in beam quality. In future, we will investigate the mechanism of the beam–gas interaction and realize more intense and stable beam operation of J-PARC.

(Ippei Yamada)

### Reference

Yamada, I. et al., High-Intensity Beam Profile Measurement Using a Gas Sheet Monitor by Beam Induced Fluorescence Detection, *Physical Review Accelerators and Beams*, vol.24, issue 4, 2021, 042801, 13p.

## 5-2 Acceleration of Neutron Measurement by Deep Learning

— Over 10-Fold Acceleration of Neutron Reflectometry Measurement by an Accurate Noise Reduction Method —

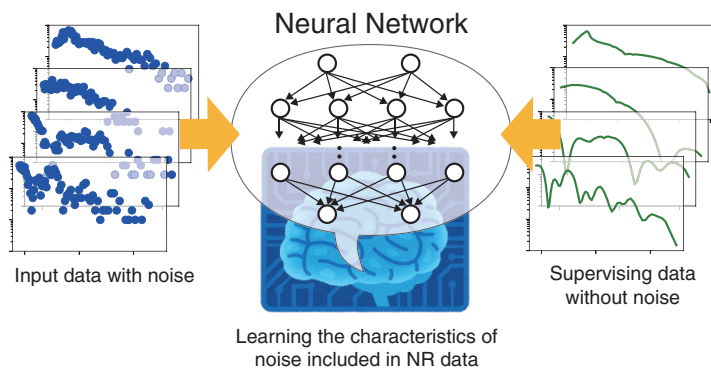


**Fig.5-5 Schematic illustration of deep learning to remove the noise from neutron reflectometry (NR) data**

The characteristics of the noise in NR measurements is revealed by deep learning by a convolutional neural network using a dataset of NR data with a statistical noise and supervising NR data without noise.

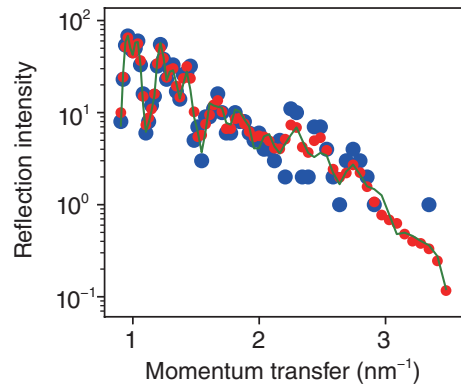


**Fig.5-6 NR data before and after noise reduction**

Statistical noise in the NR data obtained in a short measurement time (blue circles) is removed by the deep learning-based technique. The resultant NR data (red) are in good agreement with the ideal data without statistical noise (green curve).

Neutron reflectometry (NR) has been employed to analyze the structure of surface and interfaces in various materials such as polymer films and magnetic devices. A typical NR measurement requires a data acquisition time of more than several tens of minutes for a single sample of size more than a few centimeters. Therefore, the conventional NR technique cannot be used for analyzing dynamic samples whose structures vary in time at a temporal scale smaller than an hour. Moreover, because the limited machine time of neutron instruments is shared by researchers worldwide, the reduction in measurement time for a sample will be of great benefit. However, the shorter the acquisition time of NR measurements, the larger is the statistical noise in the data. The accuracy of the analysis result degrades with a decrease in the measurement time. In the current work, we developed a novel data-processing method to reduce the data acquisition time of NR measurements without compromising the accuracy of the experimental result by introducing deep learning.

A neural network with hidden layers consisting of one-dimensional convolution, batch normalization, and the rectified linear unit was used for supervised deep learning. The dataset for the training was generated by the neutron event simulator developed for the neutron reflectometer installed at Materials and Life Science Experiment Facility of the Japan Proton Accelerator Research Complex (J-PARC). After generating more than 200000 layered structures, the theoretical NR profile was calculated, and the experimental NR data with a

short acquisition time were simulated for each structure as the supervising and input data for deep learning (Fig.5-5). The blue circles in Fig.5-6 show the experimental data obtained in a 20-fold shorter acquisition time as compared with a conventional experiment. On the other hand, the green curve in Fig.5-6 indicates the data obtained over a longer acquisition time, indicating the low noise in the NR data. A comparison of these figures shows that the NR data points obtained in the short acquisition time are scattered by a large statistical noise. The red circles in Fig.5-6 were obtained by removing the noise component from the NR data obtained over the short time (blue data in Fig.5-6) by data processing with deep learning. The processed data are in good agreement with the NR data without noise (green curve). This indicates that the deep learning-based noise reduction method enables reduction of the measurement time by over 10 times without loss of accuracy of the experimental data.

The developed deep-learning technique for the NR data effectively removes the statistical noise from the experimental data acquired in a short measurement time and enables the acceleration of the NR measurement by over 10 times. This method can open up a new horizon in the structural analysis of the surface and interface of various materials.

This work was supported by JSPS KAKENHI Grant-in-Aid for Scientific Research (B) (JP19H02768) and JST-Mirai Program (JPMJMI18A2).

(Hiroyuki Aoki)

### Reference

Aoki, H. et al., Deep Learning Approach for an Interface Structure Analysis with a Large Statistical Noise in Neutron Reflectometry, Scientific Reports, vol.11, 2021, 22711, 9p.

## 5-3 Wide Bandwidth Neutron-Spin Polarizer

— A Breakthrough in Neutron-Polarizing Supermirror with Very High Critical Momentum Transfer —

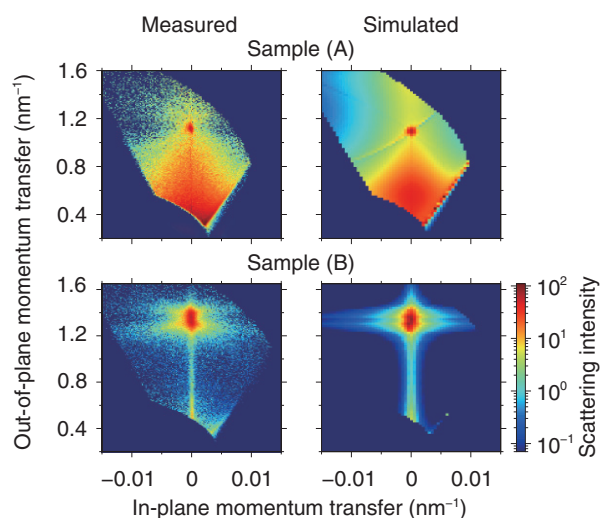


**Fig.5-7 Measured and simulated polarized neutron off-specular scattering images of Fe/Ge multilayers**

Sample (A) Fe: 3.5 nm and Ge: 2.2 nm. Sample (B) Fe: 3.5 nm and Ge: 1.2 nm, 50 bilayers. The FM interlayer exchange coupling when the Ge thickness was less than 2 nm resulted in a scattering localized at the first Bragg condition (an out-of-plane momentum transfer of  $1.34 \text{ nm}^{-1}$ ).

Polarized neutron scattering is a powerful and nondestructive technique to observe the correlation of small magnetic objects in a sample as neutrons with spin  $1/2$  are sensitive to magnetic moments in materials. To contribute to the science using polarized neutrons intensively conducted in the J-PARC MLF, we developed a high-performance neutron polarizing supermirror (PS), which is a neutron optical device used to polarize a neutron beam. The PS comprises a stack of alternating layers of ferromagnetic (FM) and nonmagnetic materials with a variation in bilayer thickness to extend the bandwidth, which is the wavelength range of the neutron polarization. Extension of the PS bandwidth is especially important for a spallation neutron source such as the J-PARC MLF, which provides a pulsed neutron beam with a broad neutron wavelength range. The critical momentum transfer of the PS defining the bandwidth is, however, limited to five times that of Ni. This is because a sputtered magnetic multilayer with a bilayer thickness less than 6 nm, which is required to realize critical momentum transfer larger than five times that of Ni, usually loses its spontaneous magnetization due to the Curie temperature becoming less than the room temperature.

The polarized neutron off-specular measurement performed

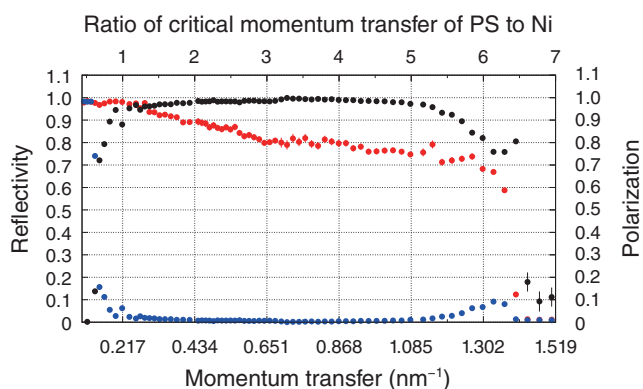


**Fig.5-8 Polarized neutron reflectivity profiles of the polarizing supermirror (PS) fabricated in this study**

Reflectivities with neutron spins that are parallel and antiparallel to the magnetic field are plotted in red and blue, respectively. The polarization is shown in black. The reflected beam is polarized to a momentum transfer larger than six times that of Ni.

using the polarized neutron reflectometer BL17 at the MLF revealed that the Fe/Ge multilayer used for the PS forms an FM–interlayer exchange coupling between neighboring Fe layers when the Ge thickness is less than 2 nm (see Fig.5-7). This coupling contributes to a stable spontaneous magnetization comparable to the bulk and soft magnetic properties even though the bilayer thickness is less than 6 nm. The performance test of the PS consisting of 10436 layers and a total thickness of  $32 \mu\text{m}$  based on the above findings revealed a critical momentum transfer greater than six (see Fig.5-8)—the highest critical momentum transfer recorded worldwide as of May 2022.

The bandwidth extension achieved in this study is not sufficient to cover the full spectrum available at the MLF. The origin of the magnetic interlayer exchange coupling across a semiconductor spacer has not been fully understood. Further study on this point is needed to improve the performance of the PS and to promote the science using polarized neutrons.

This study was supported in part by JSPS KAKENHI Grant-in-Aid for Scientific Research (C) (JP19K12647).

(Ryuji Maruyama)

### Reference

Maruyama, R. et al., Improved Performance of Wide Bandwidth Neutron-Spin Polarizer Due to Ferromagnetic Interlayer Exchange Coupling, *Journal of Applied Physics*, vol.130, issue 8, 2021, 083904, 10p.

## 5-4 Discovery of Coupled Fluctuations with Protein Domain Structures and Active Sites — Analysis of Protein Dynamics by Neutron Scattering and Molecular Simulation —

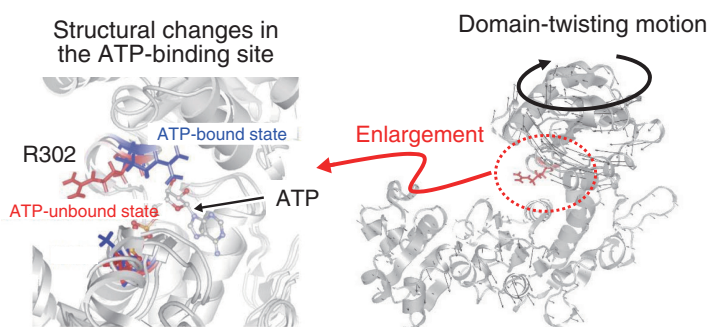


**Fig.5-9 Structural changes in the adenosine triphosphate (ATP)-binding site R302 (side chain of the 302nd arginine) (Left) and domain-twisting motion (right)**

In the ATP-unbound state, the orientation of the arginine side chain changes in conjunction with domain-twisting motion. Upon ATP binding, the orientation of R302 becomes fixed, and the domain-twisting motion ceases.

Proteins are composed of nanometer-sized three-dimensional (3D) structures called domains. Relatively large proteins are composed of multiple domains and are referred to as multidomain proteins. While each domain has a stable structure, the domains change their relative positions and orientations through flexible hinge regions that connect the domains. For example, the structure of the ATP-binding site changes with the domains (Fig.5-9). Elucidation of such domain-scale structural dynamics is considered necessary for understanding the mechanism of protein function expression. Neutron spin echo (NSE) technique has the highest energy resolution among quasielastic neutron scattering methods and is an effective method to capture the domain motions because it allows the observation of protein dynamics on the nanometer and nanosecond space–time scales.

Here, we focused on MurD, a typical multidomain protein. It is an enzyme involved in cell wall synthesis. Its conformational change upon binding with adenosine triphosphate (ATP) binding is essential for its function. We combined NSE with computational science to elucidate the correlation between the domain structure and structure of the ATP-binding site.

Fig.5-10 shows the NSE data, showing the effective diffusion coefficient derived from the domain motion of the protein with

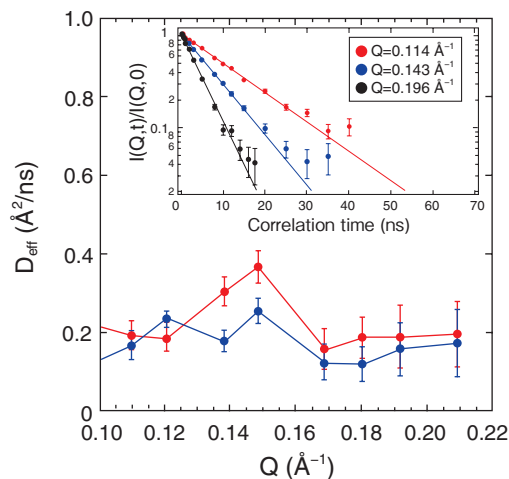


**Fig.5-10 Neutron wavenumber ( $Q$ )-dependence of the effective diffusion coefficient,  $D_{\text{eff}}$ , for ATP-unbound (red) and bound (blue) states**

The peak around  $0.15 \text{ \AA}^{-1}$  disappears because of ATP-binding. The inset shows the intermediate scattering function,  $I(Q,t)/I(Q,0)$  for the ATP-unbound state as measured by neutron spin echo spectroscopy. The effective diffusion coefficient was obtained from the equation  $I(Q,t)/I(Q,0) = \exp(-Q^2 \cdot D_{\text{eff}} \cdot t)$ .

respect to the neutron wavenumber  $Q$  ( $0.1\text{--}0.22 \text{ \AA}^{-1}$ ). The peak around  $0.15 \text{ \AA}^{-1}$  is reduced by ATP binding. Through molecular simulation, we determined the type of change in domain motion that is responsible for the reduction and found that reduction is caused by the suppression of the twisting motion of the domain (right side of Fig.5-9). Furthermore, a computational analysis showed that this domain motion is linked to the fluctuation of the side chain of the ATP-binding site (left side in Fig.5-9), indicating that the fluctuation of the local structure controlled by the domain motion is important for ATP binding. The first identification of the details of the changes in domain motions upon ATP binding has greatly advanced our understanding of the molecular mechanism of MurD enzyme activity.

These analyses reveal that the amino acid residues of the active site do not undergo random thermal fluctuations but are controlled by the cooperative fluctuations of the domain structure. The understanding the relationship of the structural dynamics between these different hierarchies is important for elucidating protein function.

This work was supported by JST-PRESTO (JPMJPR14L7).

(Hiroshi Nakagawa)

### Reference

Nakagawa, H. et al., Conformational Dynamics of a Multidomain Protein by Neutron Scattering and Computational Analysis, Biophysical Journal, vol.120, issue 16, 2021, p.3341–3354.

## 5-5 Development of Nuclear Vitrification by Neutron Scattering — Nanoscopic Structure of Borosilicate Glass with Additives —

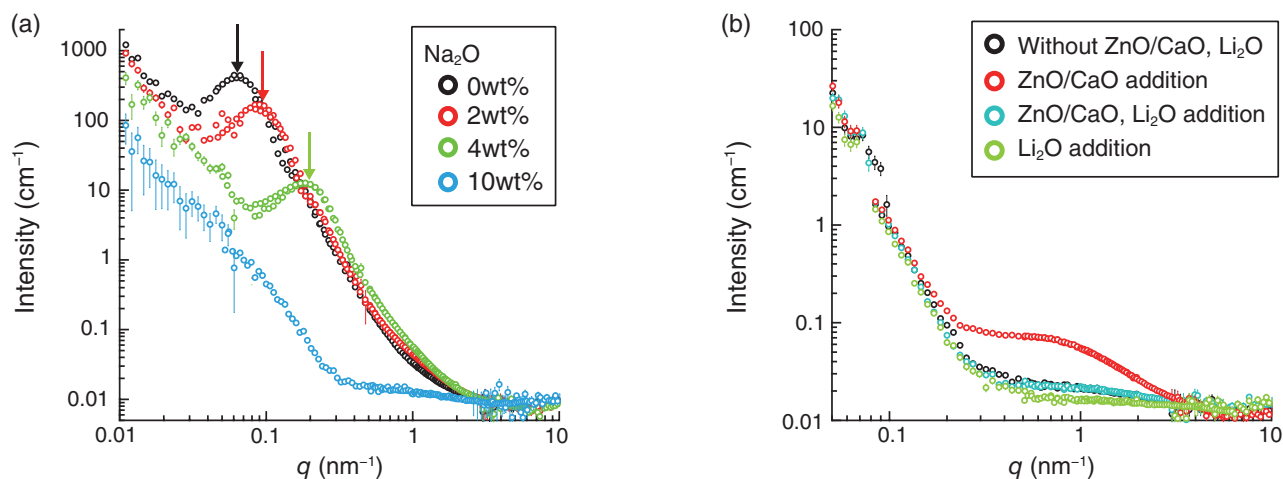


**Fig.5-11 Small-angle neutron scattering (SANS) data of borosilicate glasses specialized for nuclear waste vitrification**  
Double-logarithmic plots of the SANS profiles obtained for (a) the borosilicate glasses as a function of Na<sub>2</sub>O additive amount and (b) borosilicate glass samples with and without CaO/ZnO additives and Li<sub>2</sub>O.

We investigated the nanoscopic structure of borosilicate glasses to store for high-level radioactive liquid waste (HLLW) in the presence of typical additives Na<sub>2</sub>O and CaO/ZnO with and without Li<sub>2</sub>O by using the small-angle neutron scattering (SANS) technique. These additives have been practically used to lower the glass melting point, suppress macroscopic phase separation, and increase the chemical durability of glasses. Although the previous works successfully performed the structural analyses, they focus on length scales smaller than 1 nm. Hence, further study is necessary to identify the characteristics and microscopic structures of the glasses on the nano- and mesoscales even without HLLW.

Fig.5-11(a) shows the SANS profiles of the borosilicate glasses containing Na<sub>2</sub>O solutions of various concentrations. The scattering maximum (indicated by thick arrows) originates from the microphase separation between SiO<sub>2</sub>- and B<sub>2</sub>O<sub>3</sub>-rich domains on the nanoscale. The fraction of SiO<sub>2</sub> in the borosilicate glass was much larger than that of B<sub>2</sub>O<sub>3</sub>, and thus, the B<sub>2</sub>O<sub>3</sub> domains were likely to be dispersed in the SiO<sub>2</sub> matrix. The peak position,  $q_m$ , reflects the average distance between B<sub>2</sub>O<sub>3</sub>-rich domains,  $D$ , because  $D \approx 2\pi/q_m$ . The peak shifts toward a higher  $q$  value with increasing Na<sub>2</sub>O fraction, indicating an increase in  $D$  from 90 nm (0wt%; black) to 28 nm (4wt%; green). The peak completely disappeared at

10wt% (blue), indicating a miscible binary mixture. It is expected that each nanodomain tends to incorporate a specific component of HLLW into the glass framework.

Fig.5-11(b) shows the SANS profiles of samples. Using these profiles, the effect of CaO/ZnO addition with and without Li<sub>2</sub>O on the nanoscopic structure of the borosilicate glasses was examined. The SANS profile of the borosilicate glass containing CaO/ZnO additives (red) shows a shoulder peak, indicating the appearance of precipitates of approximately 2 nm size in the glass. Interestingly, CaO/ZnO addition was expected to suppress macroscopic phase separation; contrary to this belief, our result suggested that it induced inhomogeneities on the nanoscale. The shoulder peak was not present in the blue SANS profiles corresponding to CaO/ZnO addition with Li<sub>2</sub>O, or in the green profile corresponding to Li<sub>2</sub>O alone. Thus, the coaddition of Li<sub>2</sub>O with CaO/ZnO reduced the nanoscopic inhomogeneity of the glasses. This result suggests that CaO/ZnO should only be used in homogeneous glasses in conjunction with Li<sub>2</sub>O. We believe that the structural findings reported herein will contribute to the development of vitrification techniques for HLLW disposal treatment.

This work was supported by JSPS KAKENHI Grant-in-Aid for Scientific Research (B) (JP18H01921).

(Ryuhei Motokawa)

### Reference

Motokawa, R. et al., Nanoscopic Structure of Borosilicate Glass with Additives for Nuclear Waste Vitrification, *Journal of Non-Crystalline Solids*, vol.578, 2022, 121352, 7p.

## 5-6 Fabrication of Environment-Friendly Piezoelectric Materials

### — Local Structural Analysis of $\text{Bi}_{0.5}\text{Na}_{0.5}\text{TiO}_3$ in the High-Temperature Phase —

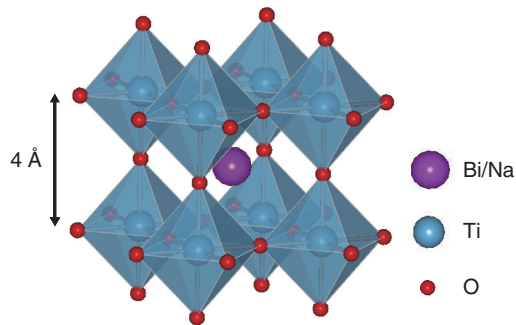


**Fig.5-12 Crystal structure of  $\text{Bi}_{0.5}\text{Na}_{0.5}\text{TiO}_3$ , which is expected to be a lead-free piezoelectric material**  
Bi/Na contains 50% Bi and 50% Na.

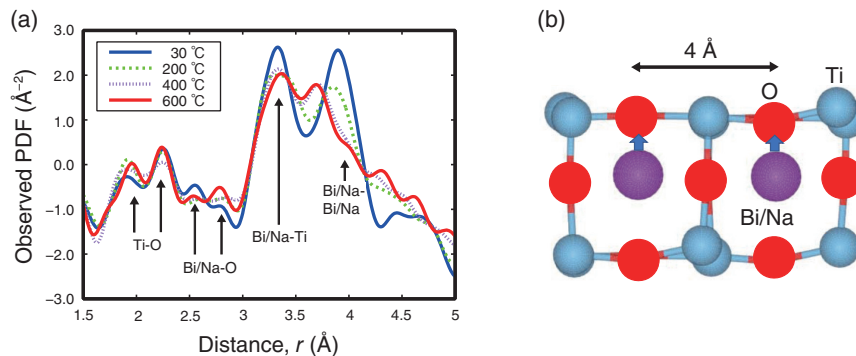


**Fig.5-13 (a) Observed pair distribution functions (PDFs) for  $\text{Bi}_{0.5}\text{Na}_{0.5}\text{TiO}_3$  at various temperatures. (b) Structure obtained by model fitting of the PDF. This is the top view of Fig.5-12**  
In the high-temperature phase of  $\text{Bi}_{0.5}\text{Na}_{0.5}\text{TiO}_3$ , Bi shifts in the direction of the arrow, resulting in large polarization.

A piezoelectric material is a unique material that expands and contracts when an electric field is applied. Piezoelectric phenomena are based on the polarization caused by the displacement of ions and cations. At present, lead is used in many piezoelectric materials; hence, the development of environment-friendly materials is desired. Bismuth sodium titanate ( $\text{Bi}_{0.5}\text{Na}_{0.5}\text{TiO}_3$ ; BNT) is expected to be a candidate for lead-free piezoelectric materials. The crystal structure of BNT is shown in Fig.5-12. Polarization occurs in BNT at room temperature. When the temperature is raised, the polarization disappears once at approximately 100 °C; a larger polarization than that observed at 30 °C is observed in the case of the high-temperature phase at temperatures above 200 °C. Clarifying the origin of the polarization mechanism in the high-temperature phase is expected to boost the development of novel piezoelectric materials.

To develop new piezoelectric materials, it is necessary to observe their microstructure. In general, in crystal structure analysis, a periodic structure is assumed to obtain the average structure. However, in piezoelectric materials, there may be interferences in the periodic structure due to compositional randomness, and it is difficult to determine the atomic positions from the traditional average structure analysis. We have proposed a method of using the pair distribution function (PDF) for synchrotron high-energy X-rays at SPring-8. This method

enables the visualization of the detailed structure from the distribution of interatomic distances. In particular, synchrotron radiation can extract the precise structural changes that deviate from periodicity.

In this study, PDF analysis was performed to clarify the positions of ions in the high-temperature phase of BNT. Fig.5-13(a) shows the PDFs obtained at 30 °C (blue line) and high-temperature phase (red line). Several peaks indicating the atomic distance were observed. In particular, in the high-temperature phase, the intensity of the peak corresponding to the distance between Bi/Na-Bi/Na at 4 Å decreases with temperature. The positions of Bi ions are shifted from the average structure. These results are shown in Fig.5-13(b). In the high-temperature phase of BNT, the displacement of Bi in the direction of the arrow produced a large polarization.

We clarified the polarization mechanism of BNT piezoelectric material by PDF analysis. To develop an excellent piezoelectric material that realizes a large displacement of Bi ions even at 30 °C, we are continuing the research and development by examining substitution with various elements.

This work was supported by JSPS KAKENHI Grant-in-Aid for Scientific Research (C) (JP19K04502), “Fabrication of artificial relaxor using hybrid structure and application to creation of next generation multifunctional materials”.

(Yasuhiro Yoneda)

#### Reference

Yoneda, Y. et al., Nanoscale Structural Analysis of  $\text{Bi}_{0.5}\text{Na}_{0.5}\text{TiO}_3$  in High-Temperature Phases, Japanese Journal of Applied Physics, vol.60, no.SF, 2021, SFFA08, 10p.

## 5-7 How Heavy Electrons are Formed in Eu-Based Compounds

— Direct Observation of the Band Structure of Eu 4f Orbitals, Which Have Magnetic and Localized Characteristics, by Synchrotron Radiation Experiments —

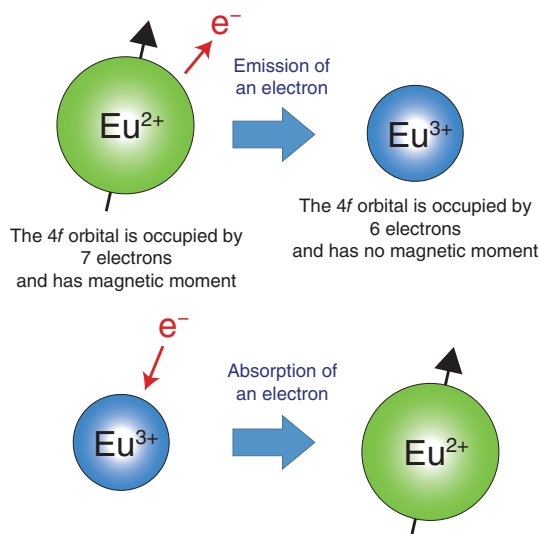


**Fig.5-14 Valence instability of Eu-based compounds**  
Because of the small energy difference between  $\text{Eu}^{2+}$  and  $\text{Eu}^{3+}$  states, the valence state of Eu atoms fluctuates as a function of time and spatial coordinates.

Rare-earth-based compounds possess various intriguing properties such as superconductivity and thus have garnered much attention in the field of strongly correlated electron physics. Moreover, these compounds have been considered as potential candidates for magnetic devices as the rare earth atoms have large magnetic moments. The physical properties of the rare-earth-based compound are accounted for by the 4f electrons of the rare earth atoms. The 4f electrons acquire itinerant properties through hybridization with other electron orbitals and form energy bands and Fermi surfaces. This hybridization is the origin of the various magnetic orderings and superconductivities of rare-earth-based compounds. However, a relatively small 4f binding energy is required to hybridize with other electron orbitals, and therefore, observations of superconductivity have been reported only for Ce- and Yb-based compounds so far. On the other hand, in recent years, it has been recognized that for some Eu-based compounds, the hybridization effect on the 4f electrons becomes important and leads to various unusual properties.

It is well known that most rare earth atoms are nearly trivalent states in intermetallic compounds. However, some Eu-based compounds show a valence instability between the trivalent  $\text{Eu}^{3+}$  and divalent  $\text{Eu}^{2+}$  states because of the small energy difference between these states. As shown in Fig.5-14, this valence fluctuation corresponds to an instability of the number of 4f electrons. Because of this instability, the 4f electrons acquire a mobility that enables them to move throughout the crystal and govern the electronic and physical properties of Eu-based compounds. Although no Eu-based superconductor has been discovered until now, it has been reported that some Eu-based compounds exhibit heavy electron behavior in which the effective

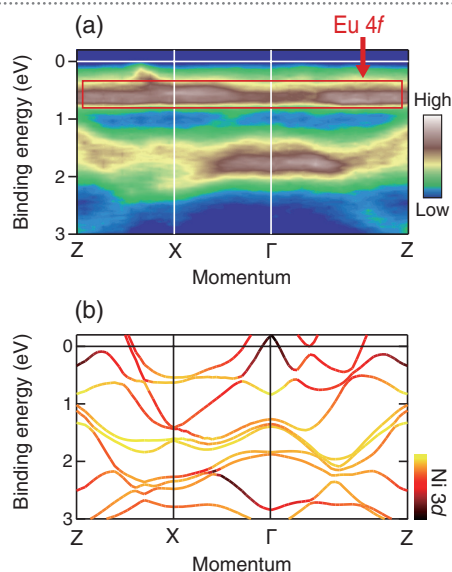


**Fig.5-15 Experimental and calculated band structures of  $\text{EuNi}_2\text{P}_2$**   
(a) The band structure of  $\text{EuNi}_2\text{P}_2$  determined by angle-resolved photoemission experiments. The abscissa represents the position in the momentum space, and the higher-intensity part corresponds to the position of the energy bands. (b) The corresponding calculated band structure of  $\text{EuNi}_2\text{P}_2$ . The color scale shows the contribution of Ni 3d state.

electron mass is strongly enhanced because of the electron correlation effect.

$\text{EuNi}_2\text{P}_2$  is known as the first heavy-electron system among the Eu-based compounds. In this study, we have performed angle-resolved photoemission experiments on  $\text{EuNi}_2\text{P}_2$  at the JAEA beamline BL23SU at SPring-8. In angle-resolved photoemission, the energy and angular distributions of the photoelectrons were measured to directly observe the band structure of the materials.

Fig.5-15(a) shows the experimental band structure determined by angle-resolved photoemission. We observed a flat band structure originating from the Eu 4f orbitals. The flatness of the bands reflects a large effective electron mass, and thus, this band shape seems to be the origin of the heavy electron behavior in  $\text{EuNi}_2\text{P}_2$ . A comparison with the calculated band structure (Fig.5-15(b)) shows that Eu 4f electrons hybridize with other orbitals such as Ni 3d. This result confirms that Eu 4f electrons interact with other electron orbitals and contribute to the formation of the band structure because of valence instability. Moreover, we confirmed the presence of Eu 4f at the Fermi level. This means that the electronic and thermodynamic properties of this compound are markedly affected by the Eu 4f-derived heavy electrons as these properties are usually governed by electron excitations at the Fermi level.

The present result provides an important clue for understanding the mechanism of formation of heavy electrons in Eu-based compounds. We hope that Eu-based superconductors will be discovered in future experimental studies. Such a discovery will further expand the research field of Eu-based compounds.

(Ikuto Kawasaki)

### Reference

Kawasaki, I. et al., Electronic Structure of the Intermediate-Valence Compound  $\text{EuNi}_2\text{P}_2$  Studied by Soft X-Ray Photoemission Spectroscopy, Physical Review B, vol.104, issue 16, 2021, 165124, 8p.

## Research and Development on HTGR, Hydrogen Production, and Heat Application Technologies

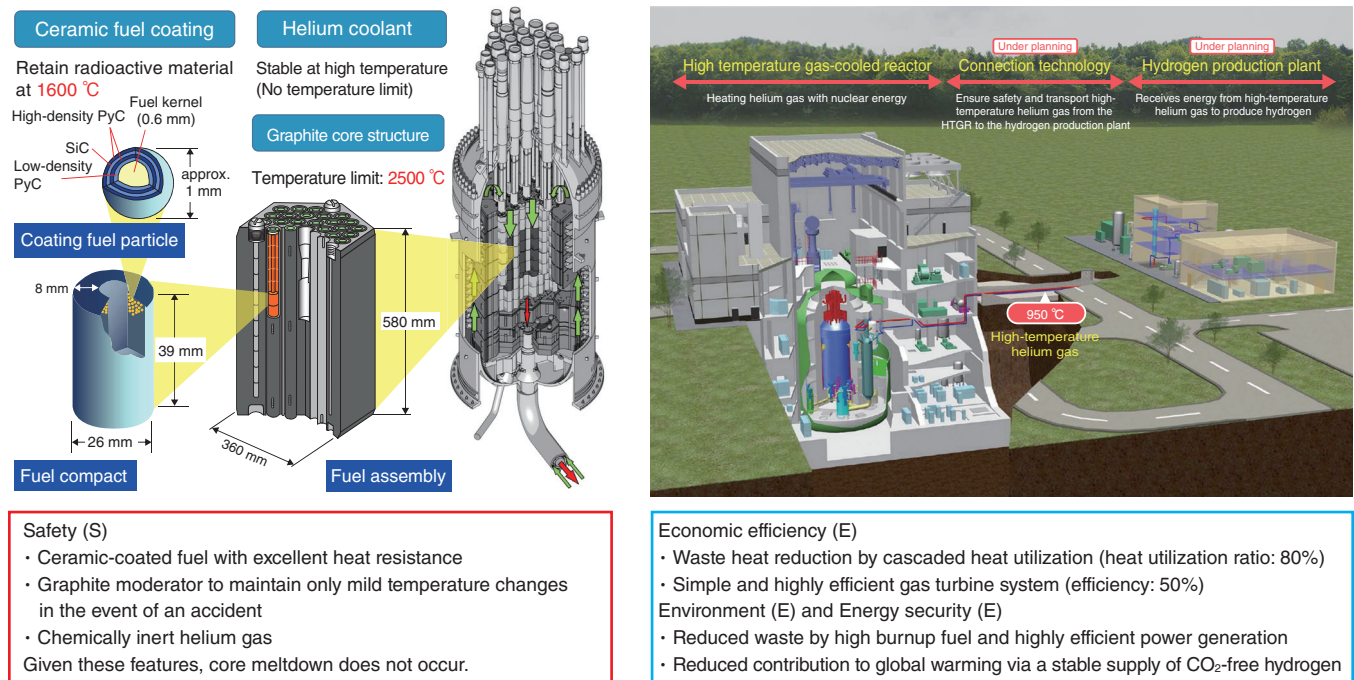


**Fig.6-1 Features of the HTGR and plan of the HTRR-heat utilization test**

The High Temperature Gas-cooled Reactor (HTGR) is a helium-gas-cooled and graphite-moderated thermal-neutron reactor with excellent inherent safety features. The HTGR meets various heat application requirements, including hydrogen production and power generation. The HTGR also meets the 3E+S policy targets in Japan's Strategic Energy Plan. JAEA's final target is the successful demonstration of coupling a nuclear reactor and heat application systems by connecting a gas turbine and hydrogen production facilities to Japan's first HTGR, that is, the HTRR.

A High Temperature Gas-cooled Reactor (HTGR) is an extremely safe reactor that can meet various industrial applications such as hydrogen production using high-temperature heat and high-efficiency power generation using helium gas turbines (Fig.6-1). Japan Atomic Energy Agency (JAEA) has been conducting various demonstration tests using the High Temperature Engineering Test Reactor (HTRR), which is a test HTGR reactor in Japan, developing hydrogen production technology and gas turbines, researching on commercial HTGRs for practical uses, and promoting international cooperation.

In 2010, the reactor outlet temperature of 950 °C was stably supplied over 50 days of continuous operation, demonstrating the ability of the HTGR to ensure a stable supply of high-temperature heat. The inherent safety feature of the HTGR was also confirmed in a loss of forced cooling test without a reactor scram. Even if the cooling and shutdown functions were not activated in the test, the reactor power dropped to zero, and the decay heat was naturally removed. After the Great East Japan Earthquake of 2011, the HTRR operation was stopped for a long time considering the safety review by the Nuclear Regulation Authority of Japan against the new nuclear regulatory standards established in 2013. In June 2020, the HTRR obtained permission to change the reactor installation, and it was restarted in July 2021.

In December 2020, the Ministry of Economy, Trade and Industry executed leadership and formulated an industrial policy, called the "Green Growth Strategy Through Achieving Carbon Neutrality in 2050," in response to the "2050 carbon neutral and a carbon free society" declared by former Prime Minister Suga in October 2020. In this Green Growth Strategy, the nuclear industry is designated as one of the 14 important fields, where future growth is expected. The future efforts with regard to HTGRs include the

following: (1) utilization of the HTRR, with government support, in addition to international safety demonstration, and the necessary technology development for massive and low-cost carbon-free hydrogen production by 2030; (2) government's participation in technology development and demonstration while considering the aspects of safety, economy, supply chain construction, regulatory compliance, and so on, and creation of overseas joint projects by the government based on the status of preceding overseas projects; and (3) promotion of cooperation with the related organizations of other countries to disseminate the Japanese standards through construction and operation.

JAEA has been working on the development of seismic importance classifications. These classifications are important for evaluating the seismic integrity of nuclear reactor facilities, utilizing the knowledge obtained from HTRR operation and testing (Topic 6-1), developing a power distribution evaluation method using the characteristics of HTGRs (Topic 6-2), developing coated fuel particles with enhanced confinement of radionuclides (Topic 6-3), researching the improvement of hydrogen production efficiency of the thermochemical water-splitting IS process (via a carbon-free hydrogen production method), and stable long-term operation (Topics 6-4 and 6-5), and conducting research on further improving the safety of HTGRs and upgrading the design methods (Topics 6-6 and 6-7). In addition, a hydrogen production project using the HTRR (Fig.6-1) was started in this fiscal year. In this project, a hydrogen production facility will be newly connected to the HTRR, and hydrogen production technology utilizing the high-temperature heat obtained from the HTRR will be confirmed. Specifically, the specifics of the modifications required to connect the HTRR to the hydrogen production facility, licensing procedures, and facility modification and testing will be conducted.

## 6-1 New Seismic Classification of the HTTR

— Appropriate Seismic Classification Based on Technical Knowledge and Operation Experience —

**Table 6-1 Classification of the HTTR facilities (Class S)**

The seismic classification was revised considering the safety characteristics of the HTGRs. Table 6-1 lists the results of the seismic classification revision (Class S). Class S facilities compose parts of the confinement function, facilities used to store fuel, etc.

Facilities belonging to Class S	Main facilities
Equipment and pipings composing a reactor coolant pressure boundary	① Reactor pressure vessel ② Vessel, pipings, gas circulators, and valves belonging to reactor coolant pressure boundary
Facilities to store spent fuel	① Spent fuel storage pool ② Spent fuel storage rack in the reactor building
Facilities to add negative reactivity for the fast shutdown of a reactor and to maintain the subcritical condition	① Control rod and control rod drive mechanism (for scramability)
Others	① Primary helium purification system (inside the containment vessel) ② Fuel failure detection system (inside the containment vessel) ③ Primary helium sampling system (inside the containment vessel) ④ Pipings and valves belonging to the reactor containment vessel boundary (contains primary coolant)

For nuclear plants, a seismic classification is classified for each facility, and seismic integrity evaluation is conducted using the seismic force corresponding to each classification. The seismic classification has three classes S, B, and C in which different degrees of seismic force are used for the evaluation. Facilities belonging to classes S, B, and C must maintain strengths of 3.0, 1.5, and 1.0 times, respectively, greater than those of the conventional industrial facilities. The acceleration of the seismic motion of the HTTR was 350 Gal at the design stage. After the Great East Japan Earthquake in 2011, the seismic motion acceleration was set to 973 Gal, which is approximately thrice the previous value. The experiences of the Earthquake show that seismic forces tend to increase. Thus, if a facility is classified into a class that is higher than necessary, its seismic evaluation will be conducted using a larger seismic force.

The seismic classification of the HTTR was formulated in the late 1980s. Because of the lack of operational experiences to sufficiently understand the safety characteristics of the HTTR, the seismic classification of commercial LWRs was applied to the HTTR. However, subsequent operational experiences and test results clarified that the seismic classification was slightly too conservative. Therefore, the seismic design of the HTTR

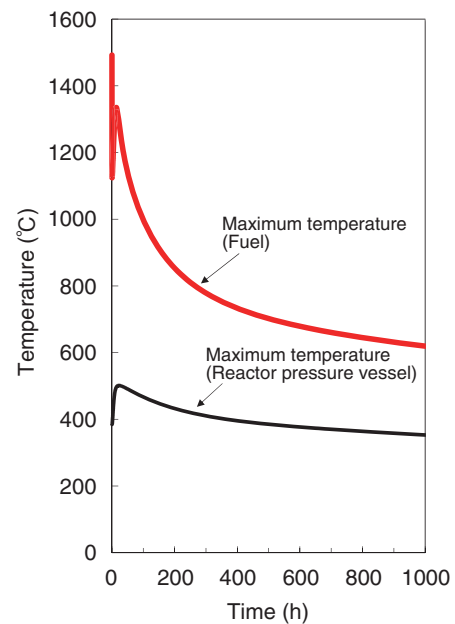


**Fig.6-2 Validation evaluation of the new seismic classification**

Fig.6-2 shows the maximum fuel temperature and maximum reactor pressure vessel temperature after the loss of the safety functions of Class B facilities. Both temperatures never exceeded the limit temperature. Thus, the new seismic classification is valid.

was revised according to current technical knowledge.

The seismic classification of Class-S facilities, as listed in Table 6-1, was prepared to maintain their function even if the safety functions of class-B and class-C facilities are lost because of an accident caused by an earthquake. Thus, accidents are safely controlled without excessive radiation exposure of the public. To validate the new seismic classification, the cooling behavior was evaluated under the malfunction of class-B and class-C facilities. With reference to the criteria of the design basis accident, the maximum temperatures of the reactor pressure vessel must not exceed 550 °C. The evaluation result is shown in Fig.6-2. The maximum fuel temperature initially decreased to 1114°C after reactor scram and increased again, but it never exceeded the limit temperature of 1600 °C. In addition, although the maximum reactor pressure vessel temperature reached 502 °C on the sidewall, it never exceeded the limit temperature of 550 °C. The effective dose equivalent was approximately 3.0 mSv during the accident.

In conclusion, the validity of the newly proposed seismic classification was verified. In June 2020, the Nuclear Regulation Authority in Japan confirmed that the seismic classification conformed to the standard rules for reactor installation changes.

(Masato Ono)

### Reference

Ono, M. et al., Seismic Classification of High Temperature Engineering Test Reactor, Nuclear Engineering and Design, vol.386, 2022, 111585, 9p.

## 6-2 Challenge to Measure the Power Distribution in Very-High-Temperature Core Environments

### — Development of a Power Distribution Measurement Method Using Neutrons Leaked from an HTGR Core —

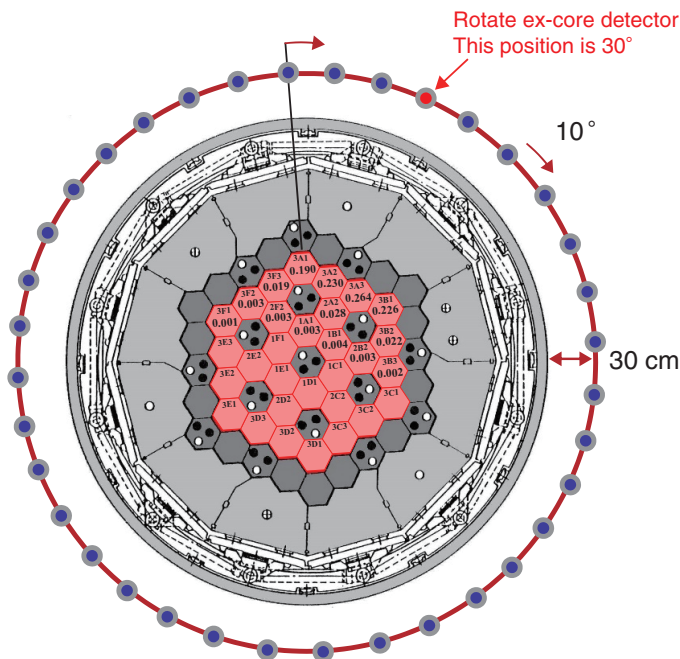


**Fig.6-3 Sensitivity of the HTGR ex-core detectors to the in-core fuel**

The sensitivity shows the contribution of neutrons generated by each fuel block to the detector signal when an ex-core detector is assumed near the pressure vessel in the HTTR geometry. The red cells are fuel blocks. The sensitivity is normalized so that the sum over all cores is unity.

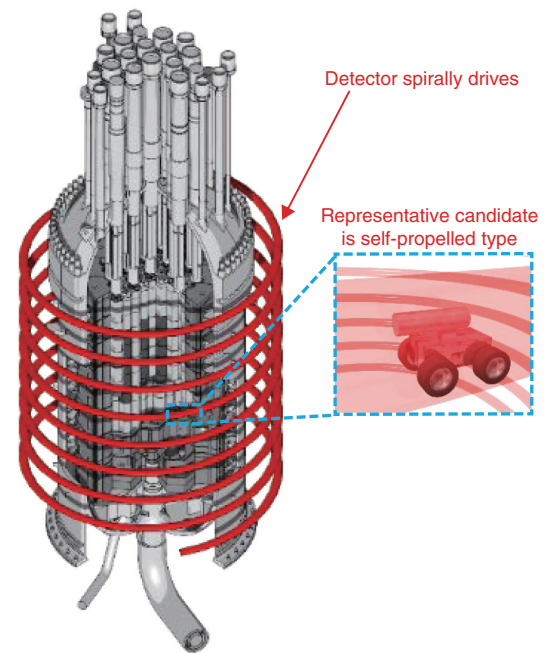


**Fig.6-4 Concept of moving an ex-core detector**

This is an example of an orbit for moving an ex-core detector. Since this concept is based on a principle similar to CT technology, the ideal method of moving the measurement detector is a spiral orbit, similar to that of CT.

The High Temperature Gas-cooled Reactor (HTGR) employs a helium gas coolant to extract fission energy in the reactor as thermal energy. The High Temperature Engineering Test Reactor (HTTR) was the first in the world to successfully achieve a reactor outlet coolant temperature of 950 °C on April 19, 2004. This high temperature is expected to help realize many possibilities, including highly efficient power generation with a thermal efficiency of 50% and hydrogen production, which is expected to become carbon neutral.

However, in the Light Water Reactors (LWRs) that are currently in commercial use, the temperature inside the core is about 300 °C; hence, it is possible to insert a neutron detector directly into the core. This in-core detector can be used to measure the power distribution of each fuel assembly, thereby enabling fuel management for efficient fuel burning.

In contrast, the HTGR has a very-high temperature environment where the temperature inside the core can reach up to 1000 °C. Therefore, it is not possible to insert detectors into the core, and some of the operation and maintenance technologies developed for the LWR cannot be applied. In addition, if the power distribution in the reactor can be measured during HTGR operation and maintenance, it will be possible to realize a more economical HTGR design by reasonably reducing the safety margin based on improved fuel temperature estimation accuracy, in addition to efficient burning through fuel management.

This perspective led us to consider a method of measuring the

power distribution in a core by observing the neutrons leaking from the core using an ex-core detector. Fortunately, we found that HTGRs have the advantage of longer neutron flight path than the LWRs because of the differences in the characteristics of the neutron moderators (LWR uses light water, whereas HTGR uses graphite). Fig.6-3 shows the sensitivity of the HTGRs to the in-core fuel as detected by the ex-core detectors. It shows the contribution of neutrons generated by each fuel block to the detector signal, and it can be seen that the sensitivity extends to the center of the core. In the case of LWRs, measurement can be made for only the outer fuel assembly.

By using the long range of sensitivity detected by the ex-core detectors in the HTTRs, we devised an inverse analysis method of the power distribution based on a principle similar to computed tomography (CT) with many measurement points, and we successfully demonstrated the principle numerically in the HTTR geometry. As shown in Fig.6-4, at present, we assume that the detector is driven by a spiral orbit as in the CT.

The significance of this idea was recognized in FY2021, and the project was selected by MEXT as Nuclear Energy System Research and Development Project (JPMXD0221459236) “Development of Nuclear Instrumentation System for Power Distribution Measurement of HTGR”, and development toward practical application is underway in collaboration with JAEA, ANSeeN Corporation, and Shizuoka University.

(Yuji Fukaya)

#### Reference

Fukaya, Y. et al., Computed Tomography Neutron Detector System to Observe Power Distribution in a Core with Long Neutron Flight Path, Annals of Nuclear Energy, vol.168, 2022, 108911, 7p.

## 6-3 For Reducing the Cost of Construction of High-Temperature Gas-Cooled Reactors — Development of Cesium Trap Material for Coated Fuel Particles —

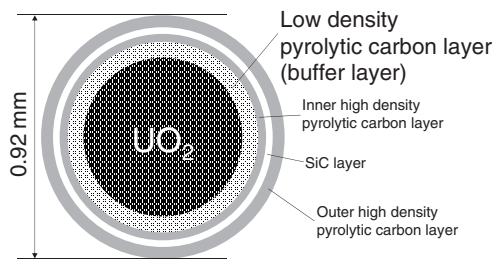


**Fig.6-5 Schematics of the cross section of a coated fuel particle (CFP) of the High Temperature Engineering Test Reactor (HTTR), which is the only high temperature gas-cooled reactor (HTGR) in Japan**

CFPs with a diameter of approximately 1 mm are used in HTGRs. Fissile materials and fission products (FPs) are retained in each CFP. In the case of the HTTR, a small sphere of  $\text{UO}_2$  (i.e., the  $\text{UO}_2$  kernel) is covered by quadruple ceramic coating layers to form the CFP. Low-density pyrolytic carbon layer (the buffer layer) is the innermost coating layer. The buffer layer provides space for the gases released from the  $\text{UO}_2$  kernel.

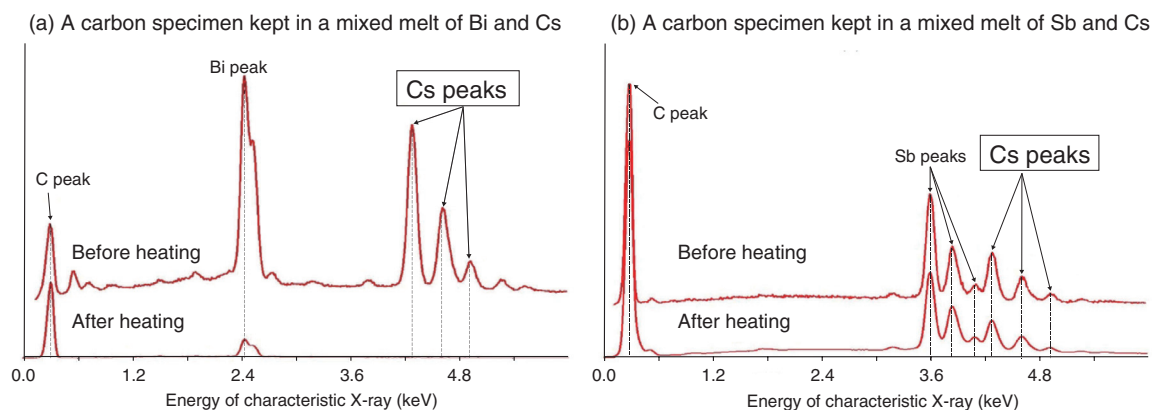


**Fig.6-6 Energy dispersion X-ray (EDX) spectra obtained from specimens before and after heating up to 1500 °C (upper: before heating, lower: after heating)**

Cs hardly remained in the carbon specimen kept in the Cs-Bi mixture after heating (a). In contrast, Cs remained in the carbon specimen kept in the Cs-Sb mixture after heating (b).

(Reprinted from below reference with permission of The American Society of Material Engineering.)

The minimum unit of the high temperature gas-cooled reactor (HTGR) fuel is a coated fuel particle (CFP) with a diameter of approximately 1 mm. In Japan, CFPs are formed by covering a small sphere of  $\text{UO}_2$  (the  $\text{UO}_2$  kernel) with quadruple ceramic coating layers (Fig.6-5). Fissile materials and fission products (FPs) are retained in each CFP. However, a calculation has showed that 0.34% of cesium can be diffusively released from intact CFPs within the lifetime\* of the HTGR fuel under normal operation. If the released amount of Cs is reduced, the construction cost can be reduced because the thickness of the shielding wall can be reduced. There are two methods to reduce the amount of Cs released from intact CFPs. One solution is to use a thicker coating layer of the CFP, and the other is to add a Cs trap material to the CFPs. This study is a feasibility study for the second approach.

Based on document search, it was predicted that pnictogens may be suitable as Cs trap material because they can easily be absorbed along with Cs by carbon and they can chemically bond with Cs. Therefore, the basic policy was decided as dispersing a pnictogen in the buffer layer to reduce the amount of Cs released.

Then, an experimental feasibility study was conducted. Specifically, the possibility that Sb or Bi, which are harmless pnictogens, can trap Cs in the buffer layer was examined. Carbon plates, which simulated the buffer layer, were kept in a mixed

melt of Cs and Sb (Cs-Sb) or Cs and Bi (Cs-Bi) at 590 °C for 1 h. The weights of Cs and (Sb or Bi) were identical in each molten mixture. The C plates were removed taken from the mixture and heated in Ar up to 1500 °C. The heating ratio was 10 °C/min. Note that 1500 °C is slightly higher than the maximum fuel temperature under normal operation. Energy dispersion X-ray (EDX) spectra were obtained before and after heating. The EDX spectra revealed that after heating, the Cs atoms almost disappeared in the Cs-Bi C specimen (Fig.6-6(a)), whereas Cs atoms remained in the Cs-Sb C specimen (Fig.6-6(b)). In addition, it was revealed that Cs atoms almost disappeared in the C specimen kept in the molten Cs.

The conclusion is that Bi cannot trap Cs in the buffer layer, but Sb can. The next step will be to conduct heating tests for longer times with the Cs-Sb C specimen.

This study is a part of the results of the cooperative research with the University of Fukui.

(Jun Aihara)

\* Sawa, K. et al., Prediction of Nongaseous Fission Products Behavior in the Primary Cooling System of High Temperature Gas-Cooled Reactor, Journal of Nuclear Science and Technology, vol.31, issue 7, 1994, p.654-661.

### Reference

Sasaki, K. et al., Development of Cesium Trap Material for Coated Fuel Particles in High Temperature Gas-Cooled Reactors, Proceedings of 28th International Conference on Nuclear Engineering (ICONE 28), Online Conference, 2021, ICONE28-61765, 6p.

## 6-4 Upgrading H<sub>2</sub> Production Efficiency in the IS Process

### — Corrosion Stability Improvement of the H<sub>2</sub> Separation Membrane for HI Decomposition —

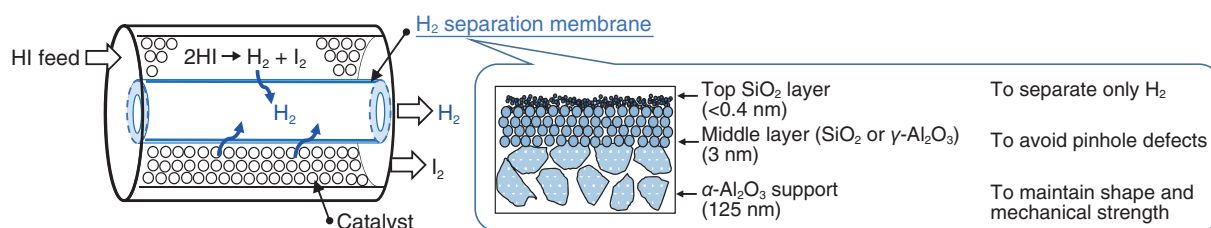


**Fig.6-7 Schematic of a membrane reactor equipped with an H<sub>2</sub> separation membrane for HI decomposition**

In a membrane reactor, HI gas is catalytically decomposed into H<sub>2</sub> and I<sub>2</sub>, and the H<sub>2</sub> produced is separated by a membrane, thereby driving HI decomposition. The membrane consists of three layers: a base  $\alpha$ -Al<sub>2</sub>O<sub>3</sub> support tube, a middle layer ( $\gamma$ -Al<sub>2</sub>O<sub>3</sub> or SiO<sub>2</sub>), and a top H<sub>2</sub>-selective SiO<sub>2</sub> layer.

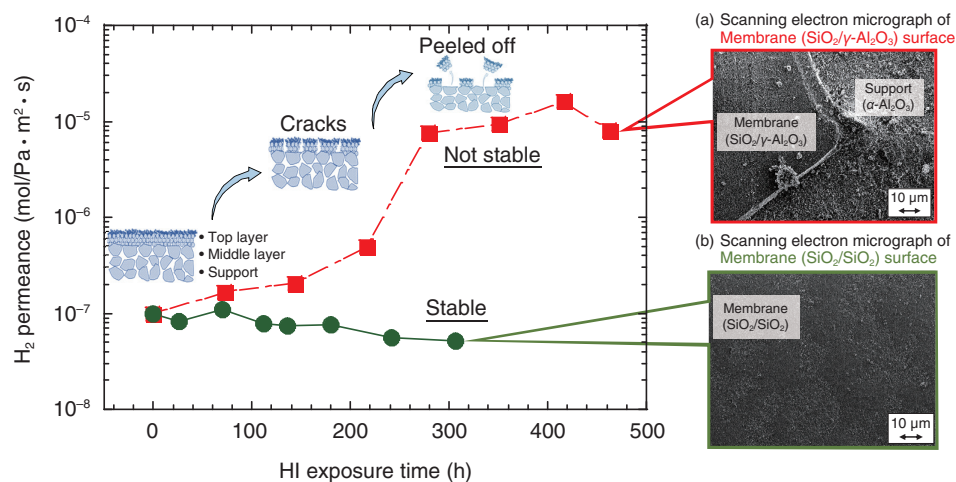


**Fig.6-8 Change in the H<sub>2</sub> permeance of membranes with middle layers composed of (a)  $\gamma$ -Al<sub>2</sub>O<sub>3</sub> and (b) SiO<sub>2</sub> under corrosive HI exposure**

The new H<sub>2</sub>-separation membrane with the middle layer changed from the conventional  $\gamma$ -Al<sub>2</sub>O<sub>3</sub> to SiO<sub>2</sub> showed stable performance in a corrosive HI environment.

Thermochemical iodine–sulfur (IS) process, which employs nuclear heat to decompose water, is considered the most suitable solution for producing large amounts of H<sub>2</sub> without emitting CO<sub>2</sub>. The IS process consists of three coupled chemical reactions (the Bunsen reaction, sulfuric acid decomposition reaction, and hydrogen iodide decomposition reaction).

One of the technical challenges in the development of the IS process is the separation of H<sub>2</sub> from the mixture of corrosive gases hydrogen iodide and iodine during hydrogen iodide decomposition ( $2\text{HI} \rightarrow \text{H}_2 + \text{I}_2$ ). To solve this problem, there is a need for a membrane reactor with an H<sub>2</sub> separation membrane (Fig.6-7) that is capable of equilibrium shifting and can handle corrosive environment.

The conventional H<sub>2</sub> separation membranes used for HI decomposition consist of three layers: a base  $\alpha$ -Al<sub>2</sub>O<sub>3</sub> support tube (average pore size: 200 nm) that maintains mechanical strength, middle  $\gamma$ -Al<sub>2</sub>O<sub>3</sub> layer (3 nm) to avoid pinhole defects in the top layer, and top SiO<sub>2</sub> layer (<0.4 nm) to selectively separate H<sub>2</sub>.

In the HI exposure tests of these conventional membranes, a considerable increase in the H<sub>2</sub> permeance was observed after

200 h. This is because the middle  $\gamma$ -Al<sub>2</sub>O<sub>3</sub> layer was corroded by HI gas and partially peeled off (Fig.6-8(a)). In other words, the large increase in H<sub>2</sub> permeance was attributed to the lack of corrosion stability of the middle layer to HI gas. Therefore, to improve corrosion stability against HI exposure, the fragile middle  $\gamma$ -Al<sub>2</sub>O<sub>3</sub> layer should be replaced by a more corrosion-resistant material. For this purpose, a new H<sub>2</sub>-separation membrane was developed with a middle SiO<sub>2</sub> layer that is thermally and chemically stable and has excellent pore size controllability. The new membrane with this middle SiO<sub>2</sub> layer showed only a slight decrease in H<sub>2</sub> permeance after 300 h of exposure to HI gas, and there were no significant changes on the membrane surface (Fig.6-8(b)); the middle SiO<sub>2</sub> layer remained unchanged and stable. Thus, we successfully developed an H<sub>2</sub> separation membrane with high corrosion stability in an HI environment. The membrane with middle SiO<sub>2</sub> layer is suitable for membrane reactors that produce H<sub>2</sub> via HI decomposition.

This work was partially supported by the Council for Science, Technology and Innovation, Cross-ministerial Strategic Innovation Promotion Program, “Energy Carrier” (Funding agency: JST).

(Odtsetseg Myagmarjav)

#### Reference

Myagmarjav, O. et al., Fabrication, Permeation, and Corrosion Stability Measurements of Silica Membranes for HI Decomposition in the Thermochemical Iodine-Sulfur Process, *International Journal of Hydrogen Energy*, vol.46, issue 56, 2021, p.28435–28449.

## 6-5 Achievement of Longer-Term H<sub>2</sub> Production in IS Process — Introduction of a Novel Operating Procedure Using a Closed-Loop System —

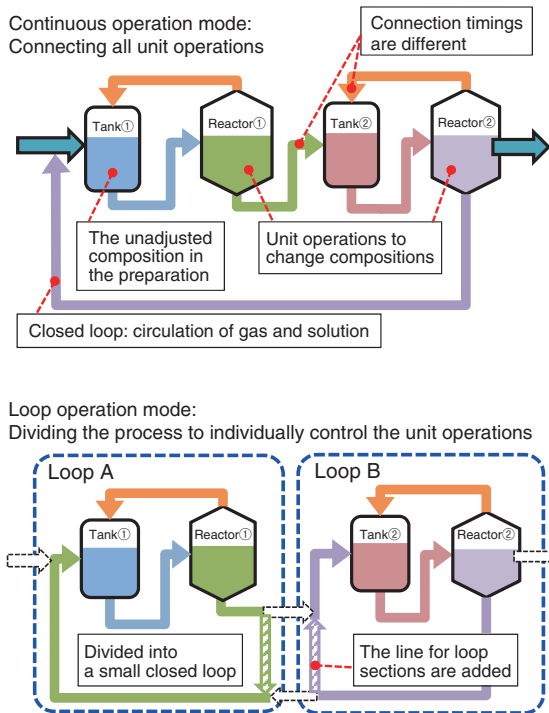


**Fig.6-9 Comparison of the continuous and loop operation modes**

The closed-loops are established by subdividing the process configuration, allowing individual control of the composition of each unit operation at beginning of the operation.

The water-splitting hydrogen (H<sub>2</sub>) production, namely, the iodine–sulfur (IS) process as a heat-based application of high-temperature gas-cooled reactors has been investigated to realize H<sub>2</sub> economy. The IS process involves the chemical reactions of sulfur and iodine (I<sub>2</sub>) and the flow of fluids with different compositions, such as I<sub>2</sub> and hydrogen iodide (HI). For stable longer-term H<sub>2</sub> production, composition fluctuations of these fluids should be canceled at the early stage of the operation.

In the previous operating procedure, many unit operations, such as those involving separators and reactors, were simultaneously connected. In this case, the deviation from the prescribed compositions might be generated by various causes: for example, an unadjusted composition during preparation and differences in the connecting timings of flows during start-up. Moreover, the fluids were circulated in all unit operations because the IS process is a large closed cycle. Therefore, the fluctuation arising in a certain reactor could affect all unit operations in the process. So far, it is challenging to predict the effect of such fluctuations on the start-up procedure, and a

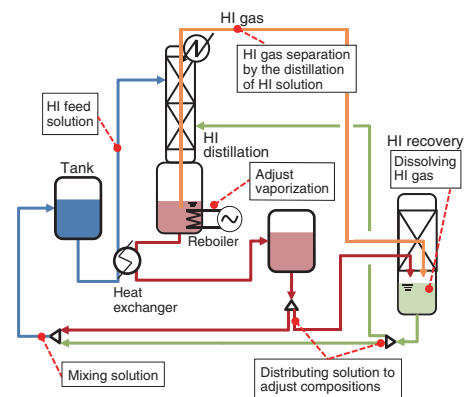


**Fig.6-10 Example of a closed-loop process configuration: HI distillation section**

The iodine–sulfur (IS) process system was reconstructed as four independent closed loops, such as in the case of the HI distillation section, by categorizing all unit operations into subsections.

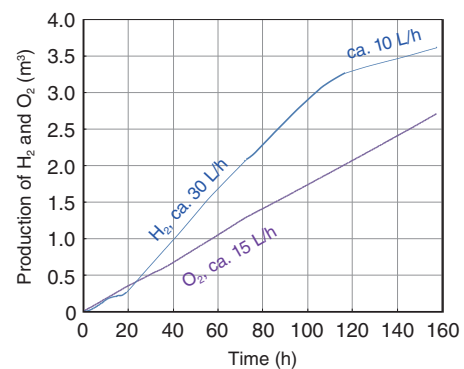


**Fig.6-11 Measurement result of continuous H<sub>2</sub> production operation**

150 h of H<sub>2</sub> production operation was achieved by applying the proposed operating procedure with the closed-loop configuration.

large fluctuation, which can cause pipe clogging, at the early stage lasting several hours could prevent the realization of stable longer-term H<sub>2</sub> production.

To solve this issue, closed loops to subdivide the process configuration are introduced as a new operation mode to individually control the composition fluctuation in each unit operation (Fig.6-9). All unit operations are categorized into subsections. The categorized subsections individually establish reversible and closed-loop processes. Based on this idea, the IS process system was reconstructed as four independent closed-loop sections (Fig.6-10). The new operating procedure that enabled us to commence stable H<sub>2</sub> production was proposed by using the subdivided closed-loop sections.

The existing H<sub>2</sub> production test facility was updated to execute the new closed-loop operation procedure. Through this procedure, 150 h of H<sub>2</sub> production was successfully achieved (Fig.6-11). As a next step, we are developing an automatic control system to stabilize the long-term operation.

(Nobuyuki Tanaka)

### Reference

Tanaka, N. et al., Introduction of Loop Operating System to Improve the Stability of Continuous Hydrogen Production for the Thermochemical Water-Splitting Iodine-Sulfur Process, *International Journal of Hydrogen Energy*, vol.46, issue 55, 2021, p.27891–27904.

# 6-6 Development of a Novel RPV Cooling System for HTGRs

— Comparison of the Structural Differences Between RPV Cooling Systems and Effects of External Parameters on RPV Cooling —

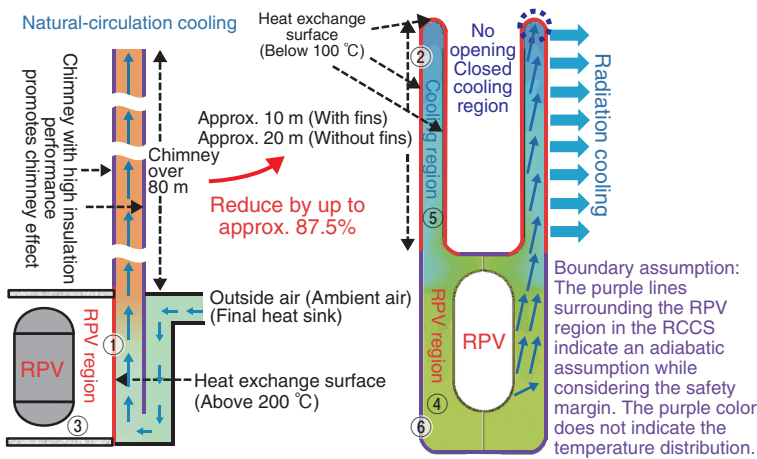


**Fig.6-12 Structural differences between a natural circulation cooling system (left) and a radiation cooling system (right)**

Natural-circulation cooling system (left): The outside air (ambient air), which is the final heat sink, is absorbed directly into the duct. The air inside the duct is heated by the heat radiated from the RPV. The heated air rises inside the chimney with high thermal insulation performance to promote the chimney effect, and subsequently, it is released to the outside air again from the chimney outlet. The height of the chimney should be 80 m or more to promote the chimney effect. Radiation cooling system (right): Heat is directly radiated from the RPV to the cooling region (5). Simultaneously, the heated air in the RPV region (4) rises to the cooling region (5) by natural convection. The air accumulated in the cooling region (5) can be cooled by radiation from the outer surface of the cooling region (2), and the air descends. The height of the cooling region of the radiation cooling system (right) is less than the chimney height of the natural circulation cooling system (left) by up to approximately 87.5%.

(a) Normal operation

Natural-circulation cooling system (Fig.6-12 left)	Radiation cooling system (Fig.6-12 right)
The temperature of the heat exchange surface (1), which is in contact with the outside air, reaches 200 °C or higher. It is necessary to consider the possibility of low-temperature ignition of combustible materials taken (that intrude) into the duct along with the outside air. If low-temperature ignition occurs, the promotion of fire (combustion) by the chimney effect should be considered. Moreover, when ducts and chimneys are clogged, the temperature rises sharply.	The temperature of the heat exchange surface (2) exposed to the outside air is 100 °C or less. There is no possibility of low-temperature ignition of combustibles taken in with the outside air because the RPV region (4) containing the RPV is wrapped by a highly insulating wall (6) and does not come into contact with the outside air.
The outside air temperature, wind speed, humidity, duct and chimney lengths, surface roughness, number of bends, etc., affect the amount of heat removed.	Only the ambient temperature affects the amount of heat removed. The parameters of wind speed and humidity are not included in the radiation formula.
Since the internal gas inside the duct and chimney is the outside air, an unstable phenomenon in natural circulation (natural convection) occurs. There is an uncontrolled increase or decrease of the amount of heat removed because of fluid vibration. It is necessary to consider the impact of this effect on structures.	Since the internal gas in the RPV region (4) and the cooling region (5) is not outside air, there is no unstable phenomenon or fluid vibration, and consequently, no impact on the structures.

(b) Natural disasters

Natural-circulation cooling system (Fig.6-12 left)	Radiation cooling system (Fig.6-12 right)
Changes in back pressure due to disturbances resulting from natural disasters, such as typhoons, hurricanes, tornadoes, and heavy rains, affect the natural circulation in ducts and chimneys. In addition, stagnation and backflow occur in ducts and chimneys.	There are no ducts or chimneys. The natural convection heat transfer coefficient of the large heat exchange surface (2) and the large depression (5) of the cooling region (5) are designed under no-wind conditions; therefore, when a natural-disaster-induced disturbance occurs, the natural convection heat-transfer coefficient will increase. Consequently, the heat removal performance can be improved.

**Table 6-2 Comparative study results of two types of passive RPV cooling systems**

Both during normal operation (Table 6-2(a)) and during natural disasters (Table 6-2(b)), safety of radiation cooling system (Fig.6-12 right) even in any accident conditions, can be enhanced because the number of external parameters and items to affect radiation cooling system (Fig.6-12 right) is smaller than those to affect natural circulation cooling system (Fig.6-12 left).

Recently, there has been increasing demand for High Temperature Gas-cooled Reactors (HTGRs) that do not cause core meltdown. Conventional cooling systems adopt active Reactor Pressure Vessel (RPV) cooling systems using the forced circulation of water, such as that achieved by pumps, to remove the heat released from the RPV. However, the pumps cannot be operated if the power supply shuts down, and there is a possibility that the heat removal activity (i.e., cooling activity) will decrease drastically. Even in this accident condition, core meltdown will not occur in the HTGR, but there is a possibility that the temperature of the RPV will exceed the operating limit temperature and its operation will be shut down.

Therefore, unlike the case of the facility where the TEPCO's Fukushima Daiichi NPS accident occurred, safer RPV cooling systems in which the heat sink is never lost and active systems or emergency power sources, etc. are never needed and wherein the decay heat can be passively removed from the reactor core even under any accident conditions are being explored.

At present, a passive RPV cooling system employing the natural circulation of outside air (ambient air) is proposed as a candidate for commercial HTGRs (Fig.6-12 left). The coolant of the outside air is never lost. However, a large number of external parameters and items are to be considered (Table 6-2), and they affect the natural-circulation cooling system (Fig.6-12 left). Therefore, we have developed a novel passive RPV cooling system based on radiative cooling (Fig.6-12 right). The amount of heat removed from the RPV for a practical HTGR should be equivalent to 3 kW/m<sup>2</sup>\* when converted to heat flux. Through experiments using the heat-transfer test equipment that can simulate an actual cooling system, we confirmed that approximately 7 kW/m<sup>2</sup> of heat can be removed.

Next, to make possible the practical use of the natural-circulation cooling system and radiation cooling system, it is necessary to evaluate their safety features to check whether both systems

can remove passively the decay heat during normal operation (Table 6-2(a)) and under any accident conditions, including natural disasters (Table 6-2(b)).

Therefore, we investigated the structural differences between the two systems and the effects of external parameters on them. During normal operation, in the natural-circulation cooling system, the combustible materials that are introduced (absorbed) into the duct along with the outside air are heated on the heat exchange surface (1), and low-temperature ignition may occur without any heat sources; consequently, temperatures in the clogged duct and chimney will increase remarkably.

In addition, there are some risks that the heat removal ability will decrease because of the large number of external parameters and factors that affect the natural-convection heat transfer coefficient. Some such factors are the occurrence of unstable phenomena in natural circulation and fluid vibration. Furthermore, when natural disasters, such as a typhoon or heavy rainfall event, occur, the disturbance of the outside air affects the natural-circulation cooling system, and there is a possibility that the heat removal ability will decrease. In contrast, in the case of the radiation cooling system, we confirmed that the system can remove heat safely and reliably both during normal operation and natural disasters and clarified the possibility of achieving better safety in the event of an accident compared to the natural-circulation cooling system. Although the RPV regions (3 and 4) of both cooling systems are closed regions, the pressure rise due to the increase in temperature of the internal gas does not pose a problem (i.e., there is no effect of the pressure rise).

This work was supported by JSPS KAKENHI Grant-in-Aid for Scientific Research (C) (JP18K05000).

(Kuniyoshi Takamatsu)

\* Argonne National Laboratory, Private Communication.

**Reference**

Takamatsu, K. et al., Comparisons Between Passive RCCSs on Degree of Passive Safety Features Against Accidental Conditions and Methodology to Determine Structural Thickness of Scaled-Down Heat Removal Test Facilities, Annals of Nuclear Energy, vol.162, 2021, 108512, 10p.

## 6-7 Toward More Accurate Core Analysis of High-Temperature Gas-Cooled Reactors — Development of a Core Analysis Method with Specified Graphite Porosities —

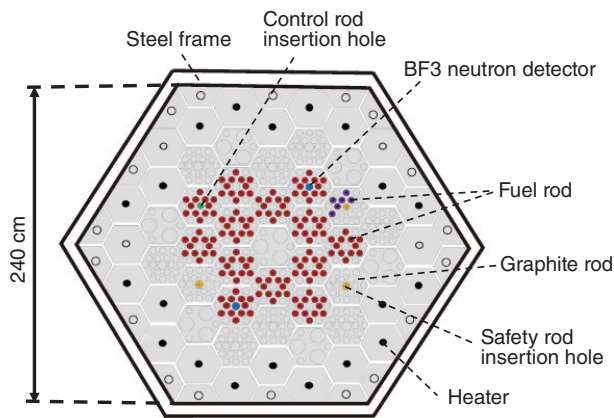


**Fig.6-13 Cross-sectional view of the Very High Temperature Reactor Critical Assembly (VHTRC)**

The VHTRC is a hexagonal, horizontal, two-part graphite-moderated critical assembly consisting of two hexagonal columns that are 240 cm high and 120 cm wide. It was used for reactor physics experiments on the high-temperature gas-cooled reactor.

In a design study for high-temperature gas-cooled reactors (HTGRs) using graphite as the moderator, it is important to accurately evaluate the behavior of thermal neutrons in core analysis because the criticality is maintained mainly via a fission chain reaction by thermal neutrons. It is necessary to quantitatively consider the interactions between thermal neutrons and low-frequency lattice vibrations of graphite crystals, which have energies as large as those of thermal neutrons.

To deal with the effects of such low-frequency vibrations, thermal neutron scattering law data are used. Until now, thermal neutron scattering law data for graphite have been evaluated for an ideal crystalline graphite, in which all the atoms are regularly aligned, but the actual graphite used in HTGRs is not an ideal crystal and comprises parts with many porosities. If the thermal neutron scattering law data for actual graphite porosity can be used, it will become possible to evaluate the thermal neutron behavior more accurately because the low-frequency lattice vibrations that contribute to the thermal neutron scattering increase near pores.

Recently, thermal neutron scattering law data corresponding to actual graphite, with graphite porosity as a parameter, were developed by Hawari et al. at North Carolina State University and were included in ENDF/B-VIII.0, the latest library of nuclear data in the US. However, these data are not sufficient because they only include graphite with 10% and 30% porosities, which do not necessarily match the porosity of the graphite used in actual HTGRs.

### Reference

Okita, S. et al., A Pseudo-Material Method for Graphite with Arbitrary Porosities in Monte Carlo Criticality Calculations, *Journal of Nuclear Science and Technology*, vol.58, issue 9, 2021, p.992-998.

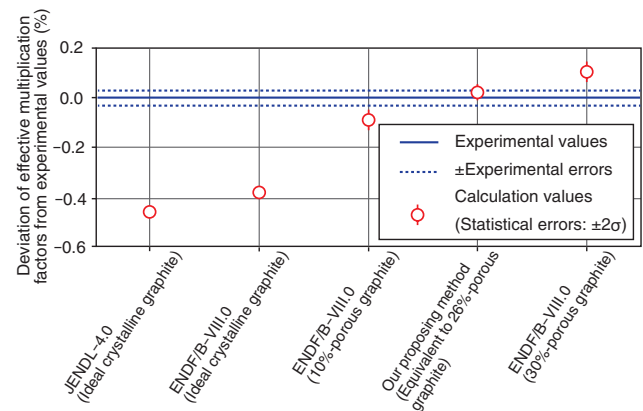


**Fig.6-14 Comparison of the effective multiplication factors obtained by using the thermal neutron scattering law data stored in each library and by using our proposing method**

The effective multiplication factors obtained from JENDL-4.0, ENDF/B-VIII.0, and our proposing method are compared with the experimentally obtained values. ENDF/B-VIII.0 yields the values for ideal crystals (10% and 30% porosity), while our proposed method yields values for an actual graphite porosity (equivalent to 26% porosity).

To address this problem, we proposed and developed a new method that allows users to freely specify the porosity of graphite and perform more accurate core analysis on HTGRs. If an exhaustive library were to be developed to cover all graphite porosities, the amount of nuclear data would be enormous, which is undesirable from the viewpoint of convenience. Therefore, to find a solution without increasing the amount of nuclear data, we focused on a method called the pseudomaterial method proposed by Conlin et al. at the University of Michigan. Originally, this method was developed to reduce the amount of nuclear data for the huge number of temperature points required in the neutronic thermohydraulic coupling analysis for light water reactors. This method utilizes nuclear data corresponding to two different temperature points and probabilistically represents the temperature point to be analyzed between them.

We thought that the thermal neutron scattering law data for graphite at two different porosity points could analogously provide a probabilistic representation of the porosity point to be analyzed between them. To demonstrate the validity of our proposed method, we calculated the deviation of the effective multiplication factors from the experimental results obtained in the past for Very High Temperature Reactor Critical Assembly VHTRC (Fig.6-13). From the results, we confirmed that the effective multiplication factor obtained by our proposed method is more consistent with the experimental data than the factors obtained from the conventional libraries (Fig.6-14).

(Shoichiro Okita)

## Development of the Technology Base and Infrastructure Toward Improving the Fast Reactor Cycle

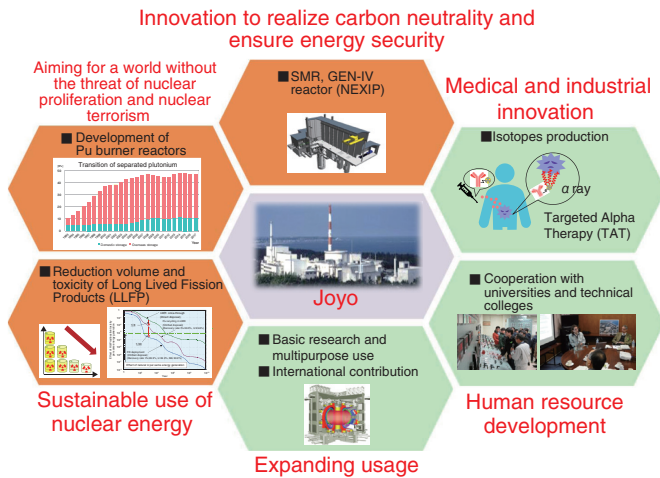


**Fig.7-1 Role of the Experimental Fast Reactor Joyo as a Research Platform**

In addition to burning plutonium fuel, waste volume reduction of long-lived nuclides, and innovation-related irradiation for the advancement of small modular reactors and next-generation reactors, the JAEA aims to achieve wide usage of Joyo for purposes, such as the creation of medical and industrial innovations.

Fast reactors and related nuclear fuel cycles offer a promising sustainable energy supply to meet the global energy demand while protecting the environment. Fast reactors can potentially supply energy for over 1000 years by using uranium resources more effectively than the traditional nuclear energy systems. Further, they can significantly reduce the exothermic heat and radiotoxicity of the vitrified bodies sent for geological disposal by transmuting the minor actinides (MAs) that have a long half-life.

The research and development (R&D) activities for fast reactors for the next decade were specified in the Strategic Roadmap presented by the National Inter-Ministerial Council for Nuclear Power in December 2018. According to this roadmap, backend actions related to the reprocessing or recycling of fast reactor technology are required to establish the significance of diversifying fast reactors. Moreover, international competitiveness should be maintained by continuing the R&D in nuclear power, human resource development, and research base while introducing cutting-edge technology domestically and internationally. Therefore, the JAEA formulated an R&D policy according to the Strategic Roadmap; the Sector of Fast Reactor and Advanced Reactor R&D (SEFARD) is now implementing an advanced integrated design evaluation method incorporating cutting-edge technologies in Japan and overseas, safety improvement technology, technology to reduce the volume and toxicity of radioactive waste, cost-effective fast reactor technology, fuel cycle technology (such as fuel fabrication and reprocessing), and the development/standardization of safety criteria, codes, and standards. Research on the reduction of the volume and toxicity of radioactive waste has been underway at the experimental fast reactor Joyo at Oarai Research Institute. Furthermore, in response to the strategic roadmap, the JAEA plans to expand the use of Joyo as a research platform in the fields shown in Fig.7-1. In particular, we plan to focus on producing medical radioisotopes, which have high expectations domestically and internationally. Based on these needs, measures according to the new regulatory standards shown in Fig.7-2 are

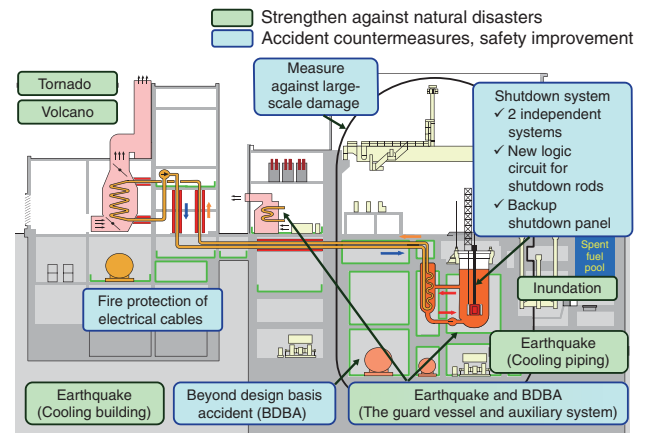


**Fig.7-2 Measurement to the new regulatory standards**

The JAEA will strengthen Joyo's resistance to earthquakes and natural disasters. Furthermore, measures to prevent the spread of accidents that release large amounts of radioactive materials will be implemented.

implemented to restart the Joyo as soon as possible.

A fast simulation method for chemically reacting flows was developed (Topic 7-1). This method can also reduce the calculation time of numerical analysis and facilitate the exploration of various new steam generator designs for developing innovative reactors.

A new experimental device was developed to visualize the sodium aerosol transfer behavior (Topic 7-2). The aerosol transport behavior and the distribution data of sedimented aerosols in cells were obtained. This result is expected to be helpful to elucidate the transport behavior of sodium fire aerosol for validating the evaluation method in the future.

A new evaluation method was developed to predict the creep-fatigue life (Topic 7-3). The predicted results obtained by the new method estimated the number of cycles corresponding to the crack initiation in creep-fatigue tests with good accuracy. These results are expected to provide a reference to improve the design procedure.

A new experimental method was developed to obtain oxygen self-diffusion coefficients of stoichiometric MOX fuels (Topic 7-4). It is possible to predict the time required for sintering and redox reactions of the MOX fuel and the time variation of oxygen retribution during irradiation.

The measurements revealed the correlation between the thermal conductivity of Am-MOX and the Am content. An equation was derived to calculate the effect of Am content on the thermal conductivity of MOX fuels. This will contribute to the design technology for determining the fuel core temperature (Topic 7-5).

Thermal contraction of CRDS was considered in the reactivity measurement. In the present study, the discrepancy between the calculation and experiment was successfully eliminated, and the experimental data are acceptable as validation data (Topic 7-6).

An evaluation method for the O/M ratio from Am and Np contents, temperature, and oxygen partial pressure was formulated. This method will contribute to improving the fuel design (Topic 7-7).

# 7-1 Fast Simulation Method for Chemically Reacting Flows

## — Efficient Numerical Simulation for Developing New-Generation Nuclear Plants —

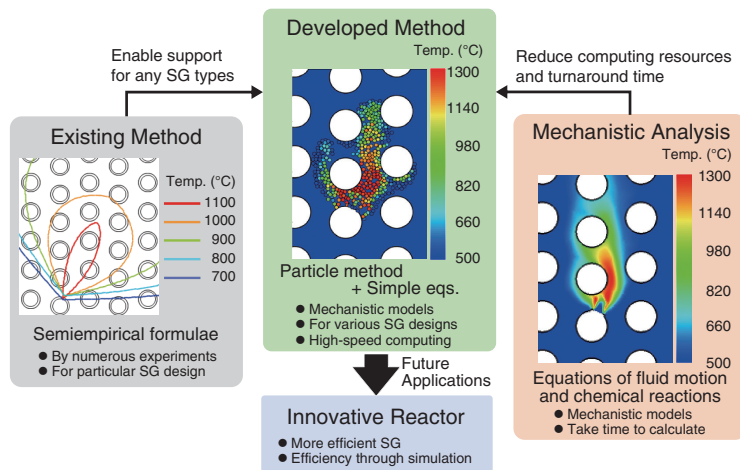


**Fig.7-3 Purpose of the developed method**

The developed method can handle a wider variety of heat-transfer tube (white circles in the figures) arrangements in steam generators (SGs). It can also reduce the calculation time required for numerical analysis. These features facilitate the exploration of various new SG designs in the development of innovative reactors.

The steam generator (SG) in a sodium-cooled fast reactor consists of many heat-transfer tubes through which water flows to produce steam for a power generation system. Figs.7-3 and 7-4 show a cross-section of an SG. When water leaks from a crack in a failed heat-transfer tube, it reacts chemically with the surrounding sodium and causes various types of damage to the SG. Therefore, evaluating the sodium–water reaction phenomena is important for the safety assessment of an SG.

As shown in Fig.7-3, the conventional method evaluates safety using some empirical formulae developed based on numerous experiments for a particular design. In recent years, numerical simulations, as well as experiments, were performed to drastically reduce the time required and cost for a new experiment. However, the sodium–water reaction phenomena are complex and involve fluid motion and chemical reactions. Hence, considerable time is required to numerically solve the exact equations of these phenomena.

For the development of innovative reactors, a variety of new SG designs has been explored and the need for a faster simulation method has been recognized. Hence, we adopted a particle method characterized by a simpler computational principle, faster calculation, and easier extension to three dimensions as compared to the conventional method.

However, it was necessary to reconsider the heat of the

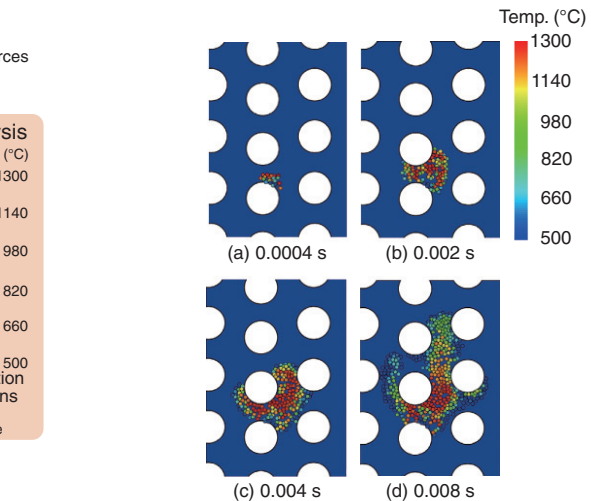


**Fig.7-4 Steam flow in an SG**

These figures show the flow and temperature distribution when steam leaks from a heat-transfer tube in the upper right direction.

sodium–water chemical reaction under the framework of the particle method. Our method treats the steam leaking from the tube as aggregation of particles. At each time step, the position, velocity, and heat by chemical reactions of individual particle are evaluated based on the equations for fluid motion and chemical reactions. Simplifying these equations could reduce the computational cost.

It is important to verify and validate the calculation results of the developed method. We compared the results obtained by the particle method with those by a mechanistic multiphase flow analysis code that has been validated previously. Fig.7-3 shows the temperature distribution generated by the sodium–water reaction. The developed method can obtain a temperature distribution comparable to that of the mechanistic code and reduce the calculation time to less than 1/10. As shown in Fig.7-4, the developed method can also simulate the time development of the sodium–water reaction phenomenon. For the safety assessment, we used the temperature distribution to evaluate the degradation of the tube wall and to predict the occurrence of tube failure.

The future work includes improvement of the applicability of this method and evaluation of multiple tube failure events for actual experiment situation.

(Wataru Kosaka)

### Reference

Kosaka, W. et al., Development of Reacting Jet Evaluation Model Based on Engineering Approaches with Particle Method for Improvement of LEAP-III Code, Proceedings of 19th International Topical Meeting on Nuclear Reactor Thermal Hydraulics (NURETH-19), Brussels (Online), Belgium, 2022, 11p.

## 7-2 Understanding Aerosol Behavior in Fast Reactor Accidents

### — Test on Aerosol Transport Behavior Using the MET Facility —

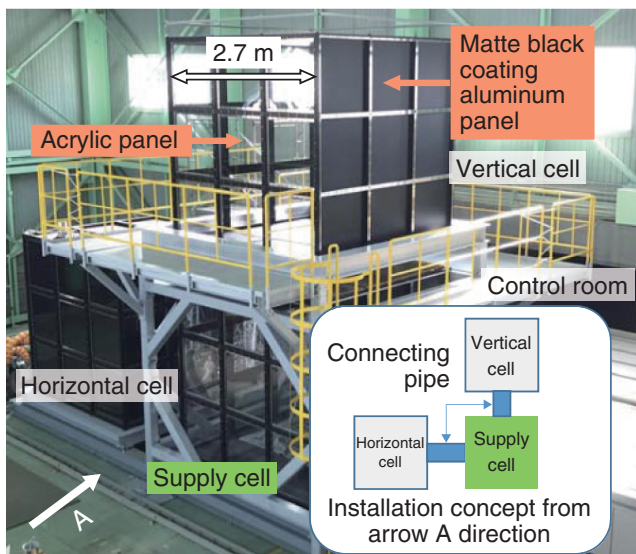


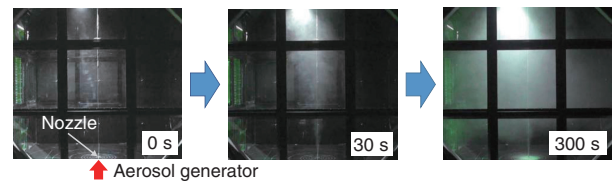
**Fig.7-5 Multiple cells with expandable connecting pipe test (MET) facility**

The simulated facility for the natural convection condition during a sodium fire event—the facility can help observe the aerosol transport behavior using silica particles to simulate sodium fire aerosol.

In fast reactors, sodium is used as a coolant with excellent coolability. However, sodium is chemically active and reacts with air, subsequently leading to combustion (i.e., sodium fire) in the event of sodium leakage. The transport of the aerosol (sodium oxide) generated by a sodium fire through the air duct between cells may have harmful effects on the human body and may damage and cause failure of the control devices. Previously, many experimental studies on sodium fires were conducted in single cell. Findings based on sodium fire experiments using multiple cells are quite limited.

Thus, multiple cells with expandable connecting pipe test (MET) facility (Fig.7-5) was developed to understand the basic aerosol behavior between cells. The MET facility comprises three cells and acrylic tubes of different shapes as the connecting pipes. The cells are designed as cubes with each side 2.7 m long based on the natural convection condition of sodium fires, and the walls of each cell are made of acrylic and with matte black coating aluminum panels to suppress the reflection of light for optical measurement with a camera and laser. Besides, each panel has easily removable structures for flexible cell arrangement and for setting the arbitrary equivalent cross-sectional area of the connecting pipe to understand the influence of these parameters. In this test, instead of performing an actual sodium fire experiment, fine silica particles were used to simulate the primary particle size and density of sodium fire aerosol. The particle was supplied from the bottom of the supply cell by an aerosol generator, which is capable of blowing the

(a) State of supply cell during supplying simulated aerosol



(b) State of transport behavior of simulated aerosol to adjacent cell

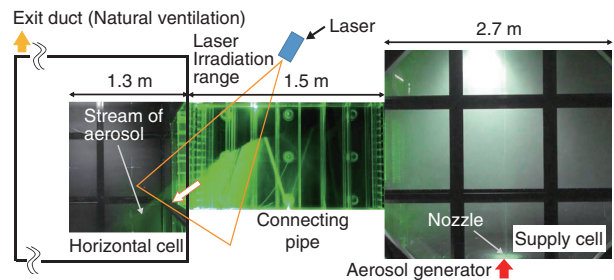


**Fig.7-6 Typical results of the visualization test for aerosol transport**

After aerosol is filled in the supply cell, it streams into the adjacent cell. The simulated aerosol is projected more clearly in the laser irradiation range.

particles upward by means of a brush and compressed air.

Fig.7-6 shows the results obtained using the horizontally arranged test apparatus. The aerosol transport behavior was observed by a camera, and clearer images of the connecting pipe were obtained by laser irradiation. In addition, this test was conducted under the basic conditions of opening the exhaust duct in the horizontal cell and equalizing the pressure in the system. Fig.7-6(a) shows the aerosol transport behavior in the supply cell. With time, the aerosol was transported upward and filled the top of the cell. With further time, the aerosol stream passed through the connecting pipe to the horizontal cell (Fig.7-6(b)). The same aerosol filling process was observed in the vertically arranged test apparatus. Moreover, the mass of the aerosol settled on the floor of each cell was measured after performing the test to support the obtained image, thereby enabling the planar distribution evaluation of aerosol sedimentation in each cell.

The above results show that the basic aerosol transport behavior to the adjacent cells was confirmed by using the MET facility. This result is expected to be helpful to elucidate the transport behavior of sodium fire aerosols for validating the evaluation method in the future.

This research is a part of the achievements of “Research and Development of Multi-Level and Multi-Scenario Plant Simulation Systems for Innovative Sodium-Cooled Fast Reactor” commissioned by MEXT.

(Ryota Umeda)

#### Reference

Umeda, R. et al., Experimental Study on Aerosol Transport Behavior in Multiple Cells with Expandable Connecting Pipe for Safety Assessment of Sodium-Cooled Fast Reactors, Proceedings of 28th International Conference on Nuclear Engineering (ICONE 28), Online Conference, 2021, ICONE28-61200, 9p.

## 7-3 Failure Prediction of Fast Reactor Components

### — Cyclic Loading Test and Failure Prediction of Multiperforated Plates —

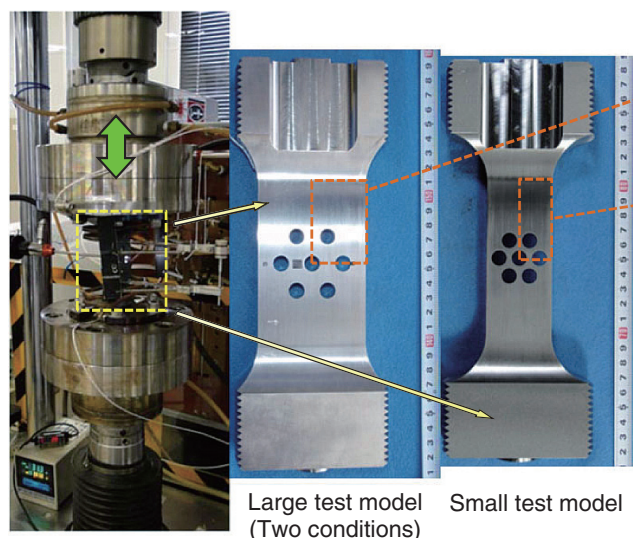


**Fig.7-7 Test situation of the multi-perforated plate**

The test models that simulate a part of the tube sheet structure of a heat exchanger were subjected to cyclic displacement loading at 550 °C to generate cracks, and the number of cycles until crack generation was experimentally determined. Two types of test models with different plate widths and hole distances were used.

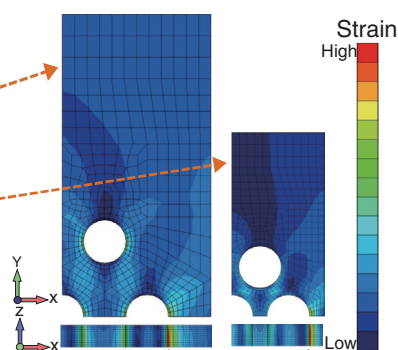


**Fig.7-8 Strain simulation by inelastic analysis**

Stress and strain were simulated by finite element analysis with 1/4 sector models. Larger strain was observed on the inner surface of the outermost hole (Red arrow).

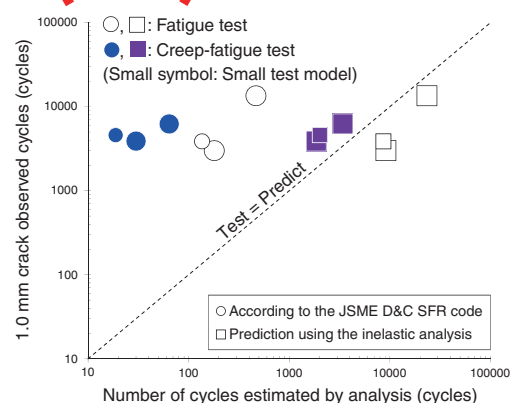


**Fig.7-9 Failure prediction**

The number of cycles (corresponding to the limit of creep-fatigue damage) as per the rule in the JSME D&C SFR code is much less than the test, i.e., the conservative, value.

Since the operating temperature, 550 °C, of sodium fast reactors (SFRs) is much higher than that of light water reactors (around 300 °C), and the temperature difference between the inlet and outlet of the reactor vessel is larger than that of light water reactors, the components of SFR are subjected to a cyclic thermal load due to thermal transitions during operation. Therefore, it is important to appropriately prevent failure due to cyclic thermal stress.

In the design of SFRs, the JSME (Japan Society of Mechanical Engineers) Code, Rules on Design and Construction for Nuclear Power Plants, Section II, SFR (the JSME D&C SFR code) is applied. To prevent failure by cyclic loads, the SFR code provides a rule regarding the creep-fatigue damage by considering the superimposition of creep and fatigue damage. Because of the difficulty in predicting the failure life by creep fatigue, the current rule is extremely conservative and should be improved.

In this study, cyclic loading tests with multiperforated plates were performed for confirming the conservativeness of the creep-fatigue damage limit rule in the JSME D&C SFR code and developing an evaluation method to predict the creep-fatigue life. We conducted fatigue and creep-fatigue tests, and finite element analysis simulating the tests were performed (Fig.7-7).

The elastic analysis used in conventional design and an inelastic analysis were performed. A material property setting guide had been constructed for the inelastic analysis. The inelastic analysis is not generally used in the design because of the difficulties in material parameter setting and calculation cost; however, it is expected to be applied to optimize the components design because it allows for more realistic simulations. The simulated result of the inelastic analysis indicated that the location where the maximum strain is generated corresponds to the crack initiation location (Fig.7-8).

According to the rule in the JSME D&C SFR code, the number of cycles corresponding to the limit of creep-fatigue damage was calculated from the elastic analysis result. The calculated result clarified that the limit has great conservativeness, though it includes the design margin. The predicted results of the inelastic analysis estimated the number of cycles corresponding to the crack initiation with good accuracy, and these results are expected to be a reference to improve the design procedure (Fig.7-9).

In the future, we plan to conduct various structural tests and their analytical evaluations to incorporate the inelastic analysis to the design rules.

(Masanori Ando)

#### Reference

Ando, M. et al., Assessment of Failure Life Evaluation Methods for Structural Discontinuities with Fatigue and Creep-Fatigue Tests on Multiperforated Plate Made of Mod.9Cr-1Mo Steel, Journal of Pressure Vessel Technology, vol.143, issue 6, 2021, 061505, 9p.

## 7-4 Capturing the Oxygen Diffusion Phenomena in Nuclear Fuel

### — Measurement and Evaluation of the Oxygen Self-Diffusion Coefficient of MOX Fuel —

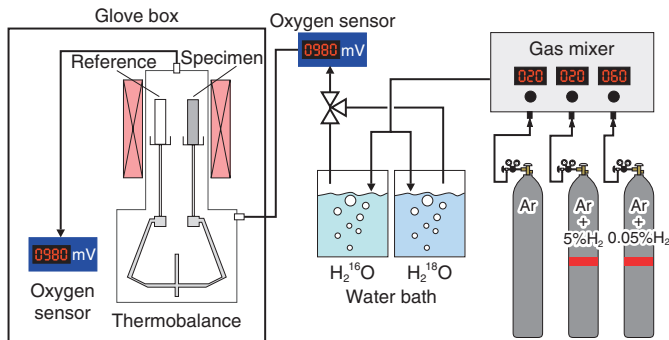


**Fig.7-10 Schematic diagram of experimental setup**

This apparatus consists of a system that controls the oxygen isotope concentration in the atmosphere and a thermobalance that measures slight weight changes of the specimen.

In mixed oxide (MOX) fuels used in fast reactors, the diffusion of uranium (U), plutonium (Pu), and oxygen (O), which are the constituent elements of the MOX fuels, is closely involved in important phenomena such as redox reactions, sintering, and element migration during irradiation. Hence, it is essential to measure and evaluate the diffusion coefficient. However, despite its importance, the experimental data of the oxygen diffusion coefficient of the MOX fuels are very limited because of the following measurement problems. The measurement procedure adopted in the tracer method, which is a general method used for measuring the diffusion coefficient, is complicated, and it is difficult to measure the coefficient directly during the diffusion process and to maintain the oxygen-to-metal ratio (O/M) of the MOX fuel.

We developed a new experimental method using oxygen-isotope water ( $\text{H}_2^{18}\text{O}$ ) with a high concentration of oxygen isotope ( $^{18}\text{O}$ ) for expanding the data of the oxygen diffusion coefficient of MOX fuel. Fig.7-10 shows a schematic diagram of the experimental setup. In this method, the oxygen self-diffusion coefficient is calculated by continuously measuring the slight change in weight when the  $^{16}\text{O}$  in the specimen is replaced by  $^{18}\text{O}$  derived from oxygen-isotope water using a thermobalance and by analyzing the rate of weight change. The amount of  $^{18}\text{O}$  in the atmosphere can be controlled by the  $\text{H}_2\text{--H}_2\text{O}$  equilibrium reaction, thereby enabling measurement while maintaining the O/M ratio. This method is simpler than the tracer method, and it enables obtaining the oxygen self-diffusion coefficient of MOX fuel with the stoichiometric composition.

#### Reference

Watanabe, M. et al., Oxygen Self-Diffusion in Near Stoichiometric (U,Pu) $\text{O}_2$  at High Temperatures of 1673–1873 K, *Journal of Nuclear Materials*, vol.542, 2020, 152472, 7p.

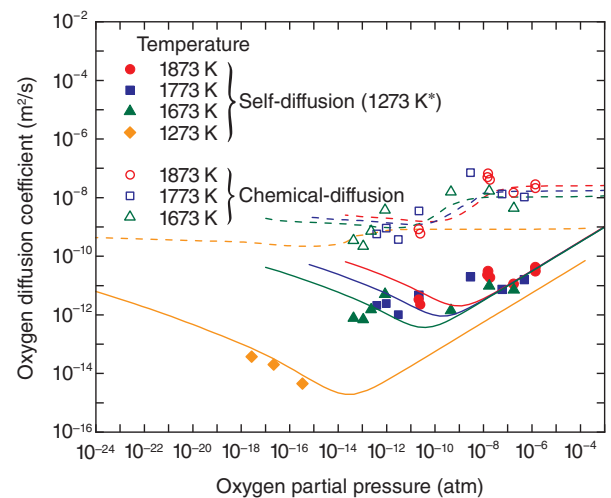


**Fig.7-11 Experimental and calculated oxygen diffusion coefficients**

Each symbol represents the experimental values of oxygen diffusion coefficients for  $(\text{U}_{0.7}\text{Pu}_{0.3})\text{O}_2$  and  $(\text{U}_{0.55}\text{Pu}_{0.45})\text{O}_2$ . The latter is the value for 1273 K as reported in literature.

The temperature dependence of the oxygen self-diffusion coefficient was clarified from the experimental data obtained by this method over a wide range of temperatures. The migration energy of oxygen defects was successfully determined. Furthermore, the relationship between the oxygen-defect concentration and the diffusion coefficient was evaluated by combining these data with thermodynamic data. Fig.7-11 shows the experimental and calculated oxygen diffusion coefficients. The chemical diffusion shown in this figure is defined as diffusion with a concentration distribution in the sample. The calculated oxygen diffusion coefficients are in good agreement with the experimental and literature data. The results also show good agreement of the calculated values with the data for different Pu contents.

The results obtained in this study make it possible to predict the time required for sintering and redox reactions of MOX fuel and the time variation of oxygen retribution during irradiation. Thus, these results will contribute to further developing fast reactor fuel technology—such as the optimization of the MOX fuel fabrication process and improvement of fuel irradiation behavior analysis codes.

(Masashi Watanabe)

\* Vauchy, R. et al., Oxygen Self-Diffusion in Polycrystalline Uranium-Plutonium Mixed Oxide  $\text{U}_{0.55}\text{Pu}_{0.45}\text{O}_2$ , *Journal of Nuclear Materials*, vol.467, part 2, 2015, p.886–893.

## 7-5 Development of Fast Reactor Fuel for Reduction of Radioactive Waste

### — Evaluation of Thermal Conductivity of High Am-Bearing Mixed Oxide Fuel on Stoichiometry —

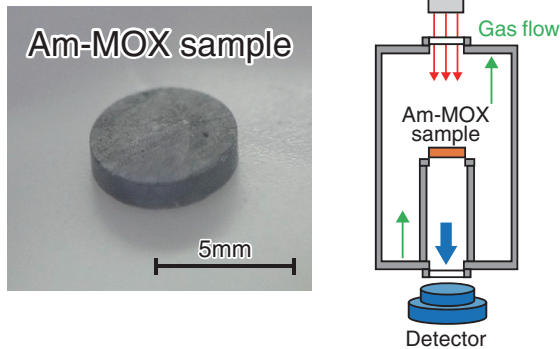


**Fig.7-12 Outline of measurement by the laser flash method**

An Am-MOX sample is indicated in the photo on the left panel. As shown in the image on the right, the sample surface is heated by laser pulses, and the change in the temperature on the back surface of the sample is measured with a detector.  $H_2$ -Ar mixed gas with moisture was fed through the specimen part, and the oxygen partial pressure was controlled.

Minor actinides (MAs) such as americium (Am) in the spent nuclear fuels have long-term radiotoxicity and generate decay heat. It is better to transmute MA into stable or less-radiotoxic nuclides in fast reactors. To reduce the amount of radioactive waste, MA-bearing uranium-plutonium mixed oxide (MOX) fuel has been developed. It is important to understand the effect of MA content on physical properties such as thermal conductivity for analyzing irradiation behavior. Thermal conductivity is an important property for determining the temperature of the fuel center, and this property is considered for preventing fuel melting. There are many reports on MA-MOX fuels with thermal conductivities within 3% Am, but there are no reports on fuels with more than 3% Am with a controlled oxygen-to-metal ratio (O/M).

In this study, three MOX pellets with 5%, 10%, and 15% Am contents were prepared. The thermal conductivity was measured using the laser flash method, depicted in Fig.7-12, in an atmosphere with controlled O/M ratio to the stoichiometric composition during testing. These measurements clarify the effect of Am content on MOX properties and enable more accurate evaluation of the irradiation behavior of Am-MOX. The temperature change of back surface of the sample is measured during testing. The thermal conductivities are calculated by the temperature change and sample characteristic such as density, heat capacity and thickness. In addition, to maintain the stoichiometric O/M ratio, the oxygen partial pressure in the atmosphere was controlled by

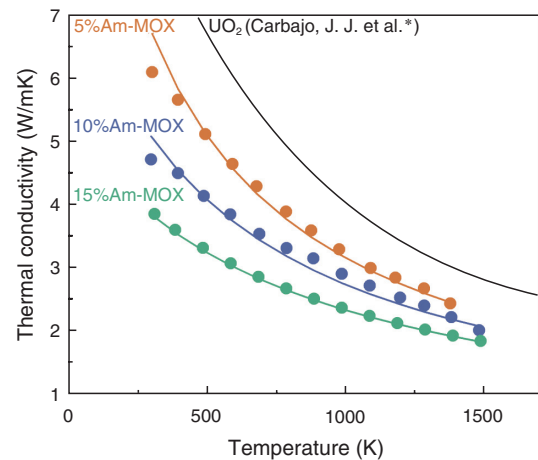


**Fig.7-13 Thermal conductivity measurement results of Am-MOX and effect of Am content**

Thermal conductivities of 5%, 10%, and 15% Am-MOX was measured by the laser flash method. Evaluation was performed from the measurement results in the stoichiometric region, and an equation was derived to calculate the effect of Am content on the thermal conductivity of MOX fuel.

using  $H_2$ -Ar mixed gas with moisture. Then, the equation for calculating the thermal conductivity of stoichiometric Am-MOX based on the phonon transport model as a function of Am content was proposed based on the experimental results.

The thermal conductivity results are shown in Fig.7-13. The thermal conductivity of Am-MOX decreased with increasing Am content. The effect of the addition of Am on thermal conductivity was remarkable at low temperatures, and this effect diminished with increasing temperature. Moreover, the calculated and measured thermal conductivities of Am-MOX are in good agreement. Thus, the equations offer a way of evaluating the temperature of fuel center accurately, thereby contributing to the development of MOX fuel design.

As a future plan, we will perform a more comprehensive evaluation and devise the formulation of the physical properties Am-MOX by measuring the thermal conductivity of nonstoichiometric composition for Am-MOX.

This study is a part of the results conducted on “Demonstration research on fast reactor recycling using low decontaminated MA-bearing MOX fuels”, supported by MEXT.

(Keisuke Yokoyama)

\* Carbajo, J. J. et al., A Review of the Thermophysical Properties of MOX and  $UO_2$  Fuels, *Journal of Nuclear Materials*, vol.299, issue 3, 2001, p.181-198.

#### Reference

Yokoyama, K. et al., Measurements of Thermal Conductivity for Near Stoichiometric  $(U_{0.7-z}Pu_{0.3}Am_z)O_2$  ( $z = 0.05, 0.10, \text{ and } 0.15$ ), *Nuclear Materials and Energy*, vol.31, 2022, 101156, 7p.

# 7-6 Evaluation of Experiments in the Prototype Fast Reactor Monju — Solving Discrepancy Between Measurement and Calculation —

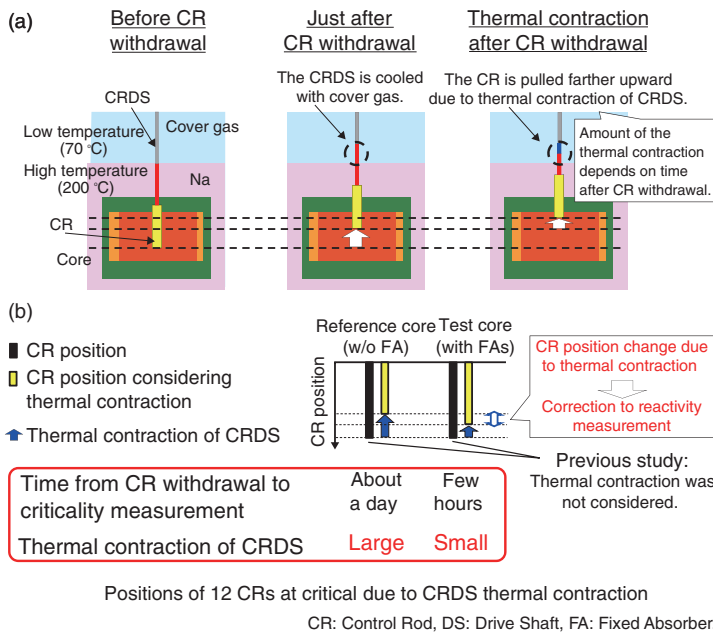


**Fig.7-14 (a) Mechanism of CRDS thermal contraction and (b) its impact on reactivity measurement**

The correction of the influence on the reactivity measurement due to the CRDS thermal contraction was considered.

The JAEA has been intensively evaluating core physics experiments conducted in the Prototype Fast Reactor Monju to utilize them for validating the neutronics calculation methodology for fast reactor designs.

Sometimes, an unexplainable discrepancy is found between the experiment and calculation results. For instance, a discrepancy was observed in the reactivity measurement of fixed absorbers (FAs), a subassembly to control reactivity like control rods (CRs) but used in the reactor start-up. In two series of experiments conducted by loading a single FA (Case1) and three FAs (Case2), a discrepancy between the experiment and calculation results beyond the total uncertainty of both was only observed in Case1.

The FA reactivity was measured from the difference between the critical CR positions of the cores before and after loading FAs (the reference and test cores). An examination of the data collection and evaluation processes indicated that changes in the CR positions due to thermal contraction of CR drive shaft (DS) were responsible for the unexplainable discrepancy. After a CR is withdrawn, it is pulled farther upward without operating the CR because a portion of a CRDS of the withdrawn CR gradually contracts due to a fall in temperature caused by movement from sodium coolant at 200 °C toward cover gas above the sodium at around 70 °C as indicated in Fig.7-14. The change in CR position is slight (smaller than 1 mm), but the change is observed in 13 CRs in the core and depends on time after CR withdrawal.

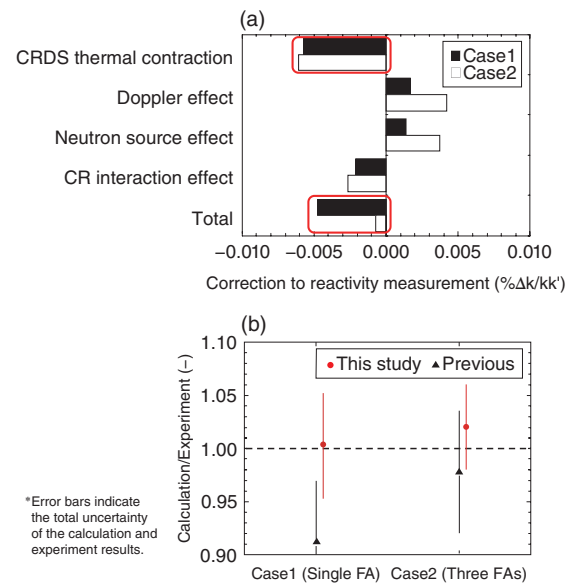


**Fig.7-15 (a) Corrections to reactivity measurements and (b) comparison of calculations and experiments**

The results of calculations and experiments in both cases agreed within their uncertainty by adopting detailed corrections including the CRDS thermal contraction.

In Case1, the FA reactivity was measured by using the CR at the core center (C1) while keeping the other 12 CRs unchanged between the reference and test cores. A detailed examination revealed that the operational histories of the 12 CRs differed depending on the cores. The critical CR position was measured approximately one day after withdrawing the CRs to the critical CR positions in the reference core, while the measurement was performed after only few hours in the test core. The resulting difference in the CRDS thermal contraction causes a clear influence on the reactivity. By correcting the reactivity attributed to the changes in the CR position in both cores, the discrepancy between the calculation and experiment results disappeared successfully, as shown in Fig.7-15. For Case2, there is no large difference between the previous study and this study since the correction factors, including the CRDS thermal contraction effect, were canceled out.

The present study successfully eliminated the discrepancy between the calculation and experiment, and the experimental data became acceptable as validation data. The finding in this study was also applied to evaluation of other experiments, such as a fuel reactivity worth measurement, to enhance their reliability. The JAEA continues to reevaluate other experiments to develop a high-quality validation database for fast reactor neutronics designs.

(Kazuya Ohgama)

**Reference**

Ohgama, K. et al., Evaluation of Fixed Absorber Reactivity Measurement in the Prototype Fast Reactor Monju, Nuclear Technology, vol.207, issue 12, 2021, p.1810–1820.

## 7-7 Toward Realization of Advanced MOX Fuels

### — Measurement of Slight Variations in the Oxygen Content of Fuels —

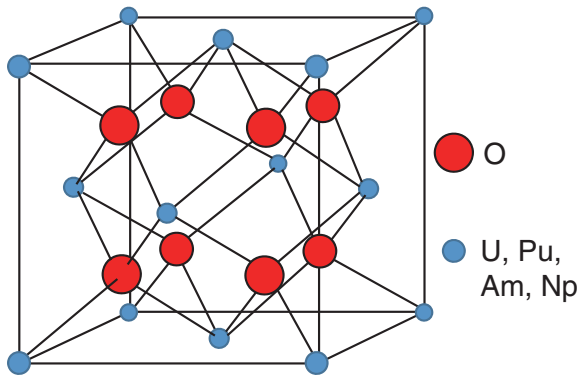


**Fig.7-16 Schematic diagram of the crystal structure of MOX**

O can be trapped in or exhausted from the crystals of MOX fuels depending on temperature and surrounding oxygen partial pressure. This results in continuous variations of the ratio of O atoms to metal (U, Pu, Am, and Np) atoms to values such as 1.999 and 1.998.

Spent fuels contain minor actinide (MA) elements such as americium (Am) and neptunium (Np) with long half-lives and strong radioactivity. Because these elements can be transmuted to other elements with shorter half-lives and weaker radioactivity by fast reactors, MOX fuels containing MA have been developed for these reactors. MOX fuels have the unique property that the ratio of the number of oxygen atoms (O) to that of metal atoms (U, Pu, Am and Np), called the O/M ratio, can vary continuously. Fig.7-16 shows a schematic diagram of the crystal structure of MOX fuels. The O/M ratio in the crystal continuously varies with exhaustion (reduction) or trapping (oxidation) of O in the crystal depending on the oxygen partial pressure of the atmosphere and atmospheric temperature. It is known that the MOX properties related to fuel design, such as thermal conductivity, are very sensitive to even slight variations in the O/M ratio. Hence, the accurate estimation of the O/M ratio is important.

Our research group used an oxygen sensor and a thermogravimeter to measure slight variations in the mass in Am-bearing MOX and Am/Np-bearing MOX during reduction or oxidation accompanied by changes in temperature or oxygen

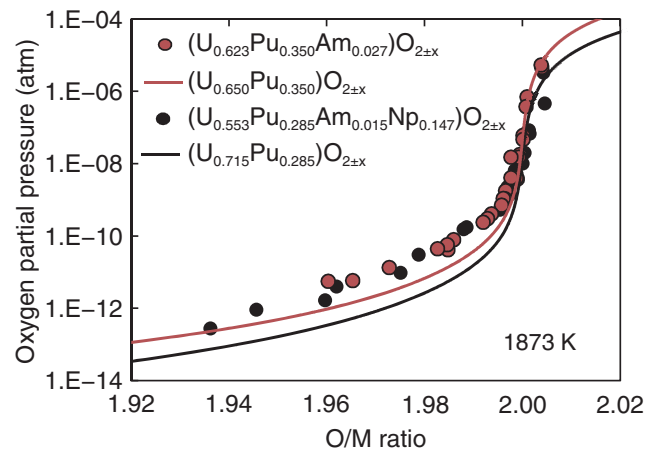


**Fig.7-17 Relation between O/M ratio in MOX and the surrounding O<sub>2</sub> partial pressure (1873 K)**

The O/M ratio in Am/Np-bearing MOX is lower than the MA-free MOX under a given condition (temperature, oxygen partial pressure, and Pu content). In particular, compared to Np addition, Am addition has a larger reducing effect on the O/M ratio.

partial pressure. Then, the data were converted to the O/M ratio equilibrated to the temperature and oxygen partial pressure.

Fig.7-17 shows the relation between the O/M ratio on the horizontal axis and the oxygen partial pressure on the vertical axis. Under a given condition of temperature and oxygen partial pressure, the O/M ratio was lower in MA-bearing MOX than in MA-free MOX. This result can possibly be attributed to the easy reduction of Am oxide.

Although studies were conducted on the O/M ratio in MOX fuels, limited data on MA-bearing MOX are available. The data obtained in this work were compared with those in the available literature and a relation for evaluating the O/M ratio from Am and Np contents, temperature, and oxygen partial pressure was modeled; to the best of our knowledge, this is first time that such a quantitative analysis has been conducted.

Hereafter, we will study the properties of MOX fuels and simulate their behaviors during irradiation in a reactor by considering the O/M ratio calculated by the model.

(Shun Hirooka)

#### Reference

Hirooka, S. et al., Oxygen Potential Measurement of (U,Pu,Am)O<sub>2±x</sub> and (U,Pu,Am,Np)O<sub>2±x</sub>, Journal of Nuclear Materials, vol.542, 2020, 152424, 9p.

## Toward Decommissioning Nuclear Facilities and Managing Radioactive Waste

To maintain and develop its research and development (R&D) capabilities by strengthening the safety of its nuclear facilities and to ensure the steady implementation of back-end measures, the JAEA issues the “Medium- and Long-Term Management Plan of our Facilities” (issued on April 1, 2017, amended on April 1, 2022) as a comprehensive plan detailing the following three points:

- the selection and consolidation of facilities,
- safety measures, and
- the management of back-end issues.

In the plan, 89 nuclear facilities were chosen for decommissioning.

Among the large facilities, the JAEA applied for permission to proceed with the decommissioning of MONJU and the Tokai Reprocessing Plant (TRP) to the Nuclear Regulation Authority (NRA). The NRA granted permission for the decommissioning of MONJU on March 28, 2018, and for the decommissioning of TRP on June 13, 2018. The application to the NRA for permission of the decommissioning of the Uranium Enrichment Demonstration Plant is under process.

The implementation of back-end measures requires long-term prospects and policies, including those regarding the processing and disposal of radioactive waste; the decommissioning of TRP is expected to take approximately 70 years to complete. The JAEA, therefore, published a long-term prospect and policy for back-end measures, the “Back-end Roadmap”, on December 26, 2018.

To ensure the safe and appropriate nuclear facility decommissioning and radioactive waste management, it is

necessary to introduce new technologies and knowledge and to promote the development of technologies for advanced safety and cost reduction. Technologies for the safe and effective dismantling of nuclear facilities, minimization and stabilization of radioactive wastes, and disposal of radioactive wastes are under development (Fig.8-1). The proposed disposal project applies to low-level radioactive wastes from research facilities of universities, private organizations, and the JAEA facilities.

The TRP was approved for the decommissioning plan on June 13, 2018, and it has entered the decommissioning stage. In the TRP, as an effort to reduce the risk of facilities, the vitrification of the high-level liquid waste is being promoted with the primary focus on safety. The JAEA produced 13 vitrified bodies in FY2021 and also developed advanced vitrification techniques.

This chapter discusses the technical development results in the relevant fields: Research that contributes to the design study of trench disposal facilities for radioactive waste containing uranium (Topic 8-1), development of a stabilization treatment method for nuclear fuel material containing organic compounds (Topic 8-2), characterization of lead stabilized with alkali-activated material for developing a stable solidification technology for radioactive waste containing environmentally hazardous substances (Topic 8-3), and the development of a surface contamination removal technology using laser cleaning technology (Topic 8-4). It also introduces the decommissioning of a facility with a history of contamination due to a fire disaster in the controlled area (Topic 8-5) and the dismantling of a tank containing liquid with  $\alpha$  nuclides (Topic 8-6) as efforts for decommissioning nuclear facilities.

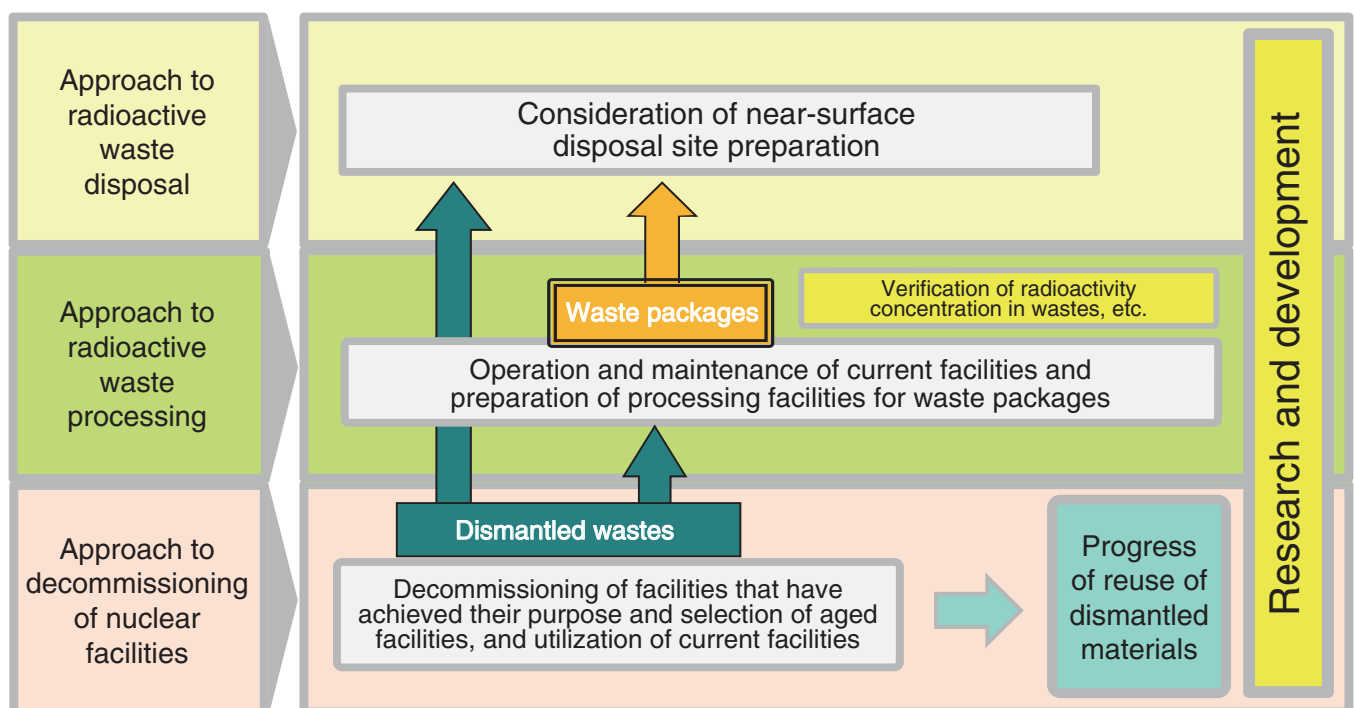


**Fig.8-1 Outline of low-level radioactive waste management**

R&D of the decommissioning of nuclear facilities and processing of radioactive wastes, including waste treatment and waste characterization, has been promoted.

## R&D to Improve the Reliability of Geological Disposal Technologies in Japan

Geological disposal is internationally recognized as the most practical method currently available for the long-term isolation of HLW, which is produced during the generation of nuclear power, from human environments. This critical issue must be approached sensibly by the present generation, and it will remain crucial regardless of any revision of the national nuclear energy policy.

In Japan, the spent fuel discharged from a nuclear reactor is reprocessed to extract reusable uranium and plutonium for power generation. The liquids separated from the spent fuel during chemical reprocessing are consolidated into a stable glass form. In accordance with the Japanese disposal policy, the vitrified waste is then encapsulated in a thick steel overpack, surrounded by highly compacted bentonite, and emplaced in a stable geological environment at a depth greater than 300 m below the surface (Fig.8-2).

R&D in relevant fields such as geoscience, repository engineering, and safety assessments of the disposal system are ongoing, as summarized in Fig.8-3, and these efforts are vital for improving their sound technical basis and get reflected in the implementation and regulatory activities.

The Horonobe Underground Research Center for sedimentary rock conducts R&D, including study on near-field system performance in geological environments (Topics 8-7 and 8-8).

At the Tono Geoscience Center, the Toki Research Institute of Isotope Geology and Geochronology is engaged in a study on the long-term stability of the geological environment (Topic 8-9), while at the Mizunami Underground Research Laboratory, the underground facilities were backfilled and

surface facilities removed by January 16, 2022.

To expand further the knowledge on geological disposal, extensive studies are being conducted to assess the behavior of the engineered barrier system and the key processes constraining the release and migration of radionuclides (Topics 8-10 and 8-11). These studies use the data on long-term stability of geological environments and the data on geological environments obtained through geoscientific research at underground research laboratories.

Results of the R&D activities during Third Medium-/Long-Term Objectives period (FY2015–FY2021) have been summarized as a next-generation web-based report (CoolRep), which has been made available on the public website of the JAEA:

CoolRep: <https://kms1.jaea.go.jp/CoolRep/index.html> (Japanese site).

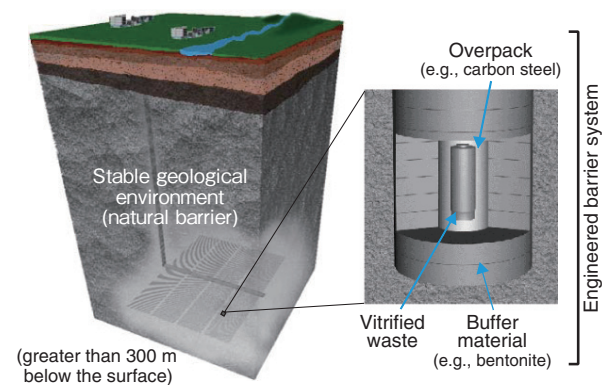


**Fig.8-2 Schematic view of the basic concept of the geological disposal of high-level waste**

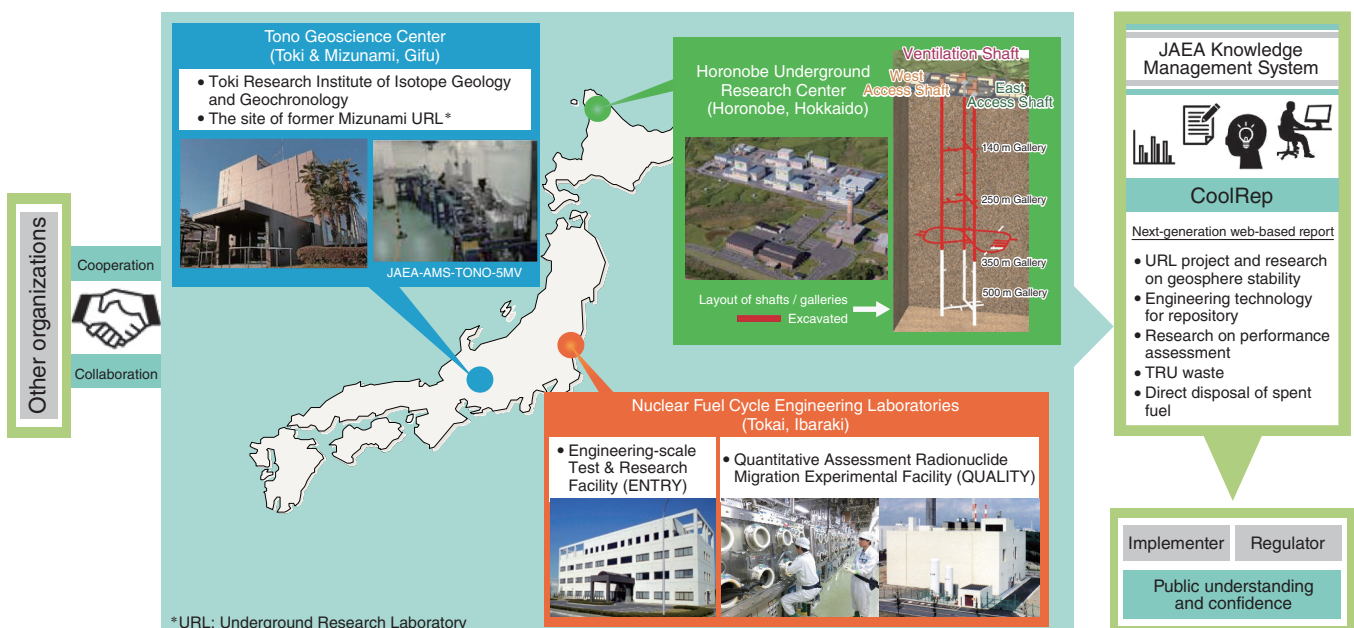


**Fig.8-3 Structure of the JAEA R&D activities**

## 8-1 Toward the Design of the Disposal Facilities Considering the Environmental Standards

### — Change in Uranium Concentration in Groundwater Depending on the Facility Layout and Structure —

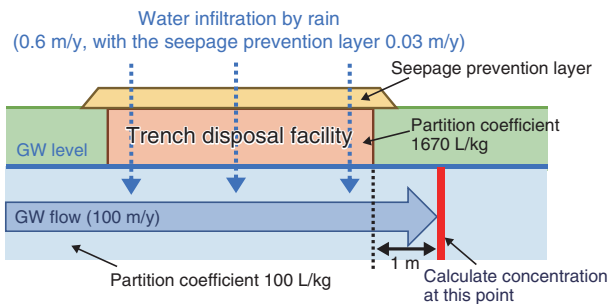


**Fig.8-4 Image of uranium leaching from the trench disposal facility**

The rate of water seepage into the facility is 0.6 m/y. If there is a seepage prevention layer, the rate water seepage is 0.03 m/y. The groundwater flow was set to 100 m/y. The distribution coefficient ( $K_d$ ) values of uranium (U) in the facility and in the aquifer were 1670 and 100 L/kg, respectively.

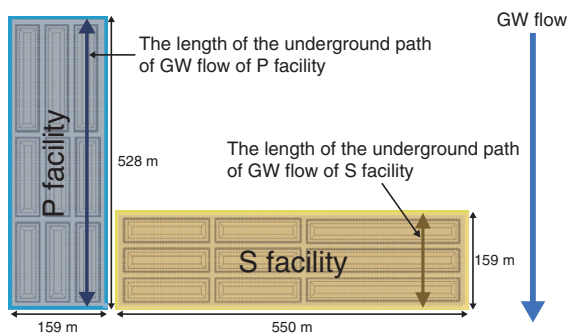


**Fig.8-5 Layout of the trench disposal facilities and direction of groundwater flow**

In the conceptual design, two trench facilities are installed as P and S facilities.

The Radioactive Waste Disposal Center has planned the design of disposal facilities for radioactive wastes generated from research facilities, etc. Uranium (U), which is one of the major radionuclides contained in radioactive waste disposed of in our disposal facility, has the characteristics of chemical toxicity as a heavy metal. Therefore, we evaluated whether the weight concentration of U in the groundwater (GW) originating from the disposal facility conformed to the Japanese environmental standard to enhance the safety of the disposal facility.

The trench facilities are divided into two sections (P and S facilities) in the conceptual design of the disposal project. In this evaluation, U migrates from the trench facility into the GW because of the permeation of rainwater into the facility (Fig.8-4). The two facilities are perpendicularly located. Therefore, the lengths of the underground paths of GW flow are different for both facilities (Fig.8-5). U concentration in the GW at the point 1 m from the edge of the facility was evaluated by using the analysis code GSA-GCL2. The total disposal weight of U

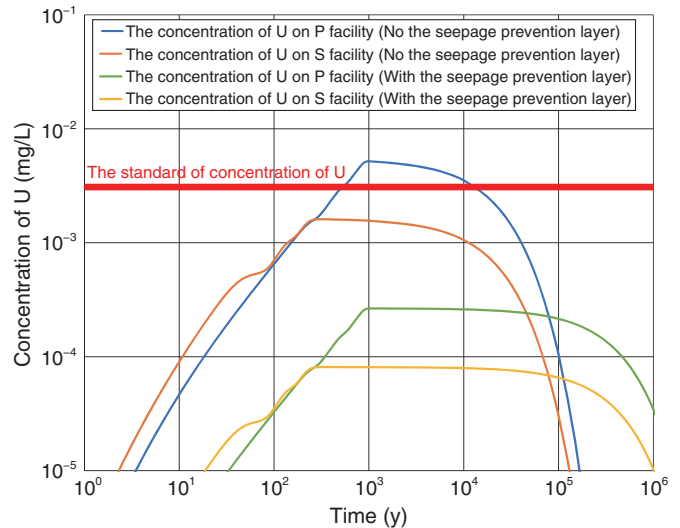


**Fig.8-6 Change in the concentration of U in groundwater leached from P and S facilities**

This graph shows the change in the concentration of U in the aquifer at a point 1 m from the facility.

was calculated from the average concentration specified by the regulations, and the parameters were the same as those used in the dose assessment at the conceptual design.

The evaluation result showed that the U concentration in the GW originating from the S facility is less than half that in the GW from the P facility (Fig.8-6). In addition, in case of the trench facility equipped with the seepage prevention layer shown in Fig.8-4, it is seen that the maximum U concentration in the GW decreased to less than 1/10th. The U concentrations in the GW from both facilities were less than 0.002 mg/L—the Japanese environmental standard.

Thus, we realize the prospect of designing the trench facility so that the U concentration in GW meets the standard. However, due attention should be paid to the degradation of the artificial equipment because the duration of leakage of U is possible in the long term. This result will be important knowledge for the basic design of the trench facilities in the future.

(Rina Ogawa)

#### Reference

Ogawa, R. et al., Preliminary Evaluation of Environmental Uranium Concentration Originated from Trench Disposal Facilities, JAEA-Technology 2022-008, 2022, 46p. (in Japanese).

## 8-2 Establishment of a Treatment Method for Nuclear Fuel Material for Safe Storage

### — Stabilization Treatment of Nuclear Fuel Material Containing Organic Compounds —

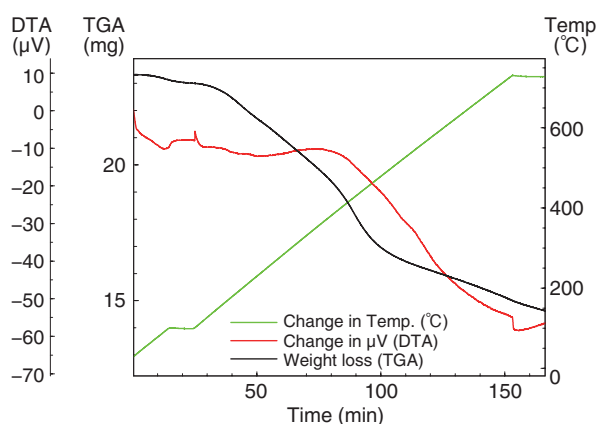


**Fig.8-7 Results of the differential thermal analysis (DTA) for nuclear fuel material containing organic compounds**

The temperature increases up to 750 °C at a rate of 5 °C/min in pure Ar atmosphere (O<sub>2</sub> concentration: 2000 ppm or less). The exothermic peak indicating abnormal heating is not observed until 750 °C.



**Fig.8-8 Change in the appearance of nuclear fuel material containing organic compounds subjected to heat treatment: (a) before heat treatment, (b) after heat treatment (200 °C), and (c) after heat treatment (700 °C)**

The appearance of the nuclear fuel material changes from light brown to light green during heat treatment. After heat treatment, the volume decreases significantly as shown figure and the weight decreases by 70% from 104.34 g.

The Nuclear Fuel Cycle Engineering Laboratories are progressing the decommissioning of nuclear facilities in a planned manner. Facility B is one of the facilities being decommissioned because it was constructed around more than 60 years ago. Therefore, the nuclear fuel materials are being transported to another facility for the decommissioning. The Chemical Processing Facility received the nuclear fuel material containing organic compounds that was stored in Facility B. However, the packing bag for the nuclear fuel material containing organic compounds swelled during storage. This swelling is attributed to any gases generated by the radiolysis of some components of the nuclear fuel material.

To prevent swelling of the packing bag because of the generation of gases, we studied the stabilization treatment of the nuclear fuel material without gas generation.

The properties of nuclear fuel material were investigated by gamma-ray spectrometry, inductively coupled plasma-atomic emission spectrometry, and mass spectrometry. These analyses indicated that the nuclear fuel material contained alpha radioactive nuclei, which were responsible for generating gases. We also found that a large amount of nitric acid solution was required when this nuclear fuel material dissolved. If this material is denitrated and converted after separating the radionuclides by solvent extraction as done in the common nuclear-fuel-reprocessing method, a large amount of nitric acid solution (50 L) and organic solvent (20 L) are required for this material (104.34 g). This method is not preferable as it produces a large amount of liquid and solvent wastes. Therefore, we explored

heat treatment instead of solvent extraction. We conducted thermogravimetric and differential thermal analysis (TG-DTA) to confirm the safety of heat treatment. No exothermic peaks were observed under 750 °C, as shown in Fig.8-7. Furthermore, a comparison of the DTA curves of the actual and simulated samples showed that the organic compounds in this nuclear fuel material were the ionic exchange resin. It is known that this resin completely decomposes under 750 °C and that heat treatment is one of the effective methods for disposing this fuel material.

Based on the above results, we conducted heat treatment for total amount of the nuclear fuel material. The temperature for heat treatment was gradually raised in steps: 200 °C (1 h)→400 °C (1 h)→700 °C (20 min). After heat treatment, the volume decreased drastically as shown as Fig.8-8, and the weight also decreased greatly from 104.34 g to 34.22 g. From these results, we can judge that these organic compounds were completely decomposed.

This nuclear fuel material was sealed in a packing bag and stored in a storage facility on October 19, 2020. We confirmed that no gas was generated via radiolysis from this nuclear fuel material by conducting monthly inspections to check the packing bag for any swelling May17, 2022.

In conclusion, this result is useful for the treatment of unknown nuclear fuel materials in various decommissioning nuclear facility, as a method to stabilize the nuclear fuel materials containing organic compounds to store them safely for a long time.

(Kohei Tada)

#### Reference

Senzaki, T., Tada, K. et al., Stabilization Treatment of Nuclear Fuel Material Contained with Organic Matter, JAEA-Testing 2022-001, 2022, 28p. (in Japanese).

## 8-3 Toward Stabilization of Hazardous and Radio-Active Wastes — Characterization of Lead Stabilized with Alkali-Activated Material —

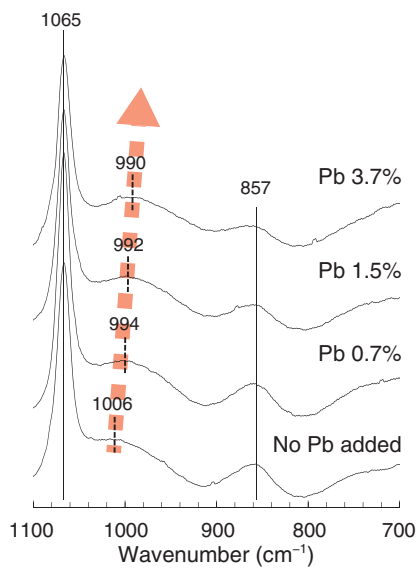


**Fig.8-9 Shifts of silica–oxygen bonding in the aluminosilicate structure**

The Raman spectra show that the silica–oxygen chemical bonding (peaks around 1000 cm<sup>-1</sup>) shifts depending on the increase in lead concentration, and lead is stabilized in the aluminosilicate structure.

Lead is widely used as a radiation-shielding material in nuclear facilities. However, it is designated as a hazardous substance in industrial wastes, and there are regulations on the amount of leachate from wastes. Although there are no regulations on the hazardous substances contained in radioactive wastes yet, the development of technology to stabilize hazardous and radioactive wastes is required to reduce the environmental impact of disposal.

The JAEA has been conducting research and development on stabilization/solidification of hazardous substances into waste forms to dispose hazardous and radioactive wastes safely. Alkali-activated materials (AAMs) are amorphous inorganic materials consisting of silica and aluminum, and they harden via a mechanism different from cementation. In addition, it was reported that AAMs can stabilize cations into a matrix. This work investigated the characterization of lead stabilized in AAMs and the applicability of AAMs as a solidification material for hazardous and radioactive wastes. The results indicated that lead is stabilized as a part of the amorphous structure of AAMs.

AAMs were prepared by using chemical reagents, and lead chloride was added with lead ratios of 0.7, 1.5, and 3.7 mass% in solidified samples. Fig.8-9 shows that in the Raman spectra

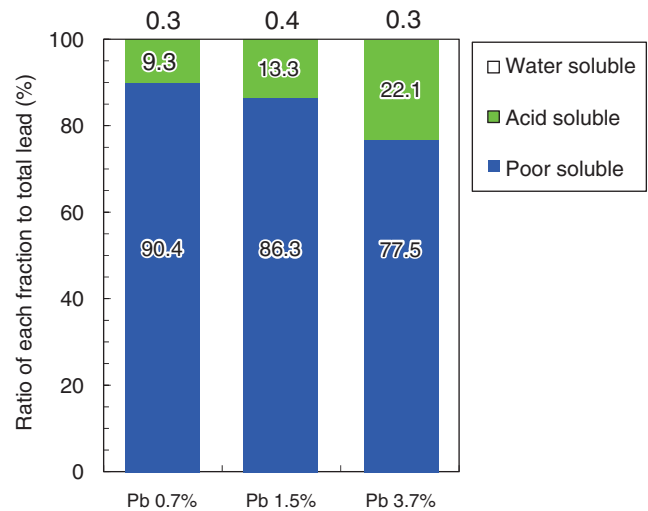


**Fig.8-10 Leachability of lead solidified in alkali-activated materials (AAMs)**

More than 75% of lead was extracted in a poor-soluble fraction. It was found that lead in AAMs is difficult to dissolve.

of solidified samples, the chemical bonding of silica to oxygen shifts depending on the lead concentration. Furthermore, the results of X-ray diffraction analysis and thermogravimetric analysis showed that lead was stabilized in an aluminosilicate matrix of the AAMs. Fig.8-10 shows that more than 75 mass% of lead in the solidified samples existed in a poorly soluble fraction in the leaching test with gradually changing strength of the acid in the solution. Lead was leached to less than 1% in a water-soluble fraction, and the remaining lead was extracted in an acid-soluble fraction. Thus, lead was stabilized as a part of an amorphous structure and existed in a poorly soluble form. These results indicate the possibility of developing a solidification/stabilization technique with the good confinement of hazardous substances.

Based on the results, the AAMs were evaluated for their applicability as a stabilization/solidification material, and the conditioning technology for hazardous and radioactive wastes has also been developed.

This work was conducted jointly with the Kyoto University under the title “Research on treatment of hazardous and radioactive wastes and changes in waste forms.”

(Junya Sato)

### Reference

Sato, J. et al., Stabilization of Lead with Amorphous Solids Synthesized from Aluminosilicate Gel, *Journal of Hazardous Materials*, vol.385, 2020, 121109, 9p.

## 8-4 Coating Removal Technique for Painted Steel Surface — Performance Evaluation of Laser Cleaning —

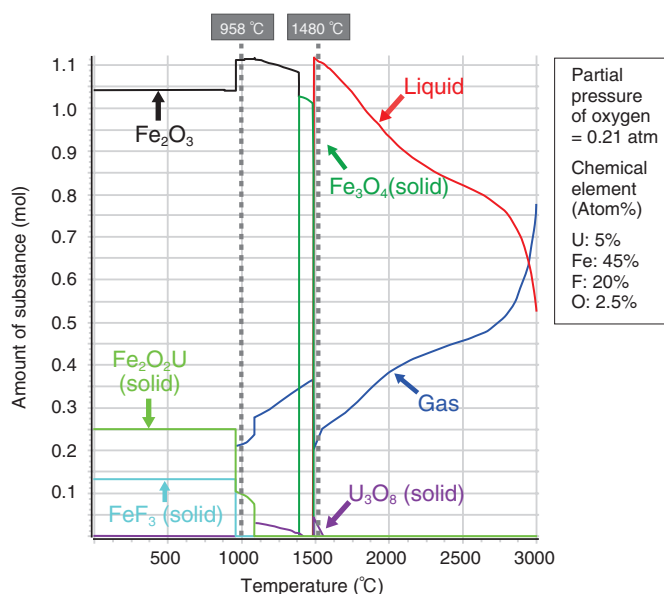


**Fig.8-11 Thermodynamically analyzed phase stability of iron and uranium compounds in the atmosphere**  
Uranium (U) vaporized at approximately 958 °C and iron (Fe) partially liquefied at approximately 1480 °C.

The dismantling of the Ningyo-toge Environmental Engineering Center generates approximately 130,000 tons of waste which contains approximately 80% nonradioactive wastes (NRs). Though some steels painted with a coating film can be disposed as NRs, there is the possibility that their painted surface are potentially contaminated. Rotary surface grinding has been conventionally used to remove such steel surface painted with a coating film, but it requires protective equipment and clothing to prevent dispersing and inhaling airborne dusts.

Laser cleaning is a promising surface removal technique, because it is an on-site surface removal technique, which allows the indirect operation keeping a safe distance from its object. Consequently, protective equipment and clothing can be less necessary, workload can be lightened in the controlled area, and secondary wastes can be reduced. However, reports of uranium and iron compounds behaviors at high temperatures under laser irradiation are limited, and it is indispensable to develop a technique to recover airborne dusts removed from the surface through laser cleaning.

In this work, we studied phase stability of uranium and iron compounds, separation behavior of powder-like uranium compounds, and scattered direction of removed airborne dusts under laser irradiation for the performance evaluation of laser cleaning applied to the uranium-contaminated steel surface painted with a coating film.

First, we thermodynamically focused the phase stability of uranium and iron compounds at high temperatures. This is because uranium compounds on the coating film could be

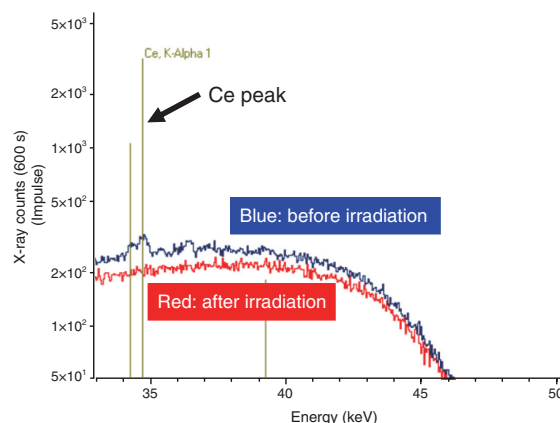


**Fig.8-12 X-ray fluorescence spectra of cerium oxide applied to the painted steel surface before (blue) and after (red) irradiations**  
After irradiation (red), cerium (Ce) peaks disappeared.

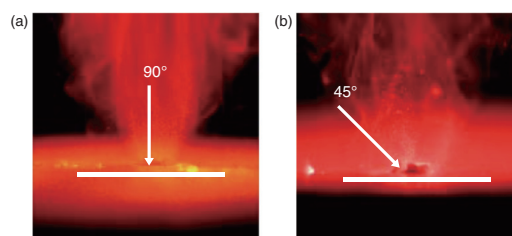


**Fig.8-13 Airborne dust behavior under different irradiation angles**

dissolved into the base metal through the heating under laser irradiation. As shown in Fig.8-11, uranium forms gas phase before iron forms liquid phase with increasing temperature. Thus, uranium can be hardly dissolved into the base metal, and uranium can be theoretically separated applying laser cleaning.

Second, we focused separation behaviors of powder-like uranium compounds on the coating film. In this work, a simulant specimen was prepared putting cerium oxide powders on the painted steel, because it was not appropriate to perform hot tests using actually uranium-contaminated specimens in this early stage of research. Shows similar behaviors to uranium oxide, since it has the same crystal structure (fluorite type structure). As shown in Fig.8-12, cerium peaks disappeared after laser irradiation, and iron and chromium peaks appeared. This result indicates that the laser cleaning performed in this work can remove both the cerium oxide powders and the coating film on the steel surface.

Finally, we focused the scattered direction of removed airborne dusts through the high-speed camera observation. As shown in Fig.8-13, most removed airborne dusts like fume scattered perpendicular to the specimen surface, and the direction was independent of the laser irradiation angle. Thus, the airborne dusts could be efficiently recovered from the vertical direction to the surface.

From these results, laser cleaning can be possibly applied to removing the uranium-contaminated coating film painted on steel. In future work, we conduct some decontamination tests using actually uranium-contaminated specimens.

(Ikumi Yamane)

### Reference

Ikumi, Y. et al., Separation/Removal of Steel Surface Coating Film by Laser Cleaning, JAEA-Technology 2021-038, 2022, 18p. (in Japanese).

## 8-5 Decommissioning of a Facility with a History of Contamination Caused by a Fire Disaster in a Controlled Area — Collective Dismantling of the Uranium Enrichment Laboratory Using a Large Isolation Tent —

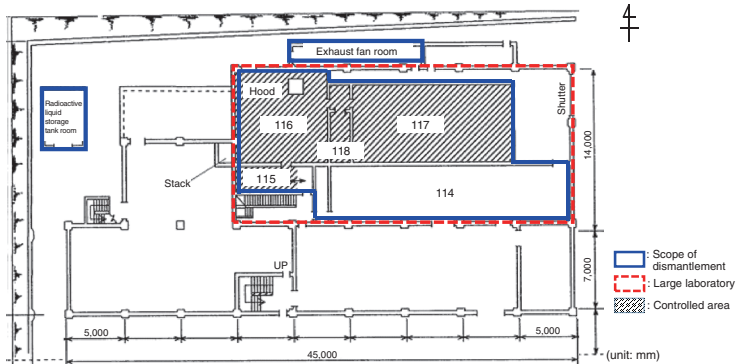


**Fig.8-14 Floor plan of the first floor of the Uranium Enrichment Laboratory**  
At the time of the decommissioning, in the Uranium Enrichment Laboratory, a part of a steel-framed room was installed in the large laboratory as a controlled area. In addition, this controlled area was equipped with exhaust and drainage facilities.

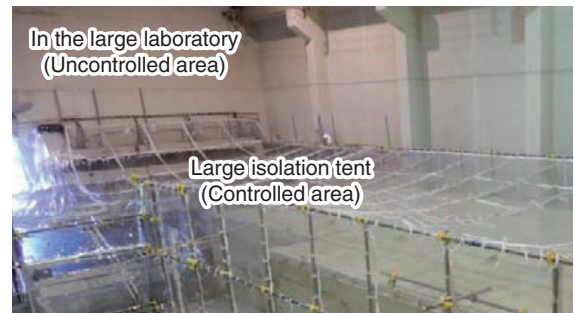


**Fig.8-15 Installation of a large isolation tent**  
To dismantle and remove the rooms, including the controlled areas, that were contaminated by the fire disaster, we installed a large isolation tent to cover these areas.



Dismantlement of room No.117



**Fig.8-16 Overview of the large laboratory before and after decommissioning**

The photographs provide an overview from the vicinity of the shutter in the northeast of the large laboratory and compare the space before and after the dismantling. After the controlled area was released, it was used as a general facility.

The Uranium Enrichment Laboratory in the Nuclear Science Research Institute was constructed in 1972 and was used for research on uranium enrichment program until 1998. Thereafter, maintenance work was conducted by dismantling the equipment whose use had been completed. In accordance with the facility mid/long-range plan, we completed the decommissioning program for dismantling and decontaminating the facilities and released the controlled area in 2019. In this facility, an independent steel-framed room was set up in an atrium room (about 420 m<sup>2</sup>), and this room was called a large laboratory in an uncontrolled area, and a part of it was used as the controlled area (about 182 m<sup>2</sup>). The floor plan is shown in Fig.8-14.

At this facility, an incipient fire trouble occurred in 1989, and a fire disaster occurred in 1997, causing uranium contamination throughout the controlled area. In the preliminary investigation of decommissioning, the residual contamination at that time was also confirmed at the boundary between the floor and wall. In this work, the walls and ceilings that divide the contaminated controlled area were completely dismantled. For achieving this purpose, it was necessary to completely prevent the contamination from leaking from the controlled area to the uncontrolled area during the equipment-dismounting work. The

large isolation tent (Fig.8-15) that covered the entire room was dismantled, and the rooms in the controlled area were carefully demolished. To prevent the scattering of contamination, an adhesive sheet was fixed to the floor surface in the contaminated area, and subsequently, the floor material was peeled off. The concrete surface where the contamination remained was removed by installing a partial isolation tent at each work site and using a power tool with a dust collecting function.

In the decommissioning of this facility, in addition to dismantling the room, the facilities inside and outside the controlled area (i.e., hood, nuclear fuel storage, etc.) were dismantled and removed.

The work toward the decommissioning of the Uranium Enrichment Laboratory was conducted based on safety considerations, such as contamination spread prevention measures and fire prevention measures, and the controlled area was released without any disaster in FY2019 as planned (Fig.8-16). The building after releasing the controlled area is being used as a general facility. We believe that the knowledge gained from the decommissioning of this facility will be useful for the safe decommissioning of facilities that are difficult to decontaminate because of the remaining contamination.

(Junya Kokusen)

### Reference

Kokusen, J. et al., Decommissioning of the Uranium Enrichment Laboratory, JAEA-Technology 2020-011, 2020, 70p. (in Japanese).

## 8-6 Dismantling a Tank Containing Liquid with $\alpha$ Nuclides

### — Exposure Reduction Measures and Acquisition of Work Data for Future —

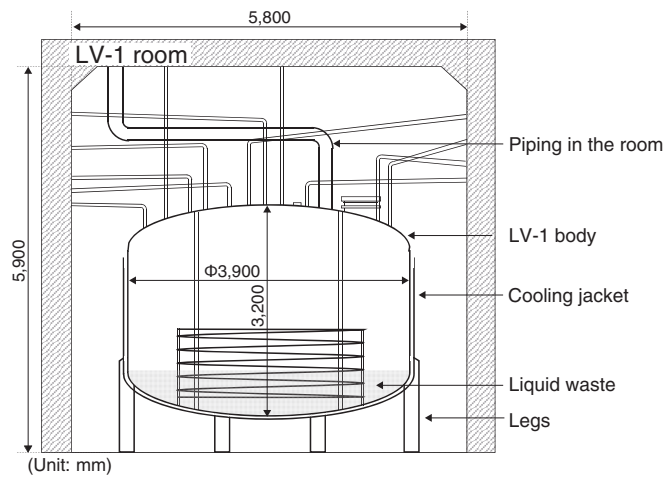


**Fig.8-17 LV-1 layout sketch**

LV-1 with high-dose residual liquid waste was installed in a very narrow space where piping was laid intricately. Therefore, the dismantling of LV-1 was conducted under various constraints.

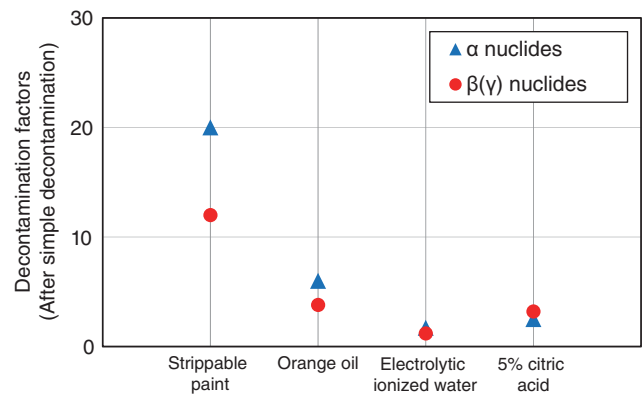


**Fig.8-18 Decontamination test result**

After simple decontamination using wet rags, where most of the free contaminants were removed, decontamination was performed using four different chemicals. Strippable paint was found to be the most effective in the subsequent decontamination.

**Table 8-1 Comparison of cutting efficiency by the equipment**

Protective equipment does not cause any remarkable difference in cutting efficiency, but there is a large difference in the cutting time ratio because of the time taken to wear and remove the ventilated suit.

	Cutting efficiency (Cutting length (cm) / Cutting time (h))	Ratio of cutting time (Cutting time (h) / GH* entry time (h))	Average cutting length per person per day (cm / (person-day))
Ventilated suit	240	0.33	324
Full face mask	300	0.49	601
Full face mask/ Ventilated suit	1.25	1.47	1.86

For the GH\* entry time per day, we used the average of all operations (4.1 hours).  
\*GH (green house) stands for a pollution spread prevention enclosure.

The JAERI's Reprocessing Test Facility became the first facility in Japan to successfully recover plutonium from spent fuel through a reprocessing test (PUREX method) in 1968. Since 1996, it has been dismantled, and its work data on work management, radiation control, waste management, etc. have been obtained for future efficient decommissioning work plan. Herein, we describe the findings obtained from the dismantling of a large tank (hereinafter, referred to as "LV-1") (Fig.8-17) that stored liquid waste containing fission products, including  $\alpha$  nuclides.

Decontamination before dismantling is very important for reducing worker exposure. To select an efficient decontamination method, we conducted a decontamination test at the inner bottom of LV-1 (material: SS304L). First, simple decontamination was performed by wiping with wet rags. Then, the bottom of LV-1 was divided into four sections that were decontaminated using one of the following four materials: 5% citric acid, electrolytic ionized water, orange oil, and strippable paint. Fig.8-18 shows the decontamination factors (the radioactivity surface density before decontamination divided by that after decontamination),

which indicate that strippable paint is effective for storage tanks with large amounts of a nuclides such as LV-1. These data are very useful for dismantling similar facilities.

To prevent an increase in the airborne radioactivity concentration as the main body of LV-1 is cut with a disk-saw, the contamination inside LV-1 was fixed with paint before cutting, and we used a full-face mask instead of a ventilated suit. From Table 8-1, the average cutting length per person per day when using the ventilated suit is more than 1.8 times that when using only the full-face mask. The total manpower for the cutting operation with the full-face mask, including decontamination and painting, was 743 labor-days. On the other hand, the estimated labor for the cutting operation was 912 labor-days without decontamination, without painting, and with the ventilated suit. Therefore, decontamination and painting are effective in reducing worker exposure and manpower.

From the dismantling of LV-1, we obtained very important work data for decommissioning. We will accumulate the work data, which can make future decommissioning more efficient.

(Yuta Yokozuka)

#### References

- Yokozuka, Y. et al., In-situ Dismantling of the Liquid Waste Storage Tank LV-1 in the JRTF—The Dismantling Work—, JAEA-Technology 2021-037, 2022, 44p. (in Japanese).  
Yokozuka, Y. et al., In-situ Dismantling of the Liquid Waste Storage Tank LV-1 in the JRTF—The Dismantling Preparation Work—, JAEA-Technology 2020-017, 2021, 56p. (in Japanese).

## 8-7 New Method to Observe Fault Displacement Using a Conventional Device

— Significant Progress Toward Greatly Enhanced Underground Utilization —

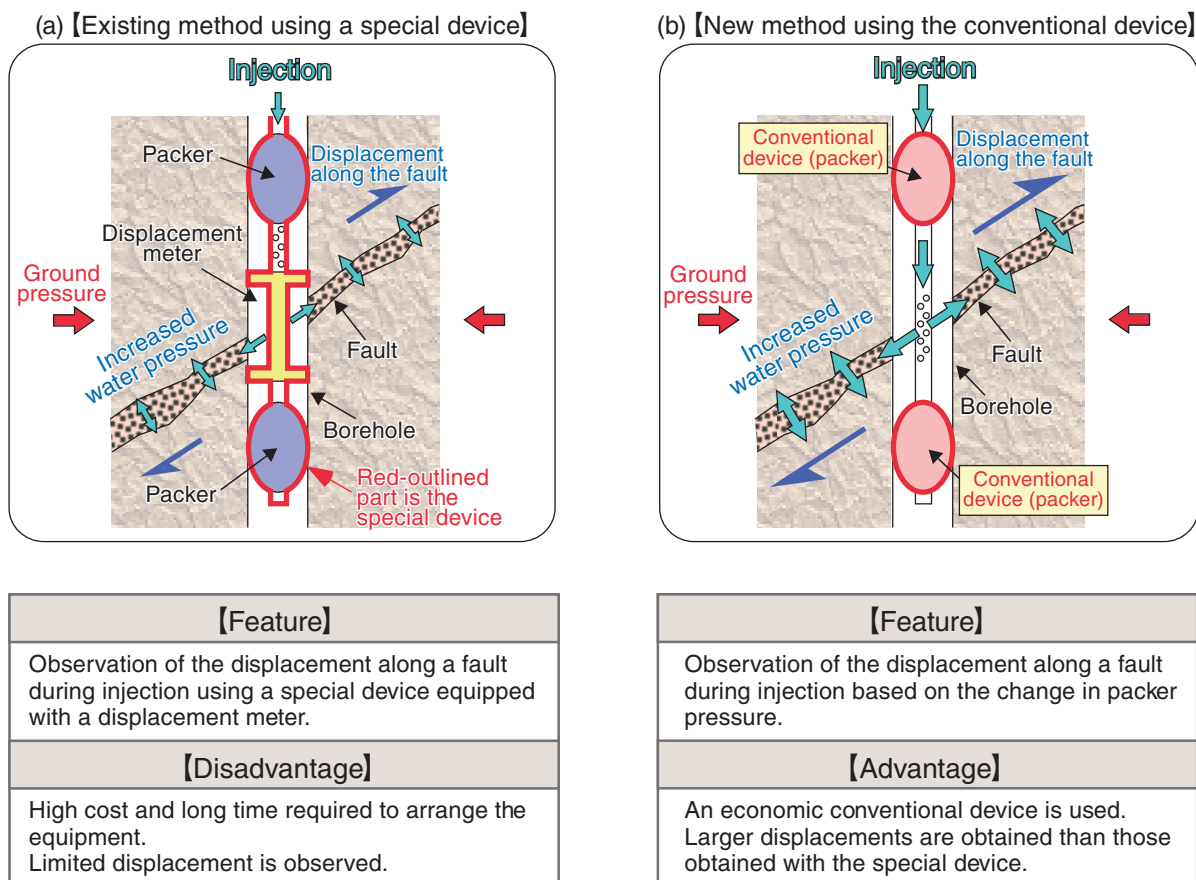


**Fig.8-19 Comparison of the existing method using a special device and the new method using a conventional device**  
Features and disadvantages/disadvantages of each method are summarized.

In the geological disposal of high-level radioactive waste, it is necessary to consider the possibility that diastrophism or other processes may displace underground faults, thereby increasing the permeability of such faults and affecting the confinement capability of geologic formations. Considering this possibility, an experiment was conducted to displace actual underground faults artificially. In the existing test method, a specifically designed device is deployed at the section of a borehole that is intersected by a fault, and the fault is artificially displaced by injecting water into it to increase the water pressure in the fault; subsequently, the displacements along the fault are measured by the special device (Fig.8-19 (a)). However, from the viewpoint of practicality, the existing test method has some disadvantages; for example, it involves high cost and long time to arrange the special device and dedicated operators, and the displacement amounts that can be observed with such equipment is limited (to several millimeters).

The Japan Atomic Energy Agency proposed a new practical test method for displacing faults using a general-purpose testing device that had been traditionally used for testing the permeability of geologic formations (Fig.8-19 (b)). The new method is based on the phenomenon that the inner pressure of two rubber tubes

(called packers) that are inflated and deployed in a borehole vary when the packer interval (i.e., the test-section length) is slightly changed by displacement along the injected fault. This phenomenon was observed in laboratory experiments, and it confirms a constant relationship between the packer pressure and change in packer interval.

By verification testing, the fault displacements of several centimeters followed by failure were observed; the observed displacements were larger than those observed with the special device. Furthermore, the testing revealed that such large displacements do not cause any remarkable changes in permeability.

The new method allows the easy examination of the impacts of fault displacement on permeability and is also applicable for studying the seismic behavior of faults during injection or the mechanical stability of faults. Thus, the new method is expected to be not only used for the geological disposal of radioactive waste or the underground storage of CO<sub>2</sub> but also helpful for solving problems in the fields associated with various underground applications such as mine development and antidisaster measures for slopes.

(Eiichi Ishii)

### Reference

Ishii, E., A Conventional Straddle-Sliding-Packer System as a Borehole Extensometer: Monitoring Shear Displacement of a Fault during an Injection Test, *Engineering Geology*, vol.275, 2020, 105748, 12p.

## 8-8 Prediction of the Low-Permeability Domain in Soft Rock — Estimation of the Effective Hydraulic Conductivity by Hydromechanical Simulation —

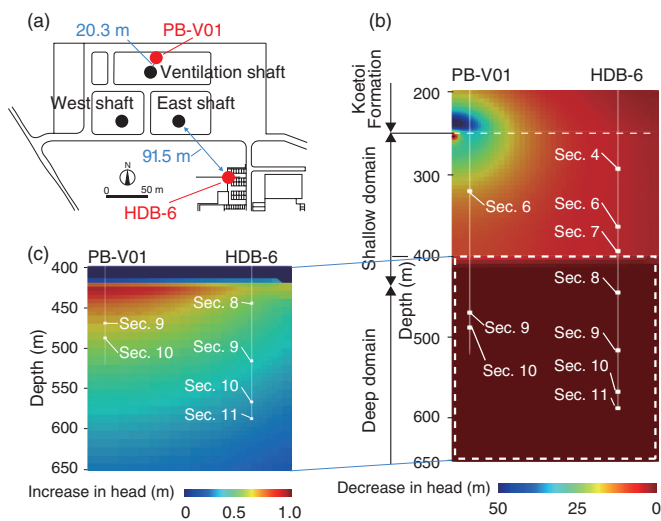


**Fig.8-20 Location of shafts and boreholes, and vertical distribution of disturbance of the hydraulic head a year after drainage by hydromechanical coupled simulation**  
(a) Location of the shafts and studied boreholes of HDB-6 and PB-V01, (b) disturbance of the hydraulic head under 200 m and location of monitoring sections in the boreholes, and (c) disturbance of the hydraulic head between 400 and 650 m depth (i.e., the deep domain of the Wakkanaï Formation).

Estimation of the low-permeability domain in the subsurface is important for the safety assessment of geological disposal because solute transportation is restrained by the low seepage of groundwater there. Drainage during the excavation of shafts has a large impact on the groundwater flow, and the hydraulic head responds to the drainage even in the low-permeability domain where only small hydraulic responses were usually obtained by conventional hydraulic tests. In this study, for evaluating the effective hydraulic conductivity in the Wakkanaï Formation located in the subsurface at depths beyond 250 m, we simulated the hydraulic head in the monitoring boreholes after the depth of the ventilation shafts of the Horonobe Underground Research Laboratory (URL) reached 250 m (Fig. 8-20(a)).

The subsurface around the Horonobe URL consists of soft sedimentary rocks. These soft rocks deform depending on the drainage of the contained groundwater, and this deformation, in turn, affects the hydraulic responses. We simulated the change in the hydraulic head during the excavation considering the coupled hydromechanical effect (i.e., the poroelastic effect).

A referential simulation model was constructed based on the geological information of the Koetoi and Wakkanaï formations in the boreholes near the URL. The Wakkanaï Formation was further divided into two domains of shallow and deep domains at a depth of 400 m according to the mechanical stress conditions. The hydraulic conductivity values measured in in situ experiments were assigned to the Koetoi Formation and the shallow domain of the Wakkanaï Formation. The hydraulic conductivity low as intact rock was assumed in the deep domain of the Wakkanaï Formation.

### Reference

Ozaki, Y. et al., Variation in Fault Hydraulic Connectivity with Depth in Mudstone: An Analysis of Poroelastic Hydraulic Response to Excavation in the Horonobe URL, *Geomechanics for Energy and the Environment*, vol.31, 2022, 100311, 13p.

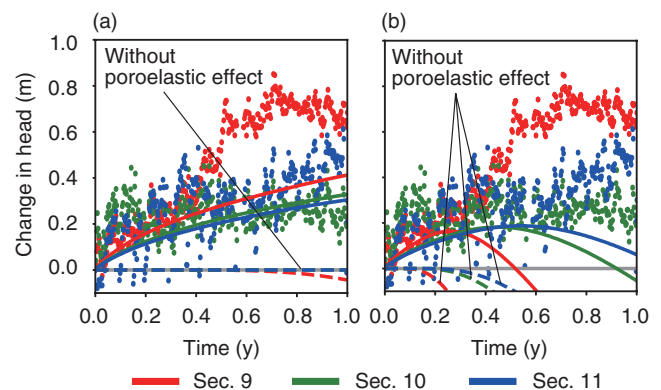


**Fig.8-21 Comparison of the simulated and observed disturbances of the hydraulic head at monitoring sections deeper than 500 m in HDB-6 borehole**

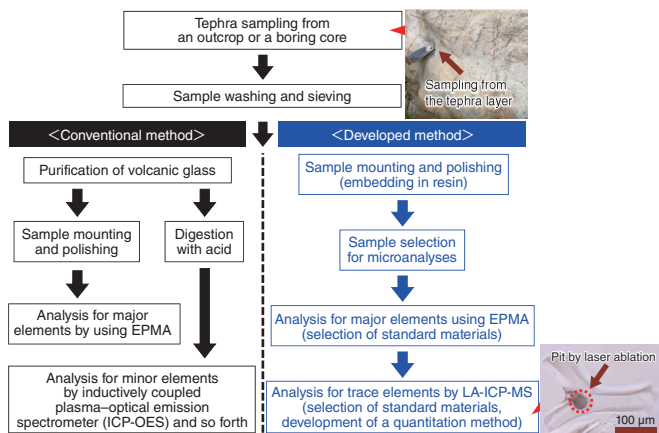
(a) Simulated results are derived from the model with high and low hydraulic conductivity values in the shallow and deep domains of the Wakkanaï Formation, respectively, and (b) the results from model with high hydraulic conductivity in both the shallow and deep domains. Results from different monitoring sections are shown by different colors, and the solid and dashed lines indicate results obtained with and without considering the poroelastic effect, respectively.

Fig.8-20(b) shows the simulation results of the disturbance of the hydraulic head in the vertical direction one year after drainage. The hydraulic head in the Koetoi Formation and shallow domain of the Wakkanaï Formation decreased depending on the drainage from the ventilation shaft. The hydraulic head in the deep domain of the Wakkanaï Formation increased because of the poroelastic effect and was maintained high because of the low hydraulic conductivity (Fig.8-20(c)). Fig.8-21 compare the observed and simulated changes in hydraulic head at the monitoring sections deeper than 500 m. Fig.8-21(a) shows the results of the referential model with high and low hydraulic conductivity values in the Wakkanaï Formation, and Fig.8-21(b) shows the model results obtained considering high hydraulic conductivity in both shallow and deep domains. Both results reproduce the increase in the hydraulic head by considering the poroelastic effect. However, the results of the referential model shown in Fig.8-21(a) are more consistent with the observed results than those shown Fig.8-21(b), and the hydraulic conductivity in the deep domain of the Wakkanaï Formation can be estimated as corresponding to low permeability considering the intact rock. In addition, comparisons of our other simulation results from models with different hydraulic conductivity values indicate that the hydraulic conductivity decreases with depth in the Wakkanaï Formation.

This result can be interpreted as indicative of a decrease in the fault hydraulic connectivity with depth in the Wakkanaï Formation because the fault hydraulic connectivity mainly dominates the hydraulic conductivity around the Horonobe URL.  
(Yusuke Ozaki)

## 8-9 Discriminating Tephra with Similar Chemical Compositions

### — Development of a Method for the in Situ Chemical Composition Analysis of Volcanic Glasses —



**Fig.8-22 Analytical flowchart of volcanic glasses**

We developed pretreatment methods suitable for volcanic glasses and analytical techniques for the major/trace element compositions of volcanic glasses using an electron probe micro analyzer (EPMA) and by laser ablation–inductively coupled plasma–mass spectrometry (LA-ICP-MS) to identify tephra samples in detail.

To assess the long-term safety for geological disposal, it is essential to predict the future stability of the geological environment based on the history of past natural phenomena. Tephra, which are ejected from volcanoes, is deposited over a wide area in a short period of time, making it a chronostratigraphic indicator. Tephrochronology is valid for revealing the history of natural phenomena. The age of a tephra-bearing layer and its surrounding strata can be determined by comparing the characterizations (shape of volcanic glasses, mineral composition, refractive index, chemical composition, etc.) of an unknown tephra with those of tephra specimens whose age is known. In particular, the chemical compositions of volcanic glasses are one of the important indicators for identifying tephra; however, in some cases, the volcanic glasses that erupted from the same source at different times have similar major element compositions. Therefore, the trace element compositions of volcanic glasses are considered an indicator for identifying tephra.

The trace element composition of volcanic glasses has been analyzed by wet analysis, in which only the volcanic glasses purified from tephra containing a large amount of minerals and then dissolved in acid for measurement. The conventional method requires complicated sample pretreatment, and the degree of the purification of the glass can drastically affect the analytical results. To overcome these problems, we developed an in situ analytical method for the trace elements in volcanic glasses; this method does not require complicated sample pretreatment.

In this study, we examined the pretreatment methods suitable for volcanic glasses and developed analytical techniques for

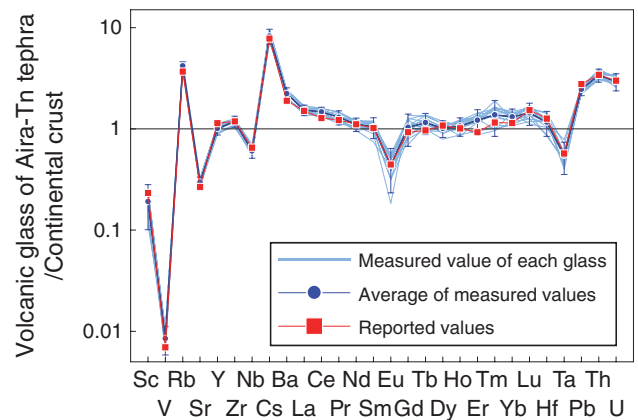


**Fig.8-23 Trace element abundances of volcanic glasses in Aira-Tn tephra measured by the method developed in this study**

Our analytical results were consistent with the previously reported values, indicating that the analysis was performed properly.

the major and trace element compositions of volcanic glasses using an electron probe micro analyzer (EPMA) and by laser ablation–inductively coupled plasma–mass spectrometry (LA-ICP-MS), respectively (Fig.8-22). This method does not require sample dissolution, instead it only requires polishing of the surface of the sample. Sample preparation involved embedding the sample in resin because the volcanic glasses are more irregularly shaped than minerals and can easily fall out during polishing. In addition, the major element composition was analyzed more precisely and accurately by selecting the glassy standard materials, which have a matrix similar to those of volcanic glasses, for comparison with the conventional method using mineral standards. In the measurement of trace element compositions by LA-ICP-MS, although the calibration curve method with only one standard material was conventionally adapted, we established a quantitative method using three standard materials, including the material with a matrix similar to that of volcanic glasses. It was confirmed that the trace element compositions of volcanic glasses were obtained with sufficient accuracy for identifying tephra (Fig.8-23), thereby enabling the rapid analysis of the chemical compositions of volcanic glasses.

The robustness of the tephra catalog is important in tephrochronology. Since there are still only a few tephra specimens with known chemical compositions, including trace element compositions, we intend to use this method of rapid analysis, to enhance the database as a basis for tephra identification.

(Saya Kagami)

#### Reference

Kagami, S. et al., Analytical Method for Chemical Compositions of Volcanic Glasses in Tono Geoscience Center –Quantitative Measurements of Major Elements by Using EPMA and Minor Elements by LA-ICP-MS–, JAEA-Testing 2021-001, 2021, 49p. (in Japanese).

## 8-10 Prediction of Radionuclide Migration by a Thermodynamic Sorption Model

### — Assessing the Impact of the Transition of Repository Condition on Radionuclide Migration —

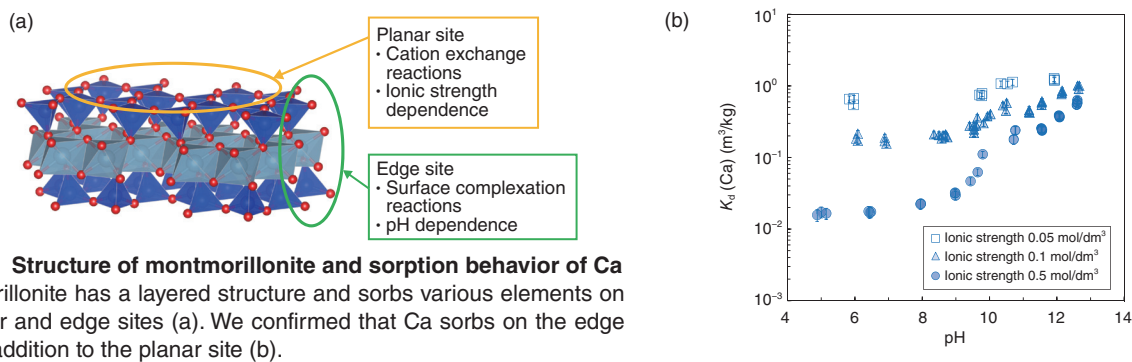


**Fig.8-24 Structure of montmorillonite and sorption behavior of Ca**  
Montmorillonite has a layered structure and sorbs various elements on its planar and edge sites (a). We confirmed that Ca sorbs on the edge sites in addition to the planar site (b).

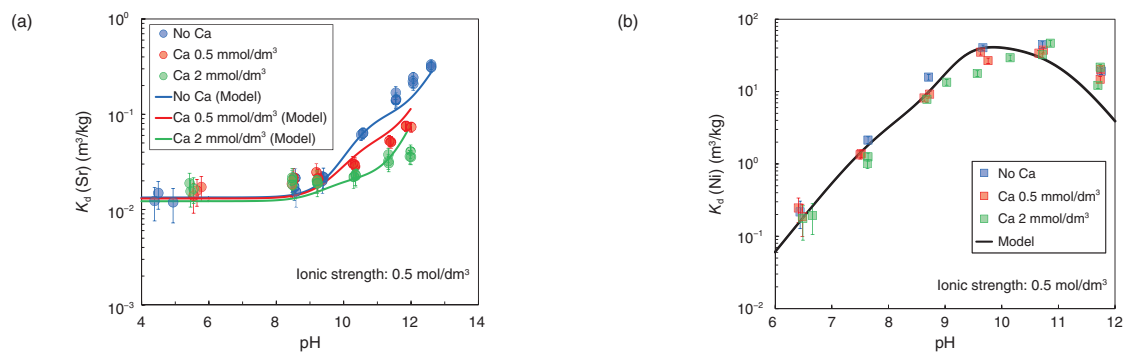


**Fig.8-25 Effect of Ca on the sorption behaviors of Sr and Ni**

The presence of Ca reduced the  $K_d$  values of Sr (a), while those of Ni were unaffected (b). The calculation by a thermodynamic sorption model using the sorption parameters obtained in this study reproduced well the results of sorption experiments.

Cementitious materials are planned to be used in high-level radioactive waste repositories. The calcium (Ca) concentration in the porewater of buffer materials will increase because of the leaching of cementitious materials. The buffer material sorbs radionuclides and retards their migration. However, the sorption of radionuclides will reduce because of the sorption competition with Ca at higher Ca concentrations. The degree of sorption of radionuclides onto the buffer material or clay minerals in rocks is expressed by the distribution coefficient ( $K_d$ ;  $\text{m}^3/\text{kg}$ ). Although it is desirable to know  $K_d$  values under various conditions to assess the safety of geological disposal, it is not realistic to measure these values under all the possible conditions expected in a repository because the  $K_d$  values depend on pH and solution composition. Therefore, the thermodynamic sorption model, which is used to predict  $K_d$  based on the sorption mechanism, has been studied. In this study, we investigated the sorption of Ca on montmorillonite, a prominent clay mineral with regard to the sorption of radionuclides sorption in the buffer material. We also evaluated the effect of Ca on the sorption of strontium (Sr) and nickel (Ni), which are important elements for safety assessment.

In general, sorption on clay minerals can be classified into cation exchange reactions at planar sites and surface complexation reactions at edge sites. The former is affected by ionic strength and the latter by pH (Fig.8-24(a)). It is known that Ca is sorbed by cation exchange reaction. However, we found that the  $K_d$  values of Ca increased significantly at high pH under conditions

of high ionic strength, and that sorption by surface complexation reactions becomes more dominant in this pH region (Fig.8-24(b)). This trend was also found for Sr, a homologous element to Ca (Fig.8-25(a)). In contrast, the  $K_d$  values of Ni increased in acidic pH region, indicating that the surface complexation reactions were dominant even at low pH (Fig.8-25(b)). Next, we performed sorption competition experiments to evaluate the effect of Ca on the sorption of Sr and Ni on the edge sites. The results indicated that Sr sorption was inhibited by the presence of Ca, while Ni sorption was not affected. This suggests that Sr sorbs at the same site a Ca, whereas Ni sorbs at a different site. Based on these results, we used a thermodynamic sorption model with a geochemical calculation code PHREEQC to reproduce the measured  $K_d$  values and derive the sorption parameters for each element. The calculations using the derived sorption parameters reproduced well the results of sorption competition experiments.

The experiments and model calculations conducted in this study clarified that elements sorb to different edge sites depending on their chemical properties. The thermodynamic sorption model can predict  $K_d$  values under various conditions arising from the long-term transition of the repository condition based on the sorption parameters obtained through various experiments.

This study was a part of “Development of enhancing the disposal system in the coastal region (FY2018)” supported by METI (Grant number JPJ007597).

(Yuki Sugiura)

#### Reference

Sugiura, Y. et al., Surface Complexation of Ca and Competitive Sorption of Divalent Cations on Montmorillonite Under Alkaline Conditions, Applied Clay Science, vol.200, 2021, 105910, 10p.

# 8-11 Migration Behavior of Carbon-14 in Buffer Material

## — Diffusion Experiments of Carboxylic Acid and Alcohol in Compacted Bentonite —

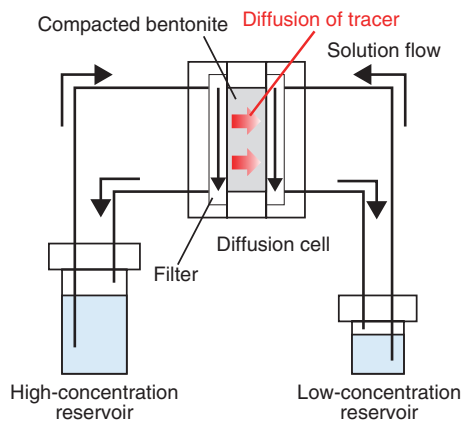


**Fig.8-26 Schematic view of diffusion experiment**

The solution from the reservoirs was recirculated through the filters placed on both sides of compacted bentonite. The tracers (acetic acid, butyric acid, and butanol) in the high-concentration reservoir diffuse through the compacted bentonite into the low-concentration reservoir. The diffusion behavior of the tracers can be observed from the change in tracer concentration in the low-concentration reservoir.

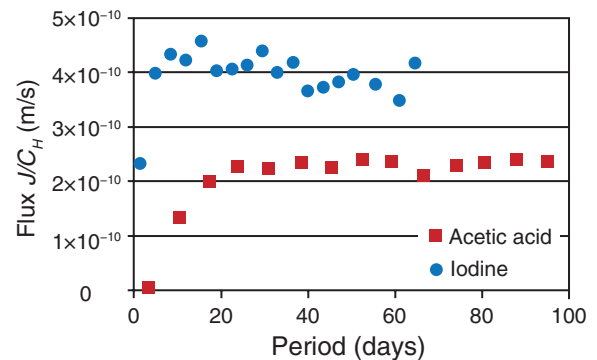


**Fig.8-27 Results of diffusion experiments**

Change in tracer flux with time for acetic acid and iodine. The flux is defined as the amount of tracer diffused from compacted bentonite per unit surface area and per unit time. The flux shown in the figure is normalized by the tracer concentration in the high-concentration reservoir.

**Table 8-2 Effective diffusion coefficients ( $D_e$ ) and formation factors ( $FF$ ) measured by the diffusion experiments**

The  $FF$  values of acetic acid (No.1, 2) and butyric acid (No.3, 4) were in good agreement with those of iodine, while the  $FF$  values of butanol were different from those of deuterated water (The  $FF$  values obtained from the same number sample were compared). These results indicate that the diffusion path of carboxylic acid was similar to that of iodine, while the diffusion property of butanol was different from that of deuterated water.

No.	Acetic acid		Butyric acid		Iodine		No.	Butanol		Deuterated water	
	$D_e$ ( $m^2/s$ )	$FF$ ( $\times 10^{-3}$ )	$D_e$ ( $m^2/s$ )	$FF$ ( $\times 10^{-3}$ )	$D_e$ ( $m^2/s$ )	$FF$ ( $\times 10^{-3}$ )		$D_e$ ( $m^2/s$ )	$FF$ ( $\times 10^{-3}$ )	$D_e$ ( $m^2/s$ )	$FF$ ( $\times 10^{-3}$ )
1	$2.3 \times 10^{-12}$	2.1	—	—	$4.0 \times 10^{-12}$	1.9	5	$2.5 \times 10^{-12}$	4.5	$1.7 \times 10^{-11}$	7.7
2	$2.6 \times 10^{-12}$	2.4	—	—	$4.4 \times 10^{-12}$	2.1	6	$3.2 \times 10^{-12}$	5.7	$2.0 \times 10^{-11}$	8.8
3	—	—	$8.0 \times 10^{-13}$	0.93	$2.0 \times 10^{-12}$	1.0					
4	—	—	$6.2 \times 10^{-13}$	0.71	$1.5 \times 10^{-12}$	0.74					

Carbon-14 ( $^{14}C$ ) is one of the radionuclides present in radioactive waste in the form of activated metal waste. In the geological disposal of radioactive waste, the radionuclides released from the waste are retarded in the compacted bentonite used as the buffer material. However, the retention of  $^{14}C$  in compacted bentonite is hardly expected because of the weak sorption of  $^{14}C$  on bentonite. Therefore,  $^{14}C$  is one of the key radionuclides in the safety assessment of geological disposal. A part of the  $^{14}C$  in the activated metals is released as low-molecular-weight organic compounds. In this study, the diffusion behavior of carboxylic acids (acetic acid and butyric acid) and alcohol (butanol) in compacted bentonite was investigated via diffusion experiments. The diffusion behavior was compared with that of iodine and deuterated water, which has been widely reported.

The changes in fluxes with time measured by the diffusion experiment (Fig.8-26) are shown in Fig.8-27. The fluxes increased with time and reached a steady state. The effective diffusion coefficient ( $D_e$ ) was calculated from the flux at the steady state based on Fick's first law. The formation factor ( $FF$ ), which indicates the diffusion path properties such as tortuosity, was calculated by dividing  $D_e$  by the self-diffusion coefficient of the tracer in water. From Table 8-2, the  $FF$  values of acetic acid and butyric acid are in good agreement with those of iodine, which diffuses as an anion similar to acetic acid and butyric acid. In contrast, the  $FF$  values of butanol were different from those

of deuterated water, though both tracers diffuse as electrically neutral species. (Note that the  $FF$  values obtained from the same number sample were compared (Table 8-2) as the  $FF$  values vary depending on the condition of the compacted bentonite sample even if the samples are prepared under identical conditions.). These results indicate that the diffusion path of carboxylic acid was similar to that of iodine, while the diffusion property of butanol differed from that of deuterated water. Thus, the difference in  $D_e$  values between carboxylic acid and iodine originates from the difference between their self-diffusion coefficients. The  $D_e$  values of carboxylic acids can be calculated from those of iodides by using their self-diffusion coefficients.

In the safety assessment for geological disposal, the  $D_e$  values of radionuclides in compacted bentonite should be evaluated with high reliability. Nevertheless, few studies reported the  $D_e$  values of carboxylic acids. The results of this study indicate that the widely reported  $D_e$  values of iodine can be utilized for setting the  $D_e$  for  $^{14}C$  in the form of carboxylic acids. This knowledge will contribute to increasing the confidence in setting the  $D_e$  for  $^{14}C$ .

This study was performed as a part of "Project on Research and Development of Spent Fuel Direct Disposal as an Alternative Disposal Option (2015-2017FY)" supported by METI (Grant number JPJ007597).

(Takamitsu Ishidera)

### Reference

Ishidera, T., Diffusion of Acetic Acid, Butyric Acid, and Butanol in Compacted Montmorillonite, Journal of Radioanalytical and Nuclear Chemistry, vol.330, issue 1, 2021, p.149-158.

## Computational Science for Nuclear Research and Development

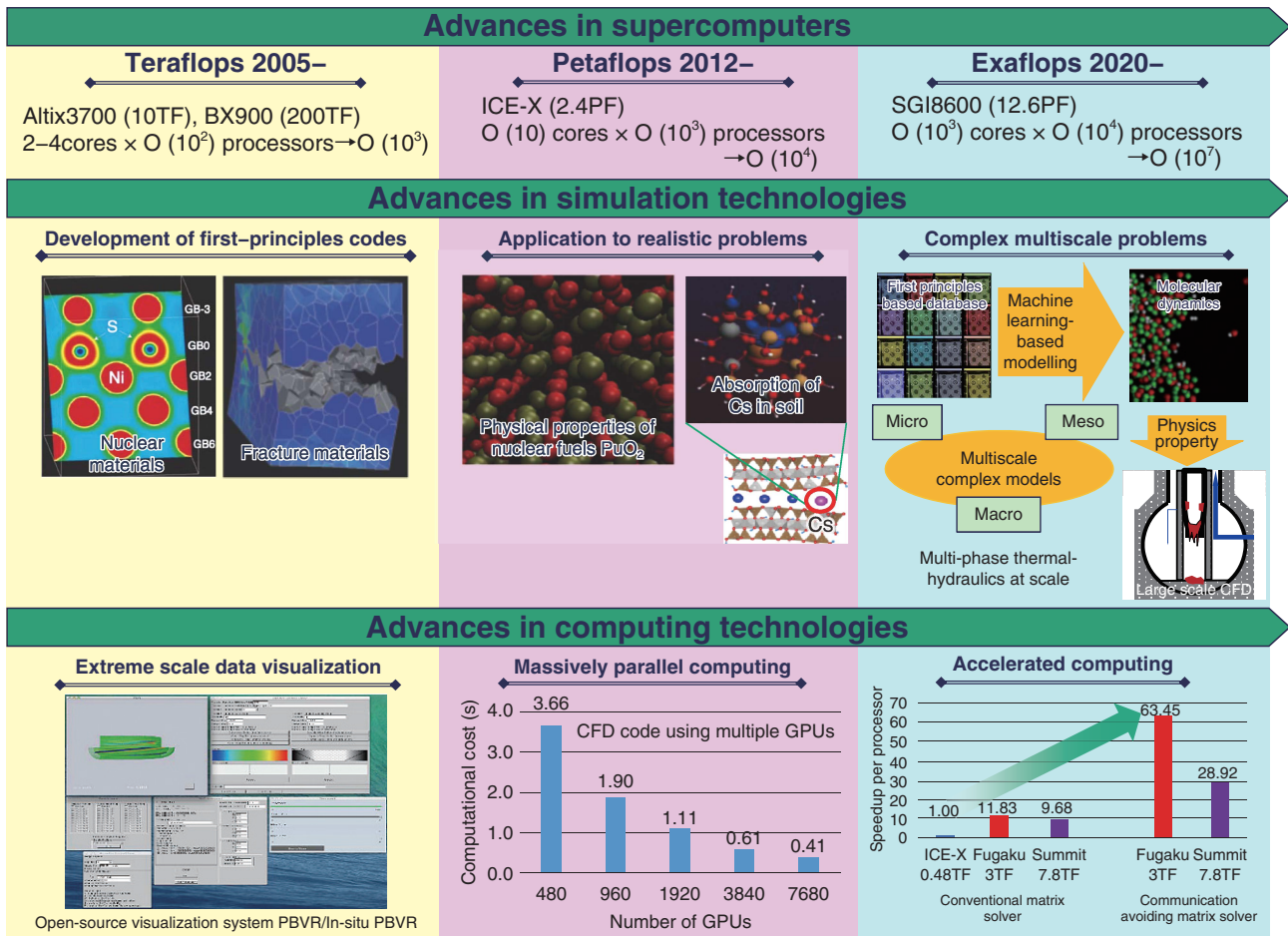


**Fig.9-1 Computational science research at the Center for Computational Science and e-Systems (CCSE)**

Complex systems in nuclear research and development are analyzed by advancing the simulation and computational technologies that have been developed and accumulated at CCSE.

Simulation techniques for analyzing complex phenomena involving various physics effects, such as the environmental dynamics of radioactive substances, the mechanism of soil contamination, and the study of severe accidents, are essential for developing future nuclear systems and for resolving issues related to the accident at TEPCO's Fukushima Daiichi NPS. For example, analyses of severe accidents require not only macroscale thermal-hydraulic simulations of the melt-relocation behavior of nuclear fuels and structural materials but also multiscale and multiphysics simulation technologies, which integrate mesoscale simulations for evaluating complicated interface formation caused by the mixing of molten debris, and microscale atomic/molecular simulations for estimating diffusion, chemical reactions, and phase transitions in extreme environments under high-temperature and -pressure conditions. In addition to these simulation technologies, the computational technologies that support high-performance computing on state-of-the-art supercomputers such as the supercomputer Fugaku are necessary.

Thus far, we have developed simulation techniques, which form the basis for analyzing complex phenomena, as well as computational technologies such as numerical algorithms and visualization systems. We will further advance these techniques and address the analyses of complex phenomena (Fig.9-1).

These simulation techniques for complex phenomena will act as a common foundation for general nuclear research and development.

In FY2021, as a contribution toward the reconstruction and revitalization of Fukushima Prefecture, we addressed the retention mechanism of radioactive cesium in lichens via quantum chemical calculations (Chapter 1, Topic 1-12). Further, in the following four topics, we discuss the development of computational technology and quantum chemical calculations of complex phenomena. Topic 9-1 presents a deep-learning-based modeling of the high-resolution simulation data obtained from intensive computational fluid dynamics (CFD) simulations and the construction of its surrogate model. In Topic 9-2, a new domain decomposition method developed for multiscale CFD simulation based on the local mesh refinement method is presented, and its improved parallel processing performance is discussed. Topic 9-3 presents an atomic simulation code PIMD, which enables the study of nuclear quantum effects; it is clarified that the nuclear quantum effects are important with regard to the physical property of water. Topic 9-4 addresses the experimental and simulation studies conducted for barium, which is similar to radium, toward the understanding of the environmental dynamics of radium, and reveals its hydrate structure.

We steadily promote research on simulation and computational techniques and make them accessible to the community.

# 9-1 Deep-Learning Model for High-Resolution Steady Flow Prediction

## — Convolutional Neural Networks for Multiresolution Steady Flow Prediction —

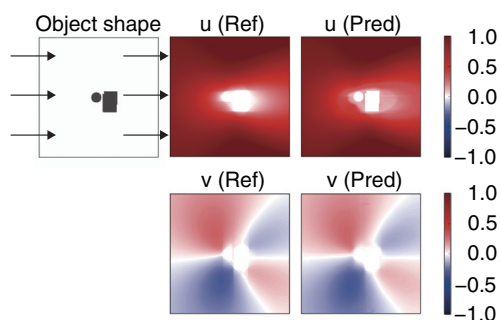


**Fig.9-2 Flow field prediction with the proposed deep-learning model**

The simulation (reference) and predicted two-dimensional steady-state flow fields around objects with a resolution of  $1024^2$ . Here,  $u$  and  $v$  are the normalized flow velocity along the  $x$  and  $y$  axes, respectively. The arrows represent the directions of the in- and out-flows from left to right.

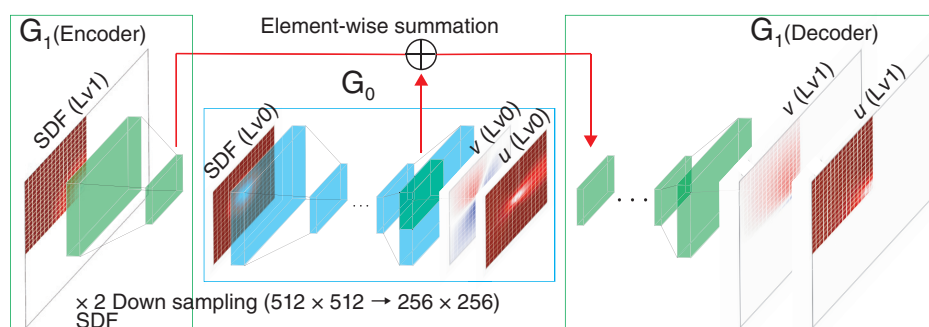


**Fig.9-3 Architecture of the proposed model**

The global low-resolution and patched high-resolution signed distance functions (SDFs) are fed to networks  $G_0$  and  $G_1$ . The patched features ( $256 \times 256$ ) from  $G_0$  are merged with the down-sampled features ( $256 \times 256$ ) by  $G_1$  to predict the patched high-resolution flow field. Since the elementwise sum of the global features from  $G_0$  and the local features from  $G_1$  allows the propagation of the global information to  $G_1$ , the predicted high-resolution flow fields maintain the consistency of the structures between the patches.

Deep-learning-based models using convolutional neural networks (CNNs) are widely used to generate photo-realistic images. These models have also been applied to surrogate models that approximate computational fluid dynamics (CFD) simulation results, which can be obtained significantly faster than CFD simulation results. A kind of surrogate models are needed for an instant prediction and large-scale parameter scans of flow fields. Because of memory-size constraints, conventional models have been applied up to a resolution of  $512 \times 512$ . For the high-resolution flow fields, a model has to predict the patched regions of flow fields independently, and this leads to inconsistency between the independently predicted flow fields.

In this work, we developed a new flow-prediction model to resolve the memory and connection issues simultaneously. A CNN-based model predicts the steady-state flow field around an object from a signed distance function (SDF), which represents both simple and complex object shapes in a universal way. Conventional models have applied CNNs to the patched SDF data to predict the patched flow field. In this work, we developed a model to use a low-resolution global SDF and a high-resolution patched SDF to predict a globally consistent high-resolution flow field (Fig. 9-2).

Here, the low-resolution SDF is constructed from a high-resolution SDF by down-sampling.

In CNNs, the input data are first encoded and then decoded to the target output data. The developed model consists of an encoder/decoder ( $G_0$ ) for low-resolution data and another encoder/decoder ( $G_1$ ) for high-resolution patched data (Fig. 9-3). Figure 9-3 shows the prediction of the flow field with  $1024 \times 1024$  resolution, where a low-resolution ( $512 \times 512$ ) global SDF and a high-resolution ( $512 \times 512$ ) patched SDF (1/4 region) are used as input data to  $G_0$  and  $G_1$ , respectively. The patched features ( $256 \times 256$ ) from  $G_0$  are merged with the down-sampled features ( $256 \times 256$ ) by  $G_1$ . By combining the global information from the low-resolution data and the local structures from the high-resolution patched data, the model can predict the global high-resolution flow field consistently. Although such a model has also been proposed in the field of image processing, it uses the global low-resolution and high-resolution data. Our model is more memory-efficient and can still predict the global high-resolution flow field by using the patched high-resolution data. Using this model, we can predict the flow fields instantly and perform large-scale parameter scans.

This work was partly supported by Joint Usage/Research Center for Interdisciplinary Large-Scale Information Infrastructures (Project ID: jh210049-MDH).

(Yuichi Asahi)

### Reference

Asahi, Y. et al., AMR-Net: Convolutional Neural Networks for Multi-Resolution Steady Flow Prediction, Proceedings of 2021 IEEE International Conference on Cluster Computing (IEEE Cluster 2021), Portland (Online), Oregon, U.S.A., 2021, p.686–691.

## 9-2 Acceleration of Multiscale Fluid Simulation on GPU Supercomputer — Communication Reducing Method for Local Mesh Refinement —

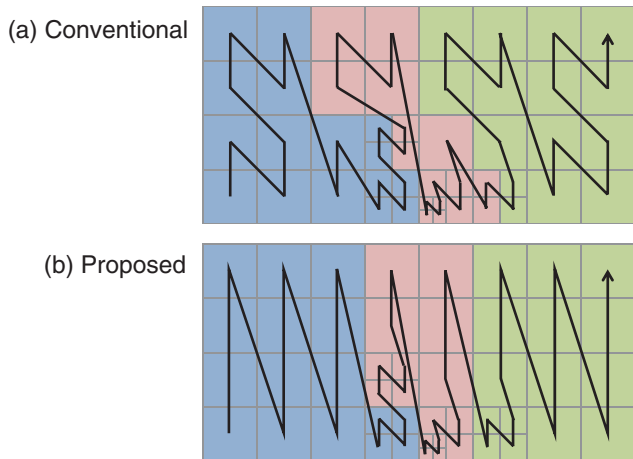


**Fig.9-4 Domain partitioning on local mesh refinement (LMR)**

A two-dimensional (2D) example of LMR. The arrows with folds denote the order of the grid scan by one-stroke writings based on the conventional (a) and proposed (b) methods, respectively. By equipartitioning them, they are divided into three subdomains (blue, red, and green).

Fluid dynamics phenomena, such as wind around objects and walls, are multiscale phenomena in which a global feature over distant regions and local tiny eddies near the wall appear simultaneously. For simulating such phenomena, the JAEA and Tokyo Institute of Technology (Tokyo Tech) developed a computational fluid dynamics (CFD) code based on the local mesh refinement (LMR) method, which changes the mesh resolution as per the scale of the flow property. The LMR-CFD code had been first developed at Tokyo Tech, and in this study, the JAEA proposed a new domain-partitioning approach to improve the computational speed.

The LMR generates locally subdivided grids by repeatedly subdividing one grid into eight grids as per the required resolution for each region. By employing a high-resolution mesh only near the object, the number of grids in the LMR was drastically reduced to 0.715% compared to that in the uniform mesh. However, domain partitioning in parallel computing with multiple processes remained a problem.

The conventional method used a single space-filling curve (SFC) for domain partitioning (Fig.9-4 (a)). The SFC is a mathematical representation of a so-called one-stroke writing, and in Fig.9-4, the SFC automatically generates an N-shaped tracing over all the grids. Because of its simplicity, the SFC is widely used for domain partitioning in the LMR; however,

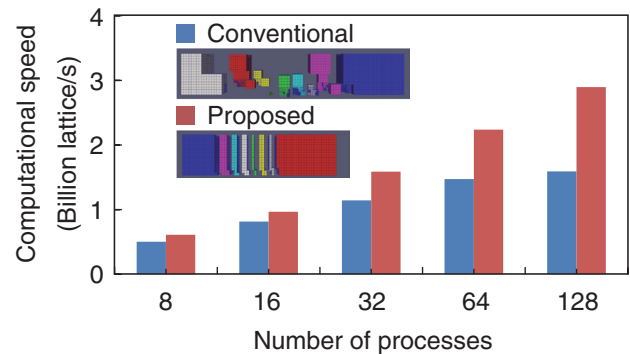


**Fig.9-5 Comparison of the domain shape and computation speed**

The computation speed of fluid simulation with 184 million grids. The pictures in the figure show the 8-partitioned subdomains, which indicate better partitioning by the proposed method than by the conventional one. Hence, the proposed method achieves  $\times 1.82$  speedup compared to the conventional one.

when the SFC generates subdomains with complex geometries (as in Fig.9-5), the amount of communication (i.e., the cross section of each subdomain) and the number of connections (i.e., the number of neighbors in each subdomain) becomes huge.

To improve the domain partitioning, this study proposes a new domain-partitioning approach, which at first partitions the domain into coarse orthogonal grids and generates local SFCs in each coarse partitioned domain and subsequently connects them to construct a one-stroke writing in different order (Fig.9-4 (b)). The proposed method reduced both the amount of communication and number of connections to  $1/3$  and  $1/2$ – $1/3$  times, respectively, those of the conventional method. These improvements enhanced the parallel performance well and resulted in  $\times 1.82$  speedup in the simulation with parallel computation involving 184 million grids using 128 processes (Fig.9-5).

This work was supported in part by JSPS KAKENHI Grant-in-Aid for Scientific Research (S) (JP26220002), Grant-in-Aid for Research Activity Start-up (JP19K24359), Grant-in-Aid for Early-Career Scientists (JP21K17755), High Performance Computing Infrastructure (Project ID: hp180146), and Joint Usage/Research Center for Interdisciplinary Large-Scale Information Infrastructures (Project ID: jh200050).

(Yuta Hasegawa)

### Reference

Hasegawa, Y. et al., Tree Cutting Approach for Domain Partitioning on Forest-of-Octrees-Based Block-Structured Static Adaptive Mesh Refinement with Lattice Boltzmann Method, *Parallel Computing*, vol.108, 102851, 2021, 12p.

## 9-3 Detecting the Quantum Fluctuation of Water

— High-Precision Calculations of Water Using the General-Purpose Molecular Simulation Code PIMD —

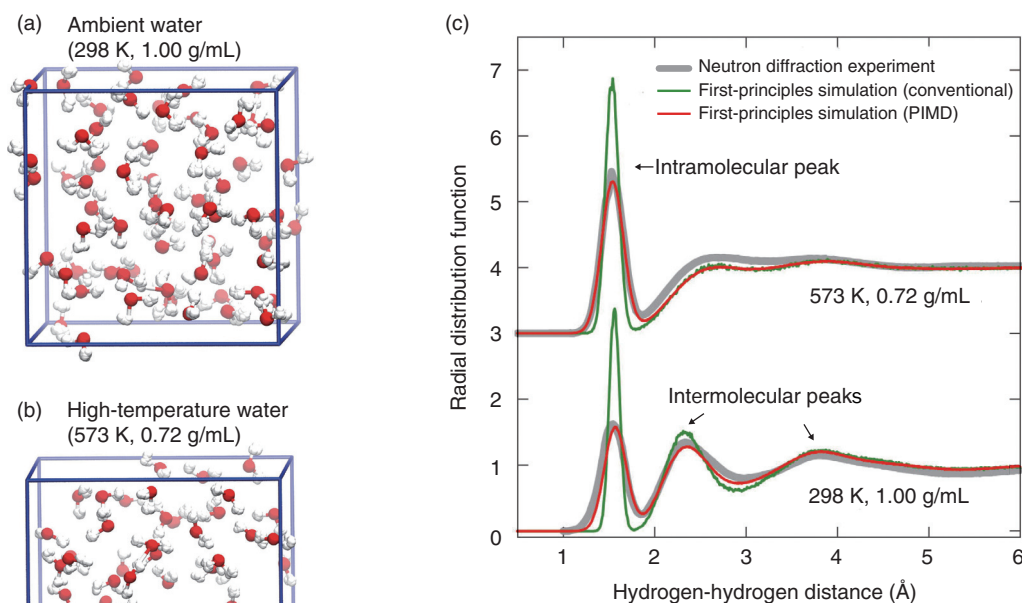


**Fig.9-6 Structure and interatomic radial distribution function of water**

(a) At ambient temperature and pressure and (b) at high temperature and pressure. The unit cell of the calculation containing 64 water atoms, consisting of hydrogen atoms (white) and oxygen atoms (red), is indicated by a blue box. (c) Comparison of the usual first-principles simulation of the radial distribution function between hydrogen atoms and the first-principles simulation, including the effect of quantum fluctuation of the nucleus, by PIMD software with the results of neutron diffraction experiments.

Matter is composed of atoms, and molecular simulations that follow the collective motion of atoms can provide information on the properties of matter. Since atomic motion is determined by the behavior of electrons in each atom, it is necessary to clarify the behavior of electrons by a method called “first-principles calculation,” which is based on the quantum mechanics governing the behavior of electrons, and to calculate the atomic motion based on the results of this calculation—this process is called “first-principles simulation.” First-principles simulations are required to further calculate atomic motion based on the results of these calculations. First-principles simulations, which require large, high-performance computers, are revealing previously unknown microscopic behaviors of various materials. It was known that the conventional first-principles simulations cannot reproduce the experimental results for determining the structure of water, which is one of the most familiar substances. This is because the hydrogen atoms in water molecules are very light and are affected by quantum mechanics in the same way as electrons, and therefore, they exhibit “quantum fluctuation” (a state in which the position of an object can exist only stochastically). Such quantum fluctuations are not taken into account in the conventional first-principles simulations. If this effect can be accurately calculated using the first-principles simulations, it will be possible to evaluate more accurately various chemical reactions in water, including the reprocessing of nuclear fuel and dynamics of radiation elements in environments. In addition to the first-principles calculations of electrons, calculations dealing with the quantum fluctuations of nuclei are necessary for this purpose. Therefore, the Center for

Computational Science & e-Systems has developed a calculation method that incorporates the quantum fluctuation of atomic nuclei and the software “PIMD” as a fundamental research technology in the field of nuclear energy. Using this technology, we performed the first-principles simulations of water. Fig.9-6 compares a conventional first-principles simulation of the radial distribution function (distribution of distances between atoms) and a first-principles simulation incorporating the quantum fluctuation using PIMD with the results of a neutron diffraction experiment (an experiment to analyze the structure of materials using neutron diffraction by crystals). The quantum fluctuation of hydrogen atoms is larger than that of oxygen atoms. The larger the quantum fluctuation of the hydrogen atom, the lower and wider are the peak of the graph. While the conventional first-principles simulations deviate from experiments in some areas, the results obtained using PIMD are in good agreement with the experiments and are expected to enable more accurate evaluation of chemical reactions such as the transfer of hydrogen from a water molecule to another molecule.

PIMD is available as open-source software at the website of the Center for Computational Science and e-Systems (<https://ccse.jaea.go.jp/software/PIMD/index.en.html>) and is used by researchers in Japan and abroad. PIMD features a variety of PIMD is characterized by its ability to be combined with various first-principles codes to perform advanced first-principles simulations, such as calculations incorporating the quantum fluctuations of atomic nuclei, and is useful in research in the fields of physics, chemistry, and materials science.

(Motoyuki Shiga)

### Reference

Thomsen, B. and Shiga, M., *Ab Initio* Study of Nuclear Quantum Effects on Sub- and Supercritical Water, *Journal of Chemical Physics*, vol.155, issue 19, 194107, 2021, 11p.

## 9-4 Clarification of the Fundamental Properties of Radium

### — *Ab Initio* Molecular Dynamics Simulations and Extended X-Ray Absorption Fine Structure Measurements Revealed the Hydration Structure of Barium —

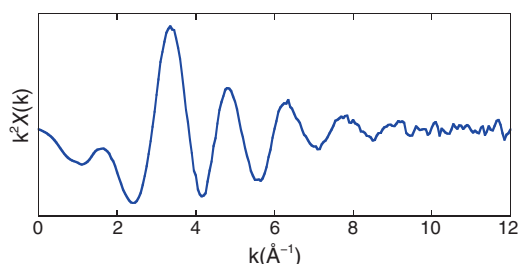


**Fig.9-7 Extended X-ray absorption fine structure (EXAFS) spectrum of the hydrated Ba<sup>2+</sup>**

This spectrum was analyzed by a theoretical equation, and the results are listed in Table 9-1.

**Table 9-1 Obtained coordination numbers (CNs) and average distances**

The value obtained by AIMD simulation with strongly constrained and appropriately normed (SCAN) is the closest to that obtained by the EXAFS experiment.

	Method or functional	CN	Average distance (nm)
Experiment	EXAFS	8.0	0.279
AIMD simulation	SCAN	7.8	0.278
	BLYP	7.3	0.283
	BLYP-D3	8.3	0.283

Radium (Ra) is an important element to be considered with regard to the disposal of radioactive waste and environmental problems related to uranium (U) ores because Ra is formed by the decay of U and thorium (Th). However, the fundamental properties of Ra, such as hydration structure, remained unclear because of the difficulty in conducting experiments on Ra. In this study, barium (Ba), an analog element of Ra was examined. Ba is an alkaline earth metal element, similar to Ra, and its ionic radius is close to that of Ra<sup>2+</sup>. Because of these similarities, Ra and Ba have similar chemical properties. The purpose of this study is to investigate the hydration structure of Ba<sup>2+</sup> via extended X-ray absorption fine structure (EXAFS) and *ab initio* molecular dynamics (AIMD) analyses.

EXAFS is a powerful tool to directly reveal the local structure of the target element. The strengths of EXAFS are its high applicability and element selectivity. This study conducted EXAFS measurement for the Ba K-edge at beamline NW10A in Photon Factory Advanced Ring (PF-AR). The measured sample was a 0.5-M solution of barium nitrate, stored in a plastic bag. The obtained spectrum is shown in Fig.9-7.

For AIMD simulations, the exchange-correlation (XC) functional is essential. Previous studies showed that the recently developed strongly constrained and appropriately normed

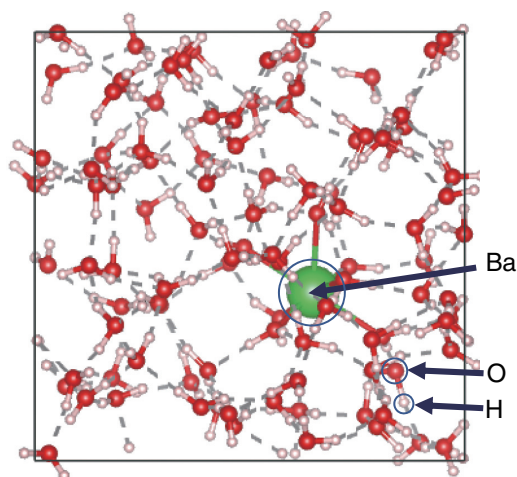


**Fig.9-8 Snap shot of the *ab initio* molecular dynamics (AIMD) simulation**

This cubic cell with  $L = 1.4457$  nm containing one Ba<sup>2+</sup> and 100 water molecules were used for the AIMD simulation for 60 ps. The results of the AIMD simulation are listed in Table 9-1.

(SCAN) functional is appropriate for simulating the hydration structures of monovalent ions. Therefore, we considered that the SCAN functional suitable also for divalent ions such as Ba<sup>2+</sup>. In this study, the commonly used Becke–Lee–Yang–Parr (BLYP) and BLYP with dispersion effect (BLYP-D3) functionals were used for comparison in addition to the SCAN functional (Fig.9-8).

The EXAFS and AIMD studies independently revealed the hydration structure of Ba<sup>2+</sup>, the number of water molecules in the first hydration shell (i.e., coordination number; CN), and the average distance between Ba<sup>2+</sup> and its neighboring oxygen atoms (Table 9-1). Therefore, the values obtained by AIMD simulation with the SCAN functional were the closest to those obtained by EXAFS. These results imply that the SCAN functional is appropriate for simulating the hydration structures of divalent ions, and hence, it is expected to be applicable for other divalent ions such as Ra<sup>2+</sup>. As future work, the methods used in this study will be applied for examining the hydration structure of Ra<sup>2+</sup> and quantitative comparison between Ba<sup>2+</sup> and Ra<sup>2+</sup>.

This study was conducted in collaboration with the University of Tokyo and Osaka University and supported by JSPS KAKENHI Grant-in-Aid for Research Activity Start-up (JP19K23432).

(Akiko Yamaguchi)

#### Reference

Yamaguchi, A. et al., Hydration Structures of Barium Ions: *Ab Initio* Molecular Dynamics Simulations Using the SCAN Meta-GGA Density Functional and EXAFS Spectroscopy Studies, *Chemical Physics Letters*, vol.780, 2021, 138945, 5p.

## Development of Technology and Human Capacity Building in the Fields of Nuclear Nonproliferation and Nuclear Security to Support the Peaceful Use of Nuclear Energy

The Integrated Support Center for Nuclear Nonproliferation and Nuclear Security (ISCN) conducted numerous activities of technological and human resources development related to nuclear nonproliferation and security in cooperation with affiliated domestic and overseas institutions toward establishing a world without the threat of nuclear weapons or nuclear terrorism (Fig.10-1).

### Technology Development for Japanese and International Applications

Numerous technologies are being developed to strengthen nuclear nonproliferation and security in line with domestic and international trends. A current project on nuclear material detection and measurement includes the development of a nondestructive assay technology to measure nuclear material retaining high radiation levels by using an external pulsed neutron source (Topic 10-1) and conducting wide-area monitoring to strengthen nuclear security at large-scale events. Nuclear forensics technology used to identify the origin and processing history of nuclear materials used in criminal acts has been improved. The development of artificial intelligence-based small, low-cost detectors for first responders following an act of nuclear terrorism and forensic nuclear signature analyzers is ongoing. These developments will help to improve nuclear forensic capabilities through international joint sample analysis exercises. Furthermore, methodologies to evaluate and reduce the attractiveness of nuclear or radioactive material for nuclear terrorism are being developed in collaboration with the United States of America (U.S.).

### Policy Research Based on Technical Expertise

Based on requests from related administrative agencies, ISCN continually researches and investigates the technical processes of methods for disposing nuclear materials that can be weaponized and rendering inoperable or dismantling materials manufacturing facilities and verifying them from the viewpoint of effective and efficient denuclearization, with reference to the case research and factor analysis for achieving the past denuclearization addressed by March 2021 and the ISCN updates “Nuclear Nonproliferation Pocketbook” and “Nuclear Nonproliferation Trends.”

### Capacity-Building Support

The ISCN has conducted capacity-building support activities targeting Asian countries since 2011. As of March 2021, about 5,300 participants—mainly from Asian countries including Japan—have joined the ISCN training activities on nuclear nonproliferation

(safeguards) and nuclear security. In fiscal year 2021, despite the persisting influence of COVID-19 pandemic, the ISCN implemented online methods, including a physical–virtual hybrid style, to continue supporting capacity building. The ISCN also developed materials using videos to provide more effective online trainings. These capacity-building support activities have contributed to human resource development in Asia and have received high praise internationally and domestically.

### Contributions to the International Verification Regime for CTBT

To establish a global verification regime for nuclear testing, the JAEA has operated provisionally the international monitoring system facilities of the Comprehensive Nuclear-Test-Ban Treaty (CTBT) and the national data center. Additionally, based on the voluntary contribution of the Government of Japan to the CTBT Organization (CTBTO) in February 2017, a joint radioactive noble-gas measurement project by the JAEA and CTBTO has been conducted in Horonobe in Hokkaido and Mutsu in Aomori since 2018 for strengthening the capability of the CTBTO to detect nuclear tests. This project continues observations to elucidate the behavior of the radioactive xenon background, mainly in the East Asian region, and is making a significant contribution to realizing national policies. It has been agreed to extend the duration of the project until March 2024 at most.

### Support for the JAEA’s Transportation of Nuclear Fuels and Procurement of Research Reactor Fuels

The ISCN coordinates and supports the research and development centers of the JAEA by procuring and transporting the necessary fresh fuel for research reactors and then transporting the spent fuel. The ISCN has been contributing to the Global Threat Reduction Initiative (GTRI), which has been strengthening global nuclear security by promoting the systematic return of highly enriched uranium to the US.

### Efforts to Promote Public Understanding on Nuclear Nonproliferation and Nuclear Security

The ISCN promotes the understanding of nuclear nonproliferation and nuclear security at home and abroad by delivering the ISCN Newsletter that publishes articles on international trends and analyses of nuclear nonproliferation and nuclear security and ISCN activities and by hosting the International Forum on Peaceful Use of Nuclear Energy.

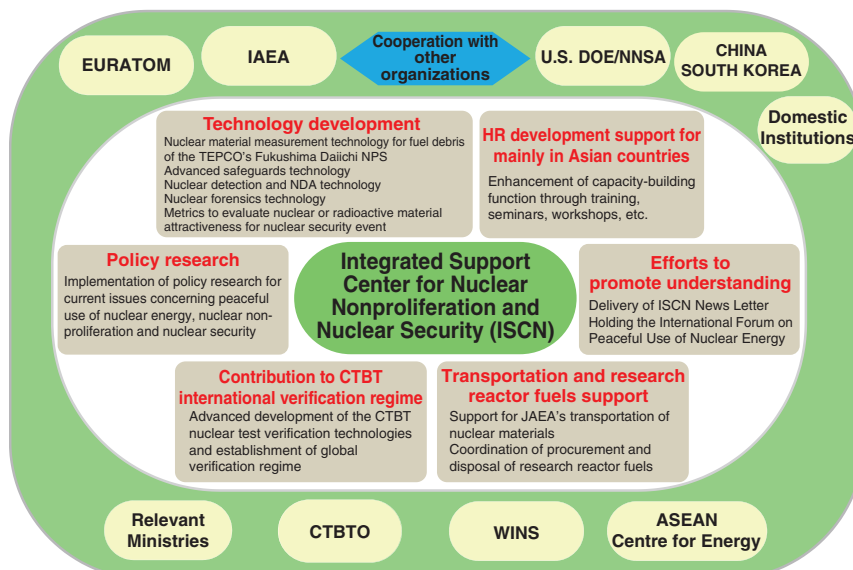


**Fig.10-1 Summary of the activities of the ISCN and affiliated institutions**

The ISCN has played an active role in strengthening nuclear nonproliferation and nuclear security in cooperation with affiliated domestic and overseas institutions.

# 10-1 Development of a Compact Nondestructive Analysis System for Measuring Nuclear Material

## — Demonstration of Neutron Resonance Transmission Analysis System Using a Laser-Driven Neutron Source —

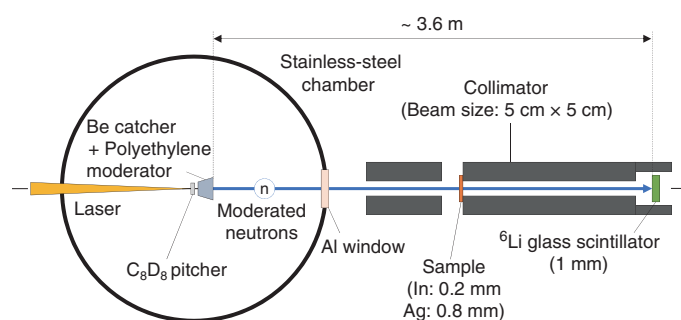


**Fig.10-2 Experimental setup of neutron transmission measurements using the Osaka laser-driven neutron source (LDNS)**

When a  $C_8D_8$  pitcher was irradiated by a pulsed laser, deuterons were generated and accelerated. The accelerated deuterons were injected into the Be catcher, and fast neutrons were produced. The fast neutrons were slowed down by a moderator and transmitted through a pair of thin sheets of indium and silver samples, which acted as mock nuclear materials. The transmitted neutrons were detected by a neutron detector installed at flight distance of 3.6 m.

To ensure the peaceful use of nuclear power, all states worldwide has undertaken the measurement of the amount of nuclear material and balance management (nuclear material accountancy). The amount of nuclear materials to be monitored by regulators is increasing with the expansion of the use of nuclear power. Therefore, to successfully monitor such nuclear materials with limited human resources, the measurement process for nuclear materials should be efficient and nondestructive analysis (NDA) systems have been used. However, installing such systems in existing nuclear facilities is difficult because the conventional systems for the accurate measurement are large. In addition, technologies for measuring nuclear fuels for new-generation reactors and highly radioactive nuclear materials are required. To meet these demands, we are developing a neutron resonance transmission analysis (NRTA) system using a laser-driven neutron source (LDNS) for miniaturizing the NDA system.

The neutron energy distribution is obtained by measuring the time-of-flight (TOF) of neutrons from a pulsed neutron source to a detector. The energy distribution of neutrons transmitted through a sample (TOF spectrum) shows the resonance dips corresponding to the nuclear reaction probability because a nucleus has large probabilities of reactions at inherent neutron resonance energies. The positions and depths of the resonance dips are determined by the nuclides and their amount in the sample. Therefore, nuclear materials in the sample can be measured by analyzing the TOF spectrum. This technique is effective for measuring highly radioactive nuclear materials such as spent nuclear fuels.

In TOF measurement, longer neutron flight distance and shorter neutron pulse width contribute to better energy resolution. However, it is desirable to shorten the flight distance

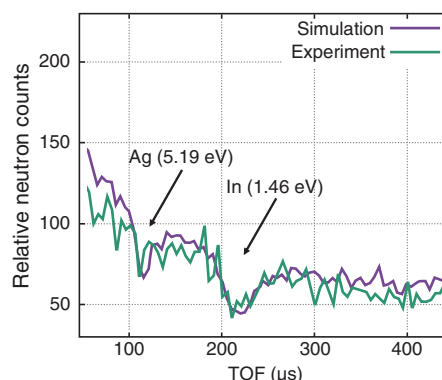


**Fig.10-3 Time-of-flight (TOF) spectra from experimental and simulation results**

The resonance dips of indium and silver can be observed in the neutron TOF spectra. This result suggests that the nuclides in the sample were successfully identified by neutron resonance transmission analysis (NRTA) and that LDNS is applicable for NRTA.

in terms of downsizing a system, and a neutron source with a much shorter pulse width is required for accurate measurement. Therefore, we focused on an LDNS that can generate neutrons with a short pulse width and is expected to be miniaturized with the rapid advancement laser technology.

To realize a compact (short flight distance) NRTA system with an LDNS, we developed a neutron detector with both low gamma-ray sensitivity and high neutron detection efficiency. We also developed a data acquisition system. The goal was to deal with both increasing gamma-ray background events and the large number of neutrons detected per unit time (i.e., high counting rate). We also designed a moderator to effectively slow down fast neutrons by performing a Monte Carlo simulation to take advantage of the short pulse width of LDNS. Additionally, we conducted a neutron transmission experiment using an LDNS developed by Osaka University to demonstrate the applicability of LDNS to NRTA. The experimental setup and measured TOF spectra are shown in Figures 10-2 and 10-3, respectively. The experimental result shows trends similar to those observed in the simulation result. Further, resonance dips indicating the presence of indium and silver were observed in the TOF spectrum. This result implies that the NRTA system equipped with the LDNS successfully identified the nuclides in the sample. Through the present research, we demonstrated that a miniaturized NDA system can be expected in the near future.

This research was implemented under the subsidy for “The promotion of strengthening nuclear security and the like”, supported by MEXT.

(Kota Hironaka, Jaehong Lee)

### Reference

K. Hironaka et al., Demonstration of a Neutron Resonance Transmission Analysis System Using a Laser-Driven Neutron Source, The 42nd Annual Meeting of INMM Japan Chapter, Online, 2021, 4p.



## **JAEA R&D Review 2022-23**

**URL:** <https://rdreview.jaea.go.jp/>

---

### **Published by**

Japan Atomic Energy Agency in January 2023

### **Editorial Board**

**Chief editor:** Michio Yoshizawa

**Editors:** Yosuke Iyatomi, Yoshio Suzuki, Mitsuo Koizumi, Tadahiro Washiya, Kazuki Iijima, Yasuhiro Chimi, Katsuhisa Nishio, Hideo Harada, Yasuji Morita, Yasuo Nishihata, Kenji Sakai, Seiji Kitamura, Hiroaki Takegami, Makoto Terauchi, Takashi Mizuno, Kazuhiko Sato

---

This publication is issued by Japan Atomic Energy Agency (JAEA) on a yearly basis. Inquiries about availability and/or copyright of the contents in this publication should be addressed to Institutional Repository and Utilization Section, JAEA Innovation Hub, JAEA.

**Address:** 2-4 Shirakata, Tokai-mura, Naka-gun, Ibaraki-ken 319-1195, Japan

**Phone:** +81-29-282-6387, **Facsimile:** +81-29-282-5920, **e-mail:** [ird-seika\\_shi@jaea.go.jp](mailto:ird-seika_shi@jaea.go.jp)

All Rights Reserved by JAEA ©2023

## About the Cover Design

The cover design depicts white hexagons that are similar to a tortoise-shell pattern. This represents the ancient Japanese symbol of the desire for long life. Coincidentally, this is also the shape of the core fuel assemblies in the high-temperature engineering test reactor, “HTTR”.

The top left figure shows a three-dimensional (3D) map visualizing the air dose rate and highly contaminated region near Unit 1/2 exhaust stack at TEPCO’s Fukushima Daiichi NPS (1F). The bottom right figure shows HTTR-Hydrogen Production Test Facility.

The 3D map visualizes the radioactive contamination situation within the 1F site and is realized by the integrated Radiation Imaging System (iRIS), which comprises a combination of technologies from different fields, including radiation measurement. This system contributes to the reduction of radiation exposure of workers and work planning. Further details can be found on page 23 in Chapter 1, Topic 1-10.

The hydrogen production project utilizing HTTR heat was launched in FY2022 to establish the technology connecting a reactor with a hydrogen production facility. Further details can be found on page 62 in Chapter 6, Highlight.



### Other Publications

Industrially applicable patented technology and know-how within the intellectual property owned by JAEA can be found on “JAEA Technology Seeds”.

The activity status of the whole agency, including CSR, can be found in the annual report, “Japan Atomic Energy Agency 2022 (Business Report FY2021)”.